Dissertation zur Erlangung des Doktorgrades
der Fakultät für Chemie und Pharmazie
der Ludwig-Maximilians-Universität München

Exploring the Interactions of Engineered Antibodies with FcRn and TRIM21 for New Avenues in Antibody Design, Analysis, and Gene Therapy Applications

Johannes Reusch

aus

Gießen, Deutschland

2024

Erklärung

Diese Dissertation wurde im Sinne von § 7 der Promotionsordnung vom 28.November 2011 von HERRN PD DR. CHRISTIAN KLEIN betreut.

License

Eidesstattliche Versicherung

Diese Dissertation wurde eigenständig und ohne unerlaubte Hilfe erarbeitet.

München, 26.5.2024

JOHANNES REUSCH

Dissertation eingereicht am:	27.05.2024
1. Gutachter:	PD DR. CHRISTIAN KLEIN
2. Gutachter:	PD DR. GREGOR WITTE
Mündfliche Prüfung am:	15.07.2024

Contents

Acronyms

AAV	Adeno-Associated Virus
ADCC	Antibody-dependent cellular cytotoxicity
ADIN	antibody-dependent intracellular neutralization
AdV5	adenovirus type 5
APC	antigen-presenting cells
CM	carboxylmethyl-dextran
complementary determining region	CDR
DR	Dynamic Response
dsDNA	double stranded deoxyribonucleic acid
EC_{50}	half maximal effective concentration
Fab	fragment antigen-binding
Fc	Fragment crystallizable
FcR	Fc receptors
FcRn	neonatal Fc receptor
FR	framework regions
HC	heavy chains
HRV-14	human rhinovirus 14
HSPG	heparan sulfate proteoglycan
Ig	Immunoglobulin
IgG-IC	IgG immune complexes
IRM	interference reflection microscopy
iSCAT	interferometric scattering microscopy
ITR	inverted terminal repeat
K_D	equilibrium dissociation constant
kDa	kilodalton
k_{OFF}	off rate / dissociation rate constant
k_{ON}	on rate / association rate constant
LC	light chain
MAV-1	mouse adenovirus type 1
MHC	major histocompatibility complex
MP	Mass Photometry

NAbs	neutralizing antibodies
NK cells	Natural killer cells
ORF	open reading frame
PLA2	phospholipase A2
rAAV	recombinant Adeno-Associated Virus
RBCC-motif	RING-B-box-coiled-coil motif
RING	Really Interesting New Gene
RU	response unit
SLE	systemic lupus erythematosus
SPR	Surface Plasmon Resonance
SS-A	Sjogren syndrome-A
TIR	total internal reflection
TRIM21	tripartite motif-containing protein 21
VP	viral protein
WT	wildtype
β2m	beta-2 microglobulin

List of Publications

Peer-reviewed publications and manuscripts that are part of this cumulative thesis, reprinted in chapter 4.2 **(Publication I)** and chapter 5.2 **(Publication II)**:

Publication I

Johannes Reusch, Jan Terje Andersen, Ulrich Rant and Tilman Schlothauer

Insight into the avidity-affinity relationship of the bivalent, pH-dependent interaction between IgG and FcRn

mAbs, 2024

Publication II

Johannes Reusch, Linda Elise Franken, Jakob Then, Philippe Ringler, Joachim Butzer, Thomas Juroschek, Christian Klein, Tilman Schlothauer and Laurent Larivière

TRIM21 and Fc-Engineered Antibodies: Decoding its complex Antibody Binding Mode with Implications for Viral Neutralization

Manuscript under review, 2024

Abstract

Monoclonal antibodies (mAbs) have emerged as pivotal therapeutic agents, with their effectiveness hinging on complex pharmacokinetic properties and interactions with immune receptors. This thesis investigates the nuanced interplay between mAbs and two key receptors: the neonatal Fc receptor (FcRn) and the tripartite motif-containing protein 21 (TRIM21). FcRn is known to affect the serum half-life of mAbs, while TRIM21 is involved in antibody-dependent intracellular neutralization (ADIN). Research has often focused on the IgG-FcRn affinity, neglecting the combined impact of both affinity and avidity, as well as the potential role of TRIM21 in antiviral therapy through Fc engineering. The research presented in this thesis aims to deepen our understanding of mAb interactions with FcRn and TRIM21, focusing on the mechanisms that govern these interactions. It employs advanced methodologies to elucidate the relationship between affinity and avidity. Specifically, it investigates the impact of Fc modifications that alter interactions with FcRn, affecting serum half-life, and with TRIM21, which is involved in viral neutralization within cells. The findings aim to guide the development of more effective therapeutic antibodies, with broad implications for the treatment of diseases.

In the publication titled 'Insight into the Avidity-Affinity Relationship of the Bivalent, pH-Dependent Interaction Between IgG and FcRn,' we explore the intricate binding dynamics between IgG and FcRn, advancing beyond traditional analyses that consider only single-affinity interactions. Utilizing switchSENSE technology, which closely mimics the membrane orientation of FcRn, we conducted a comprehensive examination of both affinity and avidity across the broad endosomal pH spectrum (pH 5.8–7.4). Our findings reveal that the engineered IgG1-YTE (M252Y/S254T/T256E) variant demonstrates a critical affinity shift at pH 7.2, indicative of its enhanced design for FcRn interaction. It also exhibits a marked avidity switch at pH 6.2, which is absent at pH 7.4. This dual engagement capability distinguishes IgG1-YTE from the wild-type, demonstrating the impact of Fc engineering on binding properties. Our research emphasizes the importance of avidity in IgG recycling, which is dictated by the variable expression of FcRn and its higher density in endosomes, necessitating a 2:1 stoichiometry for an extended serum half-life. The switchSENSE platform emerges as a powerful analytical tool, superior to traditional surface plasmon resonance (SPR), capturing a full range of kinetic parameters and accurately differentiating between monovalent and bivalent binding modes. This methodological advancement is crucial for understanding the dynamics of IgG binding in physiological contexts. The superior binding characteristics of the YTE variant suggest improved pharmacokinetics, potentially leading to increased therapeutic efficacy through an optimized recycling mechanism. The variant's higher affinity and significant contribution to avidity, especially during endosomal acidification, result in more stable FcRn complex formation, a desirable feature for

antibodies engineered for extended serum half-life. The findings confirm the importance of pH-dependent binding in antibody design and have significant implications for the development of antibodies with improved recycling and extended half-life. Future research will utilize switchSENSE to further explore molecular interactions in various antibody mutants and formats, aiming to refine FcRn-mediated recycling for next-generation antibody therapies.

In our publication titled 'TRIM21 and Fc-Engineered Antibodies: Decoding its Complex Antibody Binding Mode with Implications for Viral Neutralization, we explore the complex role of TRIM21 within the immune system, focusing on its interaction with Fc-engineered antibodies and the subsequent impact on viral neutralization. Utilizing a combination of biosensor assays, mass photometry, electron microscopy, and structural predictions, our study dissects the intricate binding dynamics between TRIM21 and various antibody Fc variants, revealing a novel binding mechanism that is pivotal for developing effective viral neutralization strategies. Our investigation employs optimized SPR assays to establish precise affinities and avidities, underscoring the importance of assay conditions in accurately analyzing interactions. We demonstrate that TRIM21 PRYSPRY domains (monomers) bind symmetrically to a single IgG Fc homodimer in a non-cooperative manner, adhering to a 2:1 stoichiometry. This symmetry is consistent with crystallographic evidence of TRIM21 PRYSPRY-IgG interactions. Significantly, we identify that Fc mutations, such as YTE and HH (T307H, N434H), reduce TRIM21 binding while enhancing interaction with FcRn in a pH-dependent manner. This dual effect underlines the complexity of antibody engineering, where mutations can differentially influence receptor interactions, which is crucial for optimizing antibody recycling and immune defense. The mutation Y436A within the Fc CH2-CH3 domain notably decreases the affinity to both FcRn and TRIM21, with the latter by 180-fold. This mutation also demonstrates a pronounced shift from micromolar affinity to nanomolar avidity and the critical role of bivalent engagement. Our structural analysis indicates that TRIM21 undergoes a dynamic rearrangement upon Fc binding, likely influencing its immune function. We propose a novel two-step binding mechanism whereby TRIM21's initial attachment to an Fc site facilitates a conformational change, enhancing its interaction with a second Fc site through increased PRYSPRY domain mobility. This process significantly boosts avidity, which is essential for effective antibody function. Using adeno-associated virus (AAV) as a model, our findings suggest that antibody clustering on the virus is possible and could activate TRIM21's E3 ligase activity, demonstrated as a crucial step in virus neutralization. These insights are vital for advancing antibody engineering and understanding TRIM21's role in immune responses, offering significant implications for therapeutic applications.

Keywords: monoclonal antibodies, FcRn, TRIM21, affinity, avidity, antibody Fc engineering, therapeutic antibodies, immune signaling, viral neutralization

1

Structure of the Thesis

This introductory chapter outlines the structure of this cumulative thesis, providing a roadmap for readers to navigate through the subsequent chapters.

This PhD thesis, structured as a cumulative compilation of scientific research, aims to contribute to the field of antibody Fc engineering and their applications in immunotherapy. The thesis specifically focuses on the interactions between Fc-engineered IgG antibodies and FcRn/TRIM21, two Fc receptors with overlapping binding sites, but counteracting functions. The structure of this thesis is carefully designed to guide the reader through a coherent journey from theoretical foundations to empirical findings and future perspectives.

Chapter 2 lays the groundwork necessary for understanding the complexities of the interactions between the FcRn/TRIM21 and Immunoglobulin G. This chapter delves into the biochemical and molecular principles underpinning FcRn/TRIM21-IgG affinity and avidity, elucidating how these interactions influence antibody recycling and viral degradation as well as highlighting major technologies to study complex molecular interactions. It provides a comprehensive review of the existing literature, highlighting key studies that have shaped our current understanding of FcRn/TRIM21 related antibody dynamics. By establishing this theoretical basis, Chapter 2 sets the stage for the empirical research presented in Chapters 4 and 5, ensuring readers are well-equipped with the knowledge required to grasp the implications of the findings. The overall aims of this cumulative thesis are highlighted in **Chapter 3**.

In **Chapter 4**, the first publication titled "Insight into the Avidity-Affinity Relationship of the bivalent, pH-dependent Interaction between IgG and FcRn" is presented (Supplementary Information **Chapter 7.1**). This study is a comprehensive investigation of the relationship between affinity and avidity in the binding of IgG to FcRn and its implications for the pharmacokinetics and functionality of therapeutic antibodies. Through experimental research, this chapter provides new insights into how modifications in the Fc region of antibodies can alter their interaction with FcRn, especially in the context of the avid binding mode and the pH dependent transition from affinity to avidity, revealing a "pH-switch", potentially responsible for enhanced therapeutic efficacy. The findings contribute to a deeper understanding of the molecular determinants of antibody Fc effector performance, offering valuable information for the characterization and design of next-generation antibody therapeutics.

Chapter 5 introduces the second research article, titled "TRIM21 and Fc-Engineered Antibodies: Decoding its complex Antibody Binding Mode with Implications for Viral Neutralization" which is currently under submission (Supplementary Information **Chapter 7.2**). This paper expands on the themes of antibody functionality by exploring how TRIM21, a receptor involved in the immune response to pathogens, interacts with Fc-modified antibodies. The study examines the impact of various Fc modifications on the binding mode and efficacy of TRIM21-mediated antibody functions. The research offers implications for the development of antibody-based therapies that leverage TRIM21 for enhanced clearance of pathogens, using rAAV as model system to show antibody mediated clustering.

The final chapter, **Chapter 6**, sets the findings from the studies presented in Chapters 4 and 5, within a broader scientific and therapeutic context. It discusses the implications of the research for understanding antibody interactions and their impact on therapeutic antibody design. Additionally, this chapter interprets the findings in light of their potential to influence future research directions, highlighting the role of avidity in antibody functions and its relevance to effective antibody-based therapies. Suggestions for future research focus are proposed, paving the way for ongoing exploration in the field of antibody engineering and immunotherapy.

2

Introduction

This chapter explores the molecular details that govern the interactions between antibodies and two key immune regulatory proteins, FcRn and TRIM21. The theoretical framework presented is rooted in a multidisciplinary approach, drawing from the fields of immunology, biochemistry, and biophysics to elucidate the complex dynamics at play.

This introduction provides a comprehensive understanding of the mechanisms by which antibodies interact with FcRn and TRIM21, as elucidated by current research findings. It also examines how these interactions can be harnessed to enhance the design and function of therapeutic antibodies. The integration of theoretical knowledge with empirical data serves as the foundation for advancing our understanding of antibody-based therapies and their potential to transform the landscape of medical treatment.

2.1 Antibodies

Antibodies, also known as immunoglobulins (IgGs), are a cornerstone of the adaptive immune system, playing a critical role in the identification and neutralization of pathogens. Their unique ability to specifically recognize and bind a vast array of antigens makes them indispensable not only for immune defense but also as a basis for the development of targeted therapeutic agents. Target interaction is mediated by their distinct structure, which is highly conserved across different species and isotypes and yet allows for immense diversity in antigen recognition.

The functional versatility of antibodies is further modulated by their Fc (Fragment crystallizable) region. This region constitutes a crucial element in the immune response, contributing significantly to the diverse effector functions of these molecules. It plays a pivotal role in mediating interactions with cellular receptors, such as FcRn and TRIM21, which can impact their stability, distribution, and efficacy within the organism.

2.1.1 Structure and Function

Antibodies represent an integral component of the adaptive immune system, serving as specialized proteins that identify and neutralize pathogenic entities. Structurally, antibodies are categorized within the broader family of proteins known as immunoglobulins (Ig), which are further subclassified into five distinct isotypes: IgA, IgD, IgE, IgG, and IgM (1, 2). Among these, IgG is the predominant antibody isotype circulating in the bloodstream. IgG antibodies are synthesized and secreted by plasma cells, which are differentiated B-lymphocytes. These plasma cells originate from B cells that have been activated by antigen exposure, typically within secondary lymphoid organs such as the spleen and lymph nodes (3, 4). Once produced, IgG antibodies are released into the bloodstream and lymphatic system, where they play a pivotal role in immune surveillance and pathogen neutralization.

The diversity of antibody classes, or isotypes, further expands their functional roles within the immune system. IgG antibodies are divided into four subclasses: IgG1, IgG2, IgG3, and IgG4. These subclasses are characterized by subtle variations in their heavy chain constant regions, which influence their binding affinities for Fc receptors, as well as their serum half-lives and interactions with other immune components, including complement proteins. Each subclass has unique functional characteristics that tailor the immune response to different types of pathogens and antigens (5-8).

Most therapeutic antibodies are based on the IgG isotype, particularly IgG1, due to its well-understood properties, long half-life in circulation, and ability to effectively recruit immune effector functions (4). Consequently, this work focuses on the characterization of IgG1.

The structure of an IgG antibody is highly conserved and yet remarkably adaptable, allowing for the specific recognition of antigens. As depicted in **Figure 1**, the archetypal structure of an IgG1 antibody is tetrameric, comprising four polypeptide chains, characterized by a total molecular weight of approximately 150 kilodaltons (kDa). The basic unit consists of two heavy chains (HC) of 50 kDa each and two light chains (LC) of 25 kDa each. These chains are conjoined via a pair of disulfide linkages between both HC and a further pair between HC and LC, culminating in the formation of a Y-shaped molecule. The heavy chain is further delineated into three constant (C) domains (C_H1, C_H2, and C_H3) and one variable (V) domain (V_H). In contrast, the light chain is composed of a single constant (C_L) and a single variable (V_L) domain. This structural configuration, consisting of variable and constant regions, dictates both the bivalent antigen binding specificity and effector function (4, 9).

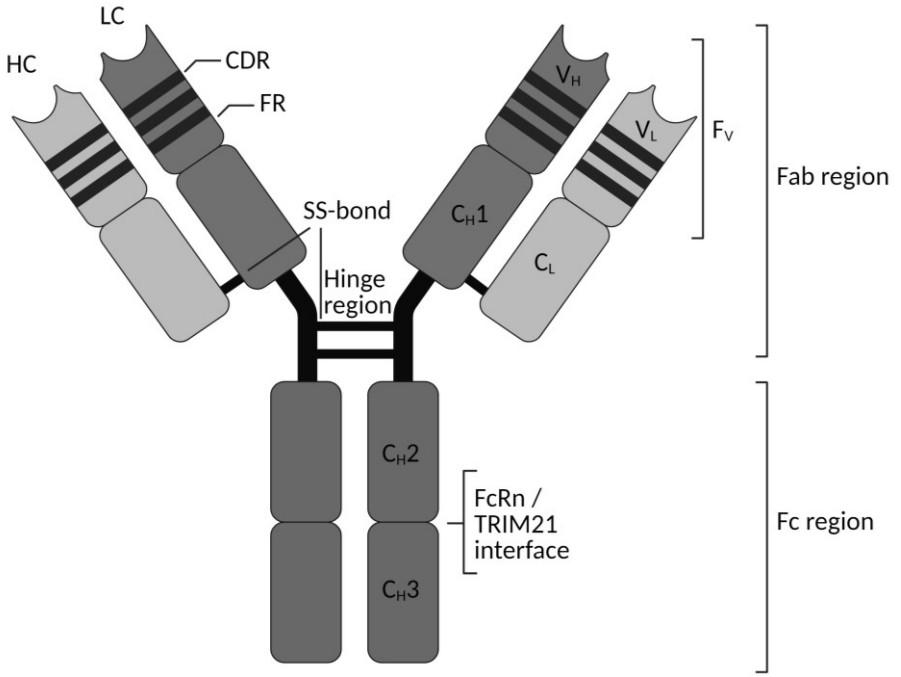

Figure 1. Structure of a Human IgG1 Antibody. This schematic illustrates the Y-shaped structure of a human Immunoglobulin G1 (IgG1) antibody, with a molecular weight of approximately 150 kDa. It is composed of two identical heavy chains (HC, each 50 kDa) and two identical light chains (LC, each 25 kDa), which are interconnected by two disulfide bonds in the hinge region. Additionally, each heavy and light chain pair is joined by a single disulfide bond. The heavy chain features three constant domains (C_H1, C_H2, and C_H3) and one variable domain (V_H), whereas the light chain contains one constant (C_L) and one variable domain (V_L). The variable domains of both chains include three complementarity-determining regions (CDRs) responsible for antigen binding, interspersed with four framework regions (FRs) that maintain structural integrity. Functionally, the antibody is divided into two regions: the antigen-binding fragment (Fab), which includes the variable and the first constant domains, and the crystallizable fragment (Fc), comprising the remaining constant domains. (Created with BioRender.com.)

Antibodies are structurally differentiated into two principal regions: the Fab (fragment antigen-binding) and the Fc (fragment crystallizable) regions. The Fab region, responsible for antigen recognition, is tethered to the Fc region through a flexible hinge region. Within the Fab portion, each variable domain is comprised of an antigen-binding site formed by three hypervariable loops known as complementarity-determining regions (CDRs), flanked by four framework regions (FRs). Especially the CDRs exhibit a high degree of variability, conferring upon the antibody its specificity - the capacity to distinguish between distinct antigens - and affinity, which is the strength of the antibody's binding to its antigen (10-12). The Fc region, being constant, is capable of engaging with various effector molecules such as proteins of the complement system and Fc receptors (FcRs).

Antibodies mediate their effects through various mechanisms:

Fab-Related Functions:

- Antigen Binding: The Fab region is responsible for recognizing and binding to specific antigens. Each Fab region has a unique binding site that is complementary to a particular antigen's structure, allowing for specificity in the immune response (5).
- Neutralization: The Fab region binds specifically to pathogens or their toxins, preventing their attachment to host cells or neutralizing their biological activity (13).
- Immune complex formation: The antigen-binding sites within the Fab regions can engage multiple antigens, forming complexes that can be cleared from circulation, thereby preventing the spread of infection (14).

Fc-Related Functions:

- Opsonization: The Fc region of IgG is recognized by Fc receptors on phagocytes, such as macrophages and neutrophils, facilitating the destruction of the opsonized pathogen (15).
- Antibody-Dependent Cellular Cytotoxicity (ADCC): A mechanism of the immune system whereby immune cells that possess Fc receptors/FcγRs (such as natural killer (NK) cells, macrophages, and neutrophils) recognize and kill target cells (such as virus-infected cells or tumor cells) that are coated with antibodies. The Fc region of the antibody binds to the Fc receptor on the immune cell, triggering the release of cytotoxic substances that lead to the destruction of the target cell (11, 16).
- Antibody-Dependent Cellular Phagocytosis (ADCP)/Phagocytosis: ADCP is similar to ADCC but involves the engulfment and internalization of target cells or particles by phagocytic immune cells through Fc receptor recognition. In ADCP, the target cells or particles are opsonized with antibodies, which facilitate their recognition by Fc receptors on phagocytes, leading to phagocytosis and subsequent degradation of the targets within the phagocytes (17).
- Complement Activation: The Fc region can activate the classical complement pathway, resulting in pathogen lysis or enhanced phagocytosis due to opsonization with complement proteins (10, 18).
- Regulation of Antibody Half-life: Interaction with the neonatal Fc receptor (FcRn) in various cell types protects IgG from degradation, recirculating it into the bloodstream and prolonging its half-life (19).
- Intracellular Neutralization: The Fc region can be involved in intracellular immunity through the interaction with the tripartite motif-containing protein 21 (TRIM21). When viruses or other pathogens enter the cytosol, TRIM21 can bind to the Fc region of antibody-coated pathogens, targeting them for proteasomal degradation (20).

These delineated functions demonstrate the dual role of the antibody's distinct regions: the Fab region is primarily responsible for antigen specificity and direct neutralization, while the Fc region mediates various effector functions that enhance the immune response. The roles of FcRn and TRIM21 are discussed in detail in subsequent chapters.

2.1.2 Therapeutic Antibodies

The therapeutic potential of antibodies has been harnessed to create monoclonal antibodies (mAbs), which are designed to target specific antigens with high precision. To date, mAbs represent a major class of biopharmaceuticals that have revolutionized the treatment of a myriad of diseases, including cancer, autoimmune disorders, and infectious diseases (21, 22). The evolution of therapeutic antibodies can be traced back to the development of hybridoma technology by *Köhler and Milstein in 1975* (23), which enabled the production of monoclonal antibodies with predefined specificity. This groundbreaking innovation laid the foundation for the subsequent advancements in antibody engineering that have expanded the therapeutic potential of mAbs.

IgG1 is the most abundant subclass in human serum and has been extensively engineered to develop mAbs (24). The specificity of mAbs is one of their most compelling attributes, as they can be designed to bind with high affinity to unique molecular targets, such as proteins expressed on the surface of cancer cells or inflammatory cytokines. This targeted approach allows for precise intervention in disease pathways while minimizing off-target effects, thereby offering a significant advantage over traditional small-molecule drugs (24).

Applications of mAbs as therapeutic modality have grown extensively, with numerous antibodies now approved for clinical use. This trend is evidenced by the late-stage commercial clinical pipeline, which has grown by approximately 20% in 2022. Furthermore, as of mid-November 2022, regulatory agencies worldwide reviewed at least 24 investigational antibody therapeutics (25). These mAbs can function through various mechanisms, including direct inhibition of target molecules, recruitment of immune effector functions to eliminate diseased cells, and modulation of immune system activity.

Advances in antibody engineering have further enhanced the efficacy, safety, and half-life of therapeutic mAbs. Techniques such as humanization, which involves grafting murine antibody CDRs onto human frameworks, have reduced immunogenicity and improved the clinical performance of these molecules. Additionally, the development of fully human antibodies through phage display and transgenic mouse technologies has circumvented the issues associated with human anti-mouse antibody responses (26, 27).

Fab engineering alters an antibody's specificity and selectivity, while Fc engineering is crucial for adjusting the Fc region to regulate interactions with immune components like FcγRs, FcRn, and TRIM21. The rationale behind Fc engineering is to enhance therapeutic efficacy by increasing effector function e.g., improving antibody-dependent cellular cytotoxicity (ADCC) and phagocytosis (ADCP), extending or shortening serum half-life, and reducing

immunogenicity. Modifications to the Fc region can significantly impact an antibody's function. Changes that improve interactions with FcRn can extend the antibody's half-life in circulation, allowing for sustained therapeutic activity (28). Furthermore, adjusting the binding strength to TRIM21 can either improve antigen cross-presentation, or reduce the neutralization of viral vectors used in gene therapy, thereby preserving the delivery of therapeutic genes (29, 30).

Moreover, antibody engineering can be applied to generate bispecific antibodies, which are capable of engaging two different antigens simultaneously, thereby facilitating novel therapeutic strategies such as redirecting immune cells to tumor sites or simultaneously blocking two pathogenic pathways (31, 32).

In summary, therapeutic mAbs and their engineered counterparts represent a significant milestone in the field of molecular medicine. Through the precise targeting of disease-associated antigens and the manipulation of antibody effector functions, these biologics offer a powerful and versatile platform for the development of next-generation therapeutics. The continued innovation in antibody engineering, particularly within the Fc domain, holds promise for the creation of more effective and safer treatments for a broad spectrum of diseases.

2.2 FcRn and TRIM21: An Overview

In the realm of IgG biology, both FcRn and TRIM21 exhibit a strong overlap for binding within the C_H2-C_H3 interdomain region of the antibody's Fc fragment. Despite sharing this binding site, the two receptors execute distinctly divergent functions. FcRn, a major histocompatibility complex class I-related (MHC-I) receptor, is instrumental in the recycling and transcytosis of IgG antibodies, thus regulating their serum half-life and ensuring a sustained immune surveillance. This is achieved through its role in the protection and transport of IgG across cellular barriers. Conversely, TRIM21, a member of the tripartite motif family, functions as an intracellular antibody receptor that mediates the ubiquitination and subsequent degradation of antibody-bound pathogens, playing a critical role in the immune defense against intracellular challenges. This dichotomy in function demonstrates the intricate nature of the immune system's utilization of conserved structural motifs to mediate a diverse array of protective mechanisms.

2.2.1 Origin, Structure and Expression of FcRn

The neonatal Fc receptor was first identified and characterized in the context of neonatal immunity. Its discovery dates back to the 1960s when Dr. Brambell and colleagues proposed the existence of a receptor responsible for the transfer of maternal immunoglobulin G (IgG) across the placenta to the fetus and through the gut epithelium to the neonate (33, 34). Also known as Brambell receptor (FcRB), this receptor-mediated transport was hypothesized to provide passive immunity to the offspring by endowing them with a repertoire of maternal antibodies against pathogens (35). Subsequent research in the 1980s and 1990s led to the molecular identification and cloning of FcRn (36).

Human FcRn is a heterodimeric protein composed of two distinct subunits: a MHC class I-like alpha chain (α-FcRn, 42 kDa) and a smaller beta-2 microglobulin (β2m) light chain (12 kDa) (36, 37). The membrane-bound alpha chain is structurally similar to MHC class I molecules and consists of three extracellular domains (α1, α2, and α3), a transmembrane region, and a short cytoplasmic tail, as depicted in **Figure 2**. The β2m is non-covalently associated with the alpha chain and is essential for the proper folding, stability, and function of the receptor (37, 38). The α1 and α2 domains of the alpha chain form a platform that resembles the peptide-binding groove of classical MHC class I molecules (39-42). However, in FcRn, this groove does not bind peptides but is involved in the high-affinity binding to the Fc portion of IgG antibodies (39, 40, 43, 44).

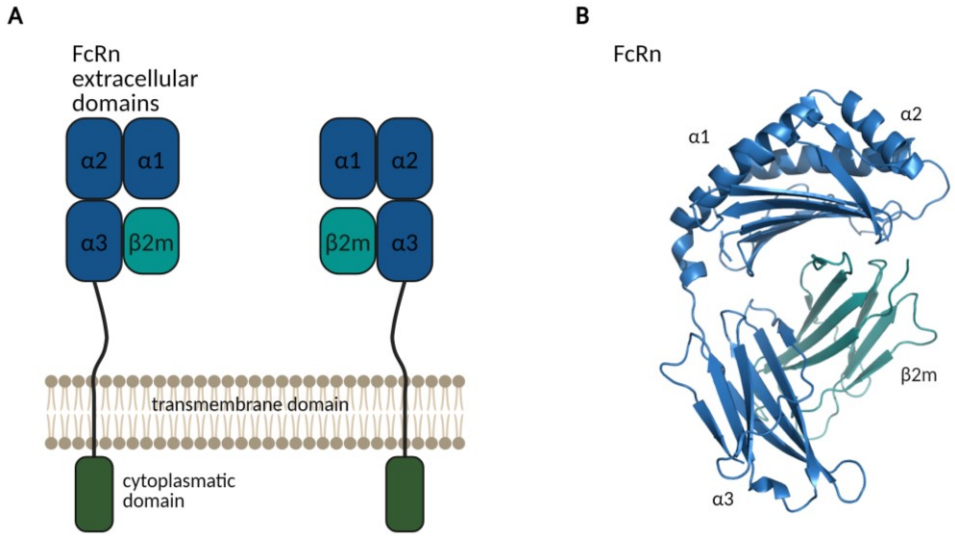

Figure 2. Structure of FcRn. A) This schematic shows the membrane-bound FcRn heterodimer, detailing its extracellular domains (α1, α2, and α3), the cytoplasmatic domain, and the associated β2-microglobulin (β2m) light chain.. **B**) The ribbon diagram depicts the human FcRn-β2m complex, with subdomains labeled according to the Protein Data Bank (PDB) entry 1EXU. These figures have been adapted from (19). (Created using PyMol 2.5.2 and BioRender.com.)

In humans, FcRn has as a broad expression profile across various cell types and organs, including endothelial and epithelial cells (45). Endothelial cells lining the blood vessels are pivotal for the recycling and transcytosis of IgG antibodies. In the epithelial cells of the

placenta, FcRn facilitates the transfer of maternal antibodies to the developing fetus, providing passive immunity (46-48). Additionally, FcRn expression is observed in epithelial cells of the intestine, liver, lung, and kidney, as well as in professional antigen-presenting cells such as dendritic cells and macrophages (49-51). While FcRn shows a basal level of surface expression on plasma membranes (52, 53), its primary functional location is within the endosomal compartments of cells (54). There, it prevents IgG from being directed to lysosomal degradation. The widespread expression of FcRn across diverse tissues demonstrates its integral role in maintaining immune surveillance and regulating the systemic levels of IgG and albumin.

2.2.2 Function and Role of FcRn in Immune Response

FcRn is a multifaceted protein that plays several roles in critical, physiological functions such as the maintenance of immune system homeostasis and the regulation of physiological processes. One primary function of FcRn is its interaction with IgG antibodies and albumin, which facilitates their protection from lysosomal degradation. This interaction also regulates and maintains their serum levels (40, 55-61). Another vital role of FcRn is in the passive transfer of immunity from mother to offspring. During pregnancy, FcRn in the placental syncytiotrophoblast cells binds maternal IgG and mediates its transplacental transport. This process provides the fetus with a repertoire of maternal antibodies that confer protection against pathogens in the early stages of life (46-48).

FcRn is also involved in the transport of IgG across mucosal barriers, such as those in the intestinal tract. This transport contributes to immune surveillance and the establishment of mucosal immunity (62-67).

Additionally, FcRn is implicated in the regulation of antigen presentation, a process essential for T cell activation. Traditional antigen presentation involves MHC class II molecules presenting antigens to CD4+ T helper cells, which then provide help and regulatory functions. In contrast, antigen cross-presentation refers to the ability of certain antigen-presenting cells (APCs), such as dendritic cells, to present extracellular antigens on MHC class I molecules, thereby activating CD8+ T cells. This activation is crucial for initiating cytotoxic responses against viral and tumor antigens (68-71). Through the involvement of FcRn in antigen (cross)- presentation, it plays a role in bridging innate and adaptive immunity. This contributes to the immune system's ability to combat intracellular pathogens and enhances the efficacy of antibody-based vaccines and immunotherapies.

The major function of FcRn in regulating IgG homeostasis is outlined in further detail. The underlying mechanism is schematically shown in **Figure 3**.

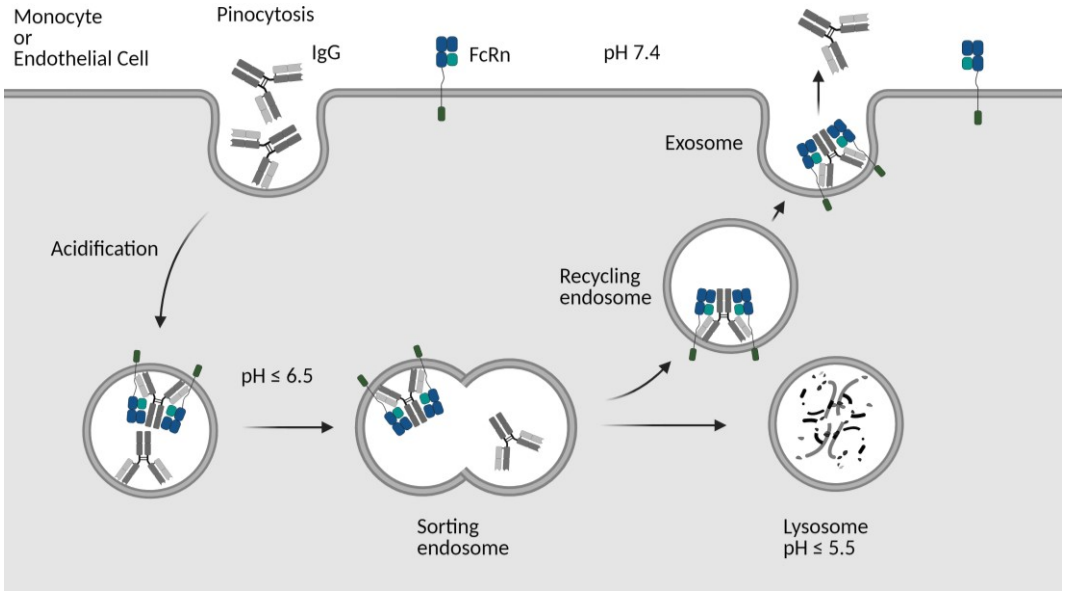

Figure 3. FcRn-Mediated IgG Recycling Mechanism. This schematic illustrates the process by which IgGs are internalized and recycled by cells such as monocytes, macrophages, or endothelial cells. At physiological pH (7.4), IgGs are taken up through pinocytosis, as they do not bind to FcRn at this pH. The subsequent acidification of endosomes to a lower pH facilitates the binding of IgGs to FcRn, which is believed to interact with both heavy chains of the IgG. FcRn then recycles the bound IgG back into the bloodstream. In cases where FcRn is saturated and cannot bind additional IgG, the unbound antibodies are directed to the lysosome for degradation at an acidic pH (≤ 5.5). Schematic adapted from (19, 50). (Created with BioRender.com.)

In humans, the subclasses IgG1, IgG2, and IgG4 exhibit a prolonged serum half-life of approximately 20-23 days, a characteristic predominantly attributed to the interaction of their Fc regions with FcRn (19). This recycling mechanism is critically dependent on pH variations, exhibiting negligible binding affinity at the neutral pH of 7.4, characteristic of the extracellular environment, and demonstrating robust binding at the acidic pH (pH ≤ 6.5), typical of endosomal compartments. Vascular endothelial cells, along with macrophages and monocytes, internalize IgGs and small IgG immune complexes (IgG-IC) through a non-specific, bulk endocytic process known as fluid-phase pinocytosis. The internalized IgG-containing vesicles then fuse with acidic endosome, where the lowered pH facilitates the binding of IgG to FcRn. The FcRn-IgG complex is then routed towards the cell surface, bypassing lysosomal degradation. Upon reaching the cell surface, the complex encounters the neutral pH of the bloodstream, prompting the release of IgG back into circulation (72, 73). This recycling process not only extends the half-life of IgG antibodies but also ensures the maintenance of adequate immunoglobulin levels for effective immune surveillance and pathogen neutralization.

The mechanistic basis for this pH-dependent binding lies in the structural design of the Fc region of IgG and FcRn itself. At an acidic pH, histidine residues within the Fc region become protonated, increasing their affinity for FcRn. This protonation induces conformational changes that enhance the interaction between IgG and FcRn, allowing the

complex to form. Conversely, at neutral pH, these histidine residues are deprotonated, leading to a conformational state that reduces affinity and promotes the dissociation of IgG from FcRn (43, 74, 75). The detailed mode of antibody binding to FcRn is described in Chapter **2.3.1 Mechanism of Antibody Binding to FcRn**.

2.2.3 Origin, Structure and Expression of TRIM21

Tripartite motif-containing protein 21 (TRIM21), also known as Ro52 or Sjogren syndrome (SS)-A, is a member of the tripartite motif (TRIM) family of proteins, which are characterized by a conserved RING domain, one or two B-box domains, and a coiled-coil region (RBCC-motif/family) (**Figure 4A and B**) (76, 77). TRIM21 was first identified as an autoantigen recognized by autoantibodies in patients with autoimmune diseases, particularly Sjögren's syndrome and systemic lupus erythematosus (SLE). The initial discovery of TRIM21 was closely linked to its role in autoimmunity, as the presence of anti-TRIM21 antibodies served as a diagnostic marker for these conditions (78-81). These autoantibodies can modulate TRIM21's function, potentially contributing to the dysregulation of immune responses observed in these conditions (82, 83). Subsequent characterization revealed that TRIM21 is ubiquitously expressed in various tissues and plays a prominent role in the immune system. This includes its relevance in other autoimmune diseases where autoantibodies against TRIM21 are present (84).

Beyond its association with autoimmune diseases, TRIM21 has been recognized for its involvement in antiviral immunity (85). It acts as an intracellular Fc receptor capable of binding to the Fc region of antibodies that are attached to viruses and other pathogens that have entered the cytosol (20, 86, 87). Upon binding, TRIM21 targets these antibody-coated pathogens for proteasomal degradation, effectively contributing to the intracellular neutralization of viruses (20). The identification and understanding of TRIM21's role in both autoimmunity and viral defense have made it a subject of interest in immunological research.

TRIM21 is a prominent member of the TRIM family and within the RING (Really Interesting New Gene) E3 ligase family. The TRIM family consists of approximately 100 members in humans (85, 88-90). While these proteins are involved in a variety of cellular functions and biological processes, including intracellular signaling, protein degradation, and immune response regulation, the majority of them exhibit functions in the context of innate immunity (89, 91).

The structural integrity and functional capacity of TRIM21 are attributed to its conserved domain arrangement (92). The N-terminal RING domain (**Figure 4C**), a zinc finger motif coordinating two zinc ions, is pivotal for its E3 ubiquitin ligase activity. This activity facilitates the ubiquitination of target proteins for subsequent proteasomal degradation (20, 93). Interactions between the RING domain and E2 conjugating enzymes, such as Ube2W and Ube2N/Ube2V2, are critical for initiating ubiquitin transfer (priming ubiquitin) and

synthesizing self-anchored K63-linked ubiquitin chains. This process is activated upon TRIM21's initial ubiquitination (94-96).

A distinctive tri-ionic motif within TRIM21 enhances the engagement with the Ube2N~Ub complex, a specificity determinant for Ube2N over other E2 enzymes, revealing a general mechanism for E2 recruitment by RING E3 ligases (95). TRIM21's RING self-ubiquitination leads to the lysosomal degradation of TRIM21 itself, the bound antibody, and the associated virus (20, 94). It is further described how a unique RING topology permits TRIM21 to ubiquitinate itself, with the RING domain acting simultaneously as enzyme and substrate (97). This process involves a RING dimer activating Ube2N~Ub for ligase activity, while a mono-ubiquitinated RING serves as the initial substrate. The formation of the first four ubiquitin molecules occurs in *trans*, followed by more rapid *cis*-elongation of the ubiquitin chain. This initial *trans* configuration is thought to be a regulatory feature that limits TRIM21 activity in the absence of its substrate, such as an antibody-coated pathogen.

Following the RING domain is the B-box domain, another type of zinc-binding domain. While less is known about the specific functions of the B-box domains in general, compared to the RING domain, it is believed to contribute to the overall structure of multi-domain proteins. In TRIM21, which contains one B-box, it plays a role in protein-protein interactions and the regulation of E3 ligase activity (95, 97-99). In the inactive RING E3 ligase state, the B-box occupies E2 enzyme binding site, functioning as an auto-inhibitory domain, thereby competing with E2 and regulating the RING activity (**Figure 4C**). To date, the exact mechanism under physiological conditions is unknown. Regarding antibody-dependent antiviral TRIM21 activity, it is thought that target-induced clustering via multiple antibodies binding to the virus, or the oligomeric state of the target itself, triggers TRIM21 RING ubiquitination activity (99). By clustering multiple TRIM21 molecules in close proximity, intermolecular RING dimerization could displace the B-box from the E2 binding site, thereby facilitating E2-Ubiquitin interaction and building K63-linked ubiquitin chains (98-100).

The coiled-coil domain is a structural motif characterized by the intertwining of alpha-helices, which facilitates the formation of protein oligomers. In TRIM21, the coiled-coil domain defines the architecture of the molecule and mediates the antiparallel self-association of the protein (**Figure 4E**, which exemplarily shows the crystal structure of the coiled-coil domain of TRIM25). By naturally facilitating dimerization between two TRIM21 monomers, a homodimer is formed, positioned two RING domains at the opposite ends of one TRIM21 dimer, separating them approximately 20 nm from each other (101-103). It has been established that RING domains are often activated by homo-dimerization (103-106). For TRIM21, it has been shown that two RING domains exhibit weak affinity for each other in the μM range (98). This steric arrangement is thought to be important for its function as an E3 ubiquitin ligase, as RING activation is unlikely to occur spontaneously.

The PRYSPRY domain (also known as B30.2) (**Figure 4D**), located at the C-terminus of TRIM21, is responsible for the specific target recognition and binding of the Fc region of IgG antibodies (86, 87). Recognized as a highly conserved domain, PRYSPRY interacts with immunoglobulins across species. This allows TRIM21 to distinguish between different antibody isotypes, binding to IgA and IgM with decreased affinity compared to IgG, and engaging with IgG-opsonized targets (92, 107). The dimeric nature of TRIM21 enables bivalent engagement with one IgG, allowing both PRYSPRY domains to interact simultaneously with both IgG heavy chains, resulting in a 1:1 stoichiometry between TRIM21 and IgG (detailed binding mode in Chapter **2.3.2 Mechanism of Antibody Binding to TRIM21** (20). The interaction between the PRYSPRY domain and the Fc region of antibodies is a key step in the intracellular immune defense mechanism, leading to the ubiquitination and degradation of antibody-bound pathogens or antigens (20).

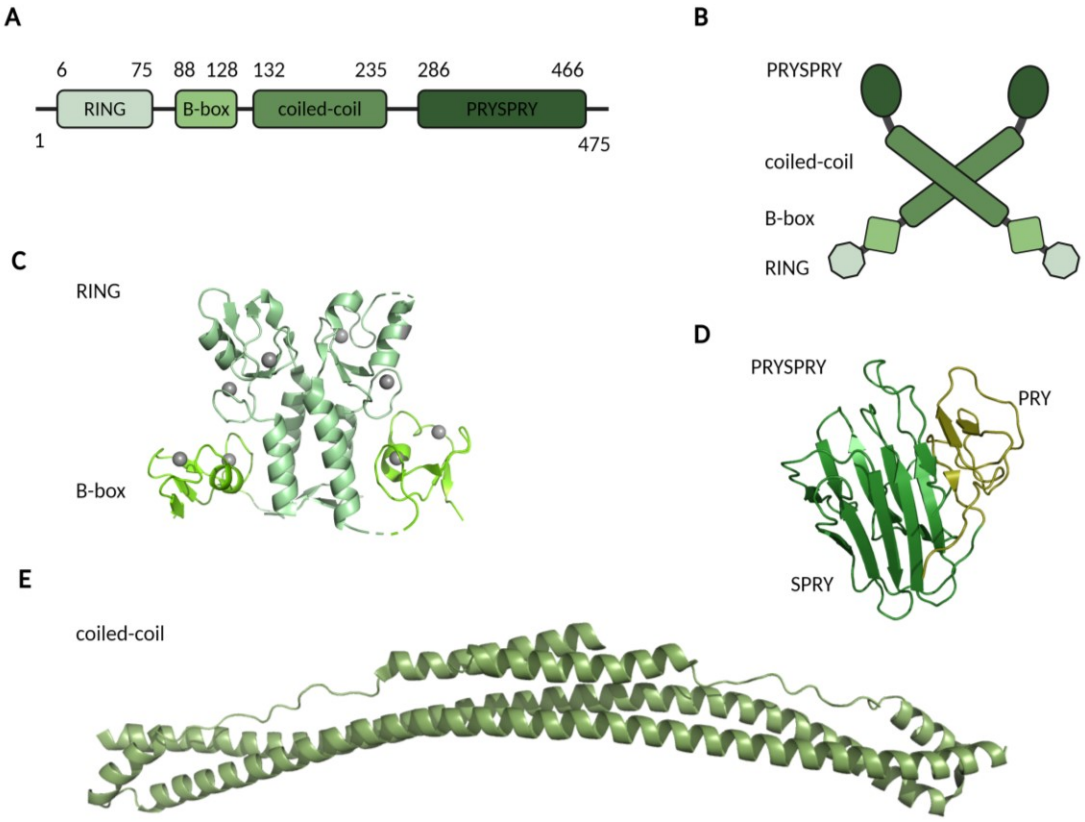

Figure 4. Structural Overview of TRIM21. A) Schematic of human TRIM21 illustrating its domains: RING, B-box, coiled coil, and PRYSPRY. Adapted from (108). **B**) Depiction of TRIM21 homodimerization, mediated by the coiled-coil domains. **C**) Crystal structure of the human TRIM21 RING and B-box domains, highlighting the autoinhibition of the RING domain, first described in (98) (PDB-ID: 5OLM). **D**) Crystal structure of human TRIM21 PRYSPRY domain, with PRY subdomain shown in "olive" and SPRY domain in "forest", first described in (86) (PDB-ID: 2IWG). **E**) Crystal structure of the human TRIM25 coiled-coil domain for comparison. (PDB-ID: 4CFG). (Structures created using PyMol 2.5.2 and BioRender.com.)

Overall, the domains of TRIM21 work in concert to facilitate its role in immune surveillance, particularly in the context of intracellular pathogen recognition and targeting for degradation, thereby contributing to the host's antiviral defense mechanisms.

TRIM21 is ubiquitously expressed across various tissues and cell types in the human body, reflecting its fundamental role in immune regulation and response to infection (86, 92). Its expression is observed in both immune cells - such as B cells, T cells, natural killer (NK) cells, dendritic cells, and macrophages - and non-immune cells, including fibroblasts and epithelial cells (109). TRIM21 expression is not restricted to a specific organ but is rather broadly distributed throughout the body, including in the spleen, liver, lungs, heart, kidneys, and muscles. The widespread expression of TRIM21 in a variety of cell types and organs demonstrates its importance in various physiological processes, including the immune response to pathogens and the regulation of cellular homeostasis.

2.2.4 Function and Role of TRIM21 in Immune Response

TRIM21 plays a crucial role in viral degradation and innate immune signaling, acting as both an effector and a sensor molecule. Upon engagement with antibodies bound to viruses, TRIM21 initiates responses that inhibit viral replication and promote an antiviral cellular state, thereby bridging the innate and adaptive immune systems (109).

As a cytosolic antibody receptor, TRIM21 is pivotal in the intracellular neutralization of virus infections, a process demonstrated for non-enveloped viruses such as adenovirus type 5 (AdV5), mouse adenovirus type 1 (MAV-1), human rhinovirus 14 (HRV-14) and rotavirus (20, 96, 110-114). This mechanism, termed antibody-dependent intracellular neutralization (ADIN), is critical for defending against viruses that have bypassed extracellular neutralization and enter the cell (**Figure 5**). The interaction with the antibody occurs through the PRYSPRY domain, which has a high affinity for the Fc region of antibodies (115). When TRIM21 binds to these immune complexes, it initiates the disassembly and degradation of viral capsids at the proteasome, effectively terminating the viral infection and neutralizing viruses that have entered the cell.

The efficacy of TRIM21 in neutralizing viruses is not solely dependent on the affinity of the antibody for the virus, as even antibodies with reduced affinity can still lead to viral neutralization via TRIM21, demonstrating its ability to mediate neutralization under a range of conditions (20, 94). The efficacy of TRIM21 in neutralizing viruses is influenced by the affinity of the antibody for TRIM21. Even antibodies with reduced affinity can still lead to viral neutralization via TRIM21, demonstrating its ability to mediate neutralization under a range of conditions (29). In contrast to many other Fc receptors that have more restricted isotype specificity, TRIM21 exhibits broad isotype specificity, binding not only to IgG but also to IgM and IgA. This feature allows TRIM21 to neutralize a wide range of viruses coated with these antibody isotypes (107, 116).

Concurrently with virus neutralization, TRIM21 acts as a sensor upon binding to the antibody-virus complex. TRIM21 triggers signaling cascades that activate the transcription factor NF-κB, leading to the production of proinflammatory cytokines and the induction of an antiviral state in the cell. This signaling function of TRIM21 is critical in initiating a broader immune response against the virus (109, 113).

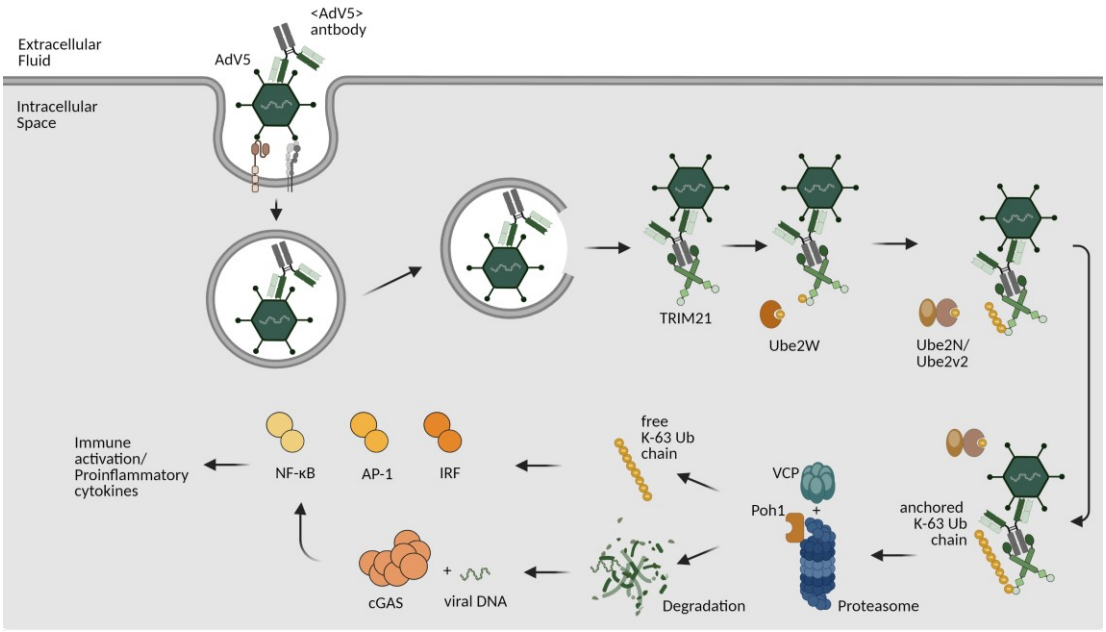

Figure 5. TRIM21 Sensor and Effector Functions in AdV5 Degradation. This schematic outlines the degradation pathway of antibody-coated adenovirus serotype 5 (AdV5) mediated by TRIM21. Upon internalization of the AdV5-antibody complex via receptor-mediated endocytosis, the complex escapes the endosome into the cytoplasm. TRIM21 then binds to the antibody heavy chains and catalyzes monoubiquitination using the E2 enzyme Ube2W. This action initiates K63-linked ubiquitin (Ub) chain extension with the help of Ube2N/Ube2v2. The ubiquitinated complex is directed to the proteasome for degradation, facilitated by valosin-containing protein (VCP), while the deubiquitinase Poh1 removes the anchored K63 Ub chains. The released K63 Ub chains, along with viral DNA, activate TRIM21's sensor function, triggering innate immune signaling pathways such as NF-κB, AP-1, and IRF 3/5/7. This activation leads to the production of pro-inflammatory cytokines and establishes an antiviral state within the cell. Adapted from (109, 117). (Created with BioRender.com.)

The dual functions of TRIM21, as an effector and sensor, are triggered by a stepwise ubiquitination mechanism, orchestrated by its E3 ligase RING domain. TRIM21 is first tagged with monoubiquitin by the E2 enzyme Ube2W. This monoubiquitin then serves as a substrate for the heterodimeric E2 enzyme Ube2N/Ube2V2, resulting in TRIM21 being anchored with K63-linked ubiquitin chains. This ubiquitination process is essential and signals for both the activation of NF-κB, as major regulator of innate immune signaling pathways, and virus neutralization. Disruption of this process impairs both functions, highlighting the importance of the ubiquitination pathway in TRIM21's antiviral activity (94, 95, 97, 98). TRIM21 auto-ubiquitination further triggers the formation of free K63 ubiquitin chains, which activate several innate immune signal pathways (NF-κB, AP-1 and IRF 3/5/7),

and these interact with and modulate the JAK-STAT pathway in various ways (96). The 19S proteasome component Poh1 plays a crucial role in deubiquitinating TRIM21, generating unanchored K63-linked ubiquitin chains, which are implicated in signaling for cytokine induction (94).

The ATPase p97/valosin-containing protein (VCP) is also a key player in the TRIM21-mediated neutralization process (118). VCP is involved in the extraction and subsequent degradation of viral capsids by the proteasome (118). The exposure of viral genomes, induced by TRIM21, enhances the immune system's ability to detect both DNA and RNA viruses. This is achieved through the activation of cGAS for the detection of DNA viruses and RIG-I for RNA viruses (114, 119). TRIM21 initiates an early and robust cytokine response, crucial for effective viral clearance. These findings highlight the involvement of other cellular factors in this antiviral mechanism.

Research has demonstrated that TRIM21 plays a role in immune complex processing. After cell entry of immune complexes (antibody bound pathogen), taken up by antigen presenting cells (APCs), downstream inflammatory signaling is initiated, targeting the immune complexes for proteasomal degradation. This enhances cross-priming and antigen-cross presentation, stimulating CD8+ T cell responses that are crucial for effective immunity against pathogens (30, 120). Increasing the affinity between immune complexes and TRIM21 can markedly improve CD8+ T cell responses (30).

TRIM21 has also been implicated in various cellular processes beyond immune defense. It may be utilized therapeutically to prevent tau aggregation in neurodegenerative disorders (121) and has been identified as a factor that can interfere with adenovirus-based gene therapy. However, it could be leveraged in other therapeutic applications, like preventing the accumulation of misfolded proteins (109, 122, 123). The role of TRIM21 in cancer cell proliferation and suppression is emerging, with evidence suggesting that TRIM21 may either enhance cancer proliferation or alternatively increase the ubiquitination of many cancer-triggering proteins, leading to their proteasomal degradation, depending on the type of cancer and the specific oncogenic drivers involved (124, 125).

Furthermore, TRIM21 mediates intracellular neutralization of antibody-coated bacteria like Salmonella enterica (126). It is recruited to intracellular pathogens in epithelial cells early in infection and mediates bacterial restriction, which is dependent on the opsonization state of the bacteria (126). TRIM proteins, such as TRIM21 act as specialized receptors for targeted autophagy (also known as precision autophagy) of key components of the inflammasome and type I interferon response systems (127).

These diverse roles highlight the significance of TRIM21 beyond its established functions in viral degradation and immune signaling. Its involvement in the pathogenesis of autoimmune diseases, the potential for therapeutic intervention in neurodegenerative disorders, its role in the intracellular neutralization of bacterial infections, its impact on cancer progression, and

its modulation of autophagic processes underline its importance across various biological contexts.

2.3 Interaction of FcRn and TRIM21 with Antibodies

FcRn and TRIM21 are both critical in the immune system's regulation and response, standing out due to their unique interactions with antibodies. The interactions of these Fc receptors extends the functionality of antibodies beyond the extracellular space into the intracellular milieu. This chapter aims to delve into the complex interplay between FcRn and TRIM21 with antibodies, elucidating their pivotal modes of binding, which are responsible for their roles in antibody and albumin homeostasis, immune regulation, and pathogen neutralization. It provides the structural basis underlying these interactions and their implications in physiological and pathological contexts. The modes of binding of FcRn and TRIM21 to antibodies, though distinct in their mechanisms, share overlapping binding sites within the IgG. This highlights the complexity and versatility of the immune system in safeguarding the body against a multitude of threats. Understanding these interactions at a molecular level offers insights into potential therapeutic strategies for enhancing immune responses, treating autoimmune diseases, and designing antibodies with tailored effector functions.

2.3.1 Mechanism of Antibody Binding to FcRn

The structural basis of the FcRn-IgG interaction is crucial for understanding the regulation of IgG and albumin half-life in serum. A key aspect of FcRn's ability to rescue IgG and albumin from lysosomal degradation is its pH-dependent binding. FcRn binds to IgG with nanomolar affinity at pH ≤ 6.5, but shows no detectable binding at pH 7.4 (128). With its α2 and β2m domains, FcRn binds to the IgG C_H2-C_H3 interface, orienting the Fab arms towards the membrane (**Figure 6A**) (43, 44, 129, 130). Key residues involved in this interaction are amino acids I253, T254, H310, H433 and H435 within the C_H2 and C_H3 domains, which interact with E115, E116, D130 and E133 on human FcRn, forming hydrogen bonds and salt bridges (50, 75, 129, 131).

Responsible for the strict pH-dependent binding and the sharp pH transition, are the histidine residues at IgG position 310, 433 and 435 (75, 129). The imidazole side chain of the histidine residues become protonated at acid pH (pH 5-6), enabling the FcRn-IgG interaction to occur, while deprotonation in a neutral environment releases the IgG from FcRn (75, 131-135). This process accounts for the significant presence of IgG in human circulation and its extended half-life in serum.

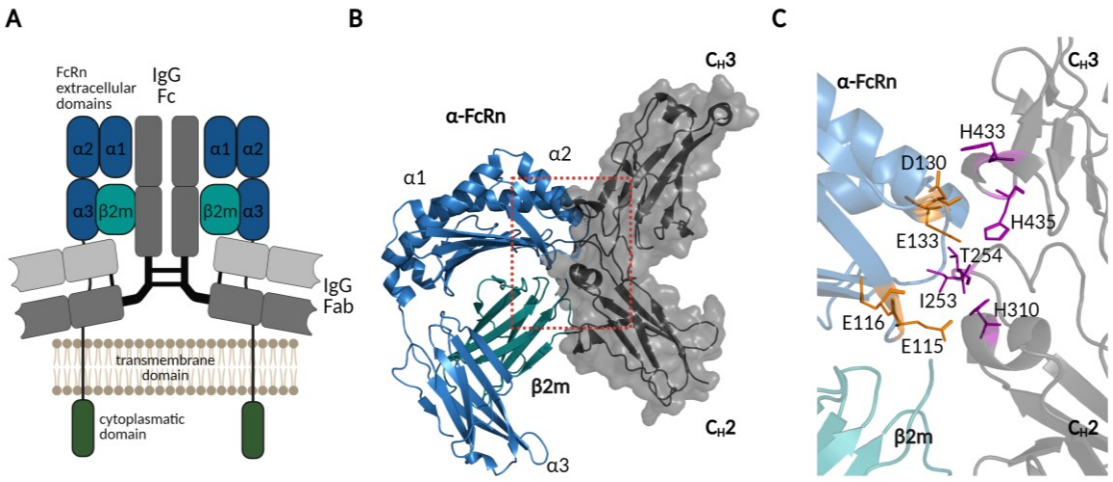

Figure 6. FcRn IgG C_H2-C_H3 Binding Interface. A) This schematic illustrates the T-shaped conformation of an IgG antibody interacting with two FcRn molecules, with each FcRn engaging one of the Fc heavy chains. This bivalent interaction is proposed to occur predominantly within the endosomal environment (136). Schema adapted from (19) **B)** The crystal structure of the FcRn-IgG C_H2-C_H3 complex is shown in a ribbon diagram. FcRn-β2m is colored blue (α-FcRn) and cyan (β2m), while the IgG C_H2-C_H3 domains are in grey (PDB ID: 4N0U). The binding interface is highlighted with red, dashed lines, with a detailed view provided in panel C. Schema adapted from (19, 75) **C)** A close-up of the hot spot region within the FcRn-IgG C_H2-C_H3 complex, displaying key residues involved in the interaction. Residues E115, E116, D130, and E133 from FcRn are shown in orange, while T254, H310, H433, and H435 from the IgG are in purple. (Created with BioRender.com and PyMol 2.5.2.)

The binding interfaces of TRIM21 and FcRn do overlap (86). It has been described that classical FcγRs bind at a different region of IgG (the upper C_H2 domain) than FcRn (137, 138). Consequently, an IgG molecule could potentially interact concurrently with both FcRn and FcγR. Engineering of antibody Fc regions to increase, decrease or block interactions with FcRn has been a focus of research to modulate the pharmacokinetics and therapeutic efficacy of monoclonal antibodies (28, 53, 139-144).

These studies demonstrate the intricate balance required in engineering antibody Fc regions to optimize interactions with FcRn, which impacts the therapeutic efficacy and pharmacokinetics of monoclonal antibodies. A prominent variant for increasing affinity at acid pH is the YTE variant (M252Y/S254T/T256E; YTE), which thereby enhances the serum half-life of IgG (145).

The homodimeric Fc part can interact with two FcRn molecules (146, 147). While the physiological relevance of this finding is still debated, it is thought that two FcRn molecules engage one IgG simultaneously in a 2:1 stoichiometry (148, 149). This binding modality transcends mere affinity interaction, where a single ligand associates with one target molecule, by incorporating the principle of avidity. This occurs when two FcRn molecules in close proximity robustly and stably interact with both heavy chains of IgG. Findings suggest that both affinity and avidity in the FcRn/IgG interaction influence the serum half-life of IgG. For example, heterodimeric IgG with only one FcRn binding site exhibited a

tremendously decreased serum half-life, supporting the notion of a 2:1 stoichiometry *in vivo* (148)

The FcRn-IgG interaction becomes more complex, as 2:1 complexes were observed with IgG Fab arms adopting a T-shaped or a mixed Y/T-shaped conformation relative to FcRn (136). The influence of Fab arm involvement on FcRn binding is corroborated by multiple investigations (71, 150-154). These studies demonstrate that a diverse array of antibodies, including constructs with identical Fc regions but different Fab arms, display varying affinities towards FcRn, leading to different serum half-lives.

The discovery of FcRn has expanded beyond its initial association with neonatal immunity. It is now recognized as a pivotal regulator of IgG homeostasis and has become a focal point in the design of therapeutic antibodies. Strategies for Fc engineering aimed at modulating interactions with FcRn are being developed to enhance the longevity and efficacy of antibodies. The ongoing research into the role of FcRn in immunity and its therapeutic potential continues to be a significant area of focus within immunology and biomedicine.

2.3.2 Mechanism of Antibody Binding to TRIM21

TRIM21 binds to the Fc C_H2-C_H3 domain of antibodies through its PRYSPRY domain. The molecule is capable of binding to all IgG subclasses and further mediates the neutralization of viruses decorated with IgM and IgA (92, 107, 155). Although the IgG binding interfaces for TRIM21 and FcRn overlap (75, 128), TRIM21 interaction is largely pH-independent (pH 5-8), and is instead dependent on salt concentrations (86). A 10-fold reduction in salt concentration from 200 to 20 mM results in a 5-fold increase in affinity, as evidenced by a decreased off-rate (86). The crystal structure of the complexed PRYSPRY domain and IgG1 Fc region by *James et al. (2007)* (86) demonstrates that the PRYSPRY domain forms a single globular fold comprising a distorted β-sandwich of two antiparallel β-sheets. The binding interface is formed by six extended loops (variable loops, VLs) that are analogous to the six CDR loops in antibodies (86). The crystal structure reveals that these six VLs create two distinct binding pockets, located within the ”PRY” and “SPRY” subunits (86). The PRY subunit's binding pocket interacts with the IgG C_H2 domain, while the SPRY subunit's pocket binds to C_H3 (86). Key residues in the Fc part include I253-C_H2 and the HNHY-motif within C_H3 from amino acid position 428 to 436, with H433-C_H3, N434-C_H3 and H435-C_H3 forming the hot spot region (86). Within the TRIM21 binding site, residue W299-T21 in the PRY subunit allows hydrophobic interaction with I253-C_H2. The larger pocket of the SPRY subunit includes residues Y328-T21, D355-T21, W381-T21, W383-T21, D452-T21, F450-T21, where C_H3 loop from positions 428 to 436 reaches into the SPRY binding pocket (86). The hot spot residues D355-T21, W381T21 and W383T2 and F450, clustered at the center of the interface, are crucial for Fc binding and make contact with the three Fc hot spot residues H433-C_H3, N434-C_H3 and H435-C_H3 (86). The structural arrangement is based on hydrophobic interactions, hydrogen bonds, and aromatic stacking interactions.

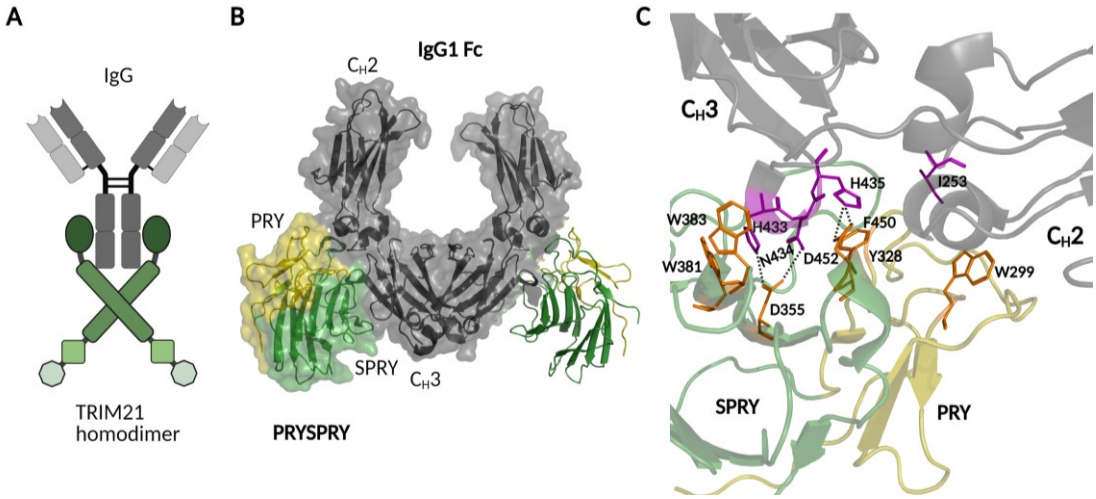

Figure 7. TRIM21 IgG C_H2-C_H3 Binding Interface. A) Schematic representation of the IgG C_H2-C_H3 region binding to a TRIM21 homodimer, forming a complex with a 1:1 stoichiometry. **B**) Ribbon diagram of the crystal structure showing the TRIM21 PRYSPRY domains in complex with the IgG C_H2-C_H3 region (PDB ID: 2IWG). The PRYSPRY domain is depicted in green (SPRY subdomain) and olive (PRY subdomain), while the IgG C_H2-C_H3 is in grey. **C**) Detailed view of the binding interface between the PRYSPRY and CH2-C_H3 regions, highlighting the hot spot area with key interacting residues. Hydrogen bonds are indicated by dashed lines. The key residues involved in the interaction are D355, W381, W383, and F450 from the PRYSPRY domain (orange) and H433, N434, and H435 from the IgG heavy chain C_H3 (grey). Panels B) and C) are adapted from (86). (Structures created using PyMol 2.5.2 and BioRender.com.)

The affinity of asingle PRYSPRY domain for an IgG1 antibody is described within a range of 37-200 nM, depending on the applied technology, while two individual PRYSPRY domains can interact with one IgG in 2:1 ratio, similar to FcRn (86, 116). The interactions of TRIM21 with IgA and IgM are much lower in binding strength, as they exhibit different residues at the HNHY-motif equivalent, with affinities of 17 μM and 50 μM, respectively (20, 107). As full-length TRIM21 naturally forms a homodimer, it has been shown that both PRYSPRY domains of a single dimer can simultaneously engage both IgG1 heavy chains in a 1:1 stoichiometry (20). The bivalent engagement (avidity) results in a dissociation constant (K_D) of 0.6 nM for IgG1, making it the Fc receptor with the highest known binding strength reported in humans (20). Mutations within the Fc interface alter TRIM21 binding in various ways; for example, the point mutation H433A abolishes TRIM21 binding but does not affect affinity for FcRn (29, 30, 86, 92, 156).

TRIM21 and its interaction with IgG represent a highly conserved binding mechanism that is structurally and functionally distinct from the binding observed with classical FcγRs (92). Specific mutations in IgG, such as P329A and L235A, can inhibit FcγR/C1q binding without compromising TRIM21 binding, yet TRIM21 competes for the same Fc binding site as proteins A and G (29, 86, 156, 157). In contrast to the conserved nature of TRIM21-IgG binding, the association of IgG with traditional FcγRs exhibits considerable interspecies variability (86, 92). This variability is partly attributed to species-specific glycosylation

patterns of IgG, highlighting a fundamental difference in the interaction dynamics between these two types of Fc receptors (155, 158, 159).

2.4 Adeno-Associated Virus (AAV): An Overview

This chapter provides insights into the role of Adeno-Associated Virus (AAV) in gene therapy. It offers a succinct introduction to AAV and its application in gene therapy, highlighting its unique attributes, such as low immunogenicity and stable expression, which make AAV an attractive vector for delivering therapeutic genes. The chapter discusses why gene therapy, and AAV-mediated approaches in particular, are increasingly being recognized for their potential to provide long-term solutions for diseases, in contrast to traditional treatments that typically manage symptoms. Gene therapy involves the delivery of genetic material into cells with the aim of treating or preventing disease, offering a potential cure by targeting the underlying genetic causes. This approach can involve various strategies, including replacing defective genes, inactivating or silencing problematic genes, or introducing new genes to help combat diseases such as cystic fibrosis, hemophilia, and muscular dystrophy.

2.4.1 Genomic Organization, Structure and Life Cycle of AAV

The discovery and structural elucidation of AAV, particularly the AAV2 serotype, represent significant milestones in virology and gene therapy (160). This introduction aims to provide insight into the origin and structure of AAV.

AAV was first identified in the 1960s as a contaminant in adenovirus preparations (161). Its dependency on co-infection with a helper virus, such as adenovirus, for productive replication marked it as unique, leading to its classification as depend-parvovirus in the *Parvoviridae* family (160, 162, 163). AAV is considered non-pathogenic and exhibits a wide host range, factors that have spurred interest in its biology and potential therapeutic applications (164).

The AAV2 serotype is one of the most studied AAV vectors and serves as a model for understanding AAV structure (160). AAV is a small, non-enveloped virus with an icosahedral capsid approximately 22-26 nm in diameter. Its capsid encloses a single-stranded DNA genome of about 4.7 kilobases (165, 166). The AAV capsid is composed of three viral proteins (VP1, VP2, and VP3) in a 1:1:10 ratio, which assemble to form the icosahedral symmetry (167-169).

The genome organization of AAV includes two open reading frames (ORFs) encoding the *rep* and *cap* genes, which are essential for the virus's life cycle (170). The genome is flanked by inverted terminal repeats (ITRs) that have a T-shaped hairpin structure (171, 172). The ITRs contain *cis*-acting elements required for AAV replication and serve as a packaging signal;

they are also responsible for the integration and rescue of the virus (173). The first ORF encodes four overlapping non-structural *rep* genes: Rep78, Rep68, Rep52 and Rep40. Rep78 and Rep68 are necessary for viral DNA replication, while Rep52 and Rep40 act as DNA helicases, which facilitate the accumulation of single-stranded progeny virus (174). The second ORF encodes three structural proteins - VP1, VP2, VP3 - and the assembly-activating protein (AAP) via alternative splicing; these proteins assemble to form the AAV virion (175-178). These proteins determine the tissue tropism of the virus and influence the efficiency of gene transfer in different tissues.

To date, 13 serotypes with various tropisms have been identified, and although extensively studied, the infectious life cycle of wild-type AAV has not been fully understood (179). The life cycle of AAV2 is shown in **Figure 8**. AAV2 primarily binds to heparan sulfate proteoglycans (HSPG) as its primary receptor on the cell surface (180). The broad expression of HSPG may explain the broad tropism of AAV2. Additional co-receptors, such as the universal AAV receptor (AVVR), have been identified as playing a role (181, 182). This binding initiates clathrin-mediated endocytosis, allowing AAV2 to be internalized into the cell, although clathrin-independent pathways have also been reported (183). The N-terminal regions of the AAV capsid proteins are crucial for endosomal escape and nuclear trafficking, though the exact mechanisms remain to be fully elucidated (184).

After endocytosis, AAV2 traffics in vesicles through the endosomal pathway. The transition from early to late endosomal compartments is crucial for AAV2's infection efficiency, and transport to the *trans*-Golgi network is necessary for AAV2 transduction, suggesting a conserved feature of AAV trafficking (185). Endosomal escape into the cytosol is triggered by endosomal acidification and mediated by the phospholipase A2 (PLA2) domain located at the N-terminus of VP1 (186, 187). PLA2 becomes exposed due to conformational changes in the capsid (VP1/VP2 region) caused by acidification during endosomal trafficking and potential involvement of cellular proteases, which are essential for infectivity (168, 188). Following endosomal escape, AAV undergoes transport to the perinuclear region via the cytoskeletal network (189, 190).

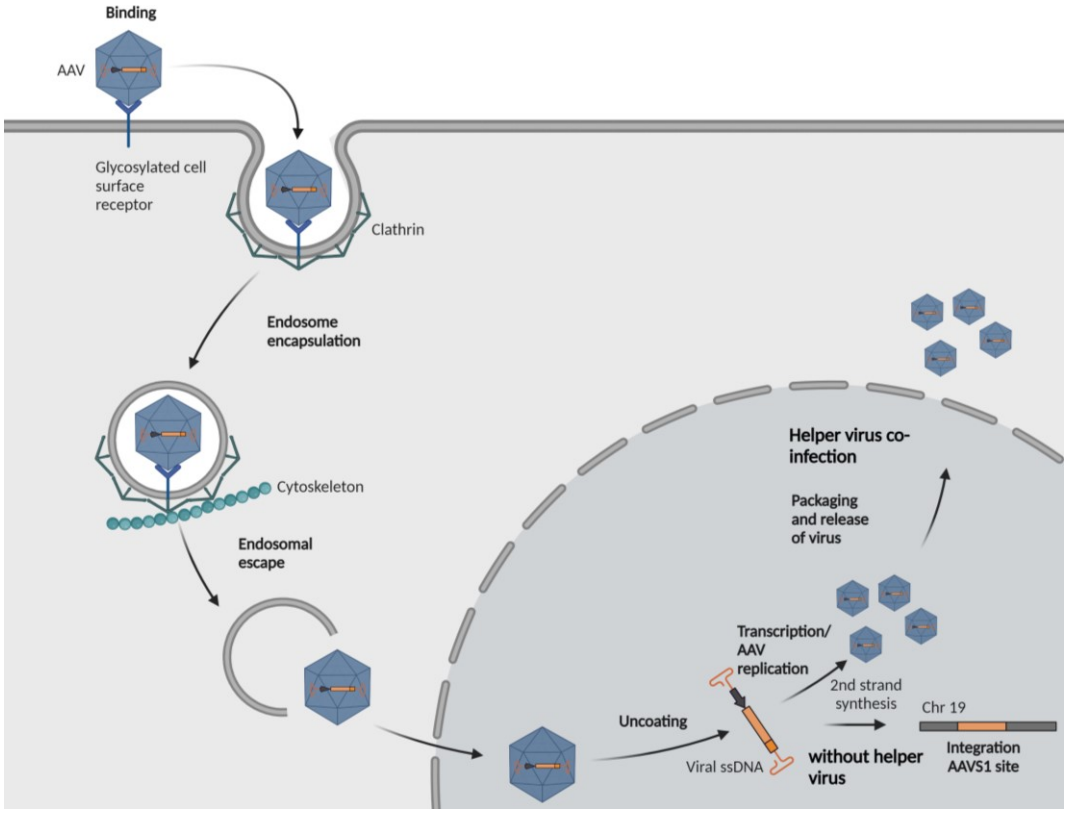

Figure 8. AAV Life Cycle. This schematic illustrates the life cycle of adeno-associated virus serotype 2 (AAV2). AAV2 initially binds to its primary receptor, HSPG, which facilitates clathrin-mediated endocytosis. The virus is then trafficked through the intracellular space, guided by the cytoskeletal network. Acidification within the endosome induces a conformational change in the viral proteins VP1/VP2, leading to the escape of AAV into the cytoplasm and subsequent nuclear entry. Inside the nucleus, the viral ssDNA is uncoated and converted into dsDNA, serving as the template for transcription. In the presence of a helper virus, such as adenovirus type 5 (AdV5), AAV can replicate, producing new virions that are released from the cell. In the absence of a helper virus, AAV establishes latency by integrating its DNA into the host genome at the AAVS1 site on chromosome 19. (Created with BioRender.com and PyMol 2.5.2.)

AAV enters the nucleus as intact particles, a process that is believed to occur via nuclear pore complexes (188, 191, 192). To facilitate capsid uncoating and the release of the single-stranded DNA genome, AAV2 is transported from the nucleolus to the nucleoplasm (191). The single-stranded DNA genome of AAV2 must be converted to a double-stranded form to enable gene expression, a process that is necessary for transcription and represents the rate-limiting step in infection (193, 194). AAV2 preferentially integrates into the host genome at the AAVS1 site on chromosome 19, although the details of this process have not been fully elucidated (195-198). In the presence of helper viruses, AAV2 enters a productive replication cycle, which involves the replication of the AAV genome and the assembly of new virions. The capsid structure and interactions with host cell factors are critical during this phase (199). Newly assembled AAV2 virions are released from the cell, a process that may involve cell lysis mediated by the helper virus. The exact mechanisms of AAV2 release

and its interactions with host cell pathways during this phase are subjects of ongoing research (200-202).

2.4.2 AAV as a Vector for Gene Therapy

The transition from wildtype AAV to recombinant AAV (rAAV) vector particles involves several key steps, primarily centered around the modification of the AAV genome and the encapsidation process, which are crucial for the use of AAV in gene therapy applications. The production of rAAV requires the expression of viral structural genes and viral ITRs in *cis*. A desired promotor and transgene, containing the gene of interest, can be inserted between the two ITRs, with the genetic payload optimally designed to be between 4.1 and 4.9 kb in size (203). In addition, the supply of *rep/cap* genes (from a second plasmid) and a third plasmid containing adenoviral helper genes required for AAV replication, such as *E2A, E4* and *VA RNA*, is crucial (203-208). To produce rAAV vector particle, the three plasmids are triple-transfected into HEK293 cells, resulting in the production of rAAVs carrying the desired transgene. After administration, the purified vector particles deliver the transgene to target cells for expression, but unlike wildtype AAV, the transgene does not integrate into the AAVS1 locus due to the absence of *rep* genes (209). It has been demonstrated that the genome of rAAV preferentially persists as an episome, contributing to stable expression (210) although the possibility of random integration of rAAV DNA into the host genome is not completely eliminated (211, 212).

Gene therapy represents a revolutionary approach in modern medicine, offering potential treatments for a wide range of genetic and acquired diseases. Rather than merely treating symptoms, gene therapy aims to rectify diseases at their genetic roots by delivering therapeutic genes into patient cells, addressing the underlying genetic causes of disease. This method has the potential to provide long-lasting, and possibly curative, treatments.

Among the various vectors used in gene therapy, Adeno-Associated Viruses (AAVs) have emerged as one of the most promising tools (213, 214). Their non-pathogenic nature, ability to target a wide range of tissues, and capacity for long-term gene expression with minimal immune response make AAVs an ideal choice for delivering therapeutic genes (215). The production process of rAAV vectors, which ensures the absence of other viral genetic material that could lead to replication-competent viruses, significantly augments the safety profile of these therapeutic agents.

Recombinant AAVs can efficiently transport genetic material into both dividing and non-dividing cells, a feature that broadens their applicability across various types of tissues and diseases. The core advantage of AAV vectors in gene therapy is their high safety profile. Unlike other viral vectors, AAVs integrate their genetic material into the host genome with low frequency, which significantly reduces the risk of insertional mutagenesis - a concern where the insertion of foreign DNA can disrupt or activate host genes, potentially leading to conditions like cancer. Instead, AAV vectors primarily exist as episomes - genetic elements

that remain separate from the chromosomes - within the nucleus, leading to sustained gene expression with minimal risk to the host's genomic integrity (216). Another significant feature of AAV-based therapy is its broad tropism - the ability to infect a wide range of cell types. This is due to the availability of multiple AAV serotypes, each with its own receptor binding preferences, allowing for targeted delivery to specific tissues or cell types, including neurons, liver cells, and muscle cells (217). For instance, AAV serotype 9 is known for its ability to cross the blood-brain barrier, making it particularly valuable for treating neurological disorders (218).

Several AAV-based therapies have made significant impacts on the market by treating genetic disorders such as inherited blindness, spinal muscular atrophy and hemophilia (219, 220). The AAV vector carries a functional copy of a gene to compensate for a defective or missing gene in patient cells, displaying the potential of gene therapy. Noteworthy examples include the approval of Luxturna (voretigene neparvovec), the first AAV2-mediated gene therapy approved by the FDA for treating an inherited retinal dystrophy caused by mutations in the RPE65 gene. The approval of Luxturna, which addresses the underlying cause of blindness, marked a significant milestone in the field of gene therapy. Another example is Zolgensma (onasemnogene abeparvovec), based on AAV9 and approved for the treatment of spinal muscular atrophy (SMA). Zolgensma has demonstrated remarkable results in improving muscle function and prolonging survival in infants with this often fatal genetic disease. AAV-mediated gene therapies for Hemophilia A and B are in advanced clinical trials and have shown promising results in reducing bleeding episodes by introducing functional copies of the Factor VIII or IX genes (221-223).

Gene therapy, particularly when mediated by AAV, is considered superior to traditional treatments for several reasons. Firstly, it provides a targeted approach to treatment, potentially offering a one-time therapy with lasting effects, in contrast to many conventional treatments that require ongoing administration and primarily manage symptoms rather than providing a cure. Additionally, AAV-based therapies can be tailored to address specific genetic mutations, offering personalized treatment options. Finally, gene therapy has the potential to treat some conditions there are no effective traditional treatments, filling a significant gap in current medical care.

Despite these advantages, challenges remain such as immune responses to the viral capsid, the limited packaging capacity of AAV for genetic material, and the need for improved target specificity and selectivity, despite the broad tropism of AAV vectors. Ongoing research is focused on engineering AAV vectors to enhance their efficiency, reduce immunogenicity, and expand their capacity for genetic cargo (224, 225). These efforts aim to broaden the potential of AAV-based gene therapies to address a wider array of genetic disorders.

2.4.3 Challenges and Implications for AAV- Mediated Gene Delivery

Recombinant AAV vectors are increasingly used for gene delivery due to their safety profile, high transduction efficiency and clinical efficacy. However, one of the significant challenges in utilizing rAAV for gene therapy is overcoming immunological barriers, particularly neutralizing antibodies (NAbs). Additionally, there is a need to improve rAAV target tissue selectivity and specificity to prevent clearance by the host immune system (226-228). Due to their natural tropism, most of the applied rAAV serotypes accumulate in the liver when administrated systemically, which poses a challenge in targeting specific tissues, cell types, and receptors (229, 230).

The challenge of NAbs is compounded by the high prevalence of pre-existing neutralizing antibodies in the human population against various AAV serotypes. Epidemiological studies indicate that the seroprevalence of antibodies against AAV ranges from 40% to 80% (231). This immune recognition can lead to a reduction or complete loss of efficacy of gene therapy, raising concerns over the possibility of re-administration and potential immunological sequelae, including local tissue damage (216, 226, 232). The humoral immune response thus presents a significant obstacle to AAV-mediated gene delivery. Neutralizing properties of antibodies can occur through mechanisms such as the disruption of receptor binding (233, 234), inhibition of uncoating, inhibition of conformational alterations in the viral capsid (235) and aggregation (236). Regarding AAV2, several neutralizing antibodies have been described and studied extensively, including mAbs A20, C24-B, C37-B, and D3 (non-neutralizing). However, the exact neutralization mode for A20 remains unknown, although it neutralizes AAV infection at a later stage following receptor attachment (188, 236-240). Despite the presence of neutralizing antibodies, there are also reports of binding antibodies (Babs) that recognize the AAV capsid but lack neutralizing properties (236, 241, 242). To date, any relationship between AAV and TRIM21 mediated by binding antibodies, which could lead to AAV degradation, remains unexplored. **Figure 9** illustrates the endosomal escape of AAV-antibody complexes, the potential binding of TRIM21, and the rerouting of the complex to the endosomal degradation machinery, a process that has been similarly shown for AdV5 (20).

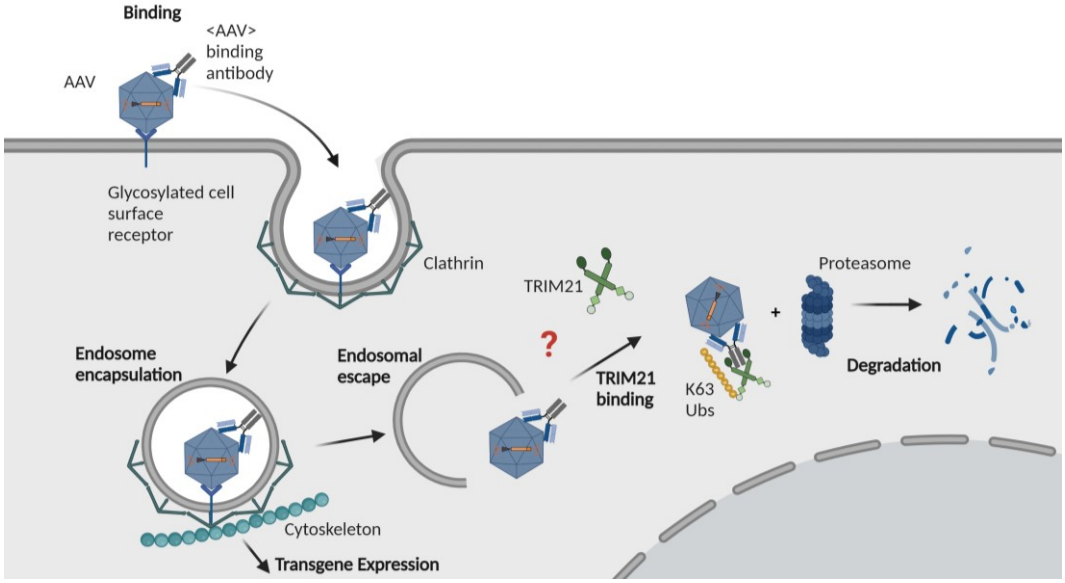

Figure 9. Potential TRIM21-Mediated Degradation Pathway of Antibody-Bound AAV. This schematic depicts a hypothesized pathway for the degradation of AAV when complexed with antibodies. Following receptor- and clathrin-mediated endocytosis, the encapsulated AAV is released from the endosome into the cytoplasm due to acidification-induced capsid conformational changes. The presence of an antibody attached to the viral capsid results in the formation of an AAV-antibody complex within the endosome. In the context of gene therapy, this complex may be directed away from transgene expression and towards proteasomal degradation. Whether TRIM21 facilitates this redirection by initiating ADIN and subsequent degradation of the immune complex remains to be elucidated. (Created with BioRender.com.)

Several strategies are being explored to overcome immunological barriers in gene therapy. One approach involves the development of novel AAV capsids with reduced immunogenicity or engineered to evade pre-existing Nabs. For instance, rAAV12, discovered through screening of natural isolates, is a unique serotype with reduced recognition by NAbs, making it a promising candidate for gene transfer applications (243). Another strategy includes the use of pharmacological immunosuppression or immunomodulation to minimize the host's immune response against the rAAV vectors (244). A prominent method is capsid engineering, which involves mutating the AAV capsid through rational design or directed evolution to eliminate epitopes responsible for Nab binding (245). Rational design entails identifying capsid regions that interact with host immunity and modifying them through amino acid point mutations, peptide domain insertions, and chemical biology approaches (238, 240). This also includes genetic modification strategies that modify the *cap* gene by introducing elements such as encoding sequences for peptides (246), nanobodies (247-249) and (bispecific) designed ankyrin repeat proteins (DARPINs) (250-252). Directed evolution is a method in which random genetic mutations are introduced into the AAV capsid genes, followed by a selection process to isolate variants with desirable properties (253). This iterative process selects for capsid variants that best meet specific therapeutic goals, effectively 'evolving' the AAV capsids towards optimal functionality for gene therapy applications (254, 255).

Capsid engineering aims to improve the vector's ability to target specific tissues, evade the immune system, and enhance gene delivery efficiency, thereby advancing the development of more effective gene therapy vectors.

2.5 Technologies for Studying Molecular Interactions

The theoretical basis of this thesis also encompasses the technologies employed to study these molecular interactions. Techniques such as Surface Plasmon Resonance (SPR), switchSENSE, and Mass Photometry (MP) are highlighted for their ability to provide real-time, label-free analysis of the binding kinetics, affinities and avidities, as well as determinations of molecular masses and stoichiometric ratios between antibodies and their interacting partners. These technologies are indispensable for the characterization of therapeutic antibodies, offering insights that drive the development of next-generation immunotherapeutics.

2.5.1 Surface Plasmon Resonance

Surface Plasmon Resonance (SPR) is a sophisticated analytical tool that has revolutionized the study and quantification of biomolecular interactions. SPR technology is a mainstay in the field of interaction analysis, particularly for examining the complex interactions between biomolecules such as antibodies and antigens.

SPR is an advanced technique used for analyzing molecular interactions without the need for labels. It operates on the principle of surface plasmons, which are collective electron oscillations that occur at the interface between a conductive metal like gold and a dielectric material such as air or water (256).

The process begins with the projection of plane-polarized light at the angle of total internal reflection (TIR) onto the gold surface of a sensor chip. This specific angle is critical because it generates an evanescent wave - a non-propagating electromagnetic wave that oscillates at the interface (256). For surface plasmons to be excited, the energy and momentum of the evanescent wave must match those of the surface plasmons (257). When this alignment occurs, it leads to the absorption of light by surface electrons, resulting in the creation of surface plasmons. This is visible as a reduction in the intensity of the reflected light at certain wavelengths (256, 257). This phenomenon, termed 'resonance', is manifested as a dip in the reflected light spectrum (256).

When molecules such as proteins bind to the surface of the chip, they alter the local refractive index at the interface. This change is directly proportional to the mass of the molecules accumulating at the sensor surface, leading to a shift in the resonance condition of the surface

plasmons (257). This shift, detected as a change in the intensity or angle of the reflected light, is indicative of the biomolecular interactions taking place on the sensor chip (257).

The change in the SPR angle (TIR angle), which signifies an increase or decrease in mass at the chip surface, is continuously monitored and recorded (257). This allows for real-time observation of the dynamics of these molecular interactions. SPR's ability to detect changes in mass through shifts in the SPR angle makes it invaluable for studying molecular binding events (257). Furthermore, its label-free nature enhances its utility and directness in measuring these interactions.

In SPR-based biosensor assays, the sensor chip is the central element, intricately connected to a detection system on one side and a fluidic system on the other, as illustrated in **Figure 10**. This chip consists of a glass substrate covered with a thin gold film, which is then coated with an interaction layer that makes direct contact with the fluidic system. The interaction layer commonly utilized is a carboxylmethyl-dextran (CM) matrix. This layer is divided into four distinct and independently operable sections, known as flow cells (Fc1-4). The fluidic system facilitates the controlled delivery of various solutions across the interaction layer of the sensor chip at a specific flow rate. This setup allows the immobilization of a biomolecule, referred to as the ligand, onto the sensor chip. Following this, a second biomolecule, the analyte, is introduced to the flow cells for interaction analysis.

The strength of SPR lies in its ability to provide detailed quantitative kinetic data across a wide range of binding strengths. The data measured by SPR is presented in a sensorgram, as illustrated in **Figure 10**. This sensorgram graphically represents the temporal progression of the interaction, with time plotted on the x-axis and the change in signal on the y-axis. The changes in refractive index detected by the SPR instrument are converted into response units (RUs). These RUs are directly proportional to the mass change at the sensor surface, allowing for the quantification of the binding event. An upward trend in RU values signifies an increase in mass, indicative of molecular binding to the sensor surface, while a downward trajectory in RU values corresponds to a loss of mass. The kinetics of the measured interaction can be characterized by calculating the association and dissociation rate constants (k_{ON} and k_{OFF}), as well as determining the equilibrium dissociation constant (K_D) for the interaction between two or more molecules. The K_D value represents the strength of the affinity of an interaction, where a lower K_D indicates a higher affinity between the interacting entities.

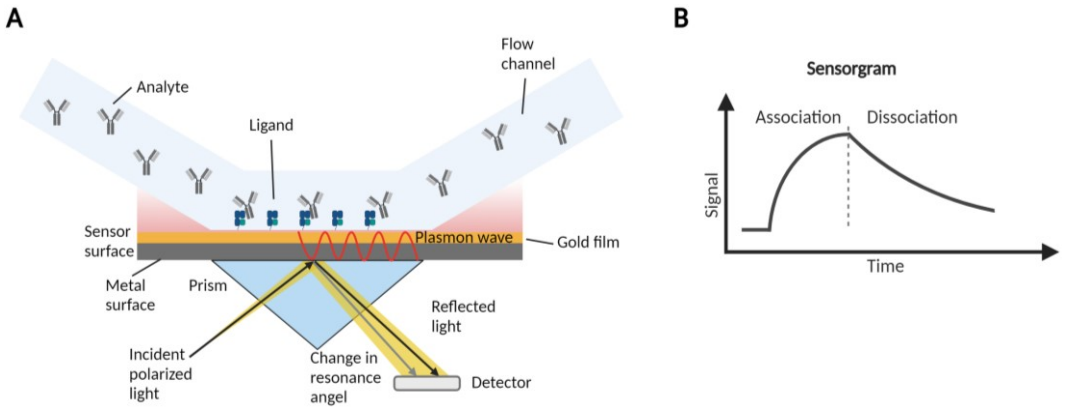

Figure 10. SPR-Based Biosensor and Sensorgram Overview. A) This schematic depicts an SPR-based biosensor within a flow channel, where analytes interact with ligands immobilized on a gold film sensor surface. Illumination of the sensor at a specific angle excites surface plasmons - coherent electron oscillations at the gold-dielectric (water/buffer) interface. This plasmon resonance is sensitive to refractive index changes near the surface, which occur when molecules bind to the receptor layer. Such binding events cause a measurable change in the SPR signal, correlating directly with the mass of the bound molecules. Adapted from (257) **B**) A typical sensorgram illustrates the signal variation resulting from analyte-ligand interactions. The association phase corresponds to analyte binding, while the dissociation phase reflects analyte release. Sensorgram analysis provides kinetic rate parameters essential for characterizing molecular interactions. (Created with BioRender.com.)

These parameters are crucial for understanding the strength and specificity of the interaction, which are key determinants of an antibody's functional efficacy. They are also essential for understanding the binding dynamics of biological molecules, such as the interaction between antibodies and antigens, receptors and ligands, or enzymes and substrates. SPR can be used to investigate the effects of antibody engineering on binding characteristics, including changes in the Fc region that may affect interactions with Fc receptors or other components of the immune system. In the context of antibody research, SPR has become an indispensable tool for characterizing the binding properties of therapeutic antibodies to their targets, allowing researchers to determine the affinity, avidity, and specificity of antibodies - key parameters for therapeutic efficacy.

SPR's versatility extends to its compatibility with various sample types, including crude serum, cell lysates, and purified proteins. This flexibility is essential for studying antibodies in different stages of development, from initial discovery through to clinical-grade material.

Although SPR technology is fundamental for the characterization of biomolecular interactions, there are challenges associated with SPR analysis. SPR is more sensitive to larger molecules, which typically induce a more significant change in the refractive index near the sensor surface. Consequently, it can be less effective for detecting small molecules or ions that might not cause a substantial change in the refractive index.

However, factors such as temperature fluctuations, buffer composition changes, or non-specific binding can affect the results. The sensor surface, often a biochip containing a dextran matrix, is critical and can lead to non-specific binding, surface degradation, or

improper ligand immobilization, which can result in poor data quality or misinterpretation of results. The data obtained from SPR experiments can be complex and often require sophisticated models for interpretation, particularly for complex interactions or when working with multi-component systems that are not covered by standard analysis software.

2.5.2 switchSENSE Technology

SwitchSENSE technology is an advanced method used for the characterization of antibodies and the analysis of their kinetic properties. It is particularly effective in determining affinity and avidity, essential aspects in the study of antibody interactions.

SwitchSENSE utilizes a microfluidic channel with an engineered DNA-based ligand surface, operating on the principle of using electro-switchable DNA nanolevers attached to a gold (Au) surface (258, 259). These nanolevers are labeled with a reporter dye and oscillate in response to alternating electric fields, which allow for the detection of molecular interactions and dynamics (260).

The biochip, connected to a fluid system, is equipped with several gold microelectrodes, where thiol modified single stranded DNA molecules (approx. 10^6 DNA strands) are covalently bound via a gold-sulfur bond, forming a self-assembled DNA monolayer (SAM) (258, 261). For optical detection (**Figure 11A**) a fluorescent dye is attached to the distal end. Introducing a complementary DNA strand, bioconjugated to a target of interest (ligand), both strands hybridize and form a double stranded DNA (dsDNA), thus the chip surface is functionalized (**Figure 11B**). The subsequent injection of a binding partner (analyte) during the association phase with the final buffer injection for the dissociation phase results in a recorded sensorgram (259). In the dynamics mode, alternating voltage (square wave potentials in the high-frequency range of 10 kHz) is applied to a microelectrode (258). This process induces a dynamic interaction between the negatively charged DNA backbone and the charged gold surface, causing the DNA to oscillate between attraction and repulsion, a phenomenon called "DNA-Switching," as illustrated **Figure 11B**. Upon exciting the fluorescent dye at a specific wavelength, the subsequent emission is detected by a time correlated single photon counter. A key observation of this technique occurs, when the dsDNA is attracted closer to the Au surface under the influence of positive potentials. This proximity results in the quenching of the dye's emission, attributable to resonant coupling between the dye's electromagnetic near field and the metal (262). This long-ranged energy transfer functions over extended distances, enabling the real-time and contactless measurement of the extension and orientation of the oligonucleotide relative to surfaces, as it results in maximal and minimal fluorescent intensity (standing/lying state of the dsDNA) (263, 264). The upward motion of a dsDNA-ligand/ligand-analyte complex in solution is decreased due to increased hydrodynamic friction compared to bare dsDNA; thus, the motion's speed correlates with the hydrodynamic drag of the analyzed complex (**Figure 11B**). The fluorescence trace of DNA that has bound an analyte shifts to the right, and the

transition region is broadened. The integral below the upward switching curves is called the Dynamic Response (DR) and when plotted over time, it yields sensorgrams that can be analyzed to measure the kinetic rate parameters of an interaction (259, 265, 266).

In the static mode, a constant negative voltage (direct current) is applied, resulting in the stabilization of the DNA in an upright orientation (**Figure 11C**). The detection principle in this mode primarily hinges on the alterations occurring within the chemical milieu surrounding the fluorophore (267, 268).

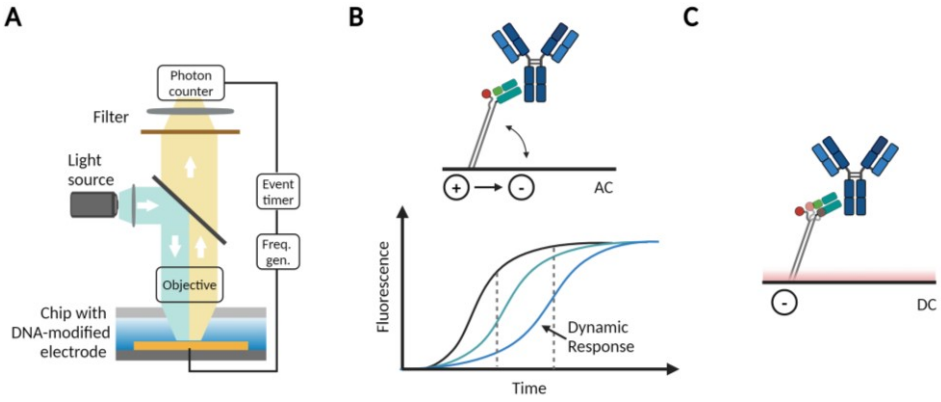

Figure 11. SwitchSENSE Biosensor Setup and Measurement Modes. A) The electro-optical detection setup enables real-time tracking of DNA dynamics. DNA strands, activated by an alternating voltage from a frequency generator, emit photons captured by an event timer for precise monitoring. The fluorescent labels on the DNA strands facilitate this detection. Schema adapted from (258). **B**) In dynamic measurement mode, an alternating voltage causes the DNA-ligand-analyte complex to exhibit specific behaviors: positive potential suppresses fluorescence near the gold (Au) surface, while negative potential increases fluorescence as the complex moves away from the surface. Analyte binding to the ligand increases hydrodynamic friction (HF), slowing the DNA's motion. This slowdown manifests in the fluorescence trace as a rightward shift and broadening during the transition, indicating increased HF due to the presence of the ligand (cyan) or ligand-analyte (blue) compared to the baseline (black). The Dynamic Response (DR) is quantified by calculating the area under the upward switching curves. **C**) In static mode, a sustained negative voltage keeps the DNA strand extended away from the surface, allowing for the detection of fluorescence changes that result from chemical environment alterations due to ligand-analyte interactions. Panels B) and C) are adapted from (268). (Created with BioRender.com.)

switchSENSE facilitates a multi-parameter characterization of binding kinetics, affinity and avidity (269, 270), enzymatic activity (271), and conformational changes (272). By providing a surface with two different dyes whose emission do not overlap, the surface can be functionalized with two independent target molecules. This allows for the simultaneous analysis of the affinity and avidity of bispecific antibodies, mimicking the biological configuration of two surface receptors (273). The conjugation of ligand molecules to DNA strands does not occur on the chip but in a separate *in vitro* reaction with subsequent purification. This process can be more labor-intensive compared to SPR (260). As

switchSENSE is a multi-parameter instrument, its handling and data analysis can be challenging and demand a certain level of expertise for effective use.

2.5.3 Mass Photometry

Mass photometry (MP), at its core, is a technique that allows for the accurate measurement of the mass of individual biomolecules in their native state, without the need for labels or complex sample preparation. Biomolecules are exposed to a light beam, where part of the light is reflected by the measurement surface and part scatters upon contacting the molecules (274). The technique measures the interference between the scattered light from the molecules and the reflected light from the surface (275). This measured interference, known as mass photometry contrast or interferometric contrast, directly correlates with the molecular mass (**Figure 12**) (275, 276).

The theoretical basis of mass photometry is anchored in two pivotal optical techniques: interference reflection microscopy (IRM) (277) and interferometric scattering microscopy (iSCAT) (278). IRM, a technique developed in the 20th century, forms the foundational principle of mass photometry. It exploits the interference of light reflected from a surface and the light reflected from the underside of a cell or particle close to that surface (277). This interference pattern is sensitive to the distance between the cell and the surface, enabling precise measurements of cell adhesion, morphology, dynamics, and offers high-contrast images through light wave interference (277, 279). ISCAT, on the other hand, is a more recent development that has extended the principles of IRM. The technique leverages the interference between the scattered light from a nanoparticle and the incident light beam, enhancing the contrast of nanoparticles against a background (278). This enhancement is crucial for detecting and analyzing particles, including biomolecules, that are otherwise too small to be observed with conventional optical microscopy. This method's ability to maintain high imaging contrast independent of exposure time or scattering cross-section allows for unique applications such as single-particle tracking and label-free imaging of biomolecular dynamics (274-276, 278).

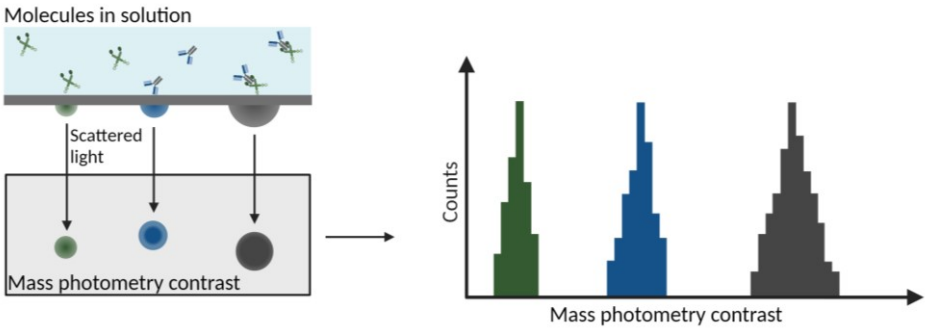

Figure 12. Schematic Mass Photometry Setup and Analysis. This schematic illustrates the setup for mass photometry, a technique that captures the light scattering patterns of individual molecules immobilized near a refractive index interface. Due to size-dependent variations in light scattering, molecules produce unique interferometric scattering (iSCAT) images. These images are then analyzed to generate scatter plots that reflect the mass distribution of the analyzed molecules. The resulting data are typically presented in a histogram format, allowing for the identification and quantification of molecular species and their binding events. Adapted from (275). (Created with BioRender.com.)

By integrating these principles, mass photometry allows for the detection and measurement of the mass of biomolecules as they freely diffuse across a biocompatible surface. When a molecule interacts with the surface, it induces a localized change in the interference pattern, which can be detected and quantified (280). This quantification is based on the relationship between the scattering intensity and the mass of the molecule, enabling the direct measurement of individual molecules' mass, even in complex mixtures (275, 276, 280).

The applications of MP are vast and impactful. It allows mass determination in the range of 30 kDa to 5 MDa (276). In drug discovery and development, mass photometry offers a powerful tool for screening proteins, biomolecular interactions, and stoichiometry (281, 282). It has been successfully applied to study IgG-FcRn and FcRn self-interaction (283), as well as to the analysis of oligomerization (284) and heterogeneity (285, 286) of samples as quality attribute. Its ability to analyze biomolecules in their native state without the need for labels or extensive sample preparation makes it an invaluable tool for studying dynamic biological processes in real time. However, it shows limitations when it comes to the interaction of biomolecules exhibiting weak affinity or a fast dissociation rate, as the complex may dissociate before it can be accurately analyzed.

3
Objectives and Scope of the Study

This thesis explores the intricate interactions between the neonatal Fc receptor (FcRn) and tripartite motif-containing protein 21 (TRIM21) within the immune system's handling of antibodies, with a particular focus on Fc-engineered antibodies. FcRn and TRIM21, though both pivotal in the immune response, operate in distinct contexts and were identified at different times. The overarching aim is to dissect these interactions and their unique binding modes with Fc-engineered antibodies that exhibit altered effector functions. Additionally, this work seeks to unravel the complexities of distinguishing affinity from avidity in these interactions. Such insights are crucial for advancing our understanding of how to target challenging molecules and will guide future research in identifying Fc mutants with desirable properties.

The FcRn protein plays a crucial role in the functioning of the immune system by protecting IgG antibodies and albumin from degradation, thereby prolonging their presence in the bloodstream. Despite being recognized and extensively studied since the late 20th century, many aspects of FcRn's interactions with engineered antibodies remain unclear, particularly regarding the strength of these interactions. Research often focuses on comparing single affinity values at extreme pH conditions (pH 5.8–6.0 and 7.4) but overlooks the significance of avidity, which involves two FcRn molecules binding to one antibody. This aspect is presumed to be crucial in acidified endosomes but is rarely studied due to the complexity of assay configuration and data analysis. In first part (Chapter 4) of this study, we explore a new method using the switchSENSE technology, which mimics the physiologically relevant assay configuration with FcRn as a membranous target, and distinguishes between affinity and avidity across a wide pH range. This research aims to lay the groundwork for future studies on engineered antibodies, offering a clearer understanding of their interactions with FcRn.

TRIM21, a more recently discovered Fc receptor, is essential for neutralizing pathogens bound to antibodies within cells and directing them for destruction. It binds to the Fc region of antibodies with strong avidity, thanks to its ability to engage two binding sites simultaneously. The discovery of TRIM21 has broadened our understanding of the immune system's ability to combat intracellular pathogens, an area previously underexplored. The effects of mutations on TRIM21's avid binding mode and its precise mechanism, especially with multiple antibody Fc mutations, remain less understood. In the second part (Chapter 5) of the thesis, we use biosensor assays (SPR), mass photometry, and electron microscopy to

analyze TRIM21's dimeric state and binding behavior, to reveal how it interacts with antibody Fc mutants and the impact on its binding strength (affinity and avidity). Our findings demonstrate the intricate dynamics of TRIM21-antibody interactions on viral particles, underlining the combined avidity effects that could enhance neutralization. As a model system, rAAV vector particles have been explored, which to date are not connected to TRIM21-mediated neutralization. This research demonstrates the importance of balancing affinity and avidity in designing antiviral antibodies, which can drastically affect immune response and signaling. It positions TRIM21 as a pivotal target for creating therapeutic antibodies with optimized functions.

4
Publication I

This chapter contains the research article

INSIGHT INTO THE AVIDITY-AFFINITY RELATIONSHIP OF THE BIVALENT, PH-DEPENDENT INTERACTION BETWEEN IGG AND FCRN

BY

Johannes Reusch, Jan Terje Andersen, Ulrich Rant and Tilman Schlothauer

PUBLISHED IN

mAbs
(2024)

4.1 Author Contributions

Johannes Reusch, Ulrich Rant, and Tilman Schlothauer were instrumental in conceptualizing the study, setting its goals, and establishing the research framework. They collaboratively developed the methodologies and selected the appropriate procedures for the research. Johannes Reusch executed the experimental investigations, employing techniques such as switchSENSE, Surface Plasmon Resonance (SPR), and FcRn affinity chromatography for data collection.

The accuracy of the results was jointly validated by Johannes Reusch, Ulrich Rant, and Tilman Schlothauer, ensuring the reliability of the data. Johannes Reusch undertook the formal analysis, utilizing statistical and mathematical models to interpret the study data. He was also responsible for data visualization, creating figures and tables that succinctly represented the findings, and managed the data curation process to maintain the data's quality and integrity.

The initial manuscript draft was composed by Johannes Reusch. Jan Terje Andersen, Ulrich Rant, and Tilman Schlothauer contributed significantly to the refinement of the paper through their critical review and editing, enhancing the overall content and presentation of the research.

4.2 Insight into the Avidity-Affinity Relationship of the bivalent, pH-dependent Interaction between IgG and FcRn

Insight into the avidity-affinity relationship of the bivalent, pH-dependent interaction between IgG and FcRn

Johannes Reusch[ab1], Jan Terje Andersen[cde], Ulrich Rant[a*†] and Tilman Schlothauer[b*†]

[a] *Dynamic Biosensors GmbH, Munich, Germany*

[b] *Roche Pharma Research and Early Development, Therapeutic Modalities, Roche Innovation Center Munich, Roche Diagnostics GmbH, Nonnenwald 2, 82377 Penzberg, Germany*

[c] *Department of Immunology, Oslo University Hospital Rikshospitalet, N-0424 Oslo, Norway*

[d] *Institute of Clinical Medicine, Department of Pharmacology, University of Oslo, N-0372 Oslo, Norway.*

[e] *Precision Immunotherapy Alliance (PRIMA), University of Oslo, N-0372 Oslo, Norway*

* Corresponding authors: rant@dynamic-biosensors.com; tilman.schlothauer@roche.com

† These authors contributed equally to this work

[1] Johannes Reusch changed affiliations from Dynamic Biosensors GmbH to Roche Innovation Center Munich since completing the research.

Johannes Reusch: Author, johannes.reusch@roche.com, https://orcid.org/0000-0002-6605-9975

M. Sc. Johannes Reusch (J. Reusch)

johannes.reusch@roche.com

Roche Diagnostics GmbH, Germany

Nonnenwald 2

82377 Penzberg

Jan Terje Andersen: Author, j.t.andersen@medisin.uio.no, https://orcid.org/0000-0003-1710-1628

Professor Dr. Jan Terje Andersen

j.t.andersen@medisin.uio.no

Institute of Clinical Medicine, Department of Pharmacology, University of Oslo Sognsvannsveien 20

Rikshospitalet

0372 Oslo, Norway

Ulrich Rant: Author, rant@dynamic-biosensors.com, https://orcid.org/0000-0002-6100-828X Dr. Ulrich Rant (U. Rant)

rant@dynamic-biosensors.com

Dynamic Biosensors GmbH, Germany

Perchtinger Str. 8-10

81379 Munich

Tilman Schlothauer: Author, tilman.schlothauer@roche.com, https://orcid.org/0000-0001-5844-4438

Dr. Tilman Schlothauer (T. Schlothauer)

tilman.schlothauer@roche.com

Roche Diagnostics GmbH, Germany

Nonnenwald 2

82377 Penzberg

Abstract

Monoclonal antibodies (mAbs) as therapeutics necessitate favorable pharmacokinetic properties, including extended serum half-life, achieved through pH-dependent binding to the neonatal Fc receptor (FcRn). While prior research has mainly investigated IgG-FcRn binding kinetics with a focus on single affinity values, it has been shown that each IgG molecule can engage two FcRn molecules throughout an endosomal pH gradient. As such, we present here a more comprehensive analysis of these interactions with an emphasis on both affinity and avidity by taking advantage of switchSENSE technology, a surface-based biosensor where recombinant FcRn was immobilized via short DNA nanolevers, mimicking the membranous orientation of the receptor. The results revealed insight into the avidity-to-affinity relationship, where assessing binding through a pH gradient ranging from pH 5.8 to 7.4 showed that the half-life extended IgG1-YTE has an affinity inflection point at pH 7.2, reflecting its engineering for improved FcRn binding compared with the wildtype counterpart. Furthermore, IgG1-YTE displayed a pH switch for the avidity enhancement factor at pH 6.2, reflecting strong receptor binding to both sides of the YTE-containing Fc, while avidity was abolished at pH 7.4. When compared with classical surface plasmon resonance (SPR) technology and complementary methods, the use of switchSENSE demonstrated superior capabilities in differentiating affinity from avidity within a single measurement. Thus, the methodology provides reliable kinetic rate parameters for both binding modes and their direct relationship as a function of pH. Also, it deciphers the potential effect of the variable Fab arms on FcRn binding, in which SPR has limitations. Our study offers guidance for how FcRn binding properties can be studied for IgG engineering strategies.

Keywords: FcRn, Therapeutic IgG, Binding Kinetics, Affinity, Avidity, switchSense, Biosensor, pH Dependency

Classification: Antibody analytics; Antibody screening; Antibody engineering; Antibody generation; FcRn; Pharmacokinetics; Characterization

Abbreviations

4PL Fit	Four Parameter Logistic Fit
Fc	Fragment crystallizable
HERA	human endothelial cell-based recycling assay
hIgG1	human Immunoglobulin G isotype 1
hsc-FcRn	human single-chain neonatal Fc receptor
hβ2M	human beta 2 microglobulin
K_D	equilibrium dissociation constant
k_{OFF}	dissociation rate constant
$k_{OFF}^{app.}$	apparent dissociation rate constant
k_{ON}	association rate constant
$k_{ON}^{app.}$	apparent association rate constant
k_{ON}^{obs}	observable association rate constant
mAb	monoclonal antibody
MTL	mass transport limitation
PK	Pharmacokinetics
pKa value	negative log base ten of the acid dissociation constant (Ka)
scFv	single-chain variable fragment
sec	seconds
SPR	surface plasmon resonance
tau_{OFF}	time constant of dissociation
WT	wildtype

Introduction

The use of monoclonal antibodies (mAbs) to treat diseases such as cancer and inflammatory diseases is rapidly expanding.[1,2] These bivalent, homodimeric and Y shaped molecules are composed of two antigen-binding fragments (Fabs), responsible for specific binding to an antigen (target) and a constant crystallizable fragment (Fc) that mediates Fc receptor functionality. Regarding monospecific therapeutic mAbs, current research activities focus on their target specificity, binding strength, and developability.[3-5] For instance, a key challenge is to achieve optimal selectivity for the recognition of (heterogeneous) antigens on tumor or immune cells or for soluble antigens while avoiding detrimental off-target binding to healthy cells.

While the constant Fc can engage Fc receptors to mediate effector functions, it is also responsible for a long serum half-life, which for natural IgG antibodies is approximately 3 weeks at average.[6] As such, IgG is the dominant antibody class in blood, and acts as a key component of humoral immunity. In this regard, the long serum half-life of natural IgG and IgG-based therapies results from engagement of the neonatal Fc receptor (FcRn).[7]

FcRn is a ubiquitously expressed cellular receptor across mammalian cells, encompassing both hematopoietic and non-hematopoietic cells.[8] In contrast to classical Fcγ receptors, which are primarily displayed on the surface of immune cells, FcRn is predominantly localized within acidified endosomes. The intricacies of FcRn's expression density within the endosome remain incompletely understood. However, *D'Hooghe et al.*[9] have proposed a dynamic model of FcRn activity that suggests an interplay between the plasma membrane and endosomal FcRn levels. According to this model, a minimal expression of FcRn is present on the plasma membrane, with the majority residing in the endosomal system. This distribution is facilitated by the fluidity of the membrane, which allows for high local concentrations of FcRn within endosomes, enabling the receptor to engage with IgGs in a unique manner. *Pzyik et al.*[10] describe a scenario in which two FcRn molecules simultaneously bind to a single IgG, a process termed avidity. Avidity is known as the cumulative binding strength that results from multiple non-covalent interactions where simultaneous binding increases the overall stability of the interaction beyond the strength of individual affinities.[11,12]

In addition, the expression level of FcRn can vary depending on the cell type and tissue, as well as species.[13] For instance, data support that FcRn is highly expressed in immune cells and epithelial cells of tissues such as the placenta, liver, intestine, and endothelial cells of blood vessels.[14,15] In disease such as cancer, different FcRn expression profiles have been observed, and the effect on tumour growth is debated.[16,17]

The long half-life of IgG is regulated by FcRn-mediated recycling of monomeric IgG molecules in a range of cell types, which happens in a strictly pH-dependent manner, with strong binding at acidic pH and no or weak binding at neutral pH. Mechanistically, cellular uptake occurs via fluid-phase pinocytosis of IgG followed by engagement of FcRn in acidified endosomes (pH < 6.0), which results in recycling and exocytosis of the FcRn-IgG

complex that, upon exposure to the physiological condition (pH 7.4) of the extracellular space, triggers release of IgG from the receptor due to negligible binding affinity.[10,18-20] As such, FcRn rescues IgG from intracellular lysosomal degradation, while other serum proteins are designated for degradation. The principle is the same for FcRn-mediated transcytosis of both monomeric IgG and IgG-immune complexes that occurs bidirectionally across polarized epithelial cells.[21-23] These transport pathways explain the high abundance of IgG in blood and its long serum half-life. In addition, FcRn has been shown to enhance processing of IgG-containing immune complexes in concert with the classical Fcɣ receptors expressed by antigen-presenting cells, such as dendritic cells, which leads to antigen presentation and activation of T cells.[24-26]

Structurally, FcRn is related to class I major histocompatibility complex (MHC) molecules, consisting of a unique membrane-bound alpha chain (alpha-FcRn) that is non-covalently associated with the common soluble beta-2-microglobulin.[27-30] The extracellular part of FcRn binds to the Fc's CH2-CH3 interface via residue Ile253 and inter- and intra-molecular interactions mediated by His310 and His 435.[28,31] These histidine residues change charge as a function of pH by becoming protonated at pH 6.0, which is required for strong binding to FcRn at acidic pH and negligible binding at pH 7.4.[32] Replacement of these or neighbouring amino acid residues could either reduce, abolish or enhance FcRn binding. For instance, mutating the three key residues to alanines (I253A, H310A, H435A; AAA) completely abolishes binding while combination of mutations has shown to improve pH-dependent binding beyond that of wildtype (WT) IgG. For the latter, examples are LS (M428L/N434S), KF (H433K/N434F) and YTE (M252Y/S254T/T256E) that all show extended serum half-life in animal models and humans.[33-38] Specifically, a YTE-containing human IgG1 that demonstrated 10-fold stronger *in vitro* binding to human FcRn at acidic pH while still showing weak binding at neutral pH exhibited an extended half-life of up to 100 days in humans compared to the WT counterpart.[33,35,39]

While the principle for pH-dependent binding between FcRn and IgG is well established, there is still a matter of debate regarding how FcRn embedded in a cell membrane engages the homodimeric IgG molecule regarding stoichiometry, orientation and binding kinetics throughout the pH gradient. *Abdiche and co-workers*[40] demonstrated that two FcRn molecules can bind independently to a homodimeric IgG1 Fc at two opposing sites with equal affinity, a finding supported by the symmetrical FcRn-Fc complex structure reported by *Burmeister et al.*[28] Furthermore, *Abdiche et al.*[40] found that heterodimeric IgG1 with only one available FcRn binding site had a significantly reduced plasma half-life compared to the WT counterpart, highlighting the need for bivalent engagement (avidity) of both IgG heavy chains for extended serum persistence. Conversely, *Gurbaxani and Morrison*[41] proposed a more intricate model with multiple binding modes, which could not account for all observed data. Avidity plays a crucial role not only in FcRn biology but is also essential across antibody biology

including antibody-antigen interactions[42] and effector functions such as complement activation[43,44].

In addition, a growing body of evidence also supports that the biophysical features of Fab arms may modulate the interaction with FcRn, and as such the half-life.[45,46] Thus, it is attractive to develop interaction assays that take this complex biology into consideration.

The interaction between FcRn and IgG, typically measured using surface plasmon resonance (SPR)[40,47] and other technologies[48], is often assessed at extreme pH values, such as acidic pH around 5.8 and neutral pH at 7.4. However, these conditions may not accurately reflect the bivalent Fc binding that occurs across a pH gradient, where two FcRn molecules can simultaneously interact with one IgG in a 2:1 stoichiometry.

To gain insights into the complexity of the FcRn-IgG interactions with the aim to determine both affinity (1:1) and avidity (2:1) as a function of pH, we explored the use of the switchSENSE technology. In contrast to direct amine coupling of a ligand to a biosensor surface or via capture molecules done by SPR[49], this technology relies on a planar gold electrode where the ligand is attached to the distal end of DNA nanolevers that are covalently attached to the surface, whereas the analyte is injected with a constant flow.[50] This setup has shown to allow measurement of complex interactions that can directly correlate affinity and avidity parameters.[51-54]

By immobilizing a recombinant human single chain FcRn (hsc-FcRn), which engages IgG monovalently, followed by injection of IgG, which engages bivalently, we demonstrate that the switchSENSE technology results in monovalent (affinity) and bivalent (avidity) receptor interactions simultaneously at a certain ligand density and pH. We performed a comprehensive analysis of the FcRn-IgG interactions revealing insights into the direct relationship between both binding modes, which could more adequately decipher affinity from avidity compared with that of comparable SPR experiments, and that complemented studies using analytical FcRn affinity chromatography and a human endothelial cell-based recycling assay (HERA).

Assay configurations differ significantly, and the resulting dissociation constants (K_Ds) for IgG-FcRn interactions can vary widely, ranging from 10 to 100 nM with immobilized FcRn, to 0.2 to 2.3 μM with immobilized IgG.[33,46,55-58] These variations in affinity measurements preclude a straightforward extrapolation of a standardized, meaningful method for comparing IgG affinities. The switchSENSE protocol presented herein promises to be a valuable tool for guiding research on the interaction dynamics between FcRn and various IgG formats, including Fc-engineered variants and other receptor-targeting modalities. This method offers a refined approach to dissecting the nuances of pH-dependent binding and provides a robust framework for differentiating between affinity and avidity, thereby enriching our understanding of FcRn-IgG interactions in a comprehensive manner.

Results

Assay Design Considerations

To investigate an interaction between an analyte and a ligand using a surface biosensor, two assay orientations are possible. Which one that is preferred will depend on the biology in question, resulting in immobilization of a bivalent or monovalent binding partner, as shown in **Figure 1**. If the bivalent binding partner, such as IgG, is immobilized (**Figure 1 A**), the monovalent partner in solution, FcRn, would be able to bind IgG in a monovalent fashion. This binding mode will occur independently from the ligand surface density, and bivalency of the immobilized partner is not relevant in orientation **A** as it merely affects the number of available binding sites on the surface. Hence, orientation **A** exclusively probes the affinity-binding mode. When measuring the interaction between FcRn and IgG in setup **A**, the pH-dependent self-interaction of the receptor should be taken into consideration, which may occur concurrently with the FcRn-IgG interaction under acidic pH conditions and pose a challenge in distinguishing between the two effects.[59] To circumvent problems with ligand density control and measurement artifacts on conventional sensors, it has been suggested as good practice to choose assay orientation **A** to avoid the occurrence of avidity altogether. This assay orientation may be beneficial for undisturbed affinity values and has also been demonstrated to resolve affinity values for FcRn[40], however the IgG-FcRn interaction reflects a more complex mechanism.

In the opposite orientation (**Figure 1 B**), the monovalent binding partner (FcRn) is immobilized and the bivalent partner is in solution (IgG). In this case, IgG may engage the immobilized receptor with either one or two Fc binding sites, which may result in measurement of both binding modes - affinity and avidity - simultaneously. At medium immobilized densities, one fraction of the receptor may become interlinked by IgG (2:1 binding) while another fraction not interlinked (1:1 binding), cf. **Figure 1 B** and **Table 1**.

Irrespective of the technology used, our approach does not rely on immobilizing an absolute number of FcRn ligand molecules, acknowledging the dynamic expression of FcRn on the membrane. We focus on achieving a ligand density that allows for the clear detection and discrimination of both affinity and avidity interactions with FcRn. By employing switchSENSE technology, we aim to simultaneously measure these binding modes of similar magnitude, ensuring accurate analysis of the FcRn-IgG interactions without the influence of artifacts.

To test this, a commercially available switchSENSE biochip was used, with medium FcRn density. Specifically, the DNA nanolevers, 32 nm in length, are covalently attached to the surface with approximately 50 nm in distance. The complementary strand is functionalized with soluble recombinant FcRn via a short linker, both (DNA + linker) allow flexibility and rotation. As such, the receptor is disengaged from the surface within the flow channel, which reduces surface related effects like steric hindrance.

Utilizing fitting models to evaluate SPR or switchSENSE-derived sensorgrams exhibiting biphasic binding behaviour typically leads to the expression of two overlapping dissociation phases. One dissociation phase results from the affine binding (fast dissociation) and the second one from the avid binding mode.

To address avidity effects, we chose orientation **B**. Model mAbs (WT vs YTE), mAb1 and mAb2, both human IgG1 (hIgG1) antibodies were characterized. Mab1 and mab2 WT as well as mab1 and mAb2 YTE variant, share the same Fc part for each set, but show different target binding (Fab patches). For immobilization, we took advantage of a recombinant human single chain FcRn (hsc-FcRn) in which the truncated alpha chain is fused to beta-2-microglobulin via a 4G4S linker to ensure a stable folded complex, as described.[60]

Here, we established a universal assay using the switchSENSE platform, without the necessity for surface density adjustment and revealed all relevant kinetic parameters, including both, affinity and, critically the avidity binding mode of FcRn. The association and dissociation kinetics of FcRn - IgG antibodies were measured by fluorescence proximity sensing (FPS) in real-time. Kinetic rates for affinity and avidity were modelled accordingly.

Comparative Interaction Analysis of Antibody Fc Variants with FcRn at pH 6.0 across different Technology Platforms

In a first set of experiments, we show that our chosen assay setup works robustly having hsc-FcRn immobilized and the model hIgG1 in solution (**Figure 1 B**). Here, we compare a mAb1 and mAb 2 (Fc WT vs. Fc YTE) at pH 6.0 with SPR and FcRn affinity chromatography. Immobilizing FcRn emulates the physiological context of cell surface interactions, representing an optimal experimental design for assay implementations across technologies. Consequently, we opted to utilize an FcRn density exhibiting complex binding kinetics. Our system is anticipated to measure both the affine (1:1) and avid (2:1) binding mode simultaneously. In accordance with these expectations, we analyzed the acquired sensorgrams by implementing a bivalent binding model that accurately represents the kinetic data (**materials and methods**). As shown in **Figure 2** bivalent binding is mainly prominent during the dissociation phase, having two species on the biosensor surface that can be resolved, while the association phase is monophasic.

The bivalent binding model we chose, revealed similar observations for both mAb1 Fc WT and YTE variant. The monophasic association phase (k_{ON}) is followed by a biphasic dissociation phase showing a fast dissociation rate ($k_{OFF,AFFINITY}$) and slow dissociation rate ($k_{OFF,AVIDITY}$) reflecting affinity and avidity binding mode (**Table 2**). The avidity effect is mainly visible via the dissociation rate k_{OFF}. To account for subtle alterations in k_{ON} we focused on assessing the dissociation constant (K_D) in the comparative evaluation of the two antibody variants and all further experiments. At pH 6.0 we find an $K_{D,AFFINITY,WT}$ of 45.4 nM for mAb1 Fc WT compared to Fc YTE showing a $K_{D,AFFINITY,YTE}$ of 3.09 nM. The second kinetic species displays a much slower dissociation rate constant ($K_{D,AVIDITY}$), reflecting the

FcRn avidity binding mode. For Fc WT and Fc YTE, $K_{D,AVIDITY,mAb1\text{-}WT}$ was 6.24 nM and $K_{D,AVIDITY,mAb1\text{-}YTE}$ was 0.29 nM. To confirm the switchSENSE affinity from the applied bivalent model, we generated a low FcRn density. The binding kinetic of mAb1 Fc WT and FcRn at pH 6.0 could be exclusively described by a monovalent fit model (**Figure S 1 A and B**). This reflects the affinity-binding mode where one IgG interacts with one FcRn. The weak interaction resulted in similar kinetic parameters in accordance with the medium ligand density showing affinity and avidity ($K_{D,AFFINITY,medium}$ 45.4 nM vs $K_{D,AFFINITY,low}$ 57.0 nM, **Table S 1**).

The second antibody set, mAb2 WT / YTE, share the same Fc regions corresponding with mAb1 variants, but bind a different target, thereby displaying different variable regions (V_H/V_L). As mAb2 shows a different Fab patch, it differs from mAb1 in affinity and avidity (different kinetic profile, **Figure S 2, Table S 2**). At pH 6.0 mAb2 WT is 21x more affine, while YTE is 5-fold stronger in affinity, compared to the mAb1 variants. For a direct comparison with Biacore SPR technology, we captured low (12 RU) and medium FcRn (140 RU) levels on a C1 chip, allowing affinity (low) and affinity and avidity (medium) to occur simultaneously. To ensure the validity of our kinetic analyses, we meticulously assessed the goodness of fit for each sensorgram. This assessment was based on the examination of residuals and the analysis of the kinetic rate parameters obtained. SPR was not capable of resolving reliable binding kinetics for mAb1 WT and mAb2 WT on both densities (**Figure S 3 A-C** and **Table S 3**). Furthermore, SPR could not distinguish between affinities and avidities and the resulting Fab influence of both YTE variants (**Figure S 3 D-E** and **Table S 3**) as switchSENSE did. In contrast to SPR, FcRn affinity column clearly resolved the varying FcRn interactions in the same ranking as switchSENSE (from weak to strong binding): mAb1 WT < mAb2 WT < mAb1 YTE < mAb1 YTE (**Figure S 4**). A human endothelial cell-based recycling assay (HERA assay, **Figure S 5**) is also in agreement with our findings (method described previously[61]). Here, the mAb1 YTE variant demonstrated improved uptake and recycling, leading to enhanced trafficking properties, in contrast to the WT, which lacked efficient trafficking.

We demonstrated the feasibility of resolving the FcRn - IgG interaction applying switchSENSE, and its superiority in differentiating between affinity and avidity within one measurement resolving all relevant kinetic rates. We confirmed that the two events correspond to interlinked (slow dissociation, avidity binding mode) and non-interlinked (fast dissociation, affinity binding mode) species. Our results indicate that there is no discernible benefit in performing additional measurements at lower or higher ligand densities that could potentially modify the affinity-avidity relationship or give rise to measurement artifacts. SwitchSENSE could also differentiate between mAb1 and mAb2, displaying a potential Fab contribution.

Considering the weak interaction of mAb1 WT - FcRn at pH 6.0 ($k_{OFF,AFFINITY}$ = 0.35 s- 1, pH 6.0), and its insignificance for antibodies with improved pharmacokinetics, an in-depth

analysis performing a pH screening is not conducive to the goal. Therefore, we decided to conduct subsequent measurements using mAb1 Fc YTE, which exhibits enhanced binding strength for FcRn, and directly compare switchSENSE with SPR in more detail.

Transition from Affinity to Avidity: A Systematic Analysis of the pH-Dependent FcRn - mAb1 (YTE) Interaction

The cell surface dynamics of FcRn are highly complex, with membrane-bound FcRn and FcRn associated with intracellular endosomal compartments (> 90%) showing significant variation.[9] It has been proposed that 50% is rapidly endocytosed and mixes with 96% of cellular FcRn in an internal pool.[9] This leads to drastically increased FcRn concentration at the acidified endosomal membrane, where avidity presumably occurs. FcRn-associated vesicular trafficking is a dynamic process with speeds up to 3 μm/s, indicating rapid IgG uptake and intracellular movement where affinity and avidity are assumed to be important.[62] Understanding FcRn-IgG interactions requires analyses of pH modulation from acidic to neutral throughout the endosomal acidification process, rather than just at extreme pH values, to assess affinity and avidity effectively.

Binding Kinetics of FcRn – mAb1 YTE applying switchSENSE and SPR

To characterize how the affinity and avidity of mAb1 YTE and hFcRn change over a pH range from 5.8 to 7.4, we inject mAb1 YTE over immobilized hFcRn while incrementally increasing the pH by 0.2. The obtained sensorgrams are shown in **Figure 3** with the derived kinetic rate parameters in **Table 3**. mAb1 YTE was injected at 5 different concentrations in a two-fold dilution series for each pH value in an overall concentration range from 3.75 nM to 800 nM. MAb1 YTE mutant shows binding over a broad range. This enables us to understand how the change in pH influences the kinetic rate parameters (k_{ON} and k_{OFF}) up to a pH of 7.4. All kinetic binding experiments were conducted with careful consideration of ligand density and the potential for measurement artifacts. Even in the case of monovalent interaction, which solely permits affinity, measurement artifacts may arise due to excessively high ligand densities and insufficiently low flow rates.

For this reason, the implementation of an assay setup that allows simultaneous analysis of affinity and avidity is explained in detail. In all kinetic measurements, especially in the assay setup presented here, control over the ligand density is critical. Ligand molecules on a biosensor surface exhibit a random distribution, rendering the interlinking of ligands by a bivalent analyte a statistically driven process. Regulation of the spatial arrangement of ligands is a crucial parameter, as it influences the extent of interlinking. There are two (hypothetical) extreme assay setups having very low density or very high densities. Analyzing 100% avidity or 100% affinity is challenging to achieve and both extremes do not reflect the real experimental situation.

For low densities, a non-negligible probability exists that two ligands are close enough to become interlinked. Due to a lower limit of detection for technologies, it might not be resolvable. For high densities, the successive adsorption of analytes to the surface results in the creation of monovalent ligand sites. Some ligands that potentially cannot engage in a bivalent interaction will always be left.

The association phase of IgG to FcRn is characterized by a monoexponential fit, while the dissociation phase displays a biphasic pattern, with relative amplitudes of (50 ± 20)%, representing equal contributions from affinity (1:1) and avidity (2:1) binding interactions. This indicates that the applied ligand density successfully captures both binding events (**Figure S 6**). Notably, the amplitudes A_{fast} and A_{slow} of each exponential term in the dissociation show a dependency of the analyte (IgG) concentration used (**Figure S 7**). With increasing concentrations of hIgG1 Fc YTE, the contribution to the fast, affinity-based species to the overall dissociation curve increases while the slow avidity driven species decreases. This phenomenon was also previously described elsewhere.[54]

The analysis of the biphasic dissociation phase using a double exponential fit model is readily achieved through non-linear least square fitting algorithms, which is a computational method employed to minimize the sum of the squares of the differences between observed and predicted values in a data set (**Materials and Methods**). However, the following preconditions have to be met. First, for a robust fit analysis, the amplitude of each component needs to be significant, i.e., larger than 10%. The amplitude reflects the respective contributions of the different dissociating species to the overall dissociation curve. Second, the measurement time selected has to long enough that the slow time constant can be analyzed (one-time the observable time constant $tau_{OFF} = 1/k_{OFF}$ as reference value). Resolving a dissociation rate of 0.01 s^{-1} requires measurement of the dissociation for 100 sec or an k_{OFF} of 0.001 s^{-1} for 1000 sec. A 5% rule is cited in literature[63], but here we exceeded this for all kinetic data sets. Next, the selected sampling rate must be high enough to generate data points (here 10 Hz) sufficient for the analysis of fast time constants. For the mathematical deconvolution of the two species, it is imperative that the two time constants exhibit a significant disparity, with a minimum factor of two distinguishing them, to ensure accurate differentiation. Ultimately, a flow rate of 1000 µL/min was implemented to effectively surmount any potential mass transport limitations that may arise during the experiment.

To strengthen the primary objective of our study to simultaneously differentiate between affinity and avidity in the context of the FcRn - IgG interaction and to elucidate the pH dependency of this interaction in detail, showing that switchSENSE is a viable and effective platform for its characterization, we performed a comparison with Biacore SPR.

We captured hsc-FcRn (via Neutravidin) at 3 different densities, low (12 RU), medium (140 RU) and high (1100 RU) on a C1 chip and injected mab1 YTE at different concentrations for 5 different pH values (5.8, 6.0, 6.4, 6.8, 7.4). Low FcRn densities could be modelled

applying a 1:1 fit (BiaEvaluation Software), displayed by the small and randomly distributed residuals, demonstrating the affinity binding mode (**Figure S 8, Table S 4**). At pH 7.4 SPR reached its limitation in reliability measuring kinetic rates (k_{ON}). SwitchSENSE and SPR dissociation rates ($k_{OFF,AFFINITY}$) are within the same range (max. 2-fold difference), but on rates (k_{ON}) determined with switchSENSE are >10-fold faster (**Table 3 vs. Table S 4**). For medium and high density, more complex models (bivalent analyte and heterogeneous ligand model) were applied (**Figure S 9**), to account for simultaneous occurrence of both affinity and avidity interactions, which was the intentional aspect of our experimental design. Both models could not resolve high FcRn density data (**Figure S 9 B+D**), shown by the systematic pattern of residuals, indicating a poor fit.

To further investigate the potential of SPR to decipher affinity and avidity within one experiment, medium FcRn density was evaluated, applying the heterogeneous ligand model (**Figure S 9 C**). Notably, the model clearly showed systematic deviations (compared to switchSENSE, **Figure 3 J**), suggest it is lacking critical factors and the underlying assumptions are not applicable to the data set in question. However, we applied it to all FcRn medium density sensorgrams (**Figure S 10 and Table S 5**), as it is the model with the highest degree of freedom available within Biacore's SPR Evaluation Software. Results were compared with switchSENSE data. The "fast" component of the model, which is intended to represent the affinity interaction, aligns approximately with the 1:1 binding model results for low FcRn density. However, the "slow" component, which is hypothesized to reflect the avidity interaction, did not yield reliable kinetic rates. The rates were similar across different pH levels, contradicting the expected trend of decreased binding with increasing pH. Additionally, the maximum response levels (R_{max}) were too low to confidently determine valid kinetic rates. Further increasing the density results in even poorer fitting as for medium density (residuals) thus was not applicable.

Here, we demonstrated the feasibility of switchSENSE in measuring, differentiating and analyzing affinity and avidity of the FcRn - mAb1 YTE interaction by using an assay setup designed to facilitate the simultaneous occurrence of both binding events. While SPR is a reliable technology in determining affinities, it was not capable of capturing the complexity of the FcRn-antibody interactions, particularly in the context of avidity.

Developing an Affinity-to-Avidity Binding Model

The elucidation of FcRn - mAb1 YTE's complex interactions provides substantial insights for the establishment of a representative model system, facilitating the characterization of the fundamental mechanisms governing this molecular interplay. Typically, the interaction dynamics of biomolecules are governed by transient, non-covalent binding occurrences. The simplest form of binding, the monovalent interaction of two molecules with exactly one binding site for each other, can be characterized by three biophysical parameters: the kinetic rate constants of association and dissociation (k_{ON} and k_{OFF}), and the dissociation constant

($K_D = k_{OFF}/k_{ON}$). When two or more binding sites are involved in a molecular interaction simultaneously, the interpretation of binding needs to be expanded by the concept of avidity, which denotes the enhancement of the overall binding strength of a molecular complex due to the formation of multiple bonds. The avidity enhancement may result from an increased formation propensity of the molecular complex (a faster k_{ON}), or a higher complex stability (a slower k_{OFF}), but frequently arises from a combination of both effects. To comprehend the mechanism of action and regulation of such systems, it is necessary to understand avidity effects in detail. However, even if the affinities of the individual binding sites are known, currently it is impossible to predict the avidity enhancement quantitatively.

Figure 4 depicts an illustration of the free state and the two types of bound states for a bivalent analyte interacting with ligands on a surface. In the simplified picture, the avidity adjusts according to the absolute and relative contributions of the individual on- and off-rates of the transitions $0 \leftrightarrow 1$ and $1 \leftrightarrow 2$.

In particular, the dynamic dissociation and re-association of one to two binding sites, namely transitions of the kind 2 to 1 to 2 ($k_{ON}^{app.}$.and $k_{OFF}^{app.}$), is crucially important for the effective off-rate ($k_{OFF,AVIDITY}$) and hence for the avidity enhancement. It is noteworthy in this context that, in the majority of experiments, distinguishing between singly bound and doubly bound states within the measurement signal is not feasible. Consequently, only 'observable' on- and off-rates ($k_{ON}^{obs.}$ and $k_{OFF}^{obs.}$) between the free and any kind of bound state are being measured, as indicated in the lower part of **Figure 4**. The transition of $2 \leftrightarrow 1 \leftrightarrow 2$ is not visible in the measurement signal. Utilizing the switchSENSE technology, we discern the transition from 1 to 0 (k_{ON1} and k_{OFF1}) in the fluorescence signal predominantly through a rapid dissociation rate, which mirrors the affinity binding mode. It is equivalent to the measured kinetic rate parameters k_{ON} and $k_{OFF,AFFINITY}$. The affinity can be distinguished from the transition of 2 to 0, reflecting the avid binding mode ($k_{OFF,AVIDITY}$). Avidity is only observed when both binding sites (Fc heavy chains) are concurrently disengaged from FcRn at a given point in time. In this scenario, a second association rate (0 to 2) is not discernible as a change in the fluorescence signal transpires through its initial contact.

Affinity-Avidity Analysis of FcRn with mAb1 Fc YTE

To comprehend how the affinity and avidity of mAb1 Fc YTE and FcRn alter over a pH range from acidic to neutral, we graphed the kinetic rates from **Table 3** in a rate scale plot (**Figure 5**). The mAb1 YTE variant demonstrates binding to FcRn across a wide range, making it an ideal candidate for such a comprehensive analysis and for examination of the kinetic rate parameters in relation to pH. All kinetic rate parameters, indicative of affinity and avidity, were computed and ascertained by applying a biphasic fit model for the dissociation phase, while the association phase was observed to be monophasic (**Materials and Methods**). The rate scale plot facilitates a systematic analysis of kinetic rate parameters from multiple conducted experiments, enabling an understanding of their correlation at a single

glance. As depicted in **Figure 5**, the upper y-axis represents the association rate constant (k_{ON}), while the lower y-axis signifies the dissociation rate constant (k_{OFF}) for affinity ($k_{OFF,AFFINITY}$) and avidity ($k_{OFF,AVIDITY}$) respectively. Both axes are on a logarithmic scale. An inference about the binding strength can be directly derived from the rate scale plot. Both binding rates (k_{ON} and k_{OFF}), each represented by a data point, with increasing pH from left to right, are linked by a vertical line. The distance between the data points, or alternatively, the length of the connecting line, mirrors the binding strength, i.e., weaker interactions result in closer points.

For the mAb1 YTE and FcRn, the association rate (k_{ON}) exhibits only a minor alteration in response to pH variation. Up to and inclusive of pH 6.6, it remains within the range of $6.14x10^6$ $M^{-1}s^{-1}$ to $9.23x10^6$ $M^{-1}s^{-1}$ ($k_{ON,pH5.8} = 7.58x10^6$ $M^{-1}s^{-1}$). Commencing at a pH value of 6.8, it slightly decreases by a factor of three up to pH 7.4 ($k_{ON,pH7.4} = 2.41x10^6$ $M^{-1}s^{-1}$). The corresponding affinity off-rates are $k_{OFF,AFFINITY,pH5.8} = 2.15x10^{-2}$ s^{-1} and $k_{OFF,AFFINITY,pH7.4} = 119x10^{-2}$ s^{-1}. The affinity dissociation rate ($k_{OFF,AFFINITY}$) increases by a factor of 54 whereas the overall change in $K_{D,AFFINITY}$ is approx. 170-fold ($K_{D,AFFINITY,pH5.8}$ = 2.84 nM vs. $K_{D,AFFINITY,pH7.4}$ = 494 nM). By using a four-parameter regression model (**Equation (6)**) on the sigmoidal, increasing affinity dissociation rates across the entire pH spectrum, an inflection point is identified at pH 7.2 (**Figure 5**, **Figure S 11**).

The avidity binding mode exhibits a low dissociation constant ($K_{D,AVIDITY}$) of $K_{D,AVIDITY,pH5.8}$ = 0.23 nM, which increases to $K_{D,AVIDITY,pH7.2}$ = 46.2 nM at pH 7.2 and becomes unobservable at pH 7.4. This results in a 200-fold change in $K_{D,AVIDITY}$. To thoroughly characterize the relationship between avidity and affinity, it is crucial to examine the pH dependency across the entire range.

Avidity Switch of FcRn - hIgG1 Fc YTE variant

To address the question how avidity and affinity for the FcRn - hIgG1 Fc YTE interaction correlate, we focused on comparing the dissociation constants $K_{D,AFFINITY}$ and $K_{D,AVIDITY}$ and performed a K_D analysis (data from **Table 3**)

In the affinity or, correspondingly, avidity case, the antibody binds through one or both Fc heavy chains to one or two FcRn molecules. The overall binding strength is a combination of both components, affinity and avidity, which are influenced by pH. As depicted in **Figure 6**, dividing $K_{D,AFFINITY}$ by $K_{D,AVIDITY}$ yields an avidity enhancement factor for each pH. Plotting the avidity enhancement factors against the corresponding $K_{D,AFFINITY}$ values generates a graph illustrating the relationship between avidity and affinity. It directly assesses the correlation between affinity and avidity as a function of pH change.

As affinity decreases (lower binding strength) from acidic to neutral pH, the avidity enhancement diminishes due to the reduced stability of the affinity binding mode. The avidity effect is primarily driven by the dissociation rate. The faster the affinity dissociation rates of FcRn to IgG Fc YTE, the less significant its contribution to the overall avidity. Conversely,

the strong affinity of FcRn and IgG at acidic pH leads to an increased contribution to the overall avidity. The IgG YTE heavy chains are stabilized in the acidic environment via FcRn and its avid binding mode.

Specific to the characterized FcRn - IgG Fc YTE interaction is the avidity enhancement factor around pH 6.2, which displays a pH-switch from strong to weak avidity enhancement, as indicated by the dashed lines. This primarily results from the interplay of the absolute and relative contributions of the individual on- and off-rates of the transitions from 2 to 1 to 2 (**Figure 6**). At a pH value of 7.4, the affinity dissociation rate is so rapid that there is no observable contribution to an avidity effect at all. Only the affinity binding mode was resolved and the avidity to affinity switch is off.

Discussion

The importance of avidity in both *in vitro* and *in vivo* studies is emphasized by the significant contrast in FcRn density between the cell membrane and the endosomal compartment, with the latter exhibiting much higher densities. This is particularly relevant given the ongoing endocytotic trafficking of FcRn at the cell surface, where avidity is favoured in the acidic environment of recycling endosomes.[9,10] *Abdiche et al.*[40] highlighted the critical role of avidity in FcRn-IgG interactions for enhancing antibody serum half-life. Conversely, *Tesar et al.*[64] suggested that while bivalent engagement is not imperative for transcytosis or recycling at elevated antibody levels, avidity may still influence FcRn-mediated IgG transport. Prior studies that focused on single equilibrium dissociation constants for IgG Fc variants fail to fully capture the intricate nature of their *in vivo* behaviour.[47] These findings collectively imply a complex interplay of affinity, avidity, antibody concentration, and FcRn expression in modulating antibody serum half-life.

Our study presents an assay using switchSENSE technology to simultaneously measure FcRn affinity and avidity in a single experiment, capturing all relevant kinetic parameters. This was achieved by examining the interaction between hsc-FcRn and human IgG1 (WT/YTE) variants across a pH range of 5.8 to 7.4. The study thoroughly explored the relationship between FcRn and IgG binding modes and compared the results with SPR, the established standard technique. The research yielded five key insights that enhance the understanding of pH-dependent FcRn-IgG binding, contribute to the broader knowledge of FcRn-IgG biology, and demonstrate how Fc engineering affects not only FcRn affinity, but also significantly increases avidity due to bivalent binding. A critical discovery was that conventional SPR assays are insufficient to capture the complexity of this interaction.

First, we highlighted the importance of assay design, ligand density regulation, and meticulous artifact evaluation in studying complex binding interactions to discern affinity and avidity accurately. By immobilizing FcRn and allowing bivalent IgG to interact with it, our assay uniquely differentiates between affinity and avidity. Considering the dynamic

expression of FcRn *in vivo*, we focus on the robust differentiation these two binding modes (**Figure S 6**) rather than a fixed FcRn ligand count on the biosensor.

Second, the process of forming bivalent or monovalent FcRn-IgG complexes is concentration-dependent during the association phase (**Figure S 7**). High concentrations of analyte favour the formation of monovalent complexes with a 1:1 stoichiometry, leading to higher contribution to affinity interactions. In contrast, at lower concentrations, bivalent complexes with a 2:1 stoichiometry are more likely, indicative of avid binding. The prevalence of monovalent binding at high analyte concentrations can be explained by the saturation of surface FcRn, thereby preventing bivalent complex formation. This concept aligns with observations from the kinetic analysis of emicizumab using switchSENSE technology[54] and suggests that high antibody concentrations could play a role in outcompeting avid binding as shown by *Tesar et al.*[64], noteworthy measured on an FcRn overexpressing cell line at pH 6.0.

Third, Biacore SPR successfully measured FcRn affinities at low ligand densities, but had limitations with medium densities, struggling to differentiate between affinity and avidity. The data's reliability was questionable due to potential biases in technique and modelling. The heterogeneous ligand model used by Biacore SPR, while flexible with two sets of rate constants, did not precisely describe the binding data. Although it is the best option available within the Biacore software, it still lacks the capability to distinguish between affinity and avidity compared to the switchSENSE model. Our switchSENSE data indicate a monophasic association phase, suggesting that a second binding event to FcRn, which would contribute to avidity, occurs almost instantaneously due to the proximity-induced high local concentration of FcRn. These findings demonstrates the need for further analytical models and technologies, such as switchSENSE, that can more accurately reflect the biophysical nature of these interactions. SwitchSENSE demonstrated superiority as reliable technology for studying the nuances of FcRn-antibody affinity to avidity relationship.

Fourth, we compare the affinities of IgG Fc YTE with IgG Fc WT. In our study, the association phase appeared to be monophasic as a signal change occurs through its initial contact. Comparing our observations with published literature revealed that changes in FcRn - IgG affinity were primarily driven by a decreasing dissociation rate (k_{OFF}), corroborating our (SPR and switchSENSE) and earlier findings.[36,65] Notably, Biacore SPR revealed > 10-fold decreased $K_{DAFFINITY}$ than switchSENSE. This distinction is primarily driven by a significantly faster association rate as measured by switchSENSE, exceeding the values obtained via SPR. Dissociation rates are consistent for both technologies. SwitchSENSE utilizes a different methodological approach in presenting the ligand onto the planar sensor surface, compared to other biophysical techniques. Under physiological conditions, the attachment of FcRn to a DNA nanolever via a short linker allows target flexibility and rotation. This configuration positions FcRn at the distal end of the nanolevers, thought to effectively eliminate potential matrix-related surface effects, ensuring optimal target

accessibility within the flow channel. A previous switchSENSE study[53] revealed similar findings (both assay orientations), while the determined dissociation constant K_D for affinity matched Kinexa data.[53,66,67]

The affinity dissociation rates for the mAb1 YTE variant, spanning from pH 5.8 to 7.4, exhibit an inflection point at pH 7.2, which could not be uniquely determined by SPR. The structural basis of the pH-dependent antibody binding to FcRn involves residue Ile253 and several histidine residues within FcRn at positions 310, 433, and 435,[28,31,32] which are implicated in the pH dependency by becoming protonated at pH 6.0 ($pKa_{Histidine}$ = 6.0).[68] At lower pH, FcRn is more thermodynamically stable and the dissociation is significantly slower than at neutral/basic pH.[57,68] In a model compound the pKa for a histidine residue is 6.6, but in an actual protein the pKa depends on the chemical surrounding of the involved histidines and the solvent, with an observed pKa of histidine residues in proteins ranging from 5 to 8.[69,70] The discovery of a pKa value of 7.2 for an Fc YTE variant indicates that the histidine molecules are deprotonated relatively late in a nearly neutral environment. This results in a strong affinity of Fc-engineered YTE antibody for FcRn ($K_{D,YTE,6.0}$ = 3.09 nM) compared to an mAb1 WT antibody ($K_{D,WT,6.0}$ =45.4 nM), which is approximately 15 times more affine. The investigated mab2 (WT/YTE), display higher affinities then mAb1, whereas both antibodies only differ in their Fab fragment (Fab patches). They vary in hydrophobic and electrostatic patches, which are known to influence FcRn binding by Fab contributions, as previously described.[45,46,48,71,72] Here, SPR data appears to be inconsistent, as it could not resolve the difference in binding of mAb1 YTE mab2 YTE nor measure the affinity for mAb1 WT, and differs with FcRn affinity chromatography data, which was in agreement with the altered interaction found via switchSENSE, as well as HERA assay showing superior recycling of YTE vs. WT.

The robust affinity of the YTE variant at pH 6.0, coupled with its late transition at pH 7.2, correlates with a weak, yet quantifiable affinity at pH 7.4. In direct comparison, we measure a K_D for FcRn - mAb1 Fc YTE at pH 5.8 of 2.84 nM and for pH 7.4 the K_D is 494 nM, suggesting a 170-fold difference in affinity ($K_{D,7.4}/K_{D,5.8}$). This extensive range of binding, due to its late deprotonation, further substantiates the superior pharmacokinetic properties of YTE compared to WT. These characteristics contribute to a prolonged half-life and decelerated clearance in transgenic mice, in comparison to the Fc wild type.

Finally, we characterized the relationship between avidity and affinity of FcRn and mAb1 Fc YTE, demonstrating that one IgG engages two FcRn via both heavy chains, resulting in a proposition for a simplified model describing the correlation. A review of the literature reveals diverse assay setups[40,73], binding modes[45,46] and complex fit models[41] primarily comparing single affinity values for both extremes[74] (pH 6.0 vs 7.4). In our work, we systematically analyzed the FcRn - Fc YTE interaction within a pH range from 5.8 to 7.4. This detailed examination of the FcRn avidity to affinity relationship for hIgG1 Fc YTE allowed us to observe a pH-switch with a transition point around pH 6.2, which SPR did not

resolve. Strong affinities from pH 5.8 to 6.2 show increased avidity contribution (13x for pH 5.8), while weak affinities from pH 6.4 to 7.2 only show minor contribution to the avidity effect (5x for pH 6.8). Notably, there is no measurable avidity contribution at pH 7.4, and exclusively affinity was analyzed. Particularly, the transitions of 2 to 1 to 2 (**Figure 4**) occur more frequently at a pH value less than 6.2, leading to a strong, observable avidity enhancement, while it is less pronounced above pH 6.2. Comparing the avidity enhancement factor of mAb1 YTE ($K_{D,AFFINITY,YTE}/K_{D,AVIDITY,YTE}$ = 11) and WT ($K_{D,AFFINITY,WT}/K_{D,AVIDITY,WT}$ = 7) at pH 6.0 shows that Fc YTE not only exhibits a higher affinity than Fc WT, but also a stronger contribution to the avidity effect. Furthermore, the YTE variant shows a 22-fold stronger avidity compared to Fc WT at pH 6.0 ($K_{D,AVIDITY,WT}/K_{D,AVIDITY,YTE}$).

Interpreting this finding in a physiological context implies that during endosomal acidification, the YTE mutant binds to FcRn much earlier than Fc WT due to its higher affinity and avidity-driven FcRn complex stability. In the extracellular space (pH 7.4), avidity is switched off, and a rapid antibody release occurs. These properties are desirable for an antibody Fc engineering with a superior recycling mechanism and an extended serum half-life.

The outcome of our study confirms previous research[48,61,75] where YTE displays a more pronounced pH-dependent binding and exhibits a decelerated elution profile within a pH gradient during FcRn affinity chromatography. This method allows functional characterization of antibodies, where the packaging density of the FcRn column defines the degree of predominantly avidly bound antibodies, and their retention time indicating pharmacokinetic properties, but does not reveal kinetic rates.

In conclusion, our research demonstrates the importance of understanding the pH-dependent FcRn-IgG recycling mechanism and its implications for antibody engineering. We highlighted the advanced capabilities of switchSENSE technology for a detailed analysis of FcRn-IgG interactions, offering quantitative insights into both affinity and avidity. The technology has proven to be particularly adept at differentiating these interactions across a spectrum of FcRn densities and pH levels, where SPR encounters limitations. Our approach aligns with complementary methods, including the HERA assay, reinforcing the robustness of our findings. SwitchSENSE is a technology that bridges SPR, which provides affinities, and FcRn chromatography to cellular assays like HERA, deciphering complex kinetic interactions.

In future work, we intend to use our assay configuration and binding model to elucidate the molecular interactions of various antibody mutants and formats. Our objective is to employ switchSENSE technology to dissect the kinetic interactions, particularly in terms of avidity, for novel antibody entities with intricate designs, such as heterodimeric Fc modifications. This will inform strategies for optimizing FcRn-mediated recycling of these antibodies. The translational potential of our work lays the groundwork for future *in vivo* investigations. Such

studies are crucial for bridging the gap between our *in vitro* findings and potential clinical applications.

Materials and Methods

FcRn protein

The recombinant human FcRn protein was generated and purified in-house (Roche) by transient transfection of HEK Expi293F cells (Thermo Fisher Scientific). One plasmid was used for the transfection reaction, which encoded for the extracellular domain of human FcRn and human beta-2-microglobluin (hβ2M) as single-chain protein. The sequence of hβ2M is encoded N terminally fused to the hFcRn extracellular domain by a 4G4S linker. The accession number and aminoacid sequence are NP_001129491 (24–297) for hFcRn and NP_004039 (20–119) for human hβ2M.

Antibodies

The recombinant human IgG1 antibodies were generated and purified in-house (Roche) by transient transfection of HEK Expi293F cells (Thermo Fisher Scientific). The formats were produced by the expression of plasmids encoding for the light and the heavy chain. Human IgG1 Fc WT and Fc YTE (M252Y, S254T, T256E) are tool antibodies that bind a target that is non-relevant *in vivo*.

switchSENSE Biosensor Experiments

Real-time binding kinetic experiments were performed with a switchSENSE DRX2 instrument (Dynamic Biosensors, Germany) on a switchSENSE chip (MPC-96-2-G1R1-S, Dynamic Biosensors, Germany) using the fluorescence proximity sensing (FPS) mode.[53] The measurements were performed at 25°C, applying a flowrate of 1000 µL/min and using a running buffer of 10 mM Na2HPO4 / NaH2PO4, 140mM NaCl supplemented with 50 µM EDTA, 50 µM EGTA and 0.05%(v/v) Tween 20 (PE140 Buffer pH 5.8 to 7.4, Dynamic Biosensors, Germany).

Binding Kinetics - switchSENSE Technology / switchSENSE Biochip

On a switchSENSE chip, ligand molecules are tethered to gold microelectrodes via short DNA duplexes (96 bp, 32 nm), termed nanolevers. In this work, a low, constant negative voltage of -100 mV was applied to repel the nanolevers from the microelectrodes. This way, the nanolevers extend away from the surface, presenting the ligands to the flow of solution in the microfluidic channel, and facilitate optimal accessibility by solute analyte (the electric potential decays to sub-mV after several nm from the surface due to ionic screening and thus hardly affects the molecules at the nanolever top). The measurement mode is called

fluorescence proximity sensing (FPS) or Static Mode at constant voltage where $V_{attrative}$ = $V_{repulsive}$ = -0.1V.

One strand of the DNA nanolever duplex is covalently connected to the surface via a gold-sulfur bond, while the other strand is exchangeable and binds to the fixed strand through DNA base pairing. For the detection of analyte and ligand molecules, a dye molecule on a flexible linker protrudes from the top end of the fixed strand. Acting as a probe on a leash, the dye rapidly diffuses atop the nanolevers and changes is fluorescence emission intensity when collisional or static quenching occurs with ligand or analyte molecules that are present in its proximity (FPS).

The single-photon counting unit of the DRX² analyzer measures the fluorescence emission from a 0.01 mm² spot, containing app. 10^7 nanolevers (depending on the adjusted density) at a sampling rate of 1 Hz (frequency setting adjusted to 10 Hz for FcRn – IgG measurements). For the preparation of low ligand densities, the switchControl software (Dynamic Biosensors) was used by applying a negative voltage ($V_{repulsive}$ = -0.6V) until an absolute fluorescence value of 30 kcps was reached. The method is previously described.[76]

In a single molecule picture, the association and dissociation of analyte and ligand molecules occur quasi-instantaneously: at any given point in time, an individual nanolever either has bound an analyte molecule, or not; accordingly, the fluorescence emission of an individual nanolever either is f_{bound} (quenched) or is $f_{unbound}$ (unquenched). Considering the ensemble of all nanolevers on a detection spot, the measured fluorescence intensity is $F_{meas}(t) = n_{bound}(t) \cdot f_{bound} + n_{unbound}(t) \cdot f_{unbound}$, with $n(t)$ being the numbers of bound or unbound ligands at time t. Hence, the sensor response $F_{meas}(t)$ is directly proportional to the number of bound molecules, i.e., the Fraction Bound. Typical fluorescence count rates are of the order of 1 million counts per second, but for straightforward comparison of different measurement series, fluorescence count rates are normalized with respect to baselines that were recorded before the injection of analyte molecules, $F_{norm}(t) = \frac{F(t)}{F_{base}}$. Further, reference data from blank runs without analyte molecules are subtracted to compensate for potential signal drifts, e.g., caused by fluorescence bleaching. Hence, signals are depicted as relative fluorescence changes ($Rel.Fluor.Change = F_{norm}^{sample} - F_{norm}^{ref}$) and start at zero; for example, a signal change of -0.15 denotes a quenching by 15% in the presence of analyte molecules.

When multivalent analytes are measured, there is a subtle, yet noteworthy difference in the signal response of the FPS mode used here versus conventional refractive index biosensors like SPR or biolayer interferometry: the fluorescence signal changes for every bond that is formed on the surface, while an SPR signal change is caused by the mere presence of analyte at the sensor surface, no matter if the analyte is engaged via one or more binding sites. In FPS mode, a bivalent binder counts twice, i.e., its FPS signal is 2 times the signal generated when a single bond is formed. This needs to be taken into account when analyzing relative

signal amplitudes (**Equation (3) and (4**). For instance, if the signal amplitudes of a biphasic dissociation fit describing affinity and avidity binding modes are equal in magnitude, it means that 2/3 of the analytes are linked monovalently and 1/3 are linked bivalently.

switchSENSE Surface Functionalization

Human FcRn molecules were immobilized on the surface of a switchSENSE multi-purpose chip (MPC-96-2-G1R1-S, Dynamic Biosensors). FcRn was covalently conjugated in-vitro to the 5' ends of the exchangeable strand of the DNA nanolever before the biosensing experiments, using an amine-reactive protein-DNA conjugation kit (CK-NH2-1-B96, Dynamic Biosensors). Conjugates were purified and a 1:1 conjugation stoichiometry was verified using a protein-DNA conjugate purifier (proFIRE®, Dynamic Biosensors). 200 µg of FcRn were used for the reaction, which produced enough FcRn-DNA conjugate to functionalize the sensor 100 times. FcRn-DNA conjugate was aliquoted in amounts required for 10 sensor regenerations each and stored at -80°C until use. This way, experiments on different days were all performed with the same batch of samples from one coupling reaction, and differing numbers of freeze-thaw cycles between experiments were avoided.

During the automated functionalization procedure, 200 nM conjugate solution was pumped across the chip surface for 6 min. Hybridization kinetics were monitored in real time until saturation was achieved to ensure complete functionalization of the sensor surface.[77] Modifying the chip surface by "zipping" protein-DNA conjugates onto it is convenient because the sensor can be regenerated quickly and repeatedly using the same standardized hybridization/denaturation protocols. To wash off used protein, the surface is exposed to basic NaOH solution (pH 13) for five seconds during the automated wash procedure performed by the DRX2 instrument. Double-stranded DNA denatures immediately into two separate single strands: the conjugate between FcRn and the exchangeable DNA strand is removed by the flow, while the fixed strand remains on the sensor unharmed and can be hybridized again with fresh conjugate for subsequent use.

switchSENSE Kinetic Data Analysis

We observed biphasic dissociation kinetics and thus used a biexponential dissociation model to account for the two binding modes, assuming a 2:1 stoichiometry, unless otherwise stated. Processing the data (normalization, referencing, fitting) was done with switchAnalysis (Dynamic Biosensors, Germany) and Origin Pro 2015 (OriginLab Corp., Northhampton, USA)

Biphasic Dissociation

$$Signal(t) = A_{fast} \cdot exp\{-k_{OFF,AFFINITY} \cdot t\} + A_{slow} \cdot exp\{-k_{OFF,AVIDITY} \cdot t\} \quad \textbf{(1)}$$

Monophasic Dissociation

$$Signal(t) = A \cdot exp\{-k_{OFF} \cdot t\} \quad \textbf{(2)}$$

$k_{OFF,AFFINITY}$ and $k_{OFF,AVIDITY}$ are the dissociation rate constants of the fast affinity and slow avidity binding modes, respectively, and A_{fast} and A_{slow} are their amplitudes following. The relative amplitudes (%) for a bivalent binder discriminating monovalent and bivalent binding are given by Equation **3** and **4** for single (A_{fast}) and double (A_{slow}) bound state respectively.

$$A_{fast}(\%) = \left(\frac{A_{fast}}{A_{fast} + \frac{A_{slow}}{2}} \right) * 100 \qquad \textbf{(3)}$$

$$A_{slow}\ (\%) = \left(\frac{\frac{A_{slow}}{2}}{A_{fast} + \frac{A_{slow}}{2}} \right) * 100 \qquad \textbf{(4)}$$

Association phases were observed to be monophasic and fitted with mono-exponential model

Association $$Signal(t) = A_{ON}(1 - exp\{-(c \cdot k_{ON} + k_{OFF}) \cdot t\}) \qquad \textbf{(5)}$$

Here, k_{ON} is the association rate constant and c is the injected analyte concentration. The fitting procedure was as follows: First, a bi-exponential least-squares fit was performed for all measured dissociation curves, optimizing for common $k_{OFF,AFFINITY}$ and $k_{OFF,AVIDITY}$ values that best fit all datasets simultaneously (global fit). The dissociation kinetics neither depend on the analyte concentration used during the association phase, nor do they depend on the achieved saturation level (fraction bound). Second, mono-exponential fits were performed for all association curves measured at different analyte concentrations, using the known c and k_{OFF} value, and k_{ON} values were determined that best fit the global dataset.

The calculation of the transition point within the affinity dissociation rates ($k_{OFF,AFFINITY}$) measured from pH 5.8 to 7.4 was performed applying a Four Parameter Logistic (4PL) Regression. Here, a is the minimum value that can be obtained d, the maximum value that can be obtained, c the point of inflection, in our case the pH value and b is the Hill's slope of the curve.

Sigmoidal 4PL Fit Model $$y = d + \frac{a - d}{1 + \left(\frac{x}{c}\right)^b} \qquad \textbf{(6)}$$

SPR Experiments

SPR measurements were performed on a Biacore T200 instrument (GE Healthcare) at 25°C. The sensor chip used was a C1 chip. The running buffer was phosphate-buffered saline with polysorbate 20 (PBS-P) at different pH levels (5.8, 6.0, 6.4, 6.8, 7.4).

Neutravidin (20 μg/mL) was amine-coupled to flow cells 1-4 of the C1 chip using standard amine coupling protocol at pH 4.5 for 200 seconds at a flow rate of 10 μL/min. Subsequently, biotinylated single-chain human FcRn was captured on the NeutrAvidin-coated surface in HBS-N buffer at pH 7.4. The captured levels of FcRn were 10-12 RU on flow cell 2, 140 RU on flow cell 3, and 110 RU on flow cell 4.

Five different concentrations of antibodies were prepared in the running buffer. Each concentration was injected over the FcRn-coated surface at a flow rate of 50 μL/min. The association phase was monitored for 180 seconds, and the dissociation phase was monitored for a time period independent of pH.

After each cycle, the surface was regenerated by injecting PBS at pH 8.0 for 45 seconds at a flow rate of 20 μL/min, twice. This ensured the complete removal of bound antibodies from the previous cycle and the restoration of the original binding capacity of the FcRn-coated surface.

The binding kinetics were analyzed using the Biacore T200 evaluation software. The data were fitted to a 1:1 binding model to determine the association and dissociation rate constants (k_{ON} and k_{OFF}) and the equilibrium dissociation constant (K_D). More complex models were also applied (Bivalent Analyte and Heterogeneous Ligand Model)

Analytical hFcRn affinity chromatography

Affinity chromatography was conducted to assess the interaction between human FcRn and antibody variants. The chromatographic analysis was performed on an ÄKTA Avant 25 chromatography system (GE Healthcare). The procedure was based on established protocols as detailed in previous studies.[48,72]

Antibody variants were prepared at a concentration of 1 mg/mL. A volume of 50 μL of each antibody variant was loaded onto the chromatography column. The elution of bound antibodies was achieved by establishing a linear pH gradient. This gradient ranged from pH 6.0 to pH 8.8 over a period of 110 minutes. The low pH buffer consisted of 20 mM MES sodium salt and 140 mM NaCl, adjusted to pH 5.5. Conversely, the high pH buffer was composed of 20 mM Tris/HCl and 140 mM NaCl, with the pH adjusted to 8.8. The buffers facilitated the dissociation of antibody variants from the hFcRn ligand, allowing for the analysis of their relative affinities based on their elution profiles.

Data acquisition and analysis were performed using the system's software and GraphPad Prism (Version 8.4.2), and the resulting chromatograms were used to evaluate the binding characteristics of the antibody variants to hFcRn.

Disclosure Statement

Johannes Reusch and Tilman Schlothauer are employees of Roche Diagnostics GmbH. Ulrich Rant (CEO) is an employee of Dynamic Biosensors GmbH. Jan Terje Andersen is a Professor at the Department of Pharmacology, Institute of Clinical Medicine, University of Oslo. All authors declare that they have no competing interests. All authors have made a substantial, direct and intellectual contribution to the work, and approved the final version.

Acknowledgements

We would like to express our sincere gratitude to Christian Klein and Laurent Larivière for scientific support and proofreading activities. We are grateful to Algirdas Grevys for providing HERA data. We acknowledge Vincent Wieser for his support in the characterization of antibodies using the analytical FcRn affinity column.

References

1. Nelson AL, Dhimolea E, Reichert JM. Development trends for human monoclonal antibody therapeutics. Nat Rev Drug Discov. 2010; 9:767-774. doi:10.1038/nrd3229. PMID: 20811384.

2. Kaplon H, Chenoweth A, Crescioli S, Reichert JM. Antibodies to watch in 2022. MAbs. 2022; 14:2014296. doi:10.1080/19420862.2021.2014296. PMID: 35030985.

3. Dostalek M, Prueksaritanont T, Kelley RF. Pharmacokinetic de-risking tools for selection of monoclonal antibody lead candidates. MAbs. 2017; 9:756-766. doi:10.1080/19420862.2017.1323160. PMID: 28463063.

4. Muller T, Tasser C, Tesar M, Fucek I, Schniegler-Mattox U, Koch J, Ellwanger K. Selection of bispecific antibodies with optimal developability using FcRn-Ph-HPLC as an optimized FcRn affinity chromatography method. MAbs. 2023; 15:2245519. doi:10.1080/19420862.2023.2245519. PMID: 37599441.

5. Fernandez-Quintero ML, Ljungars A, Waibl F, Greiff V, Andersen JT, Gjolberg TT, Jenkins TP, Voldborg BG, Grav LM, Kumar S, et al. Assessing developability early in the discovery process for novel biologics. MAbs. 2023; 15:2171248. doi:10.1080/19420862.2023.2171248. PMID: 36823021.

6. Baldwin WM, 3rd, Valujskikh A, Fairchild RL. The neonatal Fc receptor: Key to homeostasic control of IgG and IgG-related biopharmaceuticals. Am J Transplant. 2019; 19:1881-1887. doi:10.1111/ajt.15366. PMID: 30903736.

7. Ward ES, Ober RJ. Targeting FcRn to Generate Antibody-Based Therapeutics. Trends Pharmacol Sci. 2018; 39:892-904. doi:10.1016/j.tips.2018.07.007. PMID: 30143244.

8. Pyzik M, Sand KMK, Hubbard JJ, Andersen JT, Sandlie I, Blumberg RS. The Neonatal Fc Receptor (FcRn): A Misnomer? Front Immunol. 2019; 10:1540. doi:10.3389/fimmu.2019.01540. PMID: 31354709.

9. D'Hooghe L, Chalmers AD, Heywood S, Whitley P. Cell surface dynamics and cellular distribution of endogenous FcRn. PLoS ONE. 2017; 12:e0182695. doi:10.1371/journal.pone.0182695. PMID: 28817705.

10. Pyzik M, Kozicky LK, Gandhi AK, Blumberg RS. The therapeutic age of the neonatal Fc receptor. Nat Rev Immunol. 2023; 23:415-432. doi:10.1038/s41577-022-00821-1. PMID: 36726033.

11. Oostindie SC, Lazar GA, Schuurman J, Parren P. Avidity in antibody effector functions and biotherapeutic drug design. Nat Rev Drug Discov. 2022; 21:715-735. doi:10.1038/s41573-022-00501-8. PMID: 35790857.

12. Karush F. Multivalent binding and functional affinity. Contemp Top Mol Immunol. 1976; 5:217-228. doi:10.1007/978-1-4684-8142-6_8. PMID: 63353.

13. Fan YY, Farrokhi V, Caiazzo T, Wang M, O'Hara DM, Neubert H. Human FcRn Tissue Expression Profile and Half-Life in PBMCs. Biomol. 2019; 9:373. doi:10.3390/biom9080373. PMID: 31443181.

14. Roopenian DC, Akilesh S. FcRn: the neonatal Fc receptor comes of age. Nat Rev Immunol. 2007; 7:715-725. doi:10.1038/nri2155. PMID: 17703228.

15. Latvala S, Jacobsen B, Otteneder MB, Herrmann A, Kronenberg S. Distribution of FcRn Across Species and Tissues. J Histochem Cytochem. 2017; 65:321-333. doi:10.1369/0022155417705095. PMID: 28402755.

16. Rudnik-Jansen I, Howard KA. FcRn expression in cancer: Mechanistic basis and therapeutic opportunities. Journal of Controlled Release. 2021; 337:248-257. doi:10.1016/j.jconrel.2021.07.007.

17. Swiercz R, Mo M, Khare P, Schneider Z, Ober RJ, Ward ES. Loss of expression of the recycling receptor, FcRn, promotes tumor cell growth by increasing albumin consumption. Oncotarget. 2017; 8:3528-3541. doi:10.18632/oncotarget.13869. PMID: 27974681.

18. Pyzik M, Rath T, Lencer WI, Baker K, Blumberg RS. FcRn: The Architect Behind the Immune and Nonimmune Functions of IgG and Albumin. J Immunol. 2015; 194:4595-4603. doi:10.4049/jimmunol.1403014. PMID: 25934922.

19. Ward ES, Devanaboyina SC, Ober RJ. Targeting FcRn for the modulation of antibody dynamics. Mol Immunol. 2015; 67:131-141. doi:10.1016/j.molimm.2015.02.007. PMID: 25766596.

20. Ward ES, Velmurugan R, Ober RJ. Targeting FcRn for therapy: from live cell imaging to in vivo studies in mice. Immunol Lett. 2014; 160:158-162. doi:10.1016/j.imlet.2014.02.008. PMID: 24572175.

21. Dickinson BL, Badizadegan K, Wu Z, Ahouse JC, Zhu X, Simister NE, Blumberg RS, Lencer WI. Bidirectional FcRn-dependent IgG transport in a polarized human intestinal epithelial cell line. J Clin Invest. 1999; 104:903-911. doi:10.1172/JCI6968. PMID: 10510331.

22. Spiekermann GM, Finn PW, Ward ES, Dumont J, Dickinson BL, Blumberg RS, Lencer WI. Receptor-mediated immunoglobulin G transport across mucosal barriers in adult life: functional expression of FcRn in the mammalian lung. J Exp Med. 2002; 196:303-310. doi:10.1084/jem.20020400. PMID: 12163559.

23. Foss S, Grevys A, Sand KMK, Bern M, Blundell P, Michaelsen TE, Pleass RJ, Sandlie I, Andersen JT. Enhanced FcRn-dependent transepithelial delivery of IgG by Fc-engineering and polymerization. J Control Release. 2016; 223:42-52. doi:10.1016/j.jconrel.2015.12.033. PMID: 26718855.

24. Hubbard JJ, Pyzik M, Rath T, Kozicky LK, Sand KMK, Gandhi AK, Grevys A, Foss S, Menzies SC, Glickman JN, et al. FcRn is a CD32a coreceptor that determines susceptibility to IgG immune complex-driven autoimmunity. J Exp Med. 2020; 217. doi:10.1084/jem.20200359. PMID: 32658257.

25. Baker K, Qiao SW, Kuo TT, Aveson VG, Platzer B, Andersen JT, Sandlie I, Chen Z, de Haar C, Lencer WI, et al. Neonatal Fc receptor for IgG (FcRn) regulates cross-presentation of IgG immune complexes by CD8-CD11b+ dendritic cells. Proc Natl Acad Sci U S A. 2011; 108:9927-9932. doi:10.1073/pnas.1019037108. PMID: 21628593.

26. Qiao SW, Kobayashi K, Johansen FE, Sollid LM, Andersen JT, Milford E, Roopenian DC, Lencer WI, Blumberg RS. Dependence of antibody-mediated presentation of antigen on FcRn. Proc Natl Acad Sci U S A. 2008; 105:9337-9342. doi:10.1073/pnas.0801717105. PMID: 18599440.

27. Brambell FWR. THE PASSIVE IMMUNITY OF THE YOUNG MAMMAL. Biological Reviews. 1958; 33. doi:10.1111/j.1469-185X.1958.tb01412.x.

28. Wilhelm P. Burmeister AHH, Pamela J. Bjorkman. Crystal structure of the complex of rat neonatal Fc receptor with Fc. Nature. 1994; 372. doi:10.1038/372379a0.

29. Wilhelm P. Burmeister LNG, Neil E. Simister,Michael L. Blum,Pamela J. Bjorkman. Crystal structure at 2.2 Å resolution of the MHC-related neonatal Fc receptor. Nature. 1994. doi:10.1038/372336a0.

30. Neil E. Simister KEM. An Fc receptor structurally related to MHC class I antigens. 1989. doi:10.1038/337184a0.

31. Malini Raghavan VRB, Sherie L Morrison,Pamela J Bjorkman. Analysis of the pH Dependence of the Neonatal Fc Receptor/Immunoglobulin G Interaction Using Antibody and Receptor Variants. Biochemistry. 1995. doi:10.1021/bi00045a005.

32. Oganesyan V, Damschroder MM, Cook KE, Li Q, Gao C, Wu H, Dall'Acqua WF. Structural insights into neonatal Fc receptor-based recycling mechanisms. J Biol Chem. 2014; 289:7812-7824. doi:10.1074/jbc.M113.537563. PMID: 24469444.

33. Dall'Acqua WF, Kiener PA, Wu H. Properties of human IgG1s engineered for enhanced binding to the neonatal Fc receptor (FcRn). J Biol Chem. 2006; 281:23514-23524. doi:10.1074/jbc.M604292200. PMID: 16793771.

34. Zalevsky J, Chamberlain AK, Horton HM, Karki S, Leung IW, Sproule TJ, Lazar GA, Roopenian DC, Desjarlais JR. Enhanced antibody half-life improves in vivo activity. Nat Biotechnol. 2010; 28:157-159. doi:10.1038/nbt.1601. PMID: 20081867.

35. Robbie GJ, Criste R, Dall'acqua WF, Jensen K, Patel NK, Losonsky GA, Griffin MP. A novel investigational Fc-modified humanized monoclonal antibody, motavizumab-YTE, has an extended half-life in healthy adults. Antimicrob Agents Chemother. 2013; 57:6147-6153. doi:10.1128/AAC.01285-13. PMID: 24080653.

36. Booth BJ, Ramakrishnan B, Narayan K, Wollacott AM, Babcock GJ, Shriver Z, Viswanathan K. Extending human IgG half-life using structure-guided design. MAbs. 2018; 10:1098-1110. doi:10.1080/19420862.2018.1490119. PMID: 29947573.

37. Liu R, Oldham RJ, Teal E, Beers SA, Cragg MS. Fc-Engineering for Modulated Effector Functions-Improving Antibodies for Cancer Treatment. Antibodies. 2020; 9:64. doi:10.3390/antib9040064. PMID: 33212886.

38. Dall'Acqua WF, Woods RM, Ward ES, Palaszynski SR, Patel NK, Brewah YA, Wu H, Kiener PA, Langermann S. Increasing the affinity of a human IgG1 for the neonatal Fc receptor: biological consequences. J Immunol. 2002; 169:5171-5180. doi:10.4049/jimmunol.169.9.5171. PMID: 12391234.

39. Mackness BC, Jaworski JA, Boudanova E, Park A, Valente D, Mauriac C, Pasquier O, Schmidt T, Kabiri M, Kandira A, et al. Antibody Fc engineering for enhanced neonatal Fc receptor binding and prolonged circulation half-life. MAbs. 2019; 11:1276-1288. doi:10.1080/19420862.2019.1633883. PMID: 31216930.

40. Abdiche YN, Yeung YA, Chaparro-Riggers J, Barman I, Strop P, Chin SM, Pham A, Bolton G, McDonough D, Lindquist K, et al. The neonatal Fc receptor (FcRn) binds independently to both sites of the IgG homodimer with identical affinity. MAbs. 2015; 7:331-343. doi:10.1080/19420862.2015.1008353. PMID: 25658443.

41. Gurbaxani BM, Morrison SL. Development of new models for the analysis of Fc-FcRn interactions. Mol Immunol. 2006; 43:1379-1389. doi:10.1016/j.molimm.2005.08.002. PMID: 16183124.

42. Rudnick SI, Adams GP. Affinity and avidity in antibody-based tumor targeting. Cancer Biother Radio. 2009; 24:155-161. doi:10.1089/cbr.2009.0627. PMID: 19409036.

43. Diebolder CA, Beurskens FJ, de Jong RN, Koning RI, Strumane K, Lindorfer MA, Voorhorst M, Ugurlar D, Rosati S, Heck AJ, et al. Complement is activated by IgG hexamers assembled at the cell surface. Science. 2014; 343:1260-1263. doi:10.1126/science.1248943. PMID: 24626930.

44. Rouge L, Chiang N, Steffek M, Kugel C, Croll TI, Tam C, Estevez A, Arthur CP, Koth CM, Ciferri C, et al. Structure of CD20 in complex with the therapeutic monoclonal antibody rituximab. Science. 2020; 367:1224-1230. doi:10.1126/science.aaz9356. PMID: 32079680.

45. Jensen PF, Larraillet V, Schlothauer T, Kettenberger H, Hilger M, Rand KD. Investigating the interaction between the neonatal Fc receptor and monoclonal antibody variants by hydrogen/deuterium exchange mass spectrometry. Mol Cell Proteomics. 2015; 14:148-161. doi:10.1074/mcp.M114.042044. PMID: 25378534.

46. Wang W, Lu P, Fang Y, Hamuro L, Pittman T, Carr B, Hochman J, Prueksaritanont T. Monoclonal antibodies with identical Fc sequences can bind to FcRn differentially with pharmacokinetic consequences. Drug Metab Dispos. 2011; 39:1469-1477. doi:10.1124/dmd.111.039453. PMID: 21610128.

47. Yeung YA, Leabman MK, Marvin JS, Qiu J, Adams CW, Lien S, Starovasnik MA, Lowman HB. Engineering human IgG1 affinity to human neonatal Fc receptor: impact of affinity improvement on pharmacokinetics in primates. J Immunol. 2009; 182:7663-7671. doi:10.4049/jimmunol.0804182. PMID: 19494290.

48. Schlothauer T, Rueger P, Stracke JO, Hertenberger H, Fingas F, Kling L, Emrich T, Drabner G, Seeber S, Auer J, et al. Analytical FcRn affinity chromatography for functional characterization of monoclonal antibodies. MAbs. 2013; 5:576-586. doi:10.4161/mabs.24981. PMID: 23765230.

49. Muller-Landau H, Varela PF. Standard operation procedure for switchSENSE DRX systems. Eur Biophys J. 2021; 50:389-400. doi:10.1007/s00249-021-01519-3. PMID: 33772617.

50. Langer A, Hampel PA, Kaiser W, Knezevic J, Welte T, Villa V, Maruyama M, Svejda M, Jahner S, Fischer F, et al. Protein analysis by time-resolved measurements with an electro-switchable DNA chip. Nat Commun. 2013; 4:2099. doi:10.1038/ncomms3099. PMID: 23839273.

51. Knezevic J, Langer A, Hampel PA, Kaiser W, Strasser R, Rant U. Quantitation of affinity, avidity, and binding kinetics of protein analytes with a dynamically switchable biosurface. J Am Chem Soc. 2012; 134:15225-15228. doi:10.1021/ja3061276. PMID: 22946661.

52. Hampel PA, Strasser R, Fischer F, Rant U. Assembly and Characterization of a Slingshot DNA Nanostructure for the Analysis of Bivalent and Bispecific Analytes with Biosensors. Langmuir. 2018; 34:14796-14801. doi:10.1021/acs.langmuir.8b02124. PMID: 30269507.

53. Daub H, Traxler L, Ismajli F, Groitl B, Itzen A, Rant U. The trimer to monomer transition of Tumor Necrosis Factor-Alpha is a dynamic process that is significantly altered by therapeutic antibodies. Sci Rep. 2020; 10:9265. doi:10.1038/s41598-020-66123-5. PMID: 32518229.

54. Mak S, Marszal A, Matscheko N, Rant U. Kinetic analysis of ternary and binary binding modes of the bispecific antibody emicizumab. MAbs. 2023; 15:2149053. doi:10.1080/19420862.2022.2149053. PMID: 36453702.

55. Qi T, Cao Y. In Translation: FcRn across the Therapeutic Spectrum. Int J Mol Sci. 2021; 22. doi:10.3390/ijms22063048. PMID: 33802650.

56. Datta-Mannan A, Witcher DR, Tang Y, Watkins J, Jiang W, Wroblewski VJ. Humanized IgG1 variants with differential binding properties to the neonatal Fc receptor: relationship to pharmacokinetics in mice and primates. Drug Metab Dispos. 2007; 35:86-94. doi:10.1124/dmd.106.011734. PMID: 17050651.

57. Daniel E. Vaughn PJB. High-Affinity Binding of the Neonatal Fc Receptor to Its IgG Ligand Requires Receptor Immobilization †. Biochemistry. 1997. doi:10.1021/bi970841r.

58. Neuber T, Frese K, Jaehrling J, Jager S, Daubert D, Felderer K, Linnemann M, Hohne A, Kaden S, Kolln J, et al. Characterization and screening of IgG binding to the neonatal Fc receptor. MAbs. 2014; 6:928-942. doi:10.4161/mabs.28744. PMID: 24802048.

59. Soltermann F, Foley EDB, Pagnoni V, Galpin M, Benesch JLP, Kukura P, Struwe WB. Quantifying Protein-Protein Interactions by Molecular Counting with Mass Photometry. Angew Chem Int Ed Engl. 2020; 59:10774-10779. doi:10.1002/anie.202001578. PMID: 32167227.

60. Feng Y, Gong R, Dimitrov DS. Design, expression and characterization of a soluble single-chain functional human neonatal Fc receptor. Protein Expr Purif. 2011; 79:66-71. doi:10.1016/j.pep.2011.03.012. PMID: 21453773.

61. Grevys A, Nilsen J, Sand KMK, Daba MB, Oynebraten I, Bern M, McAdam MB, Foss S, Schlothauer T, Michaelsen TE, et al. A human endothelial cell-based recycling assay for screening of FcRn targeted molecules. Nat Commun. 2018; 9:621. doi:10.1038/s41467-018-03061-x. PMID: 29434196.

62. Ober RJ, Martinez C, Vaccaro C, Zhou J, Ward ES. Visualizing the site and dynamics of IgG salvage by the MHC class I-related receptor, FcRn. J Immunol. 2004; 172:2021-2029. doi:10.4049/jimmunol.172.4.2021. PMID: 14764666.

63. Katsamba PS, Navratilova I, Calderon-Cacia M, Fan L, Thornton K, Zhu M, Bos TV, Forte C, Friend D, Laird-Offringa I, et al. Kinetic analysis of a high-affinity antibody/antigen interaction performed by multiple Biacore users. Anal Biochem. 2006; 352:208-221. doi:10.1016/j.ab.2006.01.034. PMID: 16564019.

64. Tesar DB, Tiangco NE, Bjorkman PJ. Ligand valency affects transcytosis, recycling and intracellular trafficking mediated by the neonatal Fc receptor. Traffic. 2006; 7:1127-1142. doi:10.1111/j.1600-0854.2006.00457.x. PMID: 17004319.

65. Benjamin T. Walters PFJ, Vincent Larraillet,Kevin Lin,Thomas Patapoff,Tilman Schlothauer,Kasper D. Rand,Jennifer Zhang. Conformational Destabilization of Immunoglobulin G Increases the Low pH Binding Affinity with the Neonatal Fc Receptor. Journal of Biological Chemistry. 2016. doi:10.1074/jbc.m115.691568.

66. Santora LC, Kaymakcalan Z, Sakorafas P, Krull IS, Grant K. Characterization of noncovalent complexes of recombinant human monoclonal antibody and antigen using cation exchange, size exclusion chromatography, and BIAcore. Anal Biochem. 2001; 299:119-129. doi:10.1006/abio.2001.5380. PMID: 11730333.

67. Kaymakcalan Z, Sakorafas P, Bose S, Scesney S, Xiong L, Hanzatian DK, Salfeld J, Sasso EH. Comparisons of affinities, avidities, and complement activation of adalimumab, infliximab, and etanercept in binding to soluble and membrane tumor necrosis factor. Clin Immunol. 2009; 131:308-316. doi:10.1016/j.clim.2009.01.002. PMID: 19188093.

68. Daniel E Vaughn PJB. Structural basis of pH-dependent antibody binding by the neonatal Fc receptor. Structure, Cell Press 1998. doi:10.1016/s0969-2126(98)00008-2.

69. Fersht A. Enzyme structure and mechanism (Second Edition). 1985; Pp 475. W H Freeman, New York.

70. Matthew JB, Gurd FR, Garcia-Moreno B, Flanagan MA, March KL, Shire SJ. pH-dependent processes in proteins. Critical Rev Biochem. 1985; 18:91-197. doi:10.3109/10409238509085133. PMID: 3899508.

71. Piche-Nicholas NM, Avery LB, King AC, Kavosi M, Wang M, O'Hara DM, Tchistiakova L, Katragadda M. Changes in complementarity-determining regions significantly alter IgG binding to the neonatal Fc receptor (FcRn) and pharmacokinetics. MAbs. 2018; 10:81-94. doi:10.1080/19420862.2017.1389355. PMID: 28991504.

72. Schoch A, Kettenberger H, Mundigl O, Winter G, Engert J, Heinrich J, Emrich T. Charge-mediated influence of the antibody variable domain on FcRn-dependent pharmacokinetics. Proc Natl Acad Sci U S A. 2015; 112:5997-6002. doi:10.1073/pnas.1408766112. PMID: 25918417.

73. Wang X, McKay P, Yee LT, Dutina G, Hass PE, Nijem I, Allison D, Cowan KJ, Lin K, Quarmby V, et al. Impact of SPR biosensor assay configuration on antibody: Neonatal Fc receptor binding data. MAbs. 2017; 9:319-332. doi:10.1080/19420862.2016.1261774. PMID: 28001487.

74. Souders CA, Nelson SC, Wang Y, Crowley AR, Klempner MS, Thomas W, Jr. A novel in vitro assay to predict neonatal Fc receptor-mediated human IgG half-life. MAbs. 2015; 7:912-921. doi:10.1080/19420862.2015.1054585. PMID: 26018774.

75. Grevys A, Frick R, Mester S, Flem-Karlsen K, Nilsen J, Foss S, Sand KMK, Emrich T, Fischer JAA, Greiff V, et al. Antibody variable sequences have a pronounced effect on cellular transport and plasma half-life. iScience. 2022; 25:103746. doi:10.1016/j.isci.2022.103746. PMID: 35118359.

76. Arinaga K, Rant U, Knezevic J, Pringsheim E, Tornow M, Fujita S, Abstreiter G, Yokoyama N. Controlling the surface density of DNA on gold by electrically induced desorption. Biosens Bioelectron. 2007; 23:326-331. doi:10.1016/j.bios.2007.04.012. PMID: 17560778.

77. Ulrich Rant KA, Simon Scherer,Erika Pringsheim,Shozo Fujita,Naoki Yokoyama,Marc Tornow,Gerhard Abstreiter. Switchable DNA interfaces for the highly sensitive detection of label-free DNA targets. Proc National Acad Sci. 2007. doi:10.1073/pnas.0703974104.

Figures

Figure 1. Assay orientations to investigate the interaction between a monovalent and bivalent binding partner. (A) The monovalent partner as solute analyte = FcRn. (B) The bivalent partner as solute analyte = IgG. Illustrations are created with BioRender.com.

Figure 2. Kinetic analysis of immobilized human FcRn and a human IgG1 (mAb1) in solution at pH 6.0 utilizing a medium FcRn density on a switchSENSE biosensor chip. (A) shows the schematic assay configuration allowing affinity and avidity to occur simultaneously. mAb1 was injected in five different concentrations as two-fold dilution series with a highest concentration of 300 nM for hIgG1 Fc WT (B) and 60 nM for hIgG1 Fc YTE (C). Each plot (B,C) shows the measured raw data (grey) and the global fit analysis as solid lines (blue fading). The sensorgram display a monophasic association phase and biphasic dissociation phase reflecting affinity and avidity binding mode. The determined kinetic parameters are described in Table 2. Illustration A is created with BioRender.com.

Figure 3. Kinetic analysis of human FcRn immobilized and a human IgG1 (mAb1) Fc YTE mutant in solution at nine different pH values on switchSENSE biosensor chip. mAb1 Fc YTE was injected in five different concentration as two-fold dilution series with a highest concentration of (A) 60 nM at pH 5.8, (B) 60 nM at pH 6.0, (C) 100 nM at pH 6.2, (D) 150 nM at pH 6.4, (E) 200 nM at pH 6.6, (F) 300 nM at pH 6.8, (G) 400 nM at pH 7.0, (H) 800 nM at pH 7.2 and (I) 800 nM at pH 7.4. Note that the x axis for each sensorgram (A - I) has a different time scale. Each plot (A - I) shows the measured raw data (grey) and the global fit analysis as solid lines (blue fading). For (A – H) the dissociation phase is biphasic characterized by two different dissociation rate constants reflecting the affinity (1:1) and the avidity (2:1) binding mode. The interaction displays a biphasic dissociation curve reflecting affinity and avidity binding where one or two hFcRn are engaged with one mAb1 Fc YTE. The dissociation of mAb1 Fc YTE and hFcRn at pH 7.4 (I) is described by a monophasic fit model reflecting the affinity binding mode (1:1) where one hFcRn is engaged with one mAb1 Fc YTE. Panel (J) shows the applied, exemplary biphasic fit model for FcRn with mAb1 Fc YTE mutant injecting 300 nM at pH 6.0. The adequacy of the fit model is confirmed by the minimal residuals, indicating no significant deviation. The association phase occurred to be monophasic while the dissociation phase is biphasic. The overall dissociation curve is superposition of two exponential time-courses, namely the affinity binding mode (fast dissociation) and the avidity binding mode (slow dissociation). The

measured data is shown in blue and the fit in black solid lines, whereas the two deconvoluted exponential time-courses are shown in grey as dashed lines. The contribution of fast and slow dissociation to the overall signal change is shown as Amplitude A_{fast} or A_{slow}. The determined kinetic parameters are described in Table 3.

Figure 4. Schematic depiction of a bivalent analyte (IgG) interacting with a monovalent ligand (FcRn). State 0 shows the free state of monovalent FcRn (immobilized) and bivalent IgG (in solution). The transition from State 0 to State 1 illustrates that the bivalent analyte associates with one binding site on FcRn (k_{ON1} and k_{OFF1}). In its subsequent transition to State 2 the IgG concurrently binds via its second binding site to another FcRn, which is in close proximity to the first one, thereby forming a bivalent complex. The avidity occurs accordingly to the absolute and relative contributions of the individual on- and off-rates of the transitions $0 \leftrightarrow 1$ and $1 \leftrightarrow 2$. The dynamic dissociation and re-association of one to two binding sites, the transition $2 \leftrightarrow 1 \leftrightarrow 2$ ($k_{ON}^{app.}$ and $k_{OFF}^{app.}$), is crucially important for the effective off-rate and hence for the avidity. Typically, it is impossible to differentiate between singly bound and doubly bound states within the measurement signal. As a result, only the 'observable' kinetic rates ($k_{ON}^{obs.}$ and $k_{OFF}^{obs.}$) between the free and any type of bound state are measured. The illustration is created with BioRender.com.

Figure 5. Rate scale plot of FcRn (ligand) and mAb1 YTE variant (solute) at a pH from 5.8 to 7.4. The plot allows the comprehensive comparison of multiple kinetic rate parameters obtained from several kinetic experiments/sensorgrams at one glance. The upper plot shows the association rate (k_{ON}) while the lower plot shows the dissociation rate (k_{OFF}) as logarithmic scale. Each kinetic rate parameter pair is connected via a vertical line where its length or else the distance of the two data points gives insights about the binding strength of the measured interaction. The proximity of the data points corresponds to a weaker interaction, or in other words, an increase in the dissociation constant K_D. The data points are shown as mean ± SD* (*smaller than the data points, thus not visible). To obtain an inflection point the affinity dissociation rates ($k_{OFF,AFFINITY}$) are fitted by a Four Parameter Logistic (4PL) fit shown in grey (Equation (6)) resulting in a transition at pH 7.2 (Figure S 11).

Figure 6. Avidity-to-affinity relationship of FcRn and mAb1 YTE variant from pH 5.8 to 7.2. The ratio of the K_D values ($K_{D,AFFINITY}/K_{D,AVIDITY}$), referred to as avidity enhancement factor increases from neutral to acidic pH. The higher the binding strength (affinity) the more its contribution to the overall avidity enhancement. Weak affinities occurring at pH 6.4 to 7.4 only show a minor contribution to the avidity effect while strong affinities from pH 5.8 to 6.2 show higher contribution. A transition point is pH 6.2, indicated by the dashed lines. The data points are shown as mean ± SD* (*smaller than the data points, thus not visible).

Tables

Table 1. The relationship between assay orientation, ligand density, and resulting binding modes. IgG = bivalent binder, FcRn = monovalent binder.

Table 2. Summary of the affinity and avidity measurements of immobilized human FcRn and an mAb1 Fc variants in solution using a switchSENSE biosensor chip having a medium ligand density. The kinetic rate parameters are determined from analyzing the sensorgrams shown in Figure 2. The k_{ON}, k_{OFF} and K_D values are results from a global fit analysis ± fitting error.

Table 3. Summary of the affinity and avidity measurements of immobilized human FcRn and mAb1 Fc YTE mutant as solute using a switchSENSE biosensor chip having a medium ligand density. The kinetic rate parameters are determined from analyzing the sensorgrams shown in Figure 3. The k_{ON}, k_{OFF} and K_D values are results from a global fit analysis ± fitting error.

4.3 Figures

Figure 1

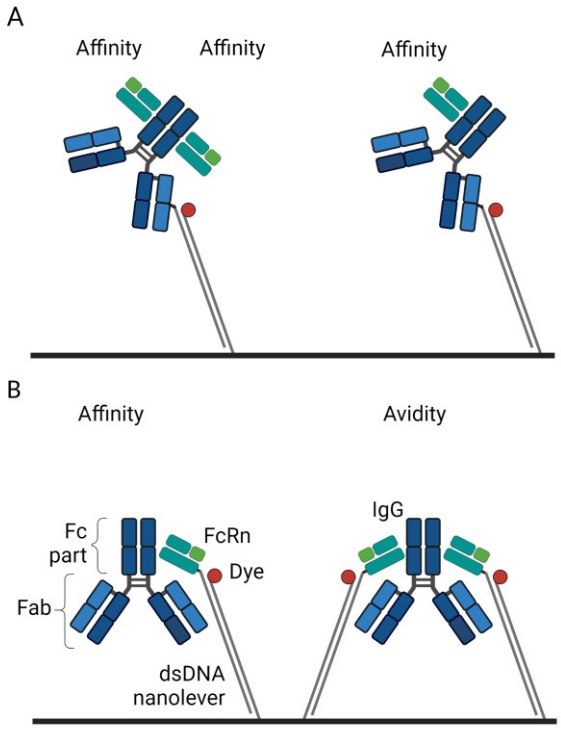

Figure 2

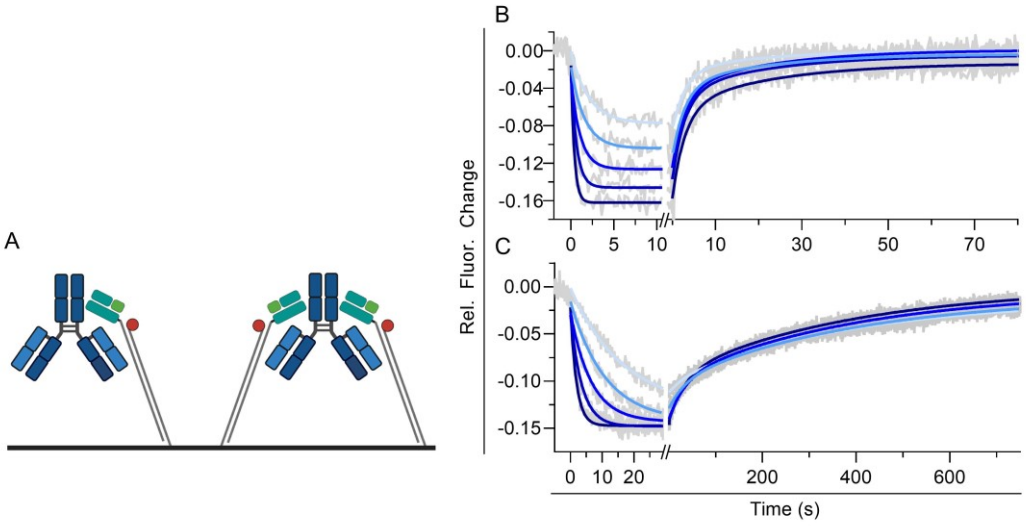

Figure 3

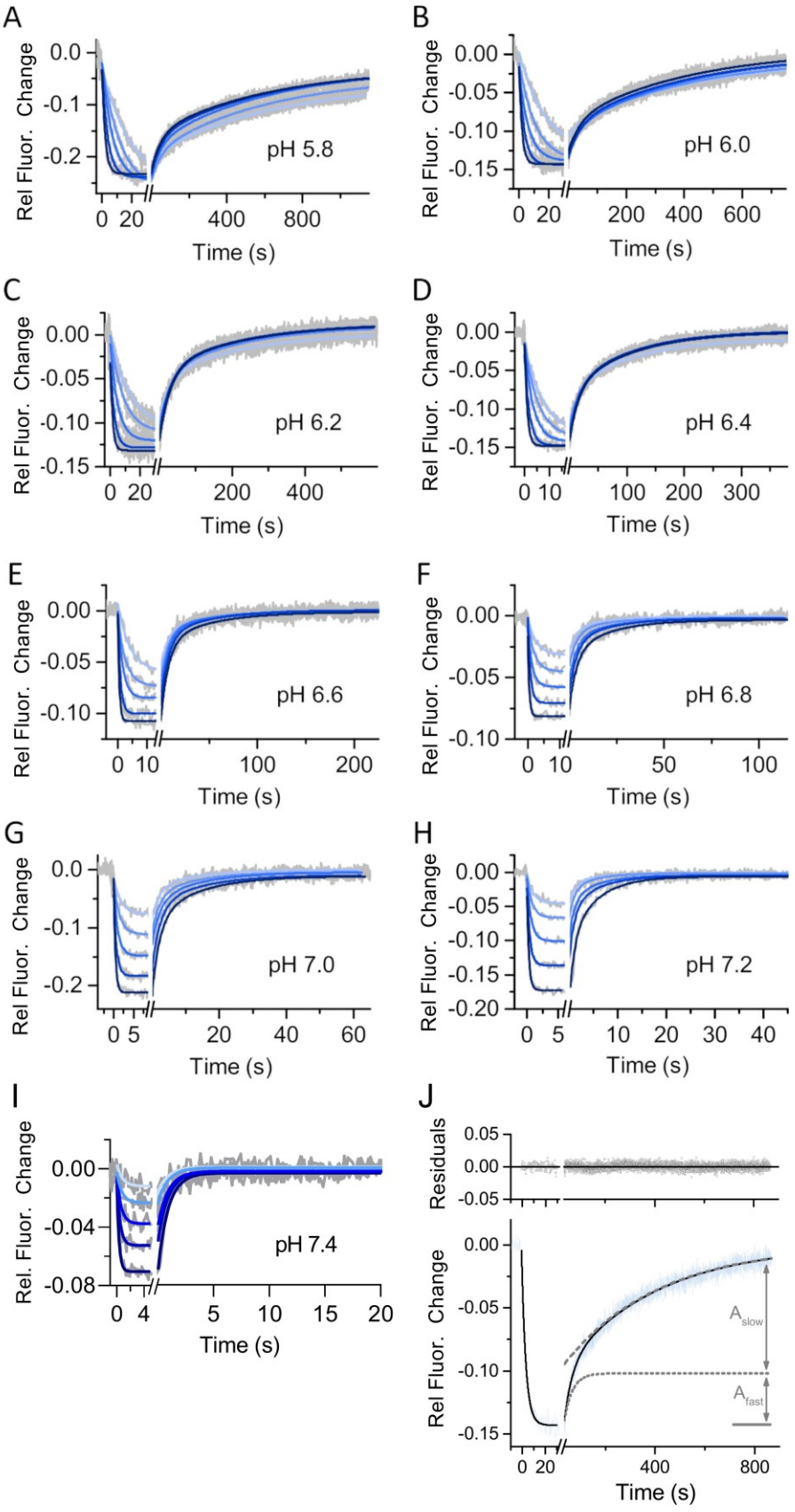
A
Rel Fluor. Change
0.0
-0.1
-0.2
pH 5.8
0 20 400 800
Time (s)
B
Rel Fluor. Change
0.00
-0.05
-0.10
-0.15
pH 6.0
0 20 200 400 600
Time (s)
C
Rel Fluor. Change
0.00
-0.05
-0.10
-0.15
pH 6.2
0 20 200 400
Time (s)
D
Rel Fluor. Change
0.00
-0.05
-0.10
-0.15
pH 6.4
0 10 100 200 300
Time (s)
E
Rel Fluor. Change
0.00
-0.05
-0.10
pH 6.6
0 10 100 200
Time (s)
F
Rel Fluor. Change
0.00
-0.05
-0.10
pH 6.8
0 10 50 100
Time (s)
G
Rel Fluor. Change
0.0
-0.1
-0.2
pH 7.0
0 5 20 40 60
Time (s)
H
Rel Fluor. Change
0.00
-0.05
-0.10
-0.15
-0.20
pH 7.2
0 5 10 20 30 40
Time (s)
I
Rel. Fluor. Change
0.00
-0.04
-0.08
pH 7.4
0 4 5 10 15 20
Time (s)
J
Residuals
0.05
0.00
-0.05
Rel Fluor. Change
0.00
-0.05
-0.10
-0.15
A slow
A fast
0 20 400 800
Time (s)

Figure 4

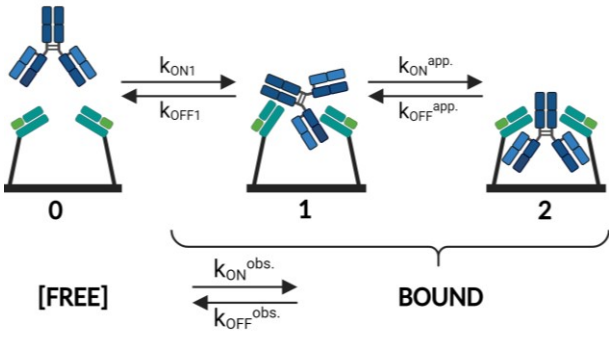

Figure 5

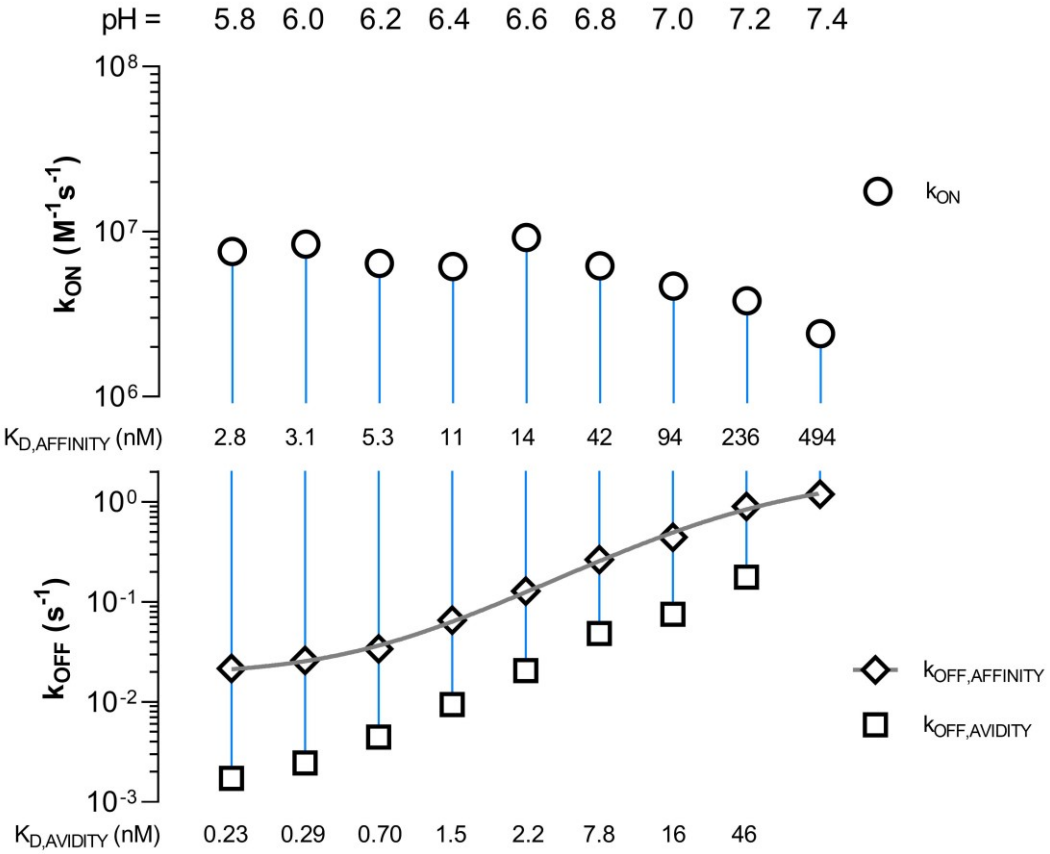

Figure 6

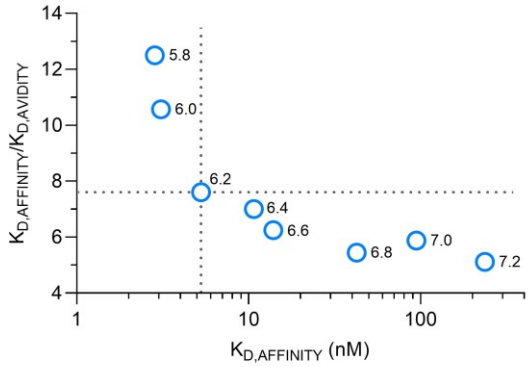

4.4 Tables

Table 1

Assay orientation	**A**	**B**
Ligand is immobilized	IgG (bivalent)	FcRn (monovalent)
Analyte in solution	FcRn (monovalent)	IgG (bivalent)
Ligand density	**Binding mode(s)**	
Low	Affinity	Affinity
Medium[1]	Affinity	Affinity/Avidity
High[2]	Affinity	Avidity

[1] Contributions of affinity and avidity modes should be of similar magnitude for good fit quality.

[2] Measurement artifacts (rebinding, mass transport limitations) are likely to occur at high ligand densities, which is why measurements have to be interpreted with care.

Table 2

Sample		**Affinity**		**Avidity**	
	k_{ON} ($x10^6$ $M^{-1}s^{-1}$)	$k_{OFF,AFFINITY}$ ($x10^{-2}$ s^{-1})	$K_{D,AFFINITY}$ (nM)	$k_{OFF,AVIDITY}$ ($x10^{-2}$ s^{-1})	$K_{D,AVIDITY}$ (nM)
hIgG1 Fc WT	7.53 ± 0.38	34.2 ± 1.50	45.4 ± 3.0	4.70 ± 0.30	6.24 ± 0.51
hIgG1 Fc YTE	8.42 ± 0.15	2.60 ± 0.06	3.09 ± 0.09	0.25 ± 0.01	0.29 ± 0.01

Table 3

hIgG1 Fc YTE		**Affinity**		**Avidity**	
pH	k_{ON} ($x10^6$ $M^{-1}s^{-1}$)	$k_{OFF,AFFINITY}$ ($x10^{-2}$ s^{-1})	$K_{D,AFFINITY}$ (nM)	$k_{OFF,AVIDITY}$ ($x10^{-2}$ s^{-1})	$K_{D,AVIDITY}$ (nM)
5.8	7.58 ± 0.11	2.15 ± 0.03	2.84 ± 0.06	0.17 ± 0.01	0.23 + 0.01
6.0	8.42 ± 0.15	2.60 ± 0.06	3.09 ± 0.09	0.25 ± 0.01	0.29 ± 0.01
6.2	6.42 ± 0.17	3.39 ± 0.07	5.28 ± 0.18	0.45 ± 0.01	0.70 ± 0.03
6.4	6.14 ± 0.14	6.57 ± 0.12	10.7 ± 0.31	0.94 ± 0.01	1.53 ± 0.04
6.6	9.23 ± 0.42	12.8 ± 0.46	13.9 ± 0.80	2.05 ± 0.12	2.22 ± 0.17
6.8	6.20 ± 0.31	26.3± 1.62	42.4 ± 3.38	4.83 ± 0.35	7.79 ± 0.69
7.0	4.69 ± 0.21	44.1 ± 1.92	94.0 ± 5.86	7.51 ± 0.37	16.0 ± 1.06
7.2	3.81 ± 0.18	90.0 ± 0.54	236 ± 18.0	17.6 ± 0.71	46.2 ± 2.87
7.4	2.41 ± 0.45	119 ±6.00	494 ± 95.5	NA	NA

5
Publication II

This chapter contains the research article

TRIM21 AND FC-ENGINEERED ANTIBODIES: DECODING ITS COMPLEX ANTIBODY BINDING MODE WITH IMPLICATIONS FOR VIRAL NEUTRALIZATION

BY

Johannes Reusch, Linda Elise Franken, Jakob Then, Philippe Ringler, Joachim Butzer, Thomas Juroschek, Christian Klein, Tilman Schlothauer and Laurent Larivière

MANUSCRIPT UNDER REVIEW

Frontiers of Immunology, Section Molecular Innate Immunity

(2024)

5.1 Author Contributions

Johannes Reusch, Christian Klein, Tilman Schlothauer, and Laurent Larivière designed the study and established its overarching research parameters. Johannes Reusch was responsible for the selection of suitable methodologies to carry out the investigation.

Johannes Reusch performed the experimental work, which spanned from the *in silico* conceptualization to the ultimate purification of anti-AAV capsid antibodies, and conducted experiments utilizing Surface Plasmon Resonance (SPR) and Mass Photometry (MP). Collaboratively, Linda Elise Franken and Johannes Reusch crafted the experimental design for Electron Microscopy (EM) studies. Linda Elise Franken, in conjunction with Philippe Ringler, then executed the EM experiments.

Johannes Reusch analyzed the data derived from the SPR and MP experiments and was responsible for the graphical representation of the results, culminating in the figures and tables presented in the final manuscript. He also composed the preliminary draft of the paper. The manuscript underwent a rigorous review and refinement process by Linda Elise Franken, Christian Klein, Tilman Schlothauer, and Laurent Larivière, which was instrumental in shaping the submitted final version of the paper.

5.2 TRIM21 and Fc-Engineered Antibodies: Decoding its complex Antibody Binding Mode with Implications for Viral Neutralization

TRIM21 and Fc-Engineered Antibodies: Decoding its complex Antibody Binding Mode with Implications for Viral Neutralization

Johannes Reusch[1], Linda Elise Franken[2], Jakob Then[1], Philippe Ringler[2,3], Joachim Butzer[1], Thomas Juroschek[1], Christian Klein[4], Tilman Schlothauer[1,*,†] and Laurent Larivière[1,*,†]

[1] Roche Pharma Research and Early Development, Therapeutic Modalities, Roche Innovation Center Munich, Roche Diagnostics GmbH, Nonnenwald 2, 82377 Penzberg, Germany

[2] Roche Pharma Research and Early Development, Therapeutic Modalities, Roche Innovation Center Basel, F.Hoffmann-La Roche Ltd, Grenzacherstrasse 124, 4070 Basel, Switzerland

[3] Biozentrum, University of Basel, 4056 Basel, Switzerland

[4] Roche Pharma Research and Early Development, Discovery Oncology, Roche Innovation Center Zurich, Roche Glycart AG, Wagistrasse 18, 8952 Schlieren, Switzerland

* Corresponding authors: laurent.lariviere@roche.com; tilman.schlothauer@roche.com

† These authors share last authorship

Number of Words: 8881
Number of Figures: 9
Number of Tables: 3

Key words: TRIM21, Therapeutic IgG, Antibody Fc mutants, Antibody mediated Viral Neutralization, Binding Kinetics, Affinity, Avidity, Structure-Function

Author Details

Johannes Reusch:

First Author, johannes.reusch@roche.com, https://orcid.org/0000-0002-6605-9975

Roche Pharma Research and Early Development, Therapeutic Modalities, Roche Innovation Center Munich, Roche Diagnostics GmbH

Linda Elise Franken:

linda_elise.franken@roche.com, https://orcid.org/0000-0002-3040-8192

Roche Pharma Research and Early Development, Therapeutic Modalities, Roche Innovation Center Basel, F.Hoffmann-La Roche Ltd

Jakob Then:

jakob.then@stud.uni-heidelberg.de

Roche Pharma Research and Early Development, Therapeutic Modalities, Roche Innovation Center Munich, Roche Diagnostics GmbH

Philippe Ringler:

philippe.ringler@roche.com

Roche Pharma Research and Early Development, Therapeutic Modalities, Roche Innovation Center Basel, F.Hoffmann-La Roche Ltd

Biozentrum, University of Basel, Switzerland

Joachim Butzer:

joachim.butzer@roche.com

Roche Pharma Research and Early Development, Therapeutic Modalities, Roche Innovation Center Munich, Roche Diagnostics GmbH

Thomas Juroschek:

thomas.juroschek@roche.com

Roche Pharma Research and Early Development, Therapeutic Modalities, Roche Innovation Center Munich, Roche Diagnostics GmbH

Dr. Christian Klein:

christian.klein.ck1@roche.com

Roche Pharma Research and Early Development, Discovery Oncology, Roche Innovation Center Zurich, Roche Glycart AG

Dr. Tilman Schlothauer:

tilman.schlothauer@roche.com,

Roche Pharma Research and Early Development, Therapeutic Modalities, Roche Innovation Center Munich, Roche Diagnostics GmbH

Dr. Laurent Larivière:

laurent.lariviere@roche.com

Roche Pharma Research and Early Development, Therapeutic Modalities, Roche Innovation Center Munich, Roche Diagnostics GmbH

Abbreviations

AAV	Adeno-Associated Virus,
ADIN	antibody-dependent intracellular neutralization
AP-1	Activator Protein 1
EM	Electron Microscopy
Fc	Fragment crystallizable
FcRn	neonatal Fc receptor
HBV	Hepatitis B virus
hIgG1	human Immunoglobulin G isotype 1
HSPG	heparan sulfate proteoglycan
IFN	Interferon
IRF 3/5/7	Interferon Regulatory Factor 3, 5, and 7
ITC	Isothermal titration calorimetry
JAK-STAT	Janus Kinase-Signal Transducer and Activator of Transcription
JEV	Japanese encephalitis virus
K_D	equilibrium dissociation constant
KiH	Knob-into-hole
k_{OFF}	dissociation rate constant
k_{ON}	association rate constant
mAb	monoclonal Antibody
MP	Mass Photometry
MTL	mass transport limitation
NFkB	Nuclear Factor kappa-light-chain-enhancer of activated B cells
PK	Pharmacokinetics
PRRS	Porcine reproductive and respiratory syndrome virus
rAAVv	recombinant Adeno-associated virus vector particles
RING	really interesting new gene
SAXS	Small-angle X-ray scattering
SPR	surface plasmon resonance
Trim	tripartite motif
TRIM21-CC	tripartite motif-containing 21 coiled-coil
UPS	ubiquitin-proteasome system
VCP	valosin-containing protein
WT	wildtype

Abstract

TRIM21 is a pivotal effector in the immune system, orchestrating antibody-mediated responses and modulating immune signaling. In this comprehensive study, we focus on the interaction of TRIM21 with Fc engineered antibodies and subsequent implications for viral neutralization. Through a series of analytical techniques, including biosensor assays, mass photometry, and electron microscopy, along with structure predictions, we unravel the intricate mechanisms governing the interplay between TRIM21 and antibodies. Our investigations reveal that the TRIM21 capacity to recognize, bind, and facilitate the proteasomal degradation of antibody-coated viruses is critically dependent on the affinity and avidity interplay of its interactions with antibody Fc regions. We suggest a novel binding mechanism, where TRIM21 binding to one Fc site results in the detachment of PRYSPRY from the coiled-coil domain, enhancing mobility due to its flexible linker, thereby facilitating the engagement of the second site, resulting in avidity due to bivalent engagement. These findings shed light on the dual role of TRIM21 in antiviral immunity, both in recognizing and directing viruses for intracellular degradation, and demonstrate its potential for therapeutic exploitation. The study advances our understanding of intracellular immune responses and opens new avenues for the development of antiviral strategies and innovation in tailored effector functions designed to leverage TRIM21s unique binding mode.

Introduction

The tripartite motif-containing 21 (TRIM21) protein also known as Ro52 or RNF81, has emerged as a pivotal player in the dynamic interface between the adaptive and innate arms of the immune system (1). With its unique functions as effector and sensor occurring simultaneously, it triggers the antibody mediated degradation of viral capsids by the proteasome and activates innate immune signaling pathways (2-5). This unique intracellular receptor exhibits an ancient origin, and its importance in immune regulation and host defense has garnered significant attention and demands further exploration (6).

In healthy cells, a functional antibody is not capable of entering the cytosol since it neither has a mechanism to penetrate the cell membrane, nor can it exit the endosome during endocytosis (7, 8). However, it was reported that antibodies bound to incoming pathogens remain attached to viral capsids, even after endosomal escape, and are thus delivered into the cytosol (9). Here, TRIM21, an E3 ubiquitin ligase ubiquitously expressed in human cells, recognizes the Fc part of antibodies (associated to viruses) and directs the complex to the ubiquitin-proteasome system (UPS) for its degradation (10). This process is called antibody-dependent intracellular neutralization (ADIN). TRIM21 expression is drastically upregulated by interferon (IFN) stimulation thereby amplifying its neutralization activities (3). As an intracellular antibody Fc receptor, TRIM21 complements the traditional extracellular functions of antibodies by allowing them to function as immune regulators within cells and

activate immune signaling pathways like the transcription factor NF-ϰB, AP-1 and IRF 3/5/7 (5, 11).

The Trim family of protein is characterized by a remarkably conserved N-terminal RBCC region(12). This region is composed of a really interesting new gene (RING) domain, one or two B-box domains, and a coiled-coil domain which represents the triumvirate giving the family its name (12-14). Trim proteins exhibit variations in their C-terminal regions, which are responsible for their specific functional attributes (15). For TRIM21, a C terminal PRYSPRY domain is responsible for target binding.

The RING domain functions as an E3 ubiquitin ligase, essential for recognizing and tagging proteins for degradation by attaching ubiquitin chains, signaling their breakdown by the proteasome (11, 16-18). The B-Box domain, specific to TRIM proteins, regulates TRIM21 by preventing auto-ubiquitination, thus regulating immune response activation (19-21). The coiled-coil domain (B-Box C-terminal; BBC) promotes dimerization of TRIM21 monomers (RBCC-PRYSPRY), positioning RING domains at either end of an elongated antiparallel coiled coil domain, which is inactivated while the PRY-SPRY domain (B30.2) binds to IgG Fc, indicating its role in immune function (15).

In mammals, the TRIM21-IgG interaction is highly conserved, allowing TRIM21 PRYSPRY domain to recognize IgGs from one species to various other species (22). Although TRIM21 has a lower affinity for the Fc region of IgA and IgM compared to IgG, targeting IgA still enables neutralization (23). As a homodimeric molecule, TRIM21 symmetrically binds to an IgG, engaging both Fc heavy chains simultaneously. This results in a 1:1 stoichiometry with the heterodimeric IgG (9). To date, only a single known apparent affinity/avidity dissociation constant ($K_{D,AVIDITY}$) for dimeric TRIM21 binding to the IgG1 Fc wild type has been reported. This value is 600 pM, as measured by fluorescence anisotropy, while the kinetic rate parameters (k_{ON} and k_{OFF}) remain undetermined. This interaction displays the strongest affinity observed in human IgG-Fc receptor interactions (9).

The binding affinity ($K_{D,AFFINITY}$) between human IgG1 Fc WT and the recombinant human PRYSPRY domain has been measured to be in the range of 40 nM by isothermal titration calorimetry (ITC) to 200 nM applying surface plasmon resonance (SPR) technology, depending on technology and assay setup (9, 10, 24). The PRYSPRY domain (antibody Fc binding domain) interacts with both CH2 and CH3 domains, although the most substantial interaction is with the CH3 domain (24, 25). Like FcRn, the neonatal Fc receptor, TRIM21 interacts with the HNYH-motif where amino acids 429 – 436, especially H433, N434, H435, and Y436 of the CH3 Fc loop as well as I253 of CH2 are inserted into the PRYSPRY binding pocket (24, 26-30). FcRn prolongs the half-life of IgG by protecting it from lysosomal degradation and mediating its recycling back into the bloodstream. Unlike FcRn, TRIM21 – IgG interaction is reported to be largely pH-independent (from pH 5- 8) but sensitive to salt. A 10-fold reduction in salt concentration from 200 to 20 mM results in a 5-fold increase in affinity, manifested in a decreased off-rate (22, 24).

For the FcRn – IgG interaction there are reported mutations within the hotspot region, like YTE (M252Y/S254T/T256E), HH (T307H, N434H), which demonstrate increased FcRn binding, while mutating key residues into alanines (H310A, H433A and Y436A; AAA) completely abolishes it (31-39). In addition, there is a reported influence of the antibody variable domain (Fabs) on FcRn binding and pharmacokinetics, which has not been studied for TRIM21 (40, 41).

Recent findings highlight that TRIM21's signaling requires higher activation than neutralization, which means that it is able to neutralize without initiating immune responses (2, 19). Engineered IgG1 variants with reduced TRIM21 binding still neutralize effectively but trigger less NF-κB signaling (10, 30). Mutations can significantly alter TRIM21 binding, with single mutations like H433A reducing activity, while others increase IgG1 Fc affinity up to 100-fold (10, 30). Slower dissociation rates from TRIM21 affect signaling more than neutralization, indicating possible low-level activity without an anti-viral state (10, 30, 42, 43). The distinction between effector and sensor activation thresholds allows for the effective clearance of minor viral threats without an extensive immune response.

Antiviral activity of TRIM21 has been demonstrated against a wide range of non-enveloped viruses, including adenovirus, Porcine reproductive and respiratory syndrome virus (PRRS), Japanese encephalitis virus (JEV), Hepatitis B virus (HBV) and rotavirus as well as certain bacteria (5, 9, 11, 44-49) . It can interfere with infection by direct interaction with the viral proteins, as well as by regulating immune responses and by recognition of antibody decorated viral complexes (50). Upon the cytosolic entry of virus complexes opsonized by antibodies, the Fc portion of the antibodies is rapidly recognized by the catalytically inactive TRIM21 dimer. A proposed mechanism for the activation of viral degradation involves target-induced clustering (51). It is postulated that the intermolecular dimerization of the TRIM21 RING (between two or more TRIM21 dimers) domains triggers ubiquitination activity (52). This process potentially alleviates B-box inhibition of the RING domain, facilitates E2-Ubiquitin interaction, and constructs K63-linked ubiquitin chains on TRIM21 (19). In contrast with earlier findings, which reported that ADIN only requires 1.6 antibodies per virus, effective neutralization, initiated by catalytically active RING dimers, necessitates the recruitment of multiple TRIM21 molecules (43, 51). Therefore, the nature of the target (oligomer) or the presence of multiple antibodies bound to the target could induce TRIM21 activation by promoting the clustering of multiple TRIM21 molecules in close proximity (51). TRIM21-antibody opsonization levels need to be above a certain threshold to enable RING dimerization, thus activating the innate neutralization pathway against the bound pathogen.

We sought to elucidate the detailed mechanism of action of the TRIM21-IgG interaction. To achieve this we generated several antibody Fc mutants, modifying TRIM21 binding. The used antibody variants express symmetrical, similar Fc heavy chains, or asymmetrical, varying heavy chains. We utilize a suite of complementary technologies to decipher TRIM21 binding. While it is established that single point mutations can modify PRYSPRY binding and that

one TRIM21 homodimer interacts with one Fc heterodimer in a 1:1 stoichiometry with strong avidity, TRIM21 detailed mode of action remains unclear. This includes the precise nature of the natural dimer state, mutations that influence avidity, and determining how a synergistic interplay of TRIM21 mediated antibody variants bound to viruses leads to amplified avidity thereby influencing its mode of action.

In this study, we explore the mechanism by which the engagement of both heavy chains mediated via TRIM21 dimers takes place and examine the impact of Fc variants of antibodies on the balance between affinity and avidity, offering detailed insights into the mechanism of antibody binding. We demonstrate the occurrence of TRIM21 - anti-AAV antibody clustering on a biosensor, unveiling intricate binding dynamics. Gaining an in-depth knowledge of TRIM21 and its interactions with antibodies paves the way for innovative therapeutic approaches targeting infectious diseases, autoimmune conditions, and immune signaling pathways.

Results

Design of TRIM21 Antibody Biosensor Assay Configuration for Dissecting its Binding Mode

To study the TRIM21 interactions in detail, there are two assay configurations possible on a (SPR) biosensor. Depending on the scientific question that should be addressed, either the antibody or TRIM21 is captured on the chip-surface (Figure 1). Furthermore, it is to be considered, that the bivalent antibody displays an Fc part with two binding moieties for TRIM21 and TRIM21 naturally forms a homodimer, which might cumulate in a more complex binding mode than a simple 1:1 interaction.

If the antibody (ligand) is captured on the surface under physiological conditions and the PRYSPRY domain (antibody Fc binding domain) (analyte) is in solution as shown in **Figure 1A**, the monovalent PRYSPRY domain binds to the Fc part exclusively in a monovalent fashion. Here, the mode of binding is independent from the ligand surface density. For the interacting pair of PRYSPRY and an antibody, this assay configuration exclusively probes the affinity mode, as the bivalent nature of the antibody Fc part is in this set-up irrelevant. Notably, this assay orientation allows the affinity characterization of various antibody Fc variants modulating the affinity towards the PRYSPRY domain. It also enables to investigate the stoichiometry for PRYSPRY and the dimeric Fc part, which we address with symmetrical and asymmetrical Fc variants. The latter abolishes TRIM21 binding for one Fc heavy chain.

The alternative orientation with PRYSPRY domain on the surface and the antibody in solution (**Figure 1B**) allows to investigate further attributes that describe the TRIM21-IgG interaction in more detail. As an example is the potential Fab contribution to TRIM21 binding efficiency as observed for FcRn binding (40, 41, 53-55). The ligand density in this assay setup is crucial. The antibody may interact with one or two PRYSPRY domains (ligand)

depending on ligand density, by interlinking two domains that are close enough for simultaneous engagement (affinity and avidity). To exclude avidity binding modes we measured at low ligand density.

To investigate the natural TRIM21-IgG binding mode, where one TRIM21 homodimer interacts with one IgG engaging both heavy chains simultaneously in a 1:1 stoichiometry, we produced a minimal dimer construct including the PRYSPRY and coiled-coil domain (**Sequence in Materials and Methods**), TRIM21-CC, which is reported to have no effect on bivalent antibody Fc binding (9). To measure the TRIM21-CC - antibody interactions, the antibody is captured on the sensor surface while TRIM21-CC is injected (**Figure 1C**). The bivalent binding of TRIM21-CC should result in an avidity effect, where an additional SPR based biosensor experiment would provide not only a dissociation constant ($K_{D,AVIDITY}$), but also the to date unknown kinetic rate parameters (k_{ON} and k_{OFF}), which describe the interaction in further detail. This assay setup also allows determining how Fc variants influence the avidity-binding mode and dissecting avidity from affinity. For all assay setups, we worked with low ligand density.

Antibody Fc engineerings to Dissect Affinity towards the PRYSPRY Domain

To resolve the influence of Fc engineerings on the affinity for the TRIM21 PRYSPRY domain we used the assay setup shown in **Figure 1A**. To determine the kinetic rate parameters of the PRYSPRY - antibody interaction and its stoichiometry, a human IgG1 Fc WT (mAb1 WT) was compared with an asymmetrical variant mAb1 WT-AAA (H310A, H433A, Y436A). SPR binding kinetic of both constructs (**Figure 2A-B**) result in the same kinetic rate parameters. To confirm loss of binding in our AAA mutant, a double AAA mutant (mAb1 AAA) was used as control (**Figure 2C**). MAb1 WT and WT-AAA demonstrate an affinity dissociation constant ($K_{D,AFFINITY}$) of 43 nM and 40 nM, respectively (**Figure 2D, detailed parameters in SI Table S 1**).

The $R_{max,Ratio}$ represents the ratio of experimental and theoretical maximal feasible SPR signal between a ligand - analyte couple, and provides information about the stoichiometry of an interaction. The interaction between mAb1 WT and mAb1 WT-AAA - PRYSPRY, with assumed binding sites of two and one, respectively, approaches 100% efficiency, leading to stoichiometries of 2:1 and 1:1, as shown in **Figure 2D**. This confirms that the IgG Fc binds two PRYSPRY domains, one at each of the CH2-CH3 interfaces. Additionally, the data shows that there is no effect of the first PRYSPRY binding event on the binding efficiency of the second monomer.

To confirm the findings from the SPR analysis we applied mass photometry (MP) for mAb1 WT/WT-AAA/AAA as a complementary method **(Figure 2E-F**). Considering the fast k_{ON} and k_{OFF} (**Figure 2D**) for the mAb1-PRYSPRY interaction, 200 nM mAb1 Fc variant were pre-incubated with 4000 nM PRYSPRY domain, and analyzed at a 1:250 dilution.

The non-binder variant mAb1 AAA with PRYSPRY (138 kDa) and without PRYSPRY domain (143 kDa), are in good agreement with each other and with the theoretical molecular weight (**Figure 2F**), demonstrating that PRYYPRY binding is abolished. An individual PRYSPRY domain appears at molecular weight of 32 kDa (**Controls: Figure S 1**). MAb1 WT + PRYSPRY gave a molecular weight of 193 kDa for the complex, which is in agreement with two PRYSPRY bound to one antibody (Gaussian Distribution Model), while mAb1 WT-AAA + PRYSPRY shows only the single bound state represented by 172 kDa.

To further examine how PRYSPRY binding can be altered by antibody constructs and Fc engineerings, we characterized additional variants, applying the assay setup shown in **Figure 1A.** All measured antibody formats share an identical IgG1 Fc framework, with or without specific mutations within TRIM21 binding interface. mAb1 WT and mAb2 WT exhibit different electrostatic and hydrophobic Fab patches. Two additionally investigated constructs are Briakinumab and Ustekinumab. Briakinumab shows a large positively charged Fab region, which is absent in Ustekinumab, and has been shown to have different FcRn affinities (40, 56). A cytokine-Fc Fusion and a Fc-only (CH2-CH3) WT were also included along with the mAb2 WT knob-into-hole (KiH) variant, which has specific mutations in the CH2-CH3 region (details in materials and methods). To compare the determined affinities, the kinetic rate parameters are displayed in a kinetic rate scale plot (**Figure 3A**). Detailed sensorgrams and kinetic parameters are shown in **SI Info Figure S 2.**

In this assay orientation, the affinities of most antibody constructs for PRYSPRY are similar. Exempt are the Fc variants YTE (M252Y, S254T, T256E), HH (T307H, N434H) and Y436A, which contain Fc mutations at key residues in the binding interface for PRYSPRY. These variants have lower affinities for the PRYSPRY domain than WT, showing a sequence from highest to lowest strength of binding as follows: WT has the strongest affinity, followed by YTE, then HH, and Y436A has the weakest.

For YTE the effect is only off rate driven (1.6x faster compared to WT), while for HH and Y436A it is a combination of both on and off rates. In contrast to WT, HH shows a 5x faster off rate, while the on rate is 2x faster, compensating for a significantly weaker affinity ($K_{D,AFFINITY}$) compared to the YTE variant. For the Y436A variant both rates are strongly decreased (8x on rate and 23x off rate compared to WT). Overlaying the normalized dissociation phases (**Figure 3B**) shows the significant effect of Fc engineering ($t_{1/2}$: 7.0 s for WT vs 0.3 s for Y436A).

Here, we showed that our assay setup (**Figure 1A**) is suitable to determine the pure, undisturbed affinity of the PRYSPRY-IgG interaction. We found a 180-fold reduced affinity for Y436A compared to WT. The SPR and MP results reveal a PRYSPRY-IgG stoichiometry of 2:1 without any binding cooperativity. The chosen assay setup does not reveal an additional contribution of Fab binding, as such we apply the reversed assay orientation to address this topic in the following section.

Impact of Antibody Variable Domain on TRIM21 PRYSPRY Binding Affinity

FcRn and TRIM21 share an overlapping CH2-CH3 binding interface. Antibodies with an identical Fc part but different Fab domains bind differently to FcRn, showing different affinities and pharmacokinetic properties (40). To uncover a potential PRYSPRY-IgG Fab contribution, we reversed the assay setup while allowing the Fab arms to move freely in solution (**Figure 1B, Figure 4, detailed data in SI Info Figure S 3**). To avoid intermolecular interaction where one antibody interacts with two adjacent PRYSPRY domains, low PRYSPRY densities were used.

The reverse assay orientation reveals a two to three-fold increase in binding strength. This effect is primarily driven by on-rate changes, not influenced by Fab regions, as evidenced by same outcomes for the control (Fc-only WT), which lacks a Fab. The affinities across the characterized antibody panel remain consistent with each other, confirming the absence of any measurable Fab effect on the Fc-PRYSPRY interaction.

The Dimeric State of TRIM21-CC

To probe the dimeric engagement of both IgG heavy changes simultaneously, we first characterized the construct TRIM21-CC (**Figure 5**). The expected theoretical molecular weight of this dimeric construct is 86 kDa. Applying SEC-MALS revealed a mass of approximately 90 kDa for 94 % of the particles (4% showed 177kDa corresponding to a tetramer) (**Figure 5A**). MP gave 99% of particles at a weight of 82±13 kDa (**Figure 5B**). Electron Microscopy analysis revealed that the PRYSPRY domains are facing away from each other with the coiled-coil domains in between mediating dimerization. Shown 2D classes indicate a variation in the position of the PRYSPRY domains with respect to each other (**Figure 5C**). Here, we confirmed the dimeric nature of TRIM21-CC with three techniques. Surprisingly, the EM data show that the coiled-coil domain is stretched and the distance between the two PRYSPRY domains is extended. The fact that we were able to resolve the shape of the coiled-coil is an indication that in its dimeric shape TRIM21 is relatively limited in its flexibility.

TRIM21-CC-Fc variant Interaction by Mass Photometry and Electron Microscopy

To investigate the TRIM21-CC - Antibody Fc binding mode, we applied MP and electron microscopy (**Figure 6**). For the MP measurements we incubated various, increasing TRIM21-CC concentrations with three antibody Fc variants (mAb1 WT, mAb1 WT-AAA and mAb1 AAA) each at different molar ratios.

As shown in **Figure 6 A-C**, incubating TRIM21-CC with mAb 1 gave peaks at approximately 80 kDa and 140 kDa, representing uncomplexed TRIM21-CC and mAb1, which is in agreement with their theoretical masses and individual mass measurements (**Figure 5 and**

SI Info Figure S 1). At approximately 230 kDa appeared a third peak whose molecular weight corresponds to a complex consisting of one TRIM21-CC with one mAb 1 WT (**Figure 6A**). With increasing TRIM21-CC concentration, the equilibrium is shifted to the complexed species until nearly all antibodies are bound. At a 10-fold molar excess of TRIM21-CC (**Figure 6D**), 24% of TRIM21-CC and mAb1 WT are complexed, revealing a 1:1 stoichiometry where one dimer and engages both IgG heavy chains simultaneously (detailed data in **SI Info Figure S 4**). Detecting the TRIM21-CC -mAb1 WT interaction at low nanomolar concentrations also allows insights into the strong interaction by the dimeric engagement, resulting in an avid binding mode.

The applied mAb1 WT-AAA concentrations showed a minor complexed fraction (approx. 2%), while the AAA variant shows no formed complexes (**Figure 6B-C**). For mAb1 WT-AAA variant, we expect binding, but only to one of the two Fc heavy chains resulting in weak affinity, which cannot be resolved at the concentrations used (similar affinities as for PRYSPRY). The symmetrical AAA mutation abolished TRIM21 binding completely.

To further elaborate the binding mode we analyzed TRIM21-CC with mAb1 WT and the Fc-only variants WT and WT-AAA applying EM (**Figure 6E-H**) and MP (**Figure S 6**). The results demonstrate that the Fc-only WT-AAA variant binds one PRYSPRY domain, compared to WT (**Figure 6E-F**). The Mab1 WT-TRIM21-CC complex confirms the binding of two PRYSPRY domains to the Fc portion compared to mAb1 WT alone (**Figure 6G-H**). Although coiled-coil dimerization domain is not visible in our 2D classes, and analysis of raw images is challenged by the complexes' size and flexibility, our findings indicate that a single TRIM21-CC is capable of binding to an Fc region through one or both PRYSPRY domains, and it possesses the ability to concurrently bind two distinct Fc molecules. As depicted in **Figure 5C**, we do not observe a pre-bound/pre-formed positioning of the PRYSPRY domains that would already fit the spatial arrangement of antibodies Fc Part (CH2-CH3). The average distance between the two PRYSPRY domains measures ~10.1 ± 2.1 nm whereas the distance between two Fc-bound PRYSPRY domains is ~5.3 ± 0.5 nm. Therefore, for one TRIM21 to engage both heavy chains, the PRYSPRY domains will have to rearrange. As can be observed in the alphafold model (Uniprot ID P19474), the PRYSPRY domain attaches to its helix with a flexible linker. This linker could allow dimeric engagement by bringing the PRYSPRY domains closer to each other.

Binding Kinetic of TRIM21-CC with Antibody Fc variants

Here, we examined the interaction between TRIM21-CC and various antibody Fc variants through SPR experiments (assay setup **Figure 1C**), focusing on the avidity binding mode influenced by Fc engineering. Utilizing a low surface density setup to exclude intermolecular interactions, we explored both symmetrical and asymmetrical Fc variants, including YTE, HH, and Y436A, to discern the relationship between antibody affinity and avidity

enhancement due to dimeric engagement (previously investigated for affinity binding, **Figure 3**).

Figure 7 shows the characterization of TRIM21-CC with (antibody) Fc variants. When several antibody concentrations were injected over 180 seconds, a 1:1 fit model describes the data. The dissociation phase is characterized by a significantly reduced dissociation rate ($k_{OFF,AVIDITY}$) in comparison to the affinity-only interactions ($k_{OFF,AFFINITY}$). The sensorgram reveals an avidity only binding mode and a consistent 1:1 stoichiometry (exemplary mAb1 WT, **Figure 7A** and SI Info*,* **Figure S 5**).

Variation in the association time for a constant TRIM21-CC concentration (25 nM) with mAb1 WT on the surface (ligand) uncovered a biphasic dissociation pattern, supporting a two-state binding model (**Figure 7B**). This model illustrates an initial rapid binding and dissociation phase (single bound state, affinity) followed by a slower, more stable avidity-driven complex formation (double bound state, avidity), each with its own association (k_{ON}) and dissociation (k_{OFF}) rates (**SI Info Figure S 5B,J**). Applying both models results in identical dissociation constants ($K_{D,AVIDITY}$ = 0.7 nM), demonstrating a substantial avidity-enhanced binding strength compared to affinity alone ($K_{D,AFFINITY}$ = 43 nM) (**Figure 7C-D**).

Comparative analysis revealed that avidity enhancements ($K_{D,AFFINITY}/K_{D,AVIDITY}$) for Fc variants were significant, with the WT variant showing a 61-fold increase, YTE 50-fold, HH 72-fold, and Y436A 14-fold, when compared to their respective affinities (**Figure 7C**). However, when compared to the WT avidity component, YTE and HH were both about 2-fold less effective, whereas Y436A's binding strength decreased dramatically by 766-fold. Despite YTE and HH having similar reductions in avidity compared to WT avidity, HH exhibited kinetic rates 5 times faster than YTE. The interaction of asymmetrical antibody Fc variants (WT-AAA, YTE-AAA, HH-AAA) with TRIM21-CC showed only the affinity binding mode (**SI Info, Figure S 5**).

Complementary MP analysis (**SI Info, Figure S 6 and Table S 2**) corroborated our SPR findings, confirming a 1:1 stoichiometry for all symmetrical constructs and showing a trend where weaker bindings resulted in fewer avid complexes as the identical the concentration of antibody-TRIM21-CC was used. Additional MP experiments with other antibody Fc WT constructs, such as mAb2 WT, Briakinumab, and Ustekinumab, revealed similar complexation levels to mAb1 WT, indicating that the variable domains of these antibodies do not affect their interaction with TRIM21-CC. This further validates our SPR-derived conclusions.

TRIM21 within the context of Viral Neutralization

We mimicked the interaction between TRIM21 and antibody-coated, recombinant adeno-associated virus vector (rAAVv) particles on a SPR chip (**Figure 8A**), alongside parallel electron microscopy (EM) imaging (**Figure 8C**). This setup emulates the scenario after endosomal escape of antibody decorated AAV particles and their encounter with cytosolic

TRIM21, proposing that TRIM21's interaction with antibody-bound virus particles triggers ubiquitination through intermolecular RING dimerization, as suggested previously (20, 51). Our assay involved TRIM21-CC, anti-AAV2 capsid antibody A20 variants (including a bivalent A20 with WT Fc and IgG variants with a single Fab arm against rAAVv-2, featuring either WT Fc or WT-AAA asymmetrical Fc), and rAAV serotype 2 (rAAV2), as depicted in (**Figure 8A**). Our research reveals complex interactions between TRIM21-CC, A20 antibody variants, and rAAVv-2, showing that binding dynamics are more intricate than simple models suggest (**Figure 8B**). These interactions involve both affinity and avidity effects, with TRIM21-CC binding to the antibodies Fc region and the Fab arm(s) binding to the rAAVv-2 capsid, contributing both to overall avidity.

All three anti-AAV2 antibody variants show affinities for the capsid in the same range ($K_{D,AFFINITY}$ 75 - 140 nM), whereas the bivalent A20 WT also demonstrated avid binding $K_{D,AVIDITY}$ = 5 nM (SI INFO, Figure S 7). The full IgG A20 Fc WT shows strong bivalent engagement with TRIM21-CC ($K_{D,AVIDITY}$ = 0.7 nM) unlike the asymmetrical AAA-WT variant, which lacks this avidity. (SI INFO Figure S 8).

The AAV2 viral capsid harbors n = 60 epitopes for A20, assuming intra- and intermolecular bivalent binding is possible, depending on antibody variant and concentration (57). By varying the A20 antibody levels (8-fold different capture level, **Figure 8B**) and analyzing EM data (Figure 8C), we observed that higher antibody densities on the virus surface enhance avidity. The bivalent A20 Fc WT variant promotes increased avidity, surpassing the monovalent A20 Fc WT and WT-AAA variants in binding efficiency, leading to faster dissociation.

Analysis of the dissociation phases indicate that all antibody variants demonstrate avidity, with slower and faster dissociating species suggesting complex formation between rAAVv-2 and antibodies. On a biosensor surface, ligands are randomly distributed by statistics. As such, two adjacent, single arm A20 constructs could still interact with one rAAVv, allowing avidity to occur. However, lower antibody densities result in a greater proportion of fast dissociating species, indicating a decrease in avidity (**Figure 8B**, low surface density).

EM images (**Figure 8C**) reveal that A20 antibodies as well as TRIM21-CC facilitate AAV particle aggregation, owing to their ability to bind two separate molecules. While A20 causes severe aggregation, to the point that an additional effect of TRIM21 can not be measured, the one-armed antibodies lose their ability to cause aggregation, allowing us to separate the effect of TRIM21 (**Figure 8C**, bottom two rows). Indeed, TRIM21 causes aggregation, albeit to a lesser extent. This confirms our SPR observation that reducing bivalent engagement modifies but does not negate avidity. Our findings emphasize the crucial role of the antibody as an immune regulator in mediating both, target binding (AAV) and effector functions via TRIM21 engagement achieving avidity, demonstrating the multifaceted nature of these interactions.

Discussion

This study systematically explores the interaction of TRIM21 with antibody Fc variants through SPR, MP, and EM to elucidate antibody binding to TRIM21 and investigate a TRIM21-mediated AAV neutralization mechanism. We meticulously optimized our SPR assays for each scientific hypothesis, facilitating low-density studies ideal for distinguishing between affinity and avidity. This approach yielded significant insights into the dynamics and mechanisms of TRIM21 interaction with human IgG Fc variants including a newly proposed binding mechanism.

TRIM21 is a highly conserved mammalian Fc receptor that is structurally and mechanistically distinct from previously identified Fc receptors (22). Our analysis confirmed the PRYSPRY–mAb1 WT interaction affinity at 43nM, aligning closely with prior ITC data (37 nM) (24) and differing from previous SPR results (212 nM) (58). This discrepancy originates from our refined assay conditions, which resulted in a 5-fold increase in binding rate (k_{ON}) without altering the dissociation rate (k_{OFF}). Our methodology, mirroring ITC gold-standard accuracy, demonstrates the benefits of optimized assay setups for enhanced target interaction analysis, thereby addressing the discrepancies observed in prior SPR experiments. Additionally, our findings on the mAb1 WT-AAA Fc variant versus symmetrical Fc WT confirmed a 2:1 stoichiometry and identical affinities of two TRIM21 PRYSPRY domains for one IgG Fc homodimer ($K_{D,AFFINITY,WT\text{-}AAA}$ = 40 nM vs $K_{D,AFFINITY,WT}$ = 43 nM), supporting a non-cooperative binding model (24). This aligns with the symmetric TRIM21-IgG interaction in the previously reported crystal structures (24).

Despite TRIM21 and FcRn sharing the Fc CH2-CH3 binding site, the HNHY motif, mutations in the Fc region affect their interactions differently. We engineered mutations within this interface (YTE, HH, Y436A, AAA), previously identified to impact FcRn binding, to assess their effect on TRIM21 (31, 32, 36-39, 59). Our findings reveal a ranking of affinities for PRYSPRY, from strong to weak: WT, YTE, HH and Y436A. Notably, the Y436A mutation significantly weakens the binding to both FcRn (39) and TRIM21, with a 180-fold decrease in TRIM21 binding affinity, a previously unexplored aspect in the context of TRIM21 interaction. Through SPR analysis, we confirmed an avid equilibrium dissociation constant ($K_{D,AVDIDITY}$) of 0.7 nM for mAb1 Fc WT (vs. 0.6 nM as determined by fluorescence anisotropy) and confirmed a 1:1 stoichiometry (9). In addition, we uncovered kinetic parameters alongside with an avidity enhancement ($K_{D,AFFINITY}/K_{D,AVIDITY}$) for the Fc variants of 14- to 72-fold. This suggests a substantial affinity to avidity transition due to bivalent engagement, particularly notable with the Y436A mutation, which demonstrates affinity in the μM range, while avidity is nM.

Interestingly, while the YTE and HH variants weaken TRIM21 binding compared to WT, they enhance FcRn binding (10-fold for YTE, HH is in similar range;) in a pH-dependent manner, highlighting a divergent influence of these mutations on the two receptors (31, 32, 36). The AAA mutation, which eliminates FcRn binding (37, 38), also abolishes TRIM21

interaction. Remarkably, we found no Fab contribution that adds an additional complexity to TRIM21 as it does for FcRn (40, 41). A possible hypothesis to explain this phenomenon could be the pH independency known for TRIM21 (22). The divergence of TRIM21 and FcRn suggests potential implications for efficient antibody recycling and ADIN. A potential intracellular transition between FcRn and TRIM21 has to be explored. Our study emphasizes the importance of considering both affinity and avidity in TRIM21 interactions and challenges the direct extrapolation from one to the other, underlining the complexity of antibody engineering with respect to receptor binding.

Our configuration of unbound TRIM21 revealed that the C-terminal PRYSPRY domains within a TRIM21 dimer, where dimerization is mediated via the coiled coil domains, are positioned at opposite ends, away from each other (60). This finding is in contrast to previous studies on TRIM family proteins, such as TRIM25. It has been suggested, that unbound C-terminal domains, responsible for substrate binding, are centrally located within an elongated structure characterized by a coiled-coil domain (61, 62). A possible explanation for the changed TRIM21 configuration in the unbound state is the truncation of TRIM21 (TRIM21-CC). Arguing against this is the fact, that the length of the coiled coil domain exceeds the distance measured between the two PRYSPRY domains by at least 3 nm. Also, the truncated sequence still maintains a stretch of 30 amino acids beyond the coiled-coil domain, suggesting a natural configuration at the observed binding location. Our analysis demonstrates that the PRYSPRY domains are spaced approximately 6-12 nm apart, diverging from the ~5 nm separation when bound to Fc, which challenges the notion of a pre-bound state compatible with the Fc structure and spatial arrangement (**Figure 5** and **Figure 6**).

Zeng and colleagues (51) have proposed a TRIM21-IgG Fc-complex structural framework based on Small-angle X-ray scattering (SAXS) data, positioning the bound PRYSPRY domains centrally, which is in agreement with our findings. This configuration also accounts for avidity due to bivalent Fc engagement, observed in our SPR (**Figure 7C**) and MP data (**Figure 6A**), as well as the positioning of the bound PRYSPRY domain indicated by our negative staining techniques (**Figure 6E-H**). Beyond previous findings, our detailed examination underpins a novel conceptual framework for TRIM21 structural dynamics in both its bound and unbound states (**Figure 9**). In its unbound state, the dimer's PRYSPRY domains converge at the coiled coil's apex, a feature discernible through negative staining (**Figure 5C**). Binding to an Fc site results in the detachment of PRYSPRY from the coil, enhancing mobility due to its flexible linker, and thereby facilitating the engagement of the second site in a spatially favorable configuration. Our SPR data confirms, that binding occurs in a two-step process, initially rapid, followed by a slower event that forms the final TRIM21-IgG complex (**Figure 7B**). The slower phase occurs over a prolonged duration to accommodate the Fc geometry (**Figure S 5J**, $k_{ON2} = 0.02s^{-1}$). The transition markedly increases the complex flexibility, rendering the coiled-coil domain indistinct in negative stain averages of the TRIM21-CC-Fc assembly.

Integrating the structural insights from PRYSPRY domains in complex with Fc (PDB-ID: 2IWG) (24) with the predictive model of TRIM21 (Uniprot ID: P19474) and its dimeric form according to AlphaFold2 (for details see materials and methods) yields diverse models (63). While a minority retains the dimeric form of TRIM21 engaging a single Fc site (**Figure S 10A1**), most predictions indicate a separation of PRYSPRY domains from the coiled-coil (**Figure S 10A2-B**) agreeing with our model (**Figure 9**).

Combining our findings, we propose a tentative model in which the PRYSPRY engagement with the Fc domain may influence its interactions with other domains of TRIM21. This observation leads us to speculate that within a TRIM21 dimer, the PRYSPRY domain might have an additional, yet uncharacterized, role in modulating the interactions of the B-Box and the RING domains. We suggest that the binding of the PRYSPRY domain to the Fc domain could potentially release these intra-domain interactions, thereby affecting RING activation.

Lastly, our study delved into the TRIM21 antiviral mechanism, particularly its role in E3 ligase activation and neutralization of adeno-associated virus (AAV) using AAV as a model. We investigated how the anti-AAV2 capsid antibody A20 interacts with TRIM21 and rAAVv-2, noting A20 unique ability to neutralize AAV2 and AAV3 by targeting a specific conformational epitope (64, 65). Despite the lack of knowledge regarding the precise neutralization mode, subsequent to initial heparan sulfate proteoglycan (HSPG) primary receptor attachment, our data suggests A20 impedes viral entry by promoting large aggregate formation (**Figure 8**), potentially blocking endocytosis-mediated cell entry (57, 65, 66). We highlight the distinction between neutralizing and non-neutralizing antibodies in human blood, with the latter capable of cytosolic entry, as antibody-AAV complexes, post-endosomal escape (67, 68). However, the role of non-neutralizing antibodies in TRIM21-mediated AAV neutralization remains unexplored due to their unavailability for testing. Our findings indicate antibody clustering on AAV is feasible, aiding in the activation of TRIM21's E3 ligase via RING dimerization, a critical step in neutralization (9, 20, 51). Comparing AAV with AdV, we noted the smaller size of AAV and fewer antibody binding sites could significantly influence its neutralization process. Unlike A20, which forms large aggregates, the anti-AdV5 antibody does not aggregate virions or hinder their attachment nor trafficking (3, 4, 42, 69, 70).

Our elucidated TRIM21 dimeric nature and its interaction with Fc-engineered antibodies revealed a new mechanism for bivalent engagement and demonstrated the impact of Fc mutations on both affinity and avidity. This knowledge is pivotal for advancing antibody engineering and understanding TRIM21 function in viral defense.

Materials and Methods

Recombinant TRIM21 Variants

Recombinant human TRIM21 proteins, including the PRYSPRY domain variant and the coiled-coil (TRIM21-CC) variant, were produced and purified by Proteros Biostructures GmbH (Planegg, Germany). The production process involved the transformation of Escherichia coli strain BL21 DE3, the overexpression of TRIM21 under standard conditions (18°C, 1mM IPTG, 16h) and the purification by Ni-NTA resin (Qiagen, Hilden, Germany) and Superdex S-200 26/60 gel filtration (GE Healthcare, IL, US). Each plasmid used for the transformation encoded either the TRIM21 PRYSPRY domain or the TRIM21-CC variant. Both variants were C-terminally fused to a His-Avi-Tag via a (4GS)1 linker. The gene used for this process is identified by NCBI Gene ID 6737, which corresponds to UniProtKB identifier P19474-1 (Isoform 1). The amino acid sequence for the TRIM21 PRYSPRY variant spans from amino acid 277 to 475, while the sequence for the TRIM21-CC variant spans from amino acid 128 to 475.

Antibody Constructs/Fc Variants

Recombinant human IgG1 Fc wildtype, Fc variants, Fc-only variants (core hinge-CH2-Ch3) with specific mutations (Fc WT, Fc WT-AAA, mAb1 WT, mAb1 WT-AAA, mAb1 AAA, mAb1 YTE, mAb1 YTE-AAA, mAb1 HH, mAb1 HH-AAA, mAb2 WT, mAb2 WT sym., anti-AAV2 capsid antibody A20 WT, A20 one arm WT, A20 one arm WT-AAA), and cytokine-Fc Fusion constructs (cytokine-Fc Fusion WT, cytokine-Fc Fusion WT-AAA, cytokine-Fc Fusion Y436A) as well as Ustekinumab and Briakinumab were produced and purified internally at Roche (Penzberg, Germany). Mutations (Kabat numbering scheme) are the following: WT: wildtype; AAA: H310A, H433A, Y436A; YTE: M252Y, S254T, T256E; HH: T307H, N434H and Y436A. The production process involved the transient transfection of HEK Expi293F cells, sourced from Thermo Fisher Scientific (MS, US), with plasmids encoding both the light and heavy chains. Asymmetrical variants were generated using the knob-into-hole technology (71). This technology refers to refers to mutations Y349C, T366S, L368A and Y407V (Hole) and S354C and T366W (Knob) both in the CH3-CH3 interface to promote heteromultimer formation (72, 73).

Virus Supply

Replication-deficient, recombinant Adeno-associated virus vector particles serotype 2 (rAAVv-2) without carrying any transgene (empty rAAVv-2) were supplied by Virovek (CA, US), aliquoted up on arrival and frozen at -80°C until required. The electron microscopy experiments were performed using genome-filled rAAV2 vectors, supplied by Sirion Biotech (Germany).

SEC-MALS

The molecular weight of the sample was determined using size-exclusion chromatography combined with multi-angle light scattering (SEC-MALS). The SEC-MALS analysis was performed using a high-performance liquid chromatography (HPLC) instrument (Superdex200 Increase 10/300 GL, GE Healthcare). The HPLC instrument was coupled with a Wyatt Heleos II 18-angle light-scattering instrument (297-TS, Wyatt Technology) and a Wyatt Optilab rEX (766-rEX, Wyatt Technology) online refractive index detector. The sample was prepared at a concentration of 1 mg/mL, and 50 μg of the sample was injected into the system. The running buffer used was phosphate-buffered saline (PBS) at pH 7.4. The system was operated at a flow rate of 0.5 mL/min. To ensure the accuracy and reliability of the system, a system suitability test was performed by injecting bovine serum albumin (BSA) prior to the sample analysis. The results from the BSA injection were used to validate the performance of the system and to confirm that it was operating within the acceptable parameters for accurate molecular weight determination.

SPR Experiments

General Assay Setup

The Biacore T200 system (GE Healthcare, Uppsala, Sweden) was used for all surface plasmon resonance (SPR) experiments. The C1 sensor chips (carboxymethylated matrix-free surface), amine coupling kit (containing 1-ethyl-3-(3-dimethylaminopropyl) carbodiimide hydrochloride (EDC), N-hydroxysuccinimide (NHS), and ethanolamine-HCl), HBS-N (10 mM HEPES, 150 mM NaCl, pH 7.4), HBS-EP+ running buffer (10 mM HEPES, 150 mM NaCl, 3 mM EDTA, 0.05% surfactant P20, pH 7.4), and regeneration solutions were also obtained from Cytiva.

The ligand was immobilized on the C1 sensor chip using standard amine coupling chemistry. Briefly, the sensor surface was conditioned with two one minute injections of conditioning solution (0.1 M glycine-NaOH, 0.3% Triton X-100, pH 12) followed by "Extra wash" and then run "Prime" using HBS-N running buffer. The Chip was then activated by injecting a mixture of 0.4 M EDC and 0.1 M NHS at a flow rate of 10 μL/min for 7 minutes. The ligand was then injected at a concentration of 20 μg/mL in 10 mM sodium acetate buffer (pH 4.5) at a flow rate of 10 μL/min for 3 minutes unless stated otherwise. Unreacted groups were blocked by injecting 1 M ethanolamine-HCl (pH 8.5) at a flow rate of 10 μL/min for 7 minutes.

Next, a molecule of interest, diluted accordingly in HBS-EP+ running buffer was captured via the amine coupled ligand to a desired Response unit (RU) level at a flow rate of 5 μL/min. Binding kinetics were measured at 25°C by injecting various concentrations of the analyte over the captured molecule of interest at a flow rate of 50 μL/min unless stated otherwise. Each injection was followed by a dissociation phase. The sensor surface was regenerated

between each cycle by injecting 10 mM glycine-HCl (pH 2 or 3, see below) at a flow rate of 30 µL/min.

The sensorgrams were analyzed using the Biacore T200 evaluation software (v3.1) and GraphPad Prism (v8.4.2). The data were fitted to a 1:1 binding model to determine the association rate constant (k_{ON}), dissociation rate constant (k_{OFF}), and equilibrium dissociation constant (K_D). The K_D was calculated as k_{OFF}/k_{ON}. For analyzing complex binding kinetics the data were fitted by applying the Two State Reaction Model obtaining a K_D value explained in more detail in the following section. The results are presented as mean ± standard deviation.

To ensure the reliability of the data, a blank run (buffer only) was performed before each experiment to check the baseline stability.

TRIM21 PRYSPRY Injections to captured Antibody (Fc) Variants, immobilized Fc only variants and captured cytokine-Fc Fusion constructs

To investigate the interactions of TRIM21 PRYSPRY with various protein constructs, we utilized a consistent methodology across different experiments, applying standard amine coupling chemistry for immobilization on a C1 sensor chip. The experiments focused on three targets: antibody (Fc) variants, Fc only variants, and cytokine-Fc Fusion constructs.

For the antibody (Fc) variants and Fc only variants, we aimed for initial immobilization to achieve response unit (RU) signals of approximately 60 for antibody variants and between 60 and 80 for Fc only variants, using the CaptureSelect™ Human Fab-kappa Kinetics Biotin Conjugate ligand (7103302100, Thermo Fisher Scientific) for the former and direct immobilization for the latter. The cytokine-Fc Fusion constructs involved capturing using an in-house anti-PGLALA F(ab')2 fragment (74) with a target RU signal between 35 and 40. Subsequent steps involved injecting five different concentrations of TRIM21 PRYSPRY, prepared in a two-fold dilution series, across all experiments. Each concentration underwent an association phase of 60 seconds and a dissociation phase of 180 seconds. The integrity of the sensor surface for subsequent cycles was maintained through a regeneration process involving twice injections of 10 mM glycine-HCl (pH adjusted according to the specific experiment - pH 2.0 for antibody variants and cytokine-Fc fusions, pH 3.0 for Fc only variants) for 60 seconds each, followed by a 120-second injection of running buffer (HBS-EP+) at a flow rate of 30 µL/min. This ensured the complete removal of any bound molecules from the previous cycle and restoration of the sensor surface to its initial state, facilitating accurate and repeatable measurements across the experiments.

Antibody (Fc) Variants / Fc only variants / cytokine-Fc Fusion constructs Injections to captured TRIM21 PRYSPRY

In the initial step, a monovalent Streptavidin (mono-SA, in house, Roche) was immobilzed on a C1 sensor chip via standard amine coupling chemistry. The ligand was introduced at a

concentration of 10 μg/mL in 10 mM sodium acetate buffer (pH 4.5) at a flow rate of 10 μL/min for 180 seconds. Subsequently, biotinylated TRIM21 PRYSPRY in running buffer (HBS-EP+) was captured via mono-SA, aiming for a response unit (RU) signal of 3 to prevent any inter-molecular interactions interlinking two TRIM21 PRYSPRY by one antibody. Following this, five different concentrations of TRIM21 PRYSPRY, as specified in the sensorgrams, were prepared in a two-fold dilution series and introduced over the sensor chip. Each concentration underwent a 60-second association phase, followed by a 180-second dissociation phase to monitor the rate of complex decay. To restore the sensor surface for subsequent cycles, a regeneration step was performed after each cycle. This involved the injection of 10 mM glycine-HCl (pH 3.0) twice, each for 15 seconds, followed by a 30-second injection of running buffer (HBS-EP+) at a flow rate of 20 μL/min. This process ensured the complete removal of any bound molecules from the previous cycle and the restoration of the sensor surface to its initial state.

TRIM21-CC Injections to immobilized Antibody (Fc) Variants or cytokine-Fc Fusion constructs

First, CaptureSelect™ Human Fab-kappa Kinetics Biotin Conjugate ligand (7103302100, Thermo Fisher Scientific) to capture Antibody (Fc) Variants or anti-PGLALA F(ab')2 fragment (in-house, Roche) to capture cytokine-Fc Fusion constructs was immobilized. The ligands were introduced at a concentration of 5 μg/mL in 10 mM sodium acetate buffer (pH 4.5) at a flow rate of 5 μL/min for 120 seconds. Second, TRIM21-CC in running buffer (HBS-EP+) was captured via the ligand, aiming for a response unit (RU) signal of 8. Following this, several different concentrations of Trim2-CC, as specified in the sensorgrams, were prepared in a two-fold dilution series and introduced over the sensor chip. Each concentration was injected for 180-second association phase, followed by a 600-second dissociation phase. To restore the sensor surface for subsequent cycles, a regeneration step was performed after each cycle. This involved the injection of 10 mM glycine-HCl (pH 2.0) twice, each for 60 seconds, followed by a 120-second injection of running buffer (HBS-EP+) at a flow rate of 30 μL/min.

Mimicking an TRIM21-CC – antibody decorated viral complex

The formation of an immune complex on a sensor chip, consisting of TRIM21-CC, an antibody, and AAV2-wt as a viral model, was achieved using surface plasmon resonance (SPR) technology on a Biacore system. Initially, monovalent Streptavidin (mono-SA, in house, Roche) was immobilized on a C1 sensor chip (Flow cells 1-4) until saturation was reached. This was achieved by injecting mono-SA at a concentration of 10 μg/mL in 10 mM sodium acetate buffer (pH 4.5) at a flow rate of 5 μL/min for 120 seconds using standard amine coupling chemistry. The running buffer during this step was HBSN. Following a buffer change to HBS-EP, biotinylated TRIM21-CC was captured on flow cell 2 to

approximately 35 RU and on flow cell 3 to approximately 190 RU to generate different ligand densities. Flow cell 1 served as a reference surface. Subsequently, different anti-AAV2 capsid antibody constructs with TRIM21 relevant Fc mutations were injected at a concentration of 5 µg/mL at a flow rate of 20 µL/min for 180 seconds until TRIM21-CC was saturated. Following this, three different concentrations of AAV2-wt-empty, as specified in the sensorgrams, were prepared in a three-fold dilution series and introduced over the sensor chip. Each concentration underwent a 180-second association phase, followed by a 900-second dissociation phase at a flow rate of 10 µL/min. To restore the sensor surface for subsequent cycles, a regeneration step was performed after each cycle. This involved the injection of 10 mM glycine-HCl (pH 3.0) for 20 seconds, followed by a 30-second injection of running buffer (HBS-EP+) at a flow rate of 20 µL/min

1:1 Binding Model

In a simple 1:1 interaction, an analyte (A) binds to a ligand (B) to form a complex (AB). The equilibrium dissociation constant ($K_{D,AFFINITY}$) was calculated using the equation:

$$K_{D,AFFINITY} = \frac{k_{OFF}}{k_{ON}} \qquad \textit{Equation 1}$$

R_{max} (maximum response) is a parameter that represents the maximum binding capacity of the ligand immobilized on the sensor chip surface. It is determined by the amount of ligand immobilized and the stoichiometry of the interaction. R_{max} is measured in response units (RU). This equation assumes that all the immobilized ligand is active and capable of binding to the analyte. In practice, not all the immobilized ligand may be active, and the observed R_{max} may be less than the calculated Rmax.

$$R_{max}(RU) = \frac{R_{ligand} * MW_{analyte} * Valency_{ligand}}{MW_{ligand}} \qquad \textit{Equation 2}$$

$MW_{analyte}$ is the molecular weight of the analyte. MW_{ligand} is the molecular weight of the ligand. R_{ligand} is the immobilization level of the ligand, measured in RU. $Valency_{ligand}$ is the number of analyte molecules that bind to each ligand molecule.

$$R_{max,ratio}(\%) = \frac{R_{max,experimentell}}{R_{max,theory}} \qquad \textit{Equation 3}$$

The $R_{max,ratio}$, calculated as provides a measure of the proportion of active ligand and thereby the Stoichiometry.

Complex Binding Kinetics – Two State Reaction

The rationale behind the Two State Model lies in its ability to account for the additional kinetic steps that occur during the binding process. In contrast to a 1:1 binding model, in some interactions, the formation of the initial complex induces a conformational change, leading to a different, usually more stable, complex (AB*). This can be represented as follows:

$$A + B \leftrightarrow AB \leftrightarrow AB^* \qquad \textit{Equation 4}$$

In this model, the analyte first associates with the ligand with an association rate constant (k_{ON1}), forming an initial complex (AB). This complex then undergoes a conformational change with a rate constant (k_{ON2}) to form the final complex (AB*). Each of these steps is reversible, with the initial complex dissociating back to the free analyte and ligand with a rate constant (k_{OFF1}), and the final complex reverting back to the initial complex with a rate constant (k_{OFF2}).

The apparent or avidity equilibrium dissociation constant (K_D) reflects the overall stability of the final AB* complex and is calculated using the formula:

$$K_{D,AVIDITY} = \frac{k_{OFF1}}{k_{ON1}} * \left(\frac{k_{OFF2}}{(k_{OFF2} + k_{ON2})}\right) \qquad \textit{Equation 5}$$

Mass Photometry Technology

The mass photometry experiments were conducted using the OneMP system, TwoMP system and OneMP-MassFluidix HC system to analyze low-affinity interactions (Refeyn Ltd., Oxford, UK) at room temperature. The sample buffer used for all experiments was 1x PBS, pH 7.4 (Roche Diagnostics GmbH). The sample carrier slides (Refeyn Ltd., Oxford, UK) were prepared by cleaning them in an isopropanol ultrasonic bath for 10 minutes, followed by consecutive rinsing with H_2O. The slides were then dried under a stream of clean nitrogen. A fourteen well, each well 3 mm in diameter, sample well gasket (Refeyn Ltd., Oxford, UK) providing four measurement spots, each capable of holding a volume of 20µL sample solution, was placed onto the carrier slide. The molecules of interest, TRIM21 PRYSPRY or TRIM21-CC with antibody Fc variants, were prepared in the sample buffer at various concentrations, specifically four times higher than in the final droplet (for final concentrations and ratios, see histograms). The samples were thoroughly mixed and incubated at room temperature for 10 minutes to allow for complex formation. Approximately 5 µL of the sample was placed on a clean glass coverslip, containing 15µL of PBS, and loaded into the mass photometry system. The system was set to acquire data using the AquireMP 2.5 software (Refeyn Ltd.) for a period of 1 minute at a 1 kHz frame rate. The mass photometry data were then analyzed using the DiscoverMP 2.5.0 software (Refeyn Ltd.) and GraphPad Prism (Version 8.4.2, GraphPad Software, Inc., CA, USA)) applying a Gaussian distribution model. The acquisition parameters were set according to the

manufacturer's instructions and optimized for the specific molecules of interest using the following parameters: number of averaged frames: 5, threshold 1: 1.5, and threshold 2: 0.25. The mass of the individual molecules and their complexes were determined from the intensity of the light scattered by the molecules. Results were reported as normalized counts, calculated by dividing events in each bin by the total number of events. To ensure the reliability of the data, a control experiment was performed with each molecule alone to confirm their individual masses (5 nM concentration in the final droplet). A mass calibration curve was generated by analyzing three different proteins with known molecular masses of approximately 66 kDa, 145.5 kDa, and 194 kDa, respectively (Roche Diagnostics GmbH). The calibration data was collected from the 2.9 μm × 10.8 μm instrument field of view for 100 seconds.

Electron Microscopy Experiments

Samples were diluted in D-PBS (Gibco Life Technologies) until a suitable concentration was reached for negative staining EM. Interaction mixtures (Figure 6) were mixed and incubated at RT for 1h prior to dilution and imaging. Recombinant AAVv-2-antibody interactions (Figure 8) were incubated for 30 minutes except for bivalent A20 Fc WT, which caused full precipitation at 30 minutes and was incubated for 5 minutes only. Images that additionally contain TRIM21-CC were incubated for 12 minutes with antibody variants, followed by 18 minutes of incubation with TRIM21-CC. Since bivalent A20 Fc WT alone was sufficient to fully precipitate rAAVv-2s, it was not possible to observe an additional effect of TRIM21-CC.Electron microscopy grids (T600H-Cu 698 l/inch Hex. mesh Thin Bar; EMS) were coated with a home-made ~2nm carbon film by floating the carbon on H2O and letting the water level drop till the carbon covered the grids. After at least 2 days of drying the grids were used. Four ul of sample was incubated on a glow-discharged carbon coated grid for 30 seconds, followed by two steps of washing with H2O, a step of washing with UAc (2%) solution and incubation with UAc for 30s. As an internal standard and to improve the quality of the negative stain, 2ul of tobacco mosaic virus in solution was incubated for 10 seconds on the grid to each sample that did not include AAVs. This step was added after the 2 rounds of washing with H2O and followed by 2 extra H2O washing steps (TMV; kindly supplied by Ruben Diaz-Avalos, New York Structural Biology Center, USA).

Grids were loaded into a Jeol JEM-1400 Plus transmission electron microscope operating a Lab6 electron source at 120 kV. Electron micrographs were recorded on TVIPS XF416 4000 by 4000 pixel charge-coupled device camera (Tietz Video and Image Processing System, Gauting, Germany) at a nominal magnification of 100,000x yielding pictures with a pixel size corresponding to 0.1149 nm at the specimen level. Images were gaussian blurred 4x in ImageJ (75) before being imported into the EMAN2 software (76). Reference-free alignment was performed on manually selected particles followed by classifications by multivariate statistical analysis.

Model Predictions

Structural model predictions were generated using AlphaFold2 with standard settings (63). To generate the multimeric Fc bound model, two copies of the TRIM21 sequence (full and truncated) were entered as separate molecules and the Fc light and heavy chain were fused into one molecule by adding a long GGGS linker between light and heavy chain. Results were visualized with ChimeraX (77, 78).

Author Contributions

Each author has contributed significantly to the conceptualization, development, and finalization of this work, approving its readiness for publication.

Conflict of Interest Statement

The authors declare that there are no commercial or financial relationships that could be interpreted as a potential conflict of interest in relation to this research. CK declares employment, patents and stock ownership with Roche.

Acknowledgements

We would like to acknowledge Matthias Lauer and Lubomir Kovacik for their contributions to the Nautilus at Roche Basel, the EM facility where the electron microscopy data was recorded. We highly appreciate Holger Kley, Roche Penzberg, providing SEC-MALS data for TRIM21.

Literature

1. Rajsbaum R, García-Sastre A, Versteeg GA. Trimmunity: The Roles of the Trim E3-Ubiquitin Ligase Family in Innate Antiviral Immunity. *J Mol Biol* (2014) 426(6):1265-84. doi: 10.1016/j.jmb.2013.12.005.

2. Foss S, Bottermann M, Jonsson A, Sandlie I, James LC, Andersen JT. Trim21—from Intracellular Immunity to Therapy. *Front Immunol* (2019) 10:2049. doi: 10.3389/fimmu.2019.02049.

3. McEwan WA, James LC. Trim21-Dependent Intracellular Antibody Neutralization of Virus Infection. *Prog Mol Biol Transl* (2015) 129:167-87. doi: 10.1016/bs.pmbts.2014.10.006.

4. Watkinson RE, McEwan WA, James LC. Intracellular Antibody Immunity. *J Clin Immunol* (2014) 34(Suppl 1):30-4. doi: 10.1007/s10875-014-0017-4.

5. Watkinson RE, Tam JCH, Vaysburd MJ, James LC. Simultaneous Neutralization and Innate Immune Detection of a Replicating Virus by Trim21. *J Virol* (2013) 87(13):7309-13. doi: 10.1128/jvi.00647-13.

6. Boudinot P, Aa LMvd, Jouneau L, Pasquier LD, Pontarotti P, Briolat V, et al. Origin and Evolution of Trim Proteins: New Insights from the Complete Trim Repertoire of Zebrafish and Pufferfish. *PLoS ONE* (2011) 6(7):e22022. doi: 10.1371/journal.pone.0022022.

7. Randow F, MacMicking JD, James LC. Cellular Self-Defense: How Cell-Autonomous Immunity Protects against Pathogens. *Science* (2013) 340(6133):701-6. doi: 10.1126/science.1233028.

8. Rhodes DA, Isenberg DA. Trim21 and the Function of Antibodies inside Cells. *Trends Immunol* (2017) 38(12):916-26. doi: 10.1016/j.it.2017.07.005.

9. Mallery DL, McEwan WA, Bidgood SR, Towers GJ, Johnson CM, James LC. Antibodies Mediate Intracellular Immunity through Tripartite Motif-Containing 21 (Trim21). *Proc National Acad Sci* (2010) 107(46):19985-90. doi: 10.1073/pnas.1014074107.

10. Foss S, Watkinson RE, Grevys A, McAdam MB, Bern M, Høydahl LS, et al. Trim21 Immune Signaling Is More Sensitive to Antibody Affinity Than Its Neutralization Activity. *J Immunol* (2016) 196(8):3452-9. doi: 10.4049/jimmunol.1502601.

11. McEwan WA, Tam JCH, Watkinson RE, Bidgood SR, Mallery DL, James LC. Intracellular Antibody-Bound Pathogens Stimulate Immune Signaling Via the Fc Receptor Trim21. *Nat Immunol* (2013) 14(4):327. doi: 10.1038/ni.2548.

12. Ozato K, Shin DM, Chang TH, Morse HC, 3rd. Trim Family Proteins and Their Emerging Roles in Innate Immunity. *Nat Rev Immunol* (2008) 8(11):849-60. Epub 2008/10/07. doi: 10.1038/nri2413.

13. Meroni G, Diez- Roux G. Trim/Rbcc, a Novel Class of 'Single Protein Ring Finger' E3 Ubiquitin Ligases. *BioEssays* (2005) 27(11):1147-57. doi: 10.1002/bies.20304.

14. Reymond A, Meroni G, Fantozzi A, Merla G, Cairo S, Luzi L, et al. The Tripartite Motif Family Identifies Cell Compartments. *Embo J* (2001) 20(9):2140-51. doi: 10.1093/emboj/20.9.2140.

15. Wang H-T, Hur S. Substrate Recognition by Trim and Trim-Like Proteins in Innate Immunity. *Semin Cell Dev Biol* (2021) 111:76-85. doi: 10.1016/j.semcdb.2020.09.013.

16. Fletcher AJ, Mallery DL, Watkinson RE, Dickson CF, James LC. Sequential Ubiquitination and Deubiquitination Enzymes Synchronize the Dual Sensor and Effector Functions of Trim21. *Proc National Acad Sci* (2015) 112(32):10014-9. doi: 10.1073/pnas.1507534112.

17. Glickman MH, Ciechanover A. The Ubiquitin-Proteasome Proteolytic Pathway: Destruction for the Sake of Construction. *Physiol Rev* (2002) 82(2):373-428. doi: 10.1152/physrev.00027.2001.

18. Hershko A, Ciechanover A. The Ubiquitin System. *Annu Rev Biochem* (1998) 67(1):425-79. doi: 10.1146/annurev.biochem.67.1.425.

19. Dickson C, Fletcher AJ, Vaysburd M, Yang J-C, Mallery DL, Zeng J, et al. Intracellular Antibody Signalling Is Regulated by Phosphorylation of the Fc Receptor Trim21. *Elife* (2018) 7:e32660. doi: 10.7554/elife.32660.

20. Kiss L, Clift D, Renner N, Neuhaus D, James LC. Ring Domains Act as Both Substrate and Enzyme in a Catalytic Arrangement to Drive Self-Anchored Ubiquitination. *Nat Commun* (2021) 12(1):1220. doi: 10.1038/s41467-021-21443-6.

21. Kiss L, Zeng J, Dickson CF, Mallery DL, Yang J-C, McLaughlin SH, et al. A Tri-Ionic Anchor Mechanism Drives Ube2n-Specific Recruitment and K63-Chain Ubiquitination in Trim Ligases. *Nat Commun* (2019) 10(1):4502. doi: 10.1038/s41467-019-12388-y.

22. Keeble AH, Khan Z, Forster A, James LC. Trim21 Is an Igg Receptor That Is Structurally, Thermodynamically, and Kinetically Conserved. *Proc National Acad Sci* (2008) 105(16):6045-50. doi: 10.1073/pnas.0800159105.

23. Bidgood SR, Tam JCH, McEwan WA, Mallery DL, James LC. Translocalized Iga Mediates Neutralization and Stimulates Innate Immunity inside Infected Cells. *Proc National Acad Sci* (2014) 111(37):13463-8. doi: 10.1073/pnas.1410980111.

24. James LC, Keeble AH, Khan Z, Rhodes DA, Trowsdale J. Structural Basis for Pryspry-Mediated Tripartite Motif (Trim) Protein Function. *Proc National Acad Sci* (2007) 104(15):6200-5. doi: 10.1073/pnas.0609174104.

25. James LC. Intracellular Antibody Immunity and the Cytosolic Fc Receptor Trim21. *Curr Top Microbiol Immunol* (2014) 382:51-66. Epub 2014/08/15. doi: 10.1007/978-3-319-07911-0_3.

26. Burmeister WP, Gastinel LN, Simister NE, Blum ML, Bjorkman PJ. Crystal Structure at 2.2 a Resolution of the Mhc-Related Neonatal Fc Receptor. *Nature* (1994) 372(6504):336-43. Epub 1994/11/24. doi: 10.1038/372336a0.

27. Oganesyan V, Damschroder MM, Cook KE, Li Q, Gao C, Wu H, et al. Structural Insights into Neonatal Fc Receptor-Based Recycling Mechanisms. *J Biol Chem* (2014) 289(11):7812-24. Epub 2014/01/29. doi: 10.1074/jbc.M113.537563.

28. Vaughn DE, Bjorkman PJ. Structural Basis of Ph-Dependent Antibody Binding by the Neonatal Fc Receptor. *Structure* (1998) 6(1):63-73. Epub 1998/03/11. doi: 10.1016/s0969-2126(98)00008-2.

29. Bottermann M, James LC. Intracellular Antiviral Immunity. *Adv Virus Res* (2018) 100(Antioxid. Redox Signal. 22 2015):309-54. doi: 10.1016/bs.aivir.2018.01.002.

30. Ng PML, Kaliaperumal N, Lee CY, Chin WJ, Tan HC, Au VB, et al. Enhancing Antigen Cross-Presentation in Human Monocyte-Derived Dendritic Cells by Recruiting the Intracellular Fc Receptor Trim21. *J Immunol* (2019) 202(8):2307-19. doi: 10.4049/jimmunol.1800462.

31. Dall'Acqua WF, Kiener PA, Wu H. Properties of Human Igg1s Engineered for Enhanced Binding to the Neonatal Fc Receptor (Fcrn). *J Biol Chem* (2006) 281(33):23514-24. Epub 2006/06/24. doi: 10.1074/jbc.M604292200.

32. Booth BJ, Ramakrishnan B, Narayan K, Wollacott AM, Babcock GJ, Shriver Z, et al. Extending Human Igg Half-Life Using Structure-Guided Design. *MAbs* (2018) 10(7):1098-110. Epub 2018/06/28. doi: 10.1080/19420862.2018.1490119.

33. Mackness BC, Jaworski JA, Boudanova E, Park A, Valente D, Mauriac C, et al. Antibody Fc Engineering for Enhanced Neonatal Fc Receptor Binding and Prolonged Circulation Half-Life. *MAbs* (2019) 11(7):1276-88. Epub 2019/06/21. doi: 10.1080/19420862.2019.1633883.

34. Liu R, Oldham RJ, Teal E, Beers SA, Cragg MS. Fc-Engineering for Modulated Effector Functions-Improving Antibodies for Cancer Treatment. *Antibodies* (2020) 9(4):64. Epub 2020/11/21. doi: 10.3390/antib9040064.

35. Qi T, Cao Y. In Translation: Fcrn across the Therapeutic Spectrum. *Int J Mol Sci* (2021) 22(6). Epub 2021/04/04. doi: 10.3390/ijms22063048.

36. MOESSNER Ekkehard, Tilman S, inventors; F HOFFMANN-LA ROCHE AG (HOFF-C), assignee. Immunoglobulin G Class Fragment Crystallizable (Fc)-Region Used for Treatment of Ocular Vascular Diseases, Comprises First Variant Fc-Region Polypeptide and Second Variant Fc-Region Polypeptide; Fc-Region Variants with Modified Fcrn-Binding and Methods of Use patent WO2016071376A2 (2015).

37. SCHLOTHAUER T, A S, inventors; HOFFMANN LA ROCHE & CO AG F (HOFF-C) assignee. New Polypeptide Used in Pharmaceutical Formulation for E.G. Treating Vascular Eye Diseases, and Transporting Soluble Receptor Ligand from Eye over Blood-Ocular-Barrier into Blood Circulation; Fc-Region Variants with Modified Fcrn- and Maintained Protein a-Binding Properties patent WO2015107026A1 (2015).

38. Joerg Thomas Regula WS, Tilman Schlothauer, inventor; F HOFFMANN-LA ROCHE assignee. New Immunoglobulin G (Igg) Class Fragment Crystallizable (Fc)-Region Useful in Antibody for Preparing Medicine Used for Treating Ocular Vascular Diseases, Comprises First and Second Variant Fc-Region Polypeptides; Fc-Receptor Binding Modified Asymmetric Antibodies and Methods of Use patent WO2014177459A2 (2014).

39. T S, inventor; HOFFMANN LA ROCHE, assignee. Fc-Region Variants with Improved Protein a-Binding; New Polypeptide Comprising First and Second Polypeptides Each Comprising Immunoglobulin (Ig) Hinge Region Comprising Cysteine Residue, Ig Constant Heavy Chain (Ch) 2 Domain and Ig Ch3-Domain, Used to Treat Vascular Eye Diseases patent WO2015107015A1 (2015).

40. Schoch A, Kettenberger H, Mundigl O, Winter G, Engert J, Heinrich J, et al. Charge-Mediated Influence of the Antibody Variable Domain on Fcrn-Dependent Pharmacokinetics. *Proc Natl Acad Sci U S A* (2015) 112(19):5997-6002. Epub 2015/04/29. doi: 10.1073/pnas.1408766112.

41. Wang W, Lu P, Fang Y, Hamuro L, Pittman T, Carr B, et al. Monoclonal Antibodies with Identical Fc Sequences Can Bind to Fcrn Differentially with Pharmacokinetic Consequences. *Drug Metab Dispos* (2011) 39(9):1469-77. Epub 2011/05/26. doi: 10.1124/dmd.111.039453.

42. Bottermann M, Lode HE, Watkinson RE, Foss S, Sandlie I, Andersen JT, et al. Antibody-Antigen Kinetics Constrain Intracellular Humoral Immunity. *Sci Rep-uk* (2016) 6(1):37457. doi: 10.1038/srep37457.

43. McEwan WA, Hauler F, Williams CR, Bidgood SR, Mallery DL, Crowther RA, et al. Regulation of Virus Neutralization and the Persistent Fraction by Trim21. *J Virol* (2012) 86(16):8482-91. doi: 10.1128/jvi.00728-12.

44. Caddy SL, Vaysburd M, Wing M, Foss S, Andersen JT, O'Connell K, et al. Intracellular Neutralisation of Rotavirus by Vp6-Specific Igg. *Plos Pathog* (2020) 16(8):e1008732. doi: 10.1371/journal.ppat.1008732.

45. Manocha GD, Mishra R, Sharma N, Kumawat KL, Basu A, Singh SK. Regulatory Role of Trim21 in the Type-I Interferon Pathway in Japanese Encephalitis Virus-Infected Human Microglial Cells. *J Neuroinflammation* (2014) 11:24. Epub 2014/02/04. doi: 10.1186/1742-2094-11-24.

46. Mu T, Zhao X, Zhu Y, Fan H, Tang H. The E3 Ubiquitin Ligase Trim21 Promotes Hbv DNA Polymerase Degradation. *Viruses* (2020) 12(3). Epub 2020/04/05. doi: 10.3390/v12030346.

47. Rakebrandt N, Lentes S, Neumann H, James LC, Neumann- Staubitz P. Antibody- and Trim21- Dependent Intracellular Restriction of Salmonella Enterica. *Pathog Dis* (2014) 72(2):131-7. doi: 10.1111/2049-632x.12192.

48. Vaysburd M, Watkinson RE, Cooper H, Reed M, O'Connell K, Smith J, et al. Intracellular Antibody Receptor Trim21 Prevents Fatal Viral Infection. *Proc National Acad Sci* (2013) 110(30):12397-401. doi: 10.1073/pnas.1301918110.

49. Wei Y, Zeng S, Zou C, Zhang H, Peng O, Xue C, et al. Porcine Trim21 Ring-Finger E3 Ubiquitin Ligase Is Essential for Anti-Prrsv Activity. *Vet Microbiol* (2021) 256:109043. Epub 2021/03/30. doi: 10.1016/j.vetmic.2021.109043.

50. Li X, Yang L, Chen S, Zheng J, Zhang H, Ren L. Multiple Roles of Trim21 in Virus Infection. *Int J Mol Sci* (2023) 24(2). Epub 2023/01/22. doi: 10.3390/ijms24021683.

51. Zeng J, Santos AF, Mukadam AS, Osswald M, Jacques DA, Dickson CF, et al. Target-Induced Clustering Activates Trim-Away of Pathogens and Proteins. *Nat Struct Mol Biol* (2021):1-12. doi: 10.1038/s41594-021-00560-2.

52. Fiorentini F, Esposito D, Rittinger K. Does It Take Two to Tango? Ring Domain Self-Association and Activity in Trim E3 Ubiquitin Ligases. *Biochem Soc Trans* (2020) 48(6):2615-24. doi: 10.1042/bst20200383.

53. Jensen PF, Larraillet V, Schlothauer T, Kettenberger H, Hilger M, Rand KD. Investigating the Interaction between the Neonatal Fc Receptor and Monoclonal Antibody Variants by Hydrogen/Deuterium Exchange Mass Spectrometry. *Mol Cell Proteomics* (2015) 14(1):148-61. Epub 2014/11/08. doi: 10.1074/mcp.M114.042044.

54. Piche-Nicholas NM, Avery LB, King AC, Kavosi M, Wang M, O'Hara DM, et al. Changes in Complementarity-Determining Regions Significantly Alter Igg Binding to the Neonatal Fc Receptor (Fcrn) and Pharmacokinetics. *MAbs* (2018) 10(1):81-94. Epub 2017/10/11. doi: 10.1080/19420862.2017.1389355.

55. Schlothauer T, Rueger P, Stracke JO, Hertenberger H, Fingas F, Kling L, et al. Analytical Fcrn Affinity Chromatography for Functional Characterization of Monoclonal Antibodies. *MAbs* (2013) 5(4):576-86. Epub 2013/06/15. doi: 10.4161/mabs.24981.

56. Grevys A, Frick R, Mester S, Flem-Karlsen K, Nilsen J, Foss S, et al. Antibody Variable Sequences Have a Pronounced Effect on Cellular Transport and Plasma Half-Life. *iScience* (2022) 25(2):103746. Epub 2022/02/05. doi: 10.1016/j.isci.2022.103746.

57. McCraw DM, O'Donnell JK, Taylor KA, Stagg SM, Chapman MS. Structure of Adeno-Associated Virus-2 in Complex with Neutralizing Monoclonal Antibody A20. *Virology* (2012) 431(1-2):40-9. Epub 2012/06/12. doi: 10.1016/j.virol.2012.05.004.

58. Foss S, Watkinson R, Sandlie I, James LC, Andersen JT. Trim21: A Cytosolic Fc Receptor with Broad Antibody Isotype Specificity. *Immunol Rev* (2015) 268(1):328-39. doi: 10.1111/imr.12363.

59. Burvenich IJ, Lee FT, O'Keefe GJ, Makris D, Cao D, Gong S, et al. Engineering Anti-Lewis-Y Hu3s193 Antibodies with Improved Therapeutic Ratio for Radioimmunotherapy of Epithelial Cancers. *EJNMMI Res* (2016) 6(1):26. Epub 2016/03/18. doi: 10.1186/s13550-016-0180-0.

60. Fletcher AJ, James LC. Coordinated Neutralization and Immune Activation by the Cytosolic Antibody Receptor Trim21. *J Virol* (2016) 90(10):4856-9. Epub 2016/03/05. doi: 10.1128/JVI.00050-16.

61. Sanchez JG, Chiang JJ, Sparrer KMJ, Alam SL, Chi M, Roganowicz MD, et al. Mechanism of Trim25 Catalytic Activation in the Antiviral Rig-I Pathway. *Cell Rep* (2016) 16(5):1315-25. Epub 2016/07/19. doi: 10.1016/j.celrep.2016.06.070.

62. Sanchez JG, Okreglicka K, Chandrasekaran V, Welker JM, Sundquist WI, Pornillos O. The Tripartite Motif Coiled-Coil Is an Elongated Antiparallel Hairpin Dimer. *Proc Natl Acad Sci U S A* (2014) 111(7):2494-9. Epub 2014/02/20. doi: 10.1073/pnas.1318962111.

63. Jumper J, Evans R, Pritzel A, Green T, Figurnov M, Ronneberger O, et al. Highly Accurate Protein Structure Prediction with Alphafold. *Nature* (2021) 596(7873):583-9. Epub 2021/07/16. doi: 10.1038/s41586-021-03819-2.

64. Moskalenko M, Chen L, van Roey M, Donahue BA, Snyder RO, McArthur JG, et al. Epitope Mapping of Human Anti-Adeno-Associated Virus Type 2 Neutralizing Antibodies:

Implications for Gene Therapy and Virus Structure. *J Virol* (2000) 74(4):1761-6. Epub 2000/01/22. doi: 10.1128/jvi.74.4.1761-1766.2000.

65. Wobus CE, Hugle-Dorr B, Girod A, Petersen G, Hallek M, Kleinschmidt JA. Monoclonal Antibodies against the Adeno-Associated Virus Type 2 (Aav-2) Capsid: Epitope Mapping and Identification of Capsid Domains Involved in Aav-2-Cell Interaction and Neutralization of Aav-2 Infection. *J Virol* (2000) 74(19):9281-93. Epub 2000/09/12. doi: 10.1128/jvi.74.19.9281-9293.2000.

66. Summerford C, Samulski RJ. Membrane-Associated Heparan Sulfate Proteoglycan Is a Receptor for Adeno-Associated Virus Type 2 Virions. *J Virol* (1998) 72(2):1438-45. Epub 1998/01/28. doi: 10.1128/JVI.72.2.1438-1445.1998.

67. Fitzpatrick Z, Leborgne C, Barbon E, Masat E, Ronzitti G, van Wittenberghe L, et al. Influence of Pre-Existing Anti-Capsid Neutralizing and Binding Antibodies on Aav Vector Transduction. *Mol Ther Methods Clin Dev* (2018) 9:119-29. Epub 2018/05/17. doi: 10.1016/j.omtm.2018.02.003.

68. Xiao PJ, Samulski RJ. Cytoplasmic Trafficking, Endosomal Escape, and Perinuclear Accumulation of Adeno-Associated Virus Type 2 Particles Are Facilitated by Microtubule Network. *J Virol* (2012) 86(19):10462-73. Epub 2012/07/20. doi: 10.1128/JVI.00935-12.

69. Varghese R, Mikyas Y, Stewart PL, Ralston R. Postentry Neutralization of Adenovirus Type 5 by an Antihexon Antibody. *J Virol* (2004) 78(22):12320-32. Epub 2004/10/28. doi: 10.1128/JVI.78.22.12320-12332.2004.

70. Wohlfart CE, Svensson UK, Everitt E. Interaction between Hela Cells and Adenovirus Type 2 Virions Neutralized by Different Antisera. *J Virol* (1985) 56(3):896-903. Epub 1985/12/01. doi: 10.1128/JVI.56.3.896-903.1985.

71. Ridgway JB, Presta LG, Carter P. 'Knobs-into-Holes' Engineering of Antibody Ch3 Domains for Heavy Chain Heterodimerization. *Protein Eng* (1996) 9(7):617-21. Epub 1996/07/01. doi: 10.1093/protein/9.7.617.

72. Spiess C, Zhai Q, Carter PJ. Alternative Molecular Formats and Therapeutic Applications for Bispecific Antibodies. *Mol Immunol* (2015) 67(2 Pt A):95-106. Epub 2015/02/01. doi: 10.1016/j.molimm.2015.01.003.

73. Vaks L, Litvak-Greenfeld D, Dror S, Shefet-Carasso L, Matatov G, Nahary L, et al. Design Principles for Bispecific Iggs, Opportunities and Pitfalls of Artificial Disulfide Bonds. *Antibodies* (2018) 7(3). Epub 2018/07/28. doi: 10.3390/antib7030027.

74. Wessels U, Schick E, Ritter M, Kowalewsky F, Heinrich J, Stubenrauch K. Novel Drug and Soluble Target Tolerant Antidrug Antibody Assay for Therapeutic Antibodies Bearing the P329g Mutation. *Bioanalysis* (2017) 9(11):849-59. Epub 2017/05/19. doi: 10.4155/bio-2017-0048.

75. Schneider CA, Rasband WS, Eliceiri KW. Nih Image to Imagej: 25 Years of Image Analysis. *Nat Methods* (2012) 9(7):671-5. Epub 2012/08/30. doi: 10.1038/nmeth.2089.

76. Tang G, Peng L, Baldwin PR, Mann DS, Jiang W, Rees I, et al. Eman2: An Extensible Image Processing Suite for Electron Microscopy. *J Struct Biol* (2007) 157(1):38-46. Epub 2006/07/25. doi: 10.1016/j.jsb.2006.05.009.

77. Goddard TD, Huang CC, Meng EC, Pettersen EF, Couch GS, Morris JH, et al. Ucsf Chimerax: Meeting Modern Challenges in Visualization and Analysis. *Protein Sci* (2018) 27(1):14-25. Epub 2017/07/16. doi: 10.1002/pro.3235.

78. Pettersen EF, Goddard TD, Huang CC, Meng EC, Couch GS, Croll TI, et al. Ucsf Chimerax: Structure Visualization for Researchers, Educators, and Developers. *Protein Sci* (2021) 30(1):70-82. Epub 2020/09/04. doi: 10.1002/pro.3943.

Figures

Figure 1. SPR assay orientations to characterize the interaction between TRIM21 and an antibody. Symmetrical and asymmetrical antibody Fc variants are investigated. In case of an asymmetrical Fc part, one Fc heavy chain contains a AAA mutation (schematically shown by red star), that completely abolishes TRIM21 binding. The used Fc variants and assay setups allow determining how Fc mutations influence the avidity-binding mode and dissecting avidity from affinity. (**A**) Antibody Fc variants are captured on the biosensor surface via an anti-Fab nanobody (vhh), Fc-only variants are coupled using standard amine coupling chemistry and cytokine Fc-Fusions are captured via anti-PGLALA F(ab')2 fragment (74), while TRIM21 PRYSPRY domain is the analyte in solution (see Materials and Methods). Configuration (**B**) schematically shows the inverse to (**A**) while the PRYSPRY domain is captured via monovalent streptavidin. (**C**) To analyze the dimeric TRIM21 engagement of both IgG heavy chains, the antibody is captured via its Fab fragment, cytokine Fc-Fusions are captured via anti-PGLALA F(ab')2 fragment (identical capture setup as in (A) and TRIM21-coiled-coil (TRIM21-CC) is injected. Illustrations are created with BioRender.com.

Figure 2. Interaction analysis of human IgG1 (mAb1) Fc variants and TRIM21 PRYSPRY domain. (**A-C**) showing sensorgrams (SPR data) where PRYSPRY was injected in five different concentrations as two-fold dilution series to immobilized mAb1 Fc variants (capture level approx. 60 RU). Each plot shows the measured raw data (colored gradient) and the global fit analysis as solid black lines. For immobilized mAb1 WT (**A**) and mAb1 WT-AAA (**B**) PRYSPRY was injected at 500 nM highest concentration and for mAb1 AAA (**C**) at 2000 nM. The sensorgrams show the affinity binding mode applying a mono-exponential fit model (Langmuir 1:1). The determined kinetic parameters are described in (**D**). The k_{ON}, k_{OFF} and K_D values are results from a global fit analysis ± fitting error. (**E-F**) show the complementary mass photometry (MP) data displaying a 2:1 binding stoichiometry confirming the SPR data. For the PRYSPRY - mAb1 WT complex, the data reveals a double bound state and for mAb1 WT-AAA a single bound state, while the control mAb1 AAA

shows no binding at all. A Gaussian distribution model was used to analyze the MP data. For individual masses of the molecules, see **SI Info Figure S 1.**

Editable, Part of Figure 2, Figure 2D

Sample	k_{ON} ($x10^6$ $M^{-1}s^{-1}$)	k_{OFF} ($x10^{-2}$ s^{-1})	K_D (nM)	$t_{1/2}$ (s)	$Valency_{ligand}$	$R_{max,Ratio}$ (%)
mAb1 WT	2.33 ± 0.01	9.94 ± 0.02	42.7 ± 0.1	7.0	2	97
mAb1 WT-AAA	2.66 ± 0.01	10.5 ± 0.08	39.5 ± 0.5	6.6	1	95
mAb1 AAA	NA	NA	NA	NA	NA	NA

Editable, Part of Figure 2, Figure 2F

Sample	$Mass_{theo.}$ (kDa)	$Mass_{exp.}$ (kDa)	Gaussian Fit (%)
mAb1 WT + PRYSPRY	196	193 ± 30	96
mAb1 WT-AAA + PRYSPRY	171	172 ± 35	100
mAb1 AAA + PRYSPRY	146	138 ± 22	100
mAb1 AAA only	146	143 ± 24	100

Figure 3. Kinetic characterization of TRIM21 PRYSPRY binding to immobilized antibody Fc variants and cytokine-Fc Fusion constructs, and Fc only variant (**Raw data SI Info Figure S 2**). Detailed SPR assay setup is described in materials and methods. (**A**) The Affinity Rate Scale Plot enables the kinetic comparison of several binding experiments at one glance. The association rate (k_{ON}) and corresponding dissociation rate (k_{OFF}) are juxtaposed in opposition, connected via a vertical line, representing the binding strength (affinity). The further apart both parameters (k_{ON} and k_{OFF}) the stronger the interaction is. Compared to mAb1 Fc WT, the Fc variants YTE (M252Y, S254T, T256E), HH (T307H, N434H) and Y436A show decreased PRYSPRY affinity. The YTE affinity is 1.7-fold, HH 2.4-fold and Y436A 180-fold decreased. As shown in (**B**) the altered binding strength is mostly off rate driven, which becomes apparent in the overlay of normalized dissociation. The start of dissociation is normalized to 100 %.

Figure 4. Affinity rate scale plot for captured TRIM21 PRYSPRY domain (ligand) and antibody (human IgG1) variable domain variants or antigen fusion constructs in solution (analyte). The injected constructs have different Fab regions but share the same Fc region. This allows the investigation of a potential Fab contribution to the PRYSPRY binding. All constructs were analyzed by applying a simple 1:1 Langmuir fit. The analyzed antibody variants do not show any Fab contribution. Notably, there is a faster on-rate (2x) for all constructs when compared to the reverse assay setup up (PRYSPRY as analyte). Raw data is shown in **SI Info Figure S 3**.

Figure 5. Characterization of the TRIM21 dimeric nature (TRIM21-CC) applying different technologies. (**A**) SEC-MALS data reveals 94 % TRIM21-CC dimer (90 kDa). (**B**) Mass photometry technology shows 99% TRIM21-CC with 82 kDa. (**C**) Selection of EM 2D classes confirming TRIM21-CC dimers. The coiled coil domains facilitate dimerization whereas the C-terminal PRYSPRY domains are placed at the opposite end of each coiled-coil domain.

Figure 6 Characterizing the interaction of TRIM21-CC with three different Antibody Fc variants. (A-D) Applying MP, dashed lines indicate the main peak of the respective species. (A) MP of TRIM21-CC with mAb 1 WT, (B) MP of TRIM21-CC with mAb 1 WT-AAA (C) MP of TRIM21-CC with mAb 1 AAA. Only mAb 1 WT shows binding to TRIM21-CC at low nM concentration in accordance with its low nM binding strength. (D) The amount (%) of TRIM21-CC-mAb1 WT complex increases with excess of TRIM21-CC, while TRIM21-CC mAb1 WT-AAA shows a minor complexed species for the applied concentrations. (E-H) selected 2D averages of EM data, resolving TRIM21-CC with Fc WT (E), TRIM21-CC with Fc WT-AAA (F), TRIM21-CC with mAb1 WT (G) and mAb1 WT alone (H).

Editable, Part of Figure 6, Figure 6D

Molar Ratios TRIM21-CC:mAb1 Fc variant			
$Mass_{theo.}$ (kDa)	86	146	232
TRIM21-CC:mAb1 WT	T21 (%)	mAb1 (%)	T21-mAb1 (%)
1:3	3	92	1.4
1:1	10	78	7
3:1	32	51	15
10:1	63	9	24
TRIM21-CC:mAb1 WT-AAA			
1:3	6	90	NA
1:1	17	80	1.8
3:1	33	64	2.0
10:1	66	34	1.6
TRIM21-CC:mAb1 AAA			
1:3	4	94	NA
1:1	18	80	NA
10:1	66	33	NA

Figure 7. Characterization of TRIM21-CC with Antibody Fc variants. (A) shows the sensorgram (SPR) of mAb1 WT (ligand, approx. 8-10 RU) and TRIM21-CC (analyte) where TRIM21-CC was injected in seven different concentration, each for 180 sec as two-fold dilution series with 100 nM as highest concentration. Applied fit model is a simple 1:1 interaction reflecting 100% avid bound, 1:1 antibody - TRIM21-CC species. (B) Variation in association time (10 -300 sec) injecting a constant concentration of 25 nM TRIM21-CC to captured mAb1 WT reveals a biphasic binding kinetic, which can be described by applying a

two state model providing fast and slow kinetic rates. (C) Rate-scale-plot comparing affinity and avidity measurements of Fc variants towards PRYSPRY or TRIM21-CC. (D) The altered binding strength from affinity to avidity is mostly off rate driven, which becomes apparent in the overlay of normalized dissociation phases ($k_{OFF,AVIDITY}$) but can also occur as combination of both kinetic rate parameters, namely on and off rate.

Figure 8 TRIM21-CC-Antibody-AAV2 Characterization. SPR Assay data is shown in (A-B). (A1-A2) Schematic SPR assay configuration to analyze the affinity to avidity interplay of TRIM21-CC, anti capsid antibody variants A20 and rAAVv-2. Biotinylated TRIM21-CC is captured via monovalent streptavidin achieving a captured level of 190 RU (A1, high density)) and 35 RU (A2, low density). Subsequent, anti-AAV2 capsid antibody variants (bivalent A20 Fc WT, one-armed A20 Fc WT and Fc WT-AAA) are injected to saturate the TRIM21-CC surface, followed by the injection of rAAV-2. (B) Overlay of the normalized dissociation phases (Start of Dissociation: 100%) after the injection of 3.32 nM rAAVv-2 over low and high TRIM21-CC-A20 densities. At higher antibody densities, more avid complexation occurs and a higher degree of rAAVv-2 surface decoration is possible. This allows less complex to dissociate over time to due to simultaneous engagement of both, TRIM21-CC and AAV2, mediated via the A20 antibody variants. (C) Electron microscopy images of rAAVv-2 interactions with antibodies alone (left column) and TRIM21 additionally (right column). The scale bars represent 50 nm.

Figure 9 Schematic model suggesting how one TRIM21 dimer engages both sites of the Fc region in a two-step process. Upon Fc binding, the PRYSPRY detaches from the coiled-coil domain. The linker domain allows enough freedom of movement to allow engagement of the second PRYSPRY domain. Only after initial binding bivalent engagement of both Fc heavy chains is possible.

5.3 Figures

Figure 1

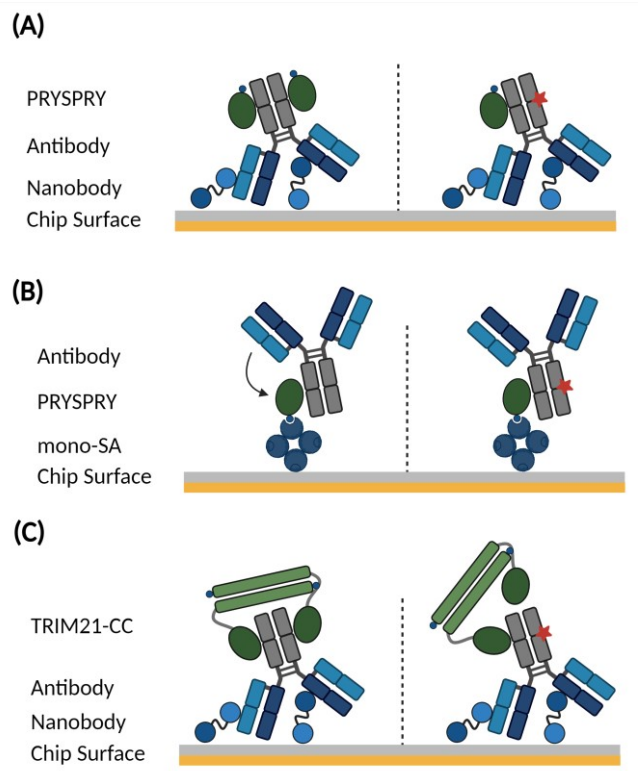

Figure 2

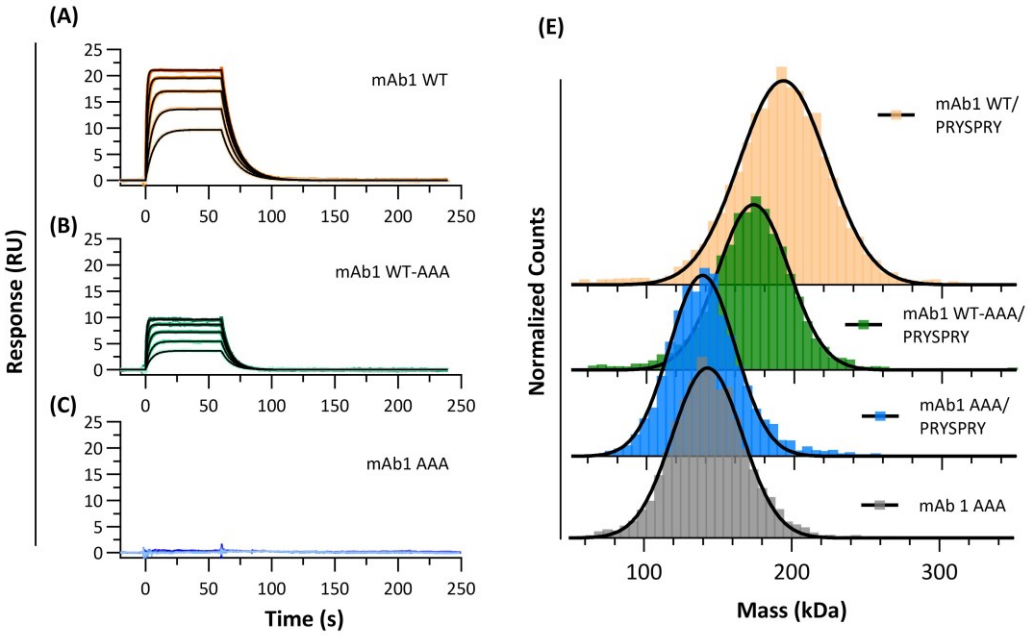

(D)

Sample	k_{ON} ($x10^6$ $M^{-1}s^{-1}$)	k_{OFF} ($x10^{-2}$ s^{-1})	K_D (nM)	$t_{1/2}$ (s)	$Valency_{ligand}$	$R_{max,Ratio}$ (%)
mAb1 WT	2.33 ± 0.01	9.94 ± 0.02	42.7 ± 0.1	7.0	2	97
mAb1 WT-AAA	2.66 ± 0.01	10.5 ± 0.08	39.5 ± 0.5	6.6	1	95
mAb1 AAA	NA	NA	NA	NA	NA	NA

(F)

Sample	$Mass_{theo.}$ (kDa)	$Mass_{exp.}$ (kDa)	Gaussian Fit (%)
mAb1 WT + PRYSPRY	196	193 ± 30	96
mAb1 WT-AAA + PRYSPRY	171	172 ± 35	100
mAb1 AAA + PRYSPRY	146	138 ± 22	100
mAb1 AAA only	146	143 ± 24	100

Figure 3

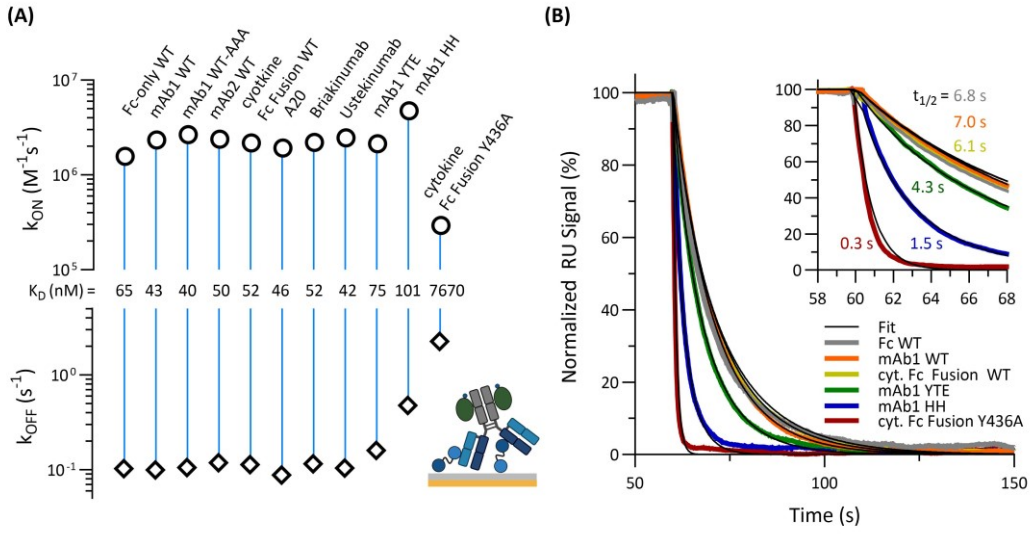

Figure 4

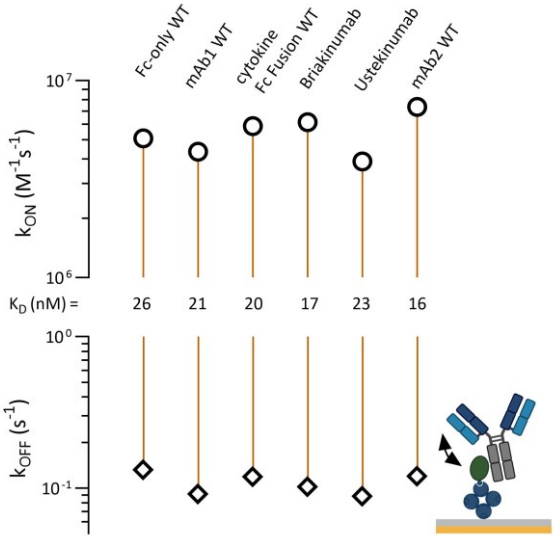

Figure 5

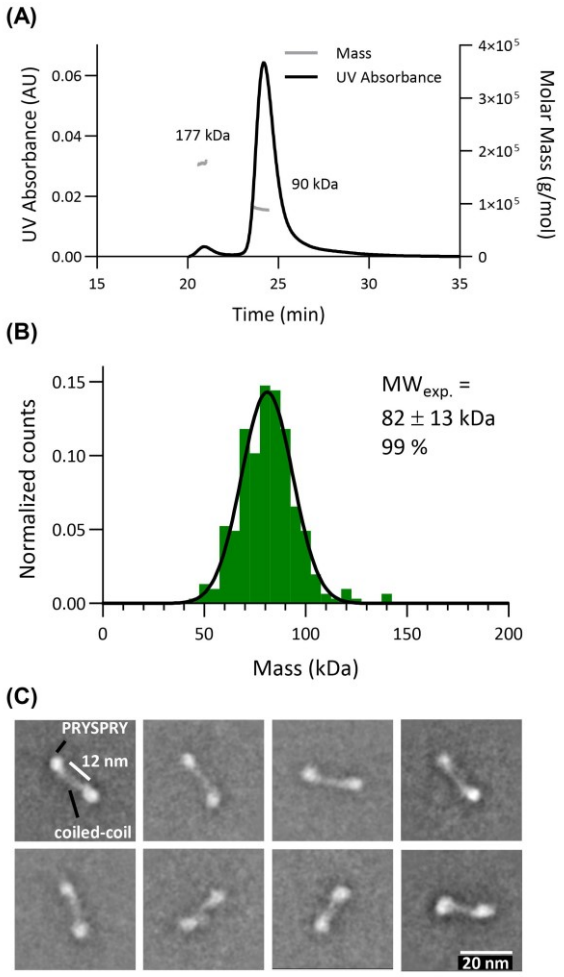

Figure 6

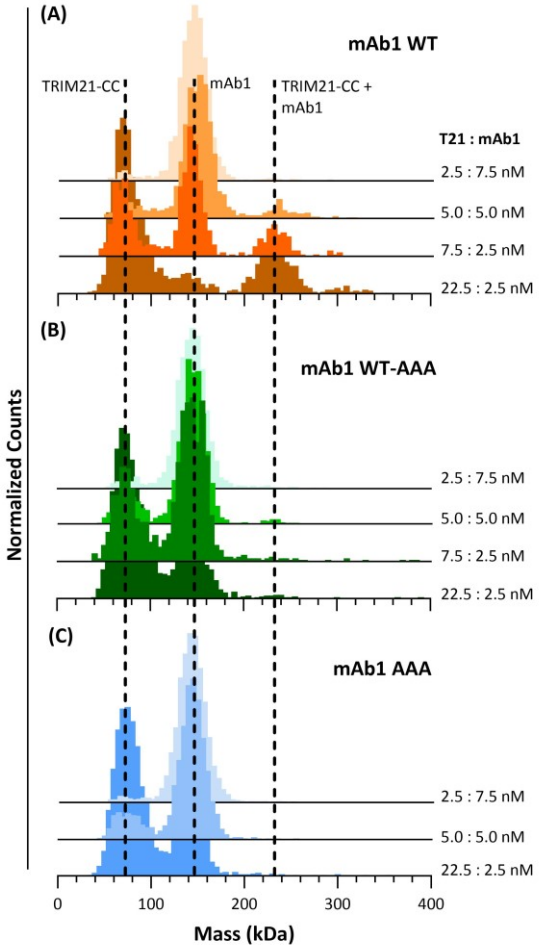

(D)

Molar Ratios TRIM21-CC:mAb1 Fc variant			
$Mass_{theo.}$ (kDa)	86	146	232
TRIM21-CC:mAb1 WT	T21 (%)	mAb1 (%)	T21-mAb1 (%)
1:3	3	92	1.4
1:1	10	78	7
3:1	32	51	15
10:1	63	9	24
TRIM21-CC:mAb1 WT-AAA			
1:3	6	90	NA
1:1	17	80	1.8
3:1	33	64	2.0
10:1	66	34	1.6
TRIM21-CC:mAb1 AAA			
1:3	4	94	NA
1:1	18	80	NA
10:1	66	33	NA

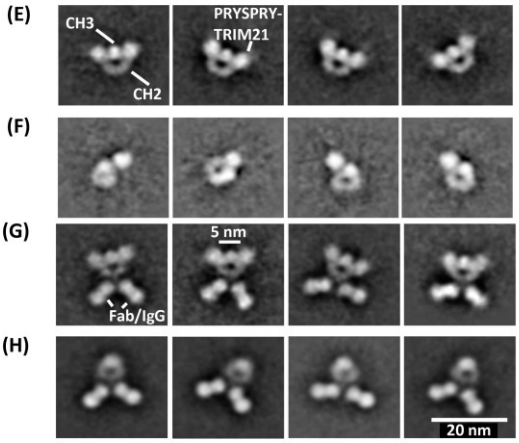

Figure 7

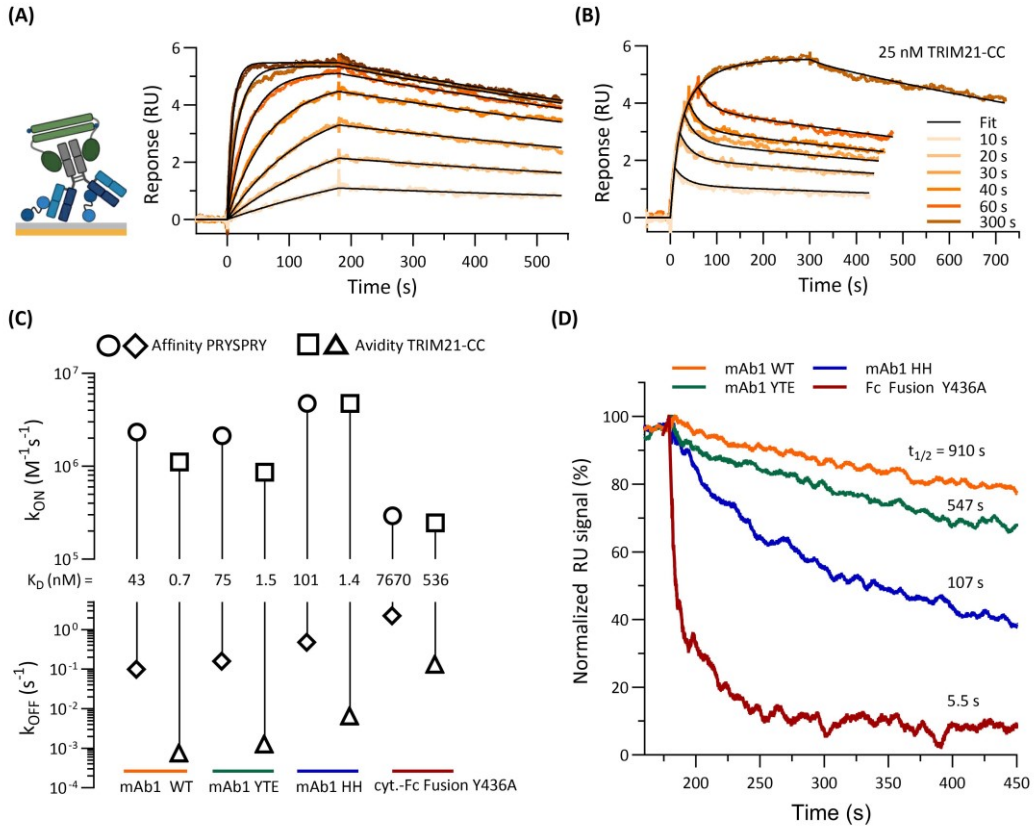
(A)
Reponse (RU)
Time (s)
(B)
25 nM TRIM21-CC
Fit
10 s
20 s
30 s
40 s
60 s
300 s
Reponse (RU)
Time (s)
(C)
Affinity PRYSPRY
Avidity TRIM21-CC
k_ON (M⁻¹s⁻¹)
K_D (nM) =
43 0.7 75 1.5 101 1.4 7670 536
k_OFF (s⁻¹)
mAb1 WT
mAb1 YTE
mAb1 HH
cyt.-Fc Fusion Y436A
(D)
mAb1 WT
mAb1 YTE
mAb1 HH
Fc Fusion Y436A
t1/2 = 910 s
547 s
107 s
5.5 s
Normalized RU signal (%)
Time (s)

Figure 8

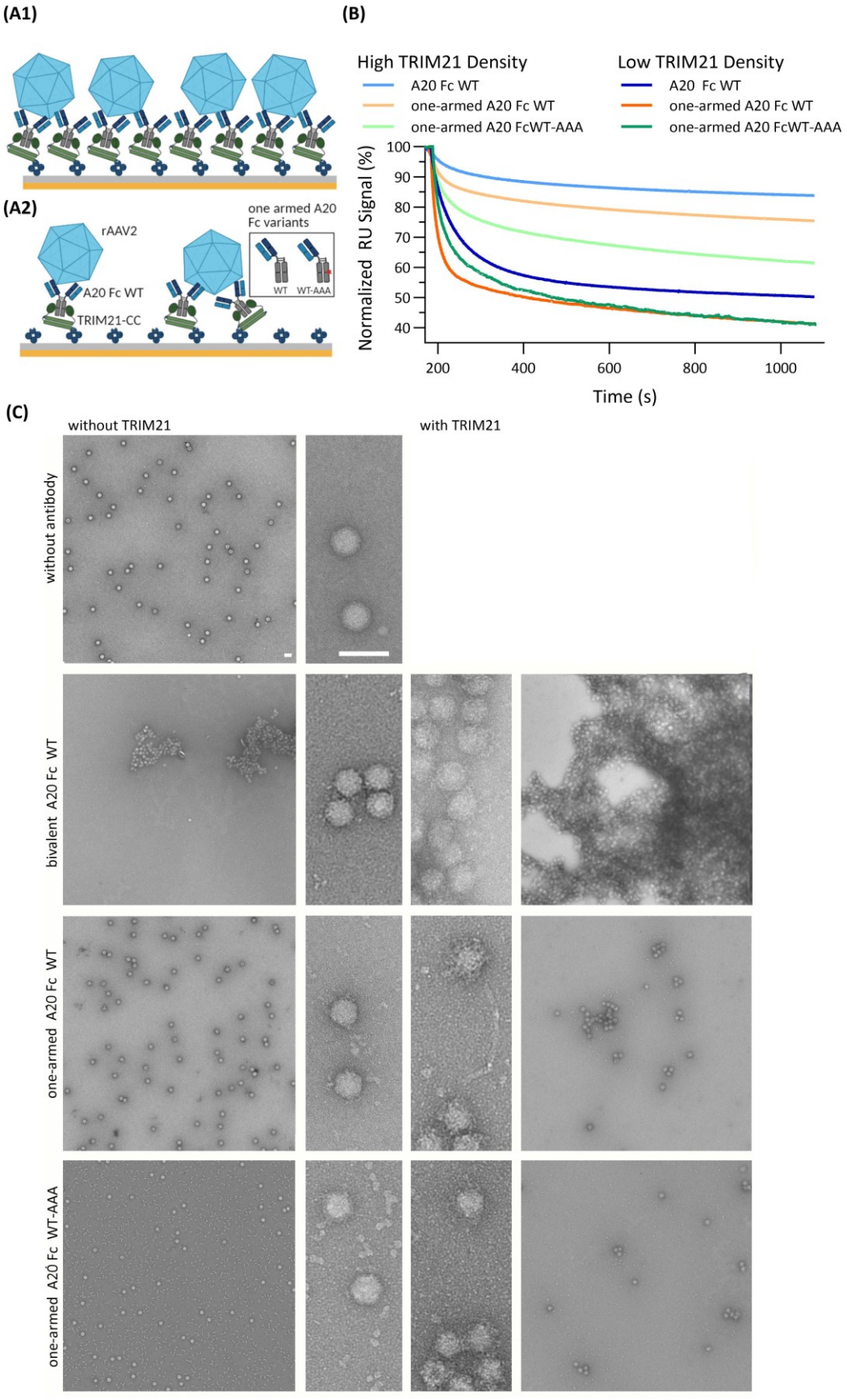
(A1)
(A2)
rAAV2
A20 Fc WT
TRIM21-CC
one armed A20 Fc variants
WT
WT-AAA
(B)
High TRIM21 Density
A20 Fc WT
one-armed A20 Fc WT
one-armed A20 FcWT-AAA
Low TRIM21 Density
A20 Fc WT
one-armed A20 Fc WT
one-armed A20 FcWT-AAA
Normalized RU Signal (%)
100
90
80
70
60
50
40
200
400
600
800
1000
Time (s)
(C)
without TRIM21
with TRIM21
without antibody
bivalent A20 Fc WT
one-armed A20 Fc WT
one-armed A20 Fc WT-AAA

Figure 9

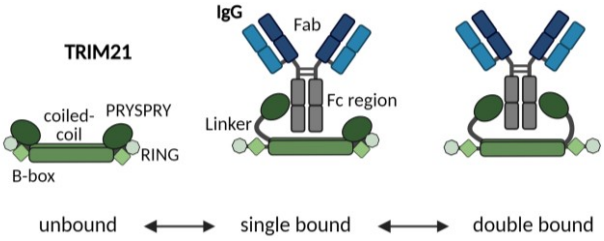
TRIM21
coiled-coil
PRYSPRY
RING
B-box
IgG
Fab
Fc region
Linker
unbound
single bound
double bound

6

Conclusion and Outlook

In this thesis, we explored the intricate world of antibody Fc engineering, highlighting the critical role of avidity in therapeutic antibody efficacy. Avidity, defined as the cumulative binding strength from multiple non-covalent interactions, is fundamental to both the science of antibodies and their clinical use. It is the collective strength of these interactions that underpins the efficacy and functionality of antibodies in therapeutic contexts. Moreover, avidity is crucial in modulating antibody effector functions and in the strategic design of biotherapeutics.

The two studies presented elucidate the nuanced relationship between affinity and avidity in the interactions of FcRn and TRIM21 with Fc-engineered antibodies. These interactions are shown to be key in refining antibody designs for improved therapeutic outcomes. Building on the discussions in separate chapters (**Chapter 4.2 and Chapter 5.2**), this conclusion seeks to integrate these findings into the broader research context, detailing the novel contributions and implications of my work.

6.1 Interpretation of Findings and Implications for Antibody Fc Engineering

To comprehensively characterize complex interactions, such as those between FcRn or TRIM21 and an IgG, the concept of affinity must be expanded to include avidity. Affinity describes the strength of the interaction between a single binding site of a molecule, such as an antibody, and its specific ligand, such as an Fc receptor. It represents how well a molecule can bind to its partner at a given site. The higher the affinity is, the stronger and more specific the binding. In contrast, avidity considers the cumulative strength of multiple affinities in multivalent interactions. Avidity refers to the overall strength of the binding between a molecule with multiple binding sites, such as an antibody with multiple antigen/FcR binding sites, and a multivalent ligand, such as an antigen/FcR with multiple epitopes. It incorporates the strength of each individual affinity interaction as well as the structural arrangement and spatial availability of the binding sites. Avidity effectively enhances the binding strength through multiple simultaneous affinity interactions, leading to a more stable and durable interaction than affinity alone would predict. This is particularly important for the success of

antibody-based therapies and is crucial for their pharmacokinetic and pharmacodyamic properties, as the combined effect of multiple weak bindings can result in a very strong overall attachment (287).

Antibody effector functions are initiated through multivalent interactions with cellular antigens, leading to IgG aggregation on cell surfaces, a process crucial for activating effector functions. *Diebolder et al. (2014)* (288) demonstrated that human IgG antibodies form hexameric structures through non-covalent Fc-Fc interactions, activating the complement system upon detecting surface antigens, underlining the role of antibody-complement coordination in immune defense. Further, *Rouge et al. (2020)* (289) showed that Rituximab induces CD20 circular assemblies, promoting Fc-hexamer formation and complement activation via C1q. *Hiramoto et al. (2018)* (290) found the IgM Fc region is essential for forming its unique pentameric structure, which binds to the AIM protein, indicating a critical role of the Fc region in immune regulation and disease repair through IgM-AIM interactions. Recent studies have demonstrated the significance of multivalent avidity in shaping the immunological response *in vivo*, particularly through interactions between IgG and Fcγ receptors (291, 292). These interactions are pivotal for the initiation of immune responses and highlight the potential of leveraging Fc receptor dynamics to develop advanced therapeutic agents. The engineering of IgG Fc domains emerges as a promising strategy for the development of immunotherapies that not only possess increased potency but also exhibit reduced adverse effects and extended half-lives. This tailored approach to immunotherapy enhances therapeutic efficacy and patient outcomes, thus marking a new horizon in the optimization of antibody-based treatments. With recent advancements, the engineering of antibodies for enhanced Fc-mediated effector functions and the creation of innovative antibody formats, including bispecific and multispecific constructs, expand the traditional scope of monospecific antibodies with native Fc regions. These developments mark a significant evolution in antibody design, offering the potential for targeted and effective therapeutic interventions (31, 293-296). In the scenarios described, avidity can reach different levels, arising from multidimensional affinity interactions that result in an overall binding strength (297). In addition to bivalent/bispecific Fab interactions, simultaneous Fab-antigen and Fc-Fc or Fc-Fc receptor interactions can occur, making the interplay even more complex.

Two FcRn molecules are intended to interact with one IgG in a 2:1 stoichiometry, engaging both heavy chains simultaneously, which presumably occurs on the membrane of acidified endosomal compartments (19). *Yeung et al. (2009)* (298) demonstrate that evaluating single affinities alone fails to capture the complete dynamics of antibody performance, particularly missing the impact of avidity enhancements *in vivo*. For instance, the N434W mutation, despite showing an 80-fold stronger affinity at pH 6.0 compared to wild-type Fc (WT), results in similar *in vivo* clearance rates to WT. This unexpected outcome is attributed to its significant binding to FcRn at physiological pH (pH 7.4), illustrating that excessive affinity

enhancement does not necessarily translate to better pharmacokinetics. *Abdiche et al. (2015)* (148) elucidated the critical role of FcRn avidity *in vivo* in maintaining extended serum half-lives of immunoglobulins, demonstrating that optimal human IgG1 functionality requires dual FcRn binding sites. Their research highlighted that a human IgG1 Fc heterodimer (AAA/WT) exhibits significantly reduced serum half-life in both mice and rats compared to its WT counterpart. Notably, attempts to enhance FcRn binding affinity on a single side of the Fc domain (N434H mutation) did not suffice to offset the reduced half-life, demonstrating the indispensability of a 2:1 stoichiometry between IgG and FcRn for critical IgG biology and sustained half-life. This finding demonstrates the necessity of maintaining bivalent FcRn engagement for the development of therapeutics with prolonged efficacy. Optimal antibody design aims for increased affinity at acidic pH with minimal binding at neutral pH, aiming to minimize Fc region interactions with FcRn at pH 7.4 while maximizing binding efficacy through avidity at pH levels below 6.0. Effective FcRn engagement at pH 6.0 necessitates careful engineering to balance increased binding potential without inadvertently enhancing binding at pH 7.4. This strategy, centered on precise pH-dependent binding characteristics, presents a significant engineering challenge but is crucial for extending IgG half-life.

Homodimeric TRIM21 also engages both heavy chains, but in contrast to FcRn, it does so in a 1:1 stoichiometry, resulting in an avid binding mode due to bivalent binding, and is currently the strongest known Fc receptor (20). Bivalent Fc engagement elucidates how low-affinity TRIM21 binders in the micromolar (μM) range still facilitate cytosolic degradation by activating TRIM21's neutralization capacity (29, 116). At elevated antibody levels, indicative of high opsonization conditions, TRIM21-mediated degradation occurs even with weak binders, attributed to an avid binding mechanism. This mechanism is further supported by the simultaneous binding of Fab to the viral capsid and Fc to TRIM21, which enhances multi-level avidity. Therefore, understanding the TRIM21 binding mode is fundamental to modulating avidity by engineering single affinities, whether the goal is to inhibit or promote this interaction based on therapeutic needs.

To accurately characterize the cumulative effects of multiple affinity interactions within an avid binding mode, developing techniques and assays that measure both affinity and avidity, while minimizing the risk of measurement artifacts, is essential. Our goal was to design assays that are as straightforward as possible, yielding data that are not only interpretable but also conducive to accurate modeling. This necessitates technologies capable of dissecting complex binding kinetics to effectively differentiate between affinity and avidity. Consequently, we selected assay configurations that closely mimic physiological conditions, recognizing that the analysis of such interactions, especially for FcRn and TRIM21, involves complex sensorgrams that do not conform to a simple 1:1 binding model.

A critical aspect of our methodology was the meticulous control of ligand density, a factor that was prioritized across different biosensor technologies. Our research provides novel

insights into the IgG-FcRn/TRIM21 interaction within its biological context, with potential implications for our understanding of antibody recycling, neutralization, and immune response pathways. These findings establish a foundation for the future characterization of Fc-engineered antibodies, integrating both affinity and avidity analyses. Understanding how Fc mutations influence the avidity binding of FcRn and TRIM21 is vital for the strategic selection and combination of mutations, and is crucial for advancing our knowledge of antibody effector functions.

6.2 The Role of Avidity in Antibody Drug Design

In antibody engineering, there is a concerted effort to develop innovative cancer treatments with multi-specific binding capabilities. In this context, the concept of avidity plays a complex yet pivotal role. Although additional binding sites might intuitively seem to increase binding strength, the reality is more nuanced, particularly when considering the implications for antibody functionality and therapeutic applications. A thorough understanding of avidity is essential for accurately characterizing antibody interactions within the immune system and leveraging this knowledge to enhance the efficacy of biotherapeutics. This insight highlights the importance of engineering antibodies to optimize their binding properties for superior therapeutic performance. Strategies such as multi-specific targeting and adjusting antibody valency are key to enhancing avidity, offering promising avenues for the creation of more effective disease treatments (31, 299-303).

In exploring the complex kinetics of biomolecular interactions, affinity and avidity data from the literature across a range of biomolecule interactions are compiled

In exploring the complex kinetics of biomolecular interactions, affinity and avidity data from a range of biomolecule interactions have been compiled (**Figure 13**). Avidity assessments have utilized both cell assays and biosensor technologies, which closely mimic *in vivo* conditions, but face challenges in consistently controlling antigen levels on cell surfaces and typically yield only EC_{50} (half maximal effective concentration) or K_D (equilibrium dissociation constant) values from dose-response analyses. In contrast, biosensor assays provide deeper insights into binding kinetics by enabling detailed studies of association and dissociation processes. Technologies such as SPR, interferometry, total internal reflection (TIR) fluorescence (304), and switchSense (273) facilitate a more comprehensive understanding of binding dynamics beyond basic equilibrium measurements.

This thesis demonstrates that the FcRn-IgG interaction encompasses both monovalent and bivalent binding, featuring correlated pairs of affinity and avidity data that systematically vary with pH across a wide range. This variability served as the foundation for the development of a generalized binding model. Additionally, this thesis explored the bivalent engagement of IgG heavy chains by TRIM21, which revealed distinct binding characteristics among various Fc mutants and characterized their affinity-avidity relationships.

Beyond FcRn- and TRIM21-IgG interactions, multivalent interactions are crucial for specificity and trigger-like responses and are widespread across proteins, nucleic acids, and small molecules, with leukocyte integrins being one such example (305, 306). The immune system, in particular, displays the significance of avidity, especially in the function of inherently bivalent IgG antibodies (302, 307). Early immune response antibodies, such as IgM, which has 10 paratopes, leverage their multiple binding sites to enhance efficacy through avidity. **Figure 13** illustrates a comparison of K_D values from the literature for mono- and multivalent interactions, as well as those for FcRn and TRIM21 presented in this work. It reveals avidity enhancement factors which are defined as the ratio of apparent K_D values for affinity to avidity ($K_{D,AFFINITY}/K_{D,AVIDITY}$), and they vary widely. For bivalent binders, these factors can reach up to approximately 1,000-fold. However, they predominantly range from 5- to 100-fold. Despite the wide range of affinity K_D values, spanning nearly eight orders of magnitude, a clear correlation between affinity levels and avidity enhancement is not evident.

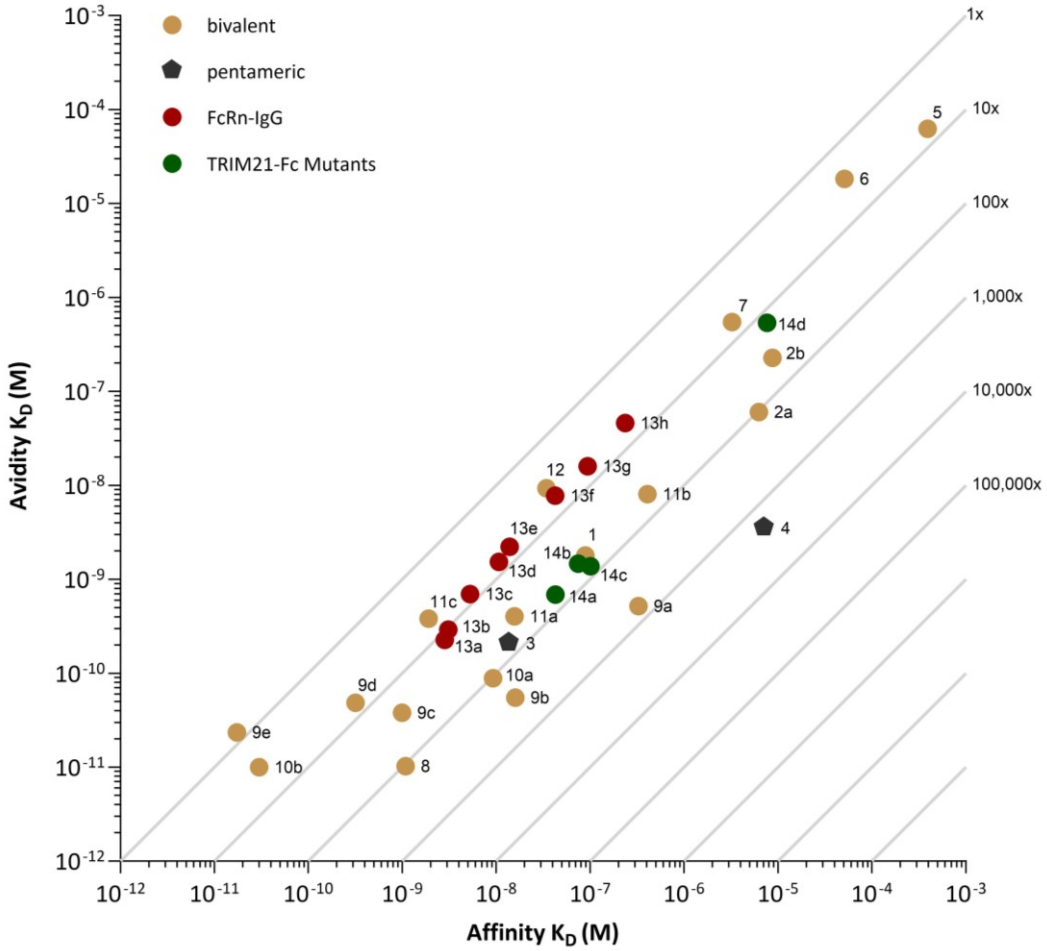

Label	Interaction	Technology	Publication
1	hCA2 monomer and dimer	SPR	*(308)*
2a	anti-polysaccharide scFv	SPR	*(309)*
2b	anti-polysaccharide Fab and IgG	SPR	*(309)*

3	anti-beta galactosidase IgM	SPR	*(310)*
4	anti-peptide pentameric nanobody	SPR	*(311)*
5	anti-mAChR and b2AR small molecule	Radiolig. cell assay	*(312)*
6	anti-DNP Fab and IgG	TIRF and microfluid.	*(304)*
7	anti-DNP Fab and IgG	TIRF	*(313)*
8	anti-Bacillus SP antigens Fab and IgG	Cell assay	*(141)*
9a-e	anti-Her2 scFv and IgG	SPR	*(314)*
10a-b	anti-CEA shMFE scFv monomer and dimer	Fluor. cell assay	*(315)*
11a-c	anti-Her2 diabody from scFv	SPR	*(316)*
12	anti-Her2 (scFv)2 and monoval. Heterodimer	SPR	*(317)*
13a-h	**FcRn-IgG: pH = 5.8, 6.0,… 7.2**	**switchSENSE**	***FcRn study, this work***
14a-d	**TRIM21-Fc Mutants: 14a WT, 14b YTE, 14c HH, 14d Y436A**	**SPR**	***TRIM21 study, this work***

Figure 13. Comparative Analysis of Apparent Dissociation Constants (K_D) This figure compiles apparent K_D values for both monovalent (affinity) and multivalent (avidity) interactions, incorporating data from various studies, including FcRn and TRIM21 interactions characterized in this work. To standardize the comparison, kinetic data from studies employing complex surface models have been converted to apparent K_D values using the ratio of the dissociation rate constant (k_{OFF}) to the association rate constant (k_{ON}). The figure demonstrates the range of enhancement factors attributable to avidity, which can amplify binding strength by up to 1,000-fold, with most observed enhancements between 5-fold and 100-fold.

In the discussion of affinity and avidity kinetics, only a select number of studies have provided comprehensive analyses. *Cooper and Williams (1999)* (310) explored the binding dynamics of IgM to beta-galactosidase anchored on a planar lipid bilayer, revealing a 64-fold increase in avidity enhancement for the off-rate, with a slight reduction in the on-rate, challenging conventional expectations. Similarly, *MacKenzie et al. (1996)* (309) examined the binding characteristics of single-chain antibody variable domains (scFv) in both monomeric and dimeric forms, as well as Fab versus full IgG molecules against polysaccharides. They found a significant 25-fold reduction in off-rates for bivalent binders compared to their monovalent counterparts, and a fivefold increase in on-rates for bivalent scFv. In contrast, the on-rate of the full IgG molecule was only marginally faster, at 1.3-fold, than that of its Fab component. Furthermore, the *Whitesides* group conducted meticulous analyses of the monomeric and dimeric forms of carbonic anhydrase binding to a small molecule inhibitor on a self-assembled monolayer (308). They identified a 42-fold avidity enhancement in the off-rate and also observed a slight reduction in the on-rates for the bivalent analyte (308).

A recurring observation across these studies is the presence of biexponential dissociation phases in experiments involving bivalent binders. The initial rapid off-rate matched that observed in monovalent interactions (affinity), while a subsequent slower off-rate demonstrated the impact of bivalent binding (avidity). Association kinetics, which were largely monophasic across various reports, were effectively modeled using single-exponential fits; this illustrates the nuanced behavior of multivalent interactions (308, 309).

6.3 Limitations and Recommendations for Future Research

In concluding this thesis, it is imperative to acknowledge that the exploration of avidity has significantly broadened our understanding of bivalent/bispecific IgG Fab interactions and Fc functions, catalyzing biotherapeutic innovations. However, this exploration also unveils considerable challenges. Limitations in specificity and control over avidity effects demonstrate the necessity for more nuanced investigations. Future research should aim to elucidate the molecular dynamics of avidity and its consequential impact on the therapeutic potential of antibodies. Such research promises to herald unprecedented breakthroughs in antibody-based treatments. The discourse presented herein provides a foundational overview of avidity, with more comprehensive analyses available in other studies (307, 308, 318-320). Crucial contributions from both experimental and theoretical domains, highlighted by several studies (307, 308, 310, 321-324), emphasize the importance of considering kinetic rates for unbound, singly bound, and doubly bound states in our understanding of bivalent binder formats. The modulation of avidity is intricately linked to the absolute and relative rates of transition for binding components between these states, including the consideration of intermediate states.

As demonstrated, assessing the *in vivo* efficacy of therapeutic antibodies transcends the mere comparison of affinity values across antibody Fc mutants and formats. Focusing solely on individual binding affinities falls short of capturing the full spectrum of antibody efficacy and avidity. The current inability to quantitatively predict avidity enhancement based on individual binding site affinities illustrates the limitations of relying solely on affinity measurements for understanding antibody binding modes. This highlights the urgent need for a more comprehensive approach to evaluating antibody interactions, one that integrates kinetic considerations and avidity effects to fully understand and leverage the therapeutic potential of antibodies.

7
Appendix

7.1 Publication I: Supplementary Information

This Chapter contains the Supplementary Information of

Insight into the avidity-affinity relationship of the bivalent, pH-dependent interaction between IgG and FcRn

7.1.1 Letter of Acceptance

May 20, 2024

To whom it may concern,

Mabs is a biomedical journal published by Taylor & Francis. The manuscript entitled "Insight into the avidity-affinity relationship of the bivalent, pH-dependent interaction between IgG and FcRn", by authors Johannes Reuschab, Jan Terje Andersen, Ulrich Ranta, and Tilman Schlothauer, was submitted to the journal in October 2023. Since then, the manuscript has undergone multiple rounds of reviews and revisions.
As of May 2024, the Assistant Editor handling the manuscript and I agree that the authors have suitably addressed the reviewers' questions and comments and the manuscript is ready for acceptance. However, due to a technical issue with the online submission system, the authors are unable to submit the final manuscript files. As of 20 May, the publisher is still working to correct the problem. Once the technical issue has been resolved, we will accept the manuscript for publication.

Please feel free to contact me if you have any questions or concerns.

Best regards,

Janice Reichert

Janice M. Reichert, Ph.D.
Editor-in-Chief, *mAbs*
508 808-8311
reichert.biotechconsulting@gmail.com

1

7.1.2 Supplementary Information

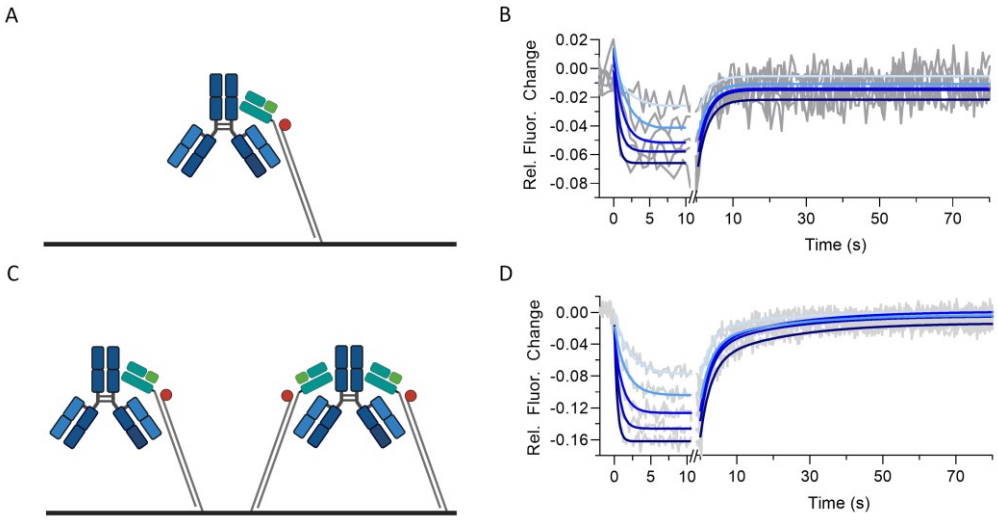

Figure S 1. Kinetic analysis of human FcRn immobilized and a human IgG1 (mAb1) Fc wildtype in solution at pH 6.0 working with ultra-low (A,B) and medium (C,D) FcRn densities on switchSENSE biosensor chip. Human IgG1 was injected in five different concentration as two-fold dilution series with a highest concentration of 300 nM. Each plot (B,D) shows the measured raw data (grey) and the global fit analysis as solid lines (blue fading). (A,B) shows the affinity case applying a mono-exponential fit model while sensorgram (C,D) display a biphasic dissociation curve reflecting affinity and avidity. The determined kinetic parameters are described in Table S 1.

Table S 1. Summary of the affinity and avidity measurements of immobilized human FcRn and an IgG1 (mAb1) Fc wildtype as solute using a switchSENSE biosensor chip having a medium ligand density. The kinetic rate parameter are determined from analyzing the sensorgrams shown in **Figure S 1**. The k_{ON}, k_{OFF} and K_D values are results from a global fit analysis ± fitting error.

Sample		**Affinity**		**Avidity**	
mAb1 WT	k_{ON} ($x10^6$ $M^{-1}s^{-1}$)	$k_{OFF,AFFINITY}$ ($x10^{-1}$ s^{-1})	$K_{D,AFFINITY}$ (nM)	$k_{OFF,AVIDITY}$ ($x10^{-1}$ s^{-1})	$K_{D,AVIDITY}$ (nM)
low density	6.17 ± 1.50	3.51 ± 0.36	57.0 ± 15.1	NA	NA
med. density	7.53 ± 0.38	3.42 ± 0.15	45.4 ± 3.0	0.47 ± 0.03	6.24 ± 0.51

(A) mAb2 WT

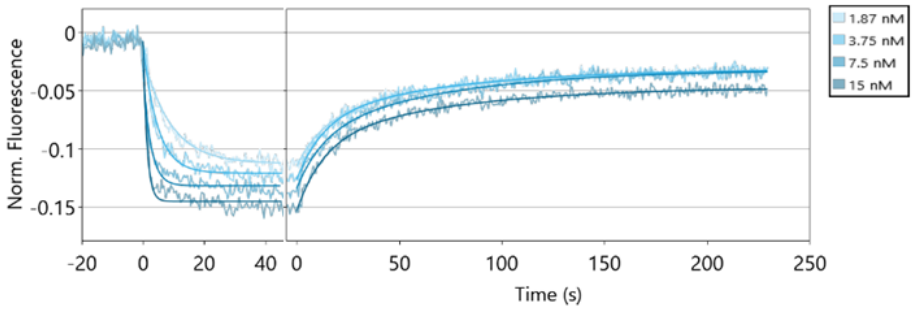

(B) mAb2 YTE

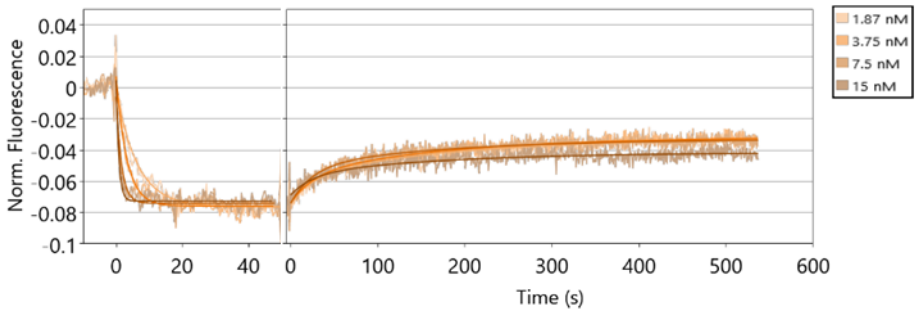

Figure S 2. Kinetic analysis of human FcRn (immobilized) and a hIgG1 (mAb2) Fc WT (A) and YTE (B) variant (in solution) at pH 6.0 on switchSENSE biosensor chip. mAb2 was injected in five different concentration as two-fold dilution series with a highest concentration of 15 nM. Each plot (A,B) shows the measured raw data and the global fit analysis as solid lines. The sensorgrams display a biphasic dissociation curve reflecting affinity and avidity, while the association is monophasic. The determined kinetic parameters are described in **Table S 2**.

Table S 2. Summary of the affinity and avidity measurements of immobilized hFcRn and mAb2 Fc variants as solute at pH 6.0. The kinetic rate parameters are determined from analyzing the sensorgrams shown in **Figure S 2**. The k_{ON}, k_{OFF} and K_D values are results from a global fit analysis ± fitting error.

Sample			AFFINITY				AVIDITY			
	k_{ON} ($M^{-1}s^{-1}$)	**err k_{ON}** ($M^{-1}s^{-1}$)	**k_{OFF1}** (s^{-1})	**err k_{OFF1}** (s^{-1})	**K_{D1}** (M)	**err K_{D1}** (M)	**k_{OFF2}** (s^{-1})	**err k_{OFF}** $(s^{-1})_2$	**K_{D2}** (M)	**err K_{D2}** (M)
(A) mAb2 WT	3.60E+07	1.10E+06	7.78E-02	4.01E-03	2.16E-09	1.29E-10	1.47E-02	7.02E-04	4.08E-10	2.31E-11
(B) mAb2 YTE	7.00E+07	2.18E+06	4.02E-02	2.99E-03	5.74E-10	4.63E-11	5.87E-03	3.15E-04	8.39E-11	5.20E-12

Antibody (hIgG1) Fc variants

(A)
mAb1 Fc WT pH 6.0, low FcRn density

(B)
mAb1 Fc WT pH 6.0, medium FcRn density

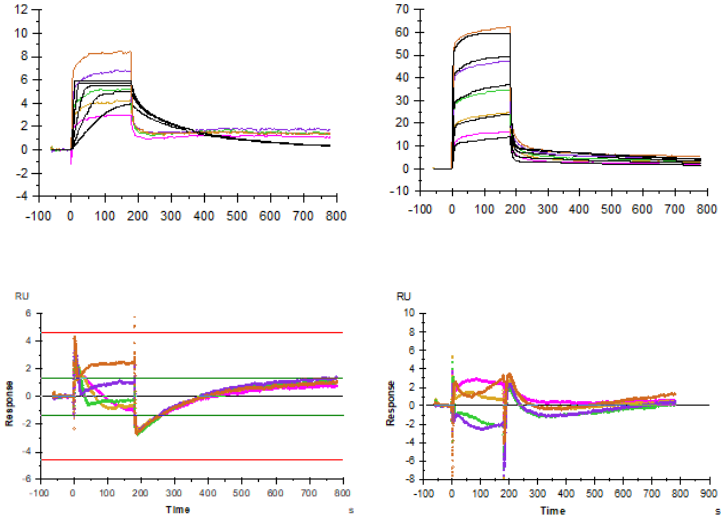

(C)
mAb2 Fc WT, pH 6.0, medium FcRn density

(D)
mAb2 Fc YTE, pH 6.0, medium FcRn density

(E)
mAb1 Fc YTE, pH 6.0, medium FcRn density

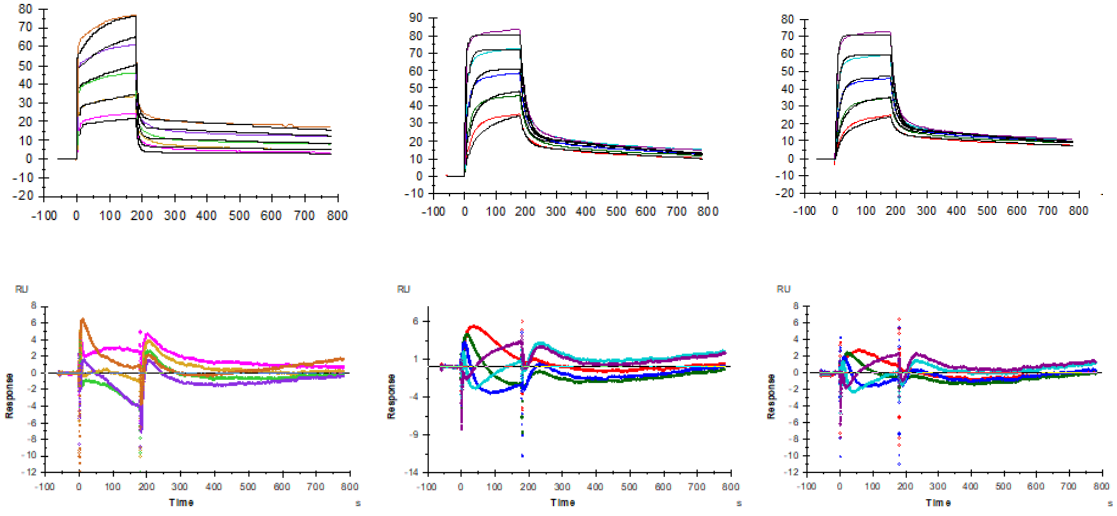

Figure S 3. SPR Sensorgrams of hFcRn (immobilized) and a hIgG1 Fc variant (in solution) at pH 6.0 on a C1 chip. FcRn (captured via Neutravidin) was captured on the surface at 140 RU (medium). mAb Fc variants were injected in five different concentration as two-fold dilution series with a highest concentration of (A) 1000 nM mAb1 Fc WT – low FcRn density, (B) 1000 nM mAb1 Fc WT – medium FcRn density (C) 1000 nM mAb2 Fc WT – medium FcRn density, (D) 200 nM mAb2 Fc YTE – medium FcRn density, (E) 200 nM mAb1 Fc YTE – medium FcRn density. Each plot shows the measured raw data and the applied (A) 1:1 Fit Model or (B-E) heterogeneous Ligand Model (BiaEvaluation Software 3.1) as solid lines (black). The goodness of the fit was evaluated by analyzing the residuals

(lower panel). The residuals show a systematic pattern, which suggests that the model is not a good fit for the data and parameters are not reliable. The determined kinetic parameters are described in **Table S 3**.

Table S 3. Summary of SPR kinetic rate parameters of immobilized hFcRn and mAb Fc variants in solution at pH 6.0. The kinetic rate parameter are determined from analyzing the sensorgrams shown in **Figure S 3**. (**A-C**) For mAb1 WT and mAb2 WT at pH 6.0 the kinetic rates are outside the limits and cannot be measured reliably (indicated by *). Kinetic constants cannot be reliable determined. Revealed kinetic parameters are not realistic nor reliable and valid. (**D - E**) For mAb1 YTE and mAb2 YTE affinity kinetic rate parameters could be modelled approximately but the residuals show a systematic pattern, which suggests that the model is not a good fit for the data and parameters are not reliable (* kinetic rates are not reliable).

Sample **pH 6.0**	**k_{ON1} ($M^{-1}s^{-1}$)**	**Err. k_{ON1} (M-1s-1)**	**k_{OFF1} (s^{-1})**	**Err.** k_{OFF1} (s-1)	**K_{D1} (M)**	**Err. K_{D1} (M)**	**Density**	**Model**
(A) mAb1 WT *	3.145E+9		92.25				low	1:1
(B) mAb1 WT *	8.06E+08	6.89E+05	2.46E+02	2.10E-01	**3.05E-07**	3.69E-10	med.	heterogeneous
(C) mAb2 WT *	2.56E+09	2.31E+06	3.88E+02	3.48E-01	**1.52E-07**	1.93E-10	med	heterogeneous
(D) mAb2 YTE	7.12E+05	4.71E+03	5.13E-02	1.43E-04	**7.21E-08 ***	5.17E-10	med	heterogeneous
(E) mAb1 YTE	7.50E+05	1.94E+03	5.50E-02	1.08E-04	**7.31E-08 ***	2.38E-10	med	heterogeneous
	k_{ON2} ($M^{-1}s^{-1}$)	**Err. k_{ON2} (M-1s-1)**	**k_{OFF2} (s^{-1})**	**Err. k_{OFF2} (s-1)**	**K_{D2} (M)**	**Err. K_{D1} (M)**		
(B) mAb1 WT *	3.89E+04	5.40E+01	1.35E-03	1.85E-06	**3.47E-08**	6.77E-11	med	heterogeneous
(C) mAb2 WT *	1.59E+04	1.99E+01	5.25E-04	7.28E-07	**3.30E-08**	6.17E-11	med	heterogeneous
(D) mAb2 YTE *	1.31E+06	2.49E+03	9.23E-04	3.91E-06	**7.05E-10**	3.27E-12	med	heterogeneous
(E) mAb1 YTE *	7.00E+05	1.84E+03	1.08E-03	3.05E-06	**1.54E-09**	5.95E-12	med	heterogeneous

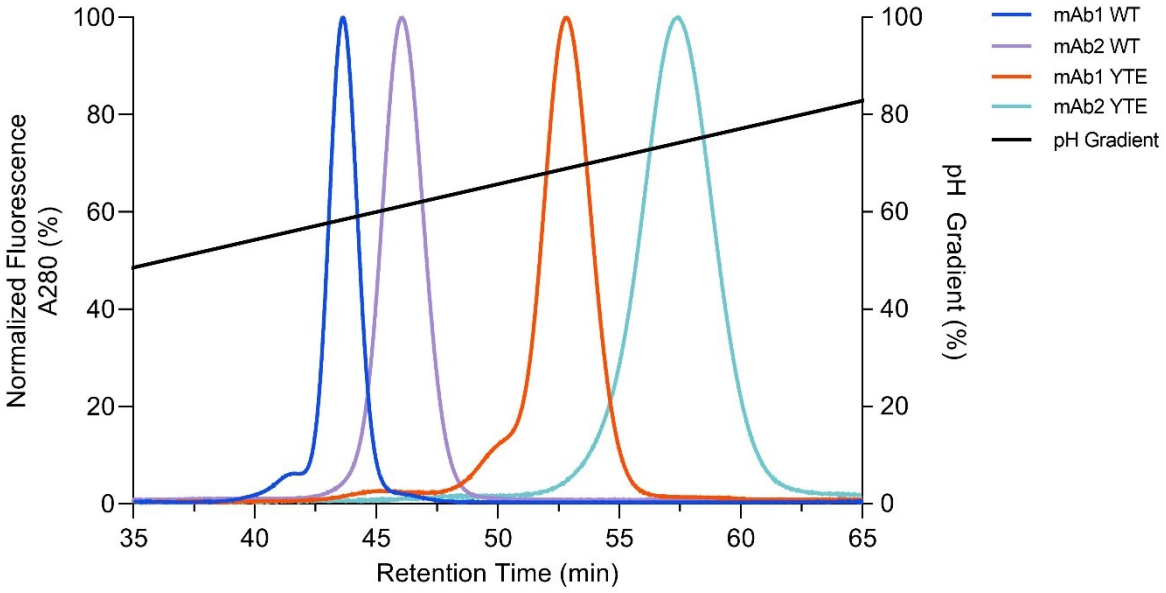

Figure S 4. Analytical hFcRn affinity chromatography for mAb1 and mAb2 Fc variants (WT vs. YTE). The elution profiles are shown as normalized fluorescence intensity (%) and as function of the pH gradient (%). Fluorescence intensity was normalized and set to 100 %.

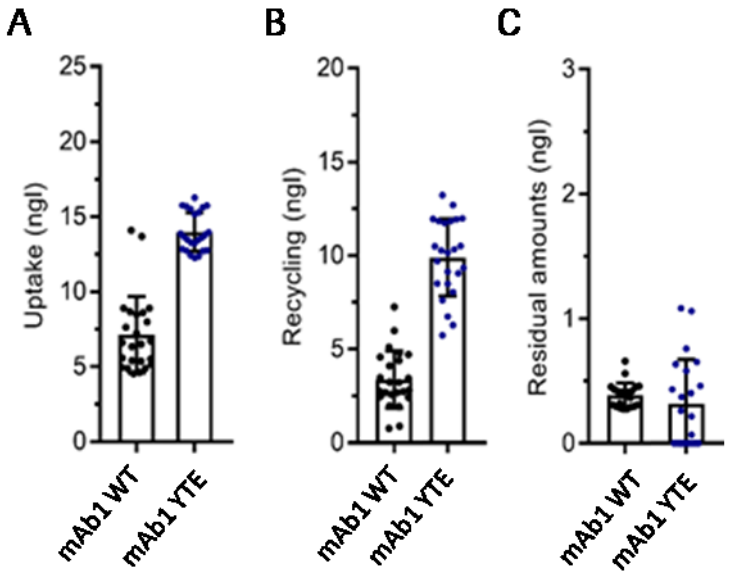

Figure S 5. HERA assay of hIgG1 (mAb1) WT and the Fc engineered YTE variant. A Uptake of WT and YTE at pH 7.4 when both constructs were added to the cells followed by 4 h incubation, washing and cell lysis. B Recycling of mAb1 WT and YTE at pH 7.4 when each antibody was added to the cells and incubated for 4 h followed by washing and additional incubation of 4 h before sample collection. C demonstrates results from the same protocol as in B followed by cell lysis.

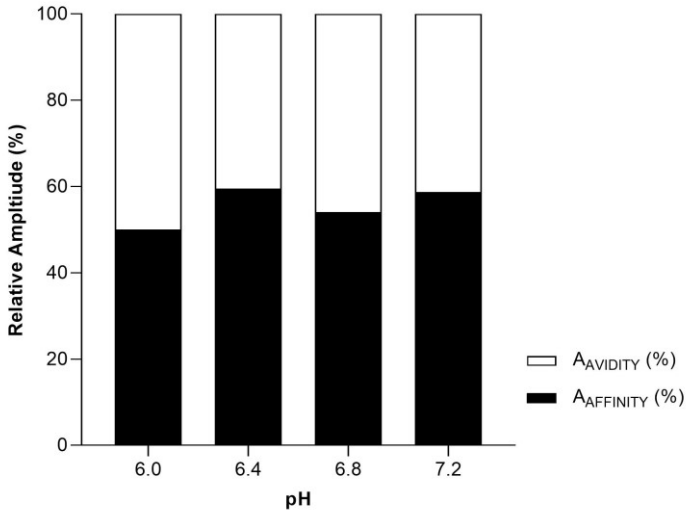

Figure S 6. The relative amplitudes of affinity and avidity are shown as a percentage for four different FcRn and mAb1 Fc YTE pH values at pH 6.0, 6.6, 6.8 and 7.2 with 60 nM, 150 nM, 300 nM and 600 nM injected hIgG1 respectively. The amplitudes are extracted from the applied biphasic fit model reflecting the FcRn - hgG1 binding mode (Equation (1)). The contribution of affinity driven (fast) and avidity driven (slow) dissociation phase to the overall signal change is shown as amplitude $A_{AFFINITY}$ (A_{fast}) or $A_{AVIDITY}$ (A_{slow}). The overall dissociation curve is a superposition of two exponential time-courses, namely the affinity binding mode (fast dissociation) and the avidity binding mode (slow dissociation) deconvoluted by two exponential time-courses. Equation (3) and (4) show the calculation for the amplitudes (materials and methods).

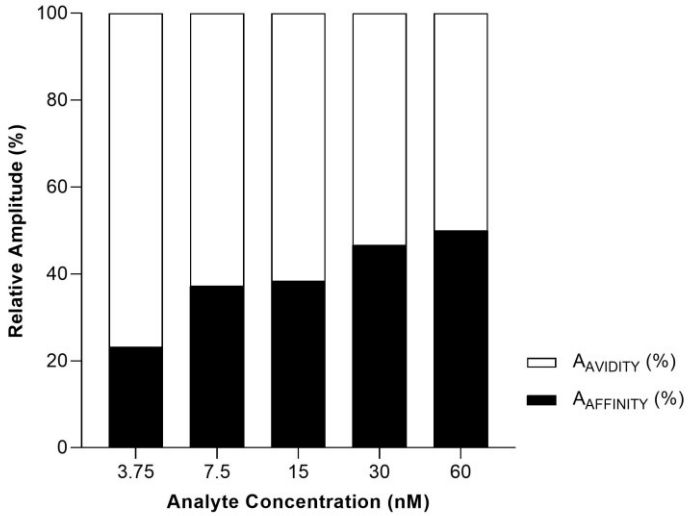

Figure S 7. presents the amplitude ratios of affinity and avidity binding mode, expressed in percentages, for FcRn and hIgG1 Fc YTE at pH 6.0 across five injected antibody concentrations. As the injected analyte concentration increases, the affine species becomes more prominent.

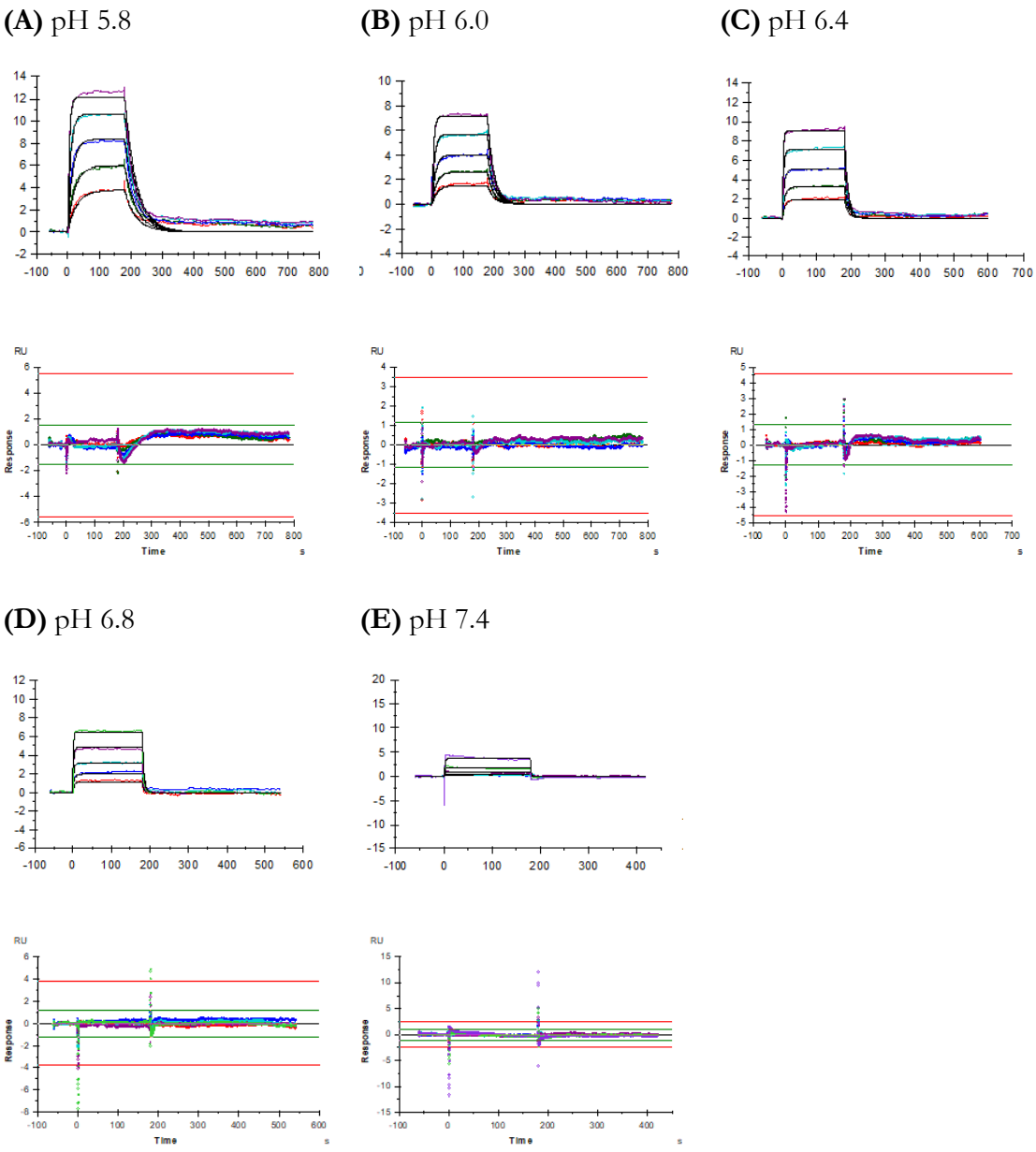

Figure S 8. SPR Sensorgrams of hFcRn (immobilized) and a hIgG1 (mAb1) Fc YTE variant (in solution) from pH 5.8 to 7.4 on a C1 chip. FcRn (captured via Neutravidin) was captured on the surface at 12 RU (low). mAb1 Fc YTE was injected in five different concentration as two-fold dilution series with a highest concentration of (A) 200 nM for pH 5.8, (B) 200 nM for pH 6.0, (C) 600 nM for pH 6.4, (D) 1500 nM for pH 6.8 and (E) 3000 nM for pH 7.4. Each plot shows the measured raw data and a simple 1:1 global fit analysis as solid lines (black). The goodness of the fit was evaluated by analyzing the residuals (lower panel). The residuals are small and randomly distributed around zero. This means that the model's predictions are close to the actual observed data. The determined kinetic parameters are described in **Table S 4**.

Table S 4. Summary of SPR kinetic rate parameters of immobilized hFcRn (12 RU, low density) and mAb1 Fc YTE in solution. The kinetic rate parameter are determined from analyzing the sensorgrams shown in **Figure S 8**. The k_{ON}, k_{OFF} and K_D values are results from a global 1:1 fit analysis ± fitting error, determining the FcRn affinity (* kinetic rates are not reliable).

Sample / Density	pH	k_{ON1} ($M^{-1}s^{-1}$)	Error k_{ON1} (M-1s-1)	k_{OFF1} (s^{-1})	Error k_{OFF1} (s-1)	K_{D1} (M)	Error K_{D1} (M)	$t_{1/2}$ (s)
mAb1 Fc YTE / low FcRn density	**(A)** 5.8	7.52E+05	3.74E+05	0.027	2.50E-04	**3.54E-08**	1.76E-08	26.1
	(B) 6.0	7.36E+05	9.25E+03	0.050	6.03E-04	**6.83E-08**	1.19E-09	13.8
	(C) 6.4	4.82E+05	8.09E+03	0.102	1.68E-03	**2.12E-07**	4.98E-09	6.8
	(D) 6.8	3.12E+05	7.12E+03	0.248	5.58E-03	**7.95E-07**	2.55E-08	2.8
	(E) 7.4 *	7.14E+03	2.21E+02	0.587	1.42E-02	**8.22E-05**	3.23E-06	1.2

mAb1 Fc YTE, pH 5.8

Medium FcRn density (140 RU)

(A) Bivalent Model

High FcRn density (1100 RU)

(B) Bivalent Model

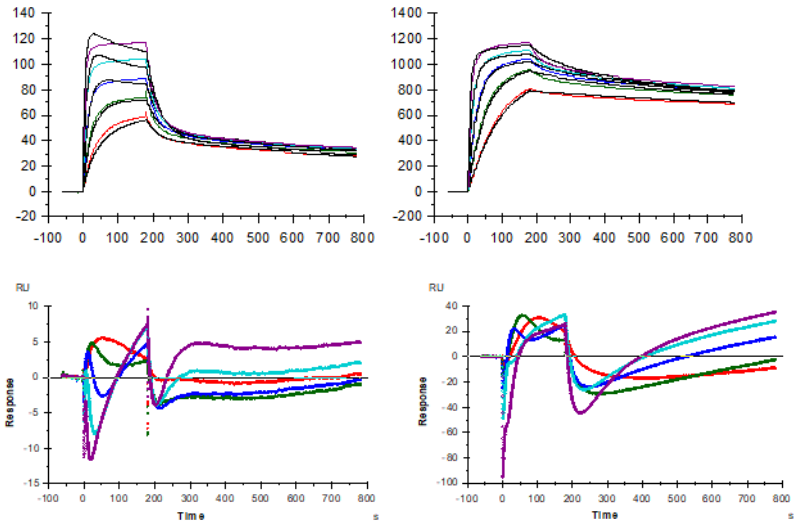

(C) Heterogeneous (Ligand) Model

(D) Heterogeneous (Ligand) Model

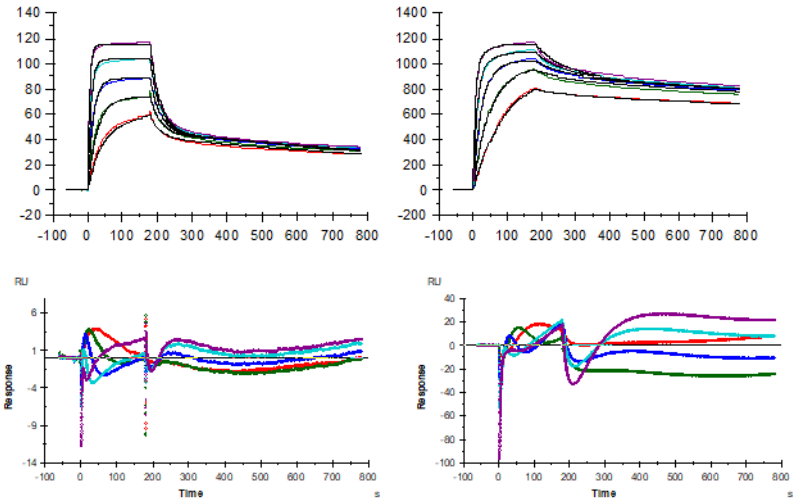

Figure S 9. SPR Sensorgrams of hFcRn (immobilized) and a hIgG1 (mAb1) Fc YTE variant (in solution) at pH 5.8 on a C1 chip. FcRn (captured via Neutravidin) was captured on the surface at medium (140 RU) and high (1100 RU) density. mAb1 Fc YTE was injected in five different concentration as two-fold dilution series with a highest concentration of (A-D) 200 nM. Each plot shows the measured raw data and the applied fit model as solid lines (black). For (A,B) the bivalent analyte model and for (C,D) the heterogeneous (Ligand) Model, provided by BiaEvaluation Software 3.1, was applied. The goodness of the fit was evaluated by analyzing the residuals, whereas they show significant, systematic patterns, which results

in a poor fit. The determined kinetic parameters are not shown as they lack reliability and are not valid (see residuals). Condition (C) was chosen for further analysis.

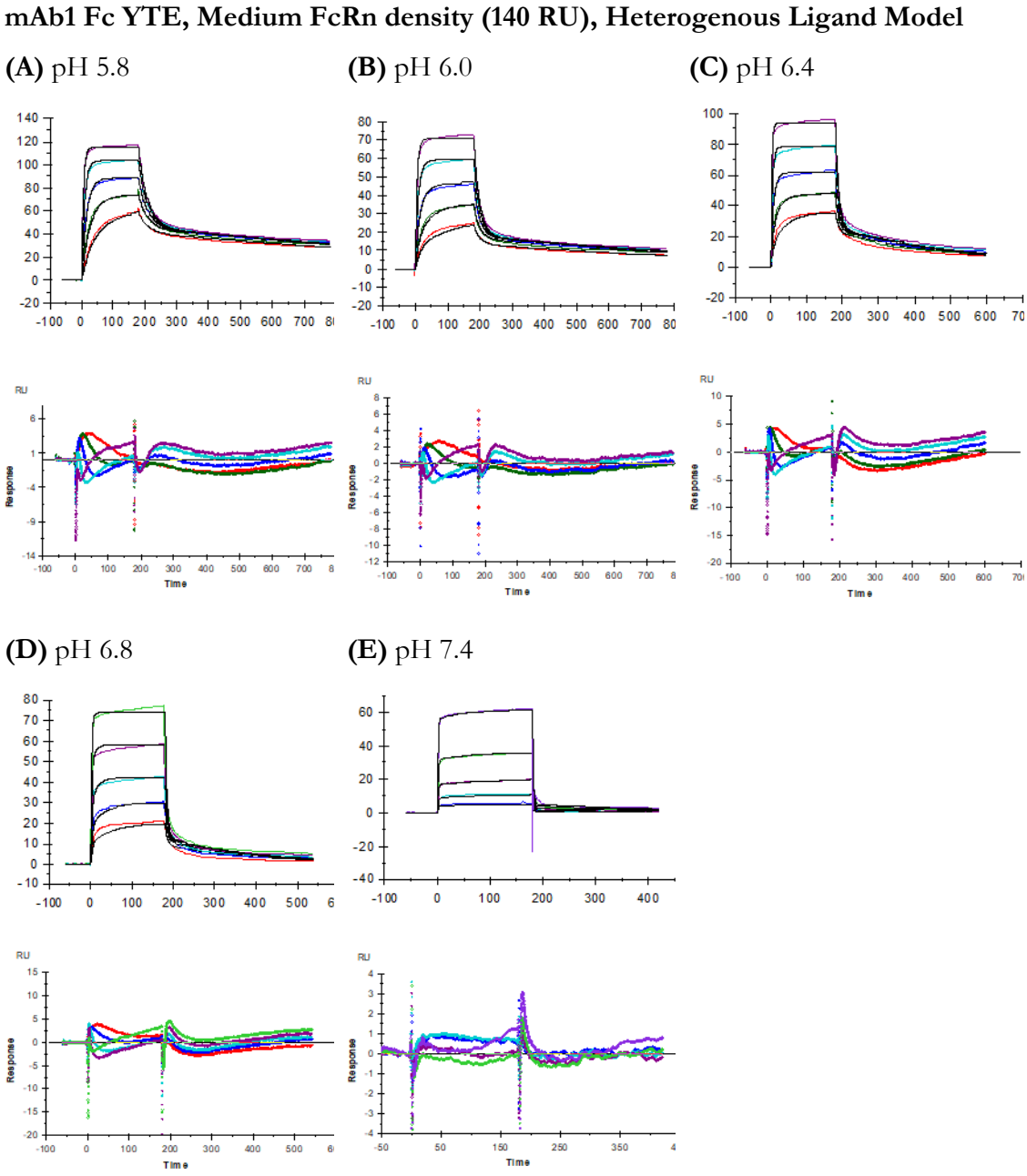

Figure S 10. SPR Sensorgrams of hFcRn (immobilized) and a hIgG1 (mAb1) Fc YTE variant (in solution) from pH 5.8 to 7.4 on a C1 chip. FcRn (captured via Neutravidin) was captured on the surface at 140 RU (medium). MAb1 Fc YTE was injected in five different concentration as two-fold dilution series with a highest concentration of (A) 200 nM for pH 5.8, (B) 200 nM for pH 6.0, (C) 600 nM for pH 6.4, (D) 1500 nM for pH 6.8 and (E) 3000 nM for pH 7.4. Each plot shows the measured raw data and the applied heterogeneous Ligand Model (BiaEvaluation Software 3.1) as solid lines (black). The goodness of the fit was

evaluated by analyzing the residuals (lower panel). The residuals show a systematic pattern, which suggests that the model is not a good fit for the data and parameters are not reliable. The determined kinetic parameters are described in **Table S 5**.

Table S 5. Summary of SPR kinetic rate parameters of immobilized hFcRn (140 RU, medium density) and mAb1 Fc YTE in solution. The kinetic rate parameter are determined from analyzing the sensorgrams shown in **Figure S 10**. The k_{ON}, k_{OFF} and K_D values are results from a global heterogeneous ligand fit analysis ± fitting error (* kinetic rates are not reliable).

Sample / Density	pH	k_{ON1} ($M^{-1}s^{-1}$)	Err. k_{ON1} (M-1s-1)	k_{OFF1} (s^{-1})	Err. k_{OFF1} (s-1)	K_{D1} (M)	Err. K_{D1} (M)	$t_{1/2,1}$ (s)	R_{max1} (%)
mAb1 Fc YTE medium FcRn density	(A) 5.8	7.18E+05	1.86E+03	0.036	6.76E-05	5.06E-08	1.61E-10	19.1	65
	(B) 6.0	7.50E+05	1.94E+03	0.055	1.08E-04	7.31E-08	2.38E-10	12.6	79
	(C) 6.4	4.65E+05	2.19E+03	0.105	4.02E-04	2.26E-07	1.37E-09	6.6	79
	(D) 6.8	2.88E+05	1.70E+03	0.223	1.19E-03	7.74E-07	6.16E-09	3.1	88
	(E) 7.4 *	1.12E+05	3.28E+03	1.11	3.21E-02	9.91E-06	4.08E-07	0.6	97
	pH	k_{ON2} ($M^{-1}s^{-1}$)	Err. k_{ON2} (M-1s-1)	k_{OFF2} (s^{-1})	Err. k_{OFF2} (s-1)	K_{D2} (M)	Err. K_{D1} (M)	$t_{1/2,2}$ (s)	R_{max2} (%)
mAb1 Fc YTE medium FcRn density	(A) 5.8 *	1.14E+06	2.25E+03	6.60E-04	1.60E-06	5.79E-10	1.81E-12	1050.2	35
	(B) 6.0 *	7.00E+05	1.84E+03	1.08E-03	3.05E-06	1.54E-09	5.95E-12	641.8	21
	(C) 6.4 *	5.48E+05	3440.000	2.44E-03	7.99E-06	4.45E-09	3.15E-11	284.1	21
	(D) 6.8 *	1.44E+05	1370.000	4.53E-03	2.42E-05	3.15E-08	3.43E-10	153.0	12
	(E) 7.4 *	6.16E+03	1.31E+02	3.44E-03	7.28E-05	5.58E-07	1.68E-08	201.5	3

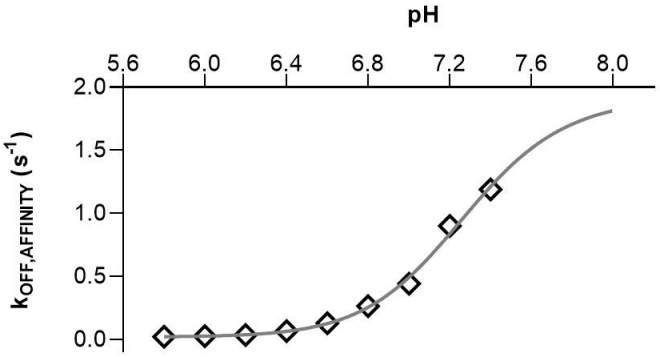

Figure S 11. The plot shows the affinity dissociation rates $k_{OFF,AFFINITY}$ in dependence of the pH ranging from 5.8 to 7.4 at a linear scale. Applying a Four Parameter Regression Model (grey) results in a transition point at pH 7.2.

7.2 Publication II: Supplementary Information

This Chapter contains the Supplementary Information of

TRIM21 and Fc-Engineered Antibodies: Decoding its complex Antibody Binding Mode with Implications for Viral Neutralization

Sample	k_a ($M^{-1}s^{-1}$)	Error k_a (M-1s-1)	k_{d1} (s^{-1})	Error k_d (s-1)	K_D (M)	Error K_D (M)	$t_{1/2}$ (s)	MW Ligand (Da)	Ligand Level, $R_{ligand\text{-}exp}$ (RU)	Ligand Binding Sites / Valency	MW Analyte (Da)	$R_{max,exp.}$ (RU)	$R_{max,theo.}$ (RU)	$R_{max,Ratio}$ (%)
mAb1 WT	2.33E+06	5.22E+03	9.94E-02	2.11E-04	4.27E-08	1.32E-10	7.0	146000	67.1	2	25714	22.9	23.64	97
mAb1 WT-AAA	2.66E+06	1.41E+04	1.05E-01	8.48E-04	3.95E-08	4.58E-10	6.6	146000	66.9	1	25714	11.2	11.78	95
mAb1 AAA	NA	NA	NA	NA	NA	NA	NA	NA	NA	NA	NA	NA	NA	NA

Table S 1. Summary of the SPR affinity measurements of immobilized mAb1 Fc variants and TRIM21 PRYSPRY domain in solution using a C1 chip. The kinetic rate parameters are determined from analyzing the sensorgrams shown in Figure 2. The k_{ON}, k_{OFF} and K_D values are results from a global fit analysis (Langmuir 1:1) ± fitting error.

(**A**) 10nM PRYSPRY domain

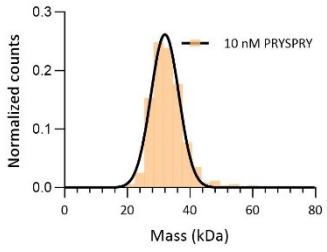

(**B**) 5 nM mAb1 variants

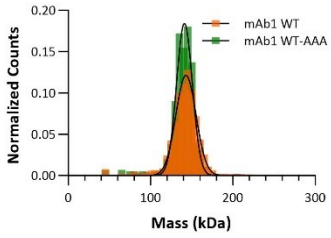

(**C**)

Sample	$Mass_{theo.}$ (kDa)	$Mass_{exp.}$ (kDa)
(A) PRYSPRY	25	32 ± 5
(B) mAb1 WT	146	143 ± 12
(B) mAb1 WT-AAA	146	141 ± 11

Figure S 1 Mass photometry measurements of individual PRYSPRY domain and mAb1 Fc Variants WT, WT-AAA (**A-C**). Molecular weight determined via mass photometry of individual PRYSPRY domain and mAb1 Fc variants WT, WT-AAA applying Gaussian distribution fit model to measurements. A single PRYSPRY domain appears on the lower limit of detection (25 kDa for Refeyn TwoMP, according to the manufacturer). Results shown in (**C**).

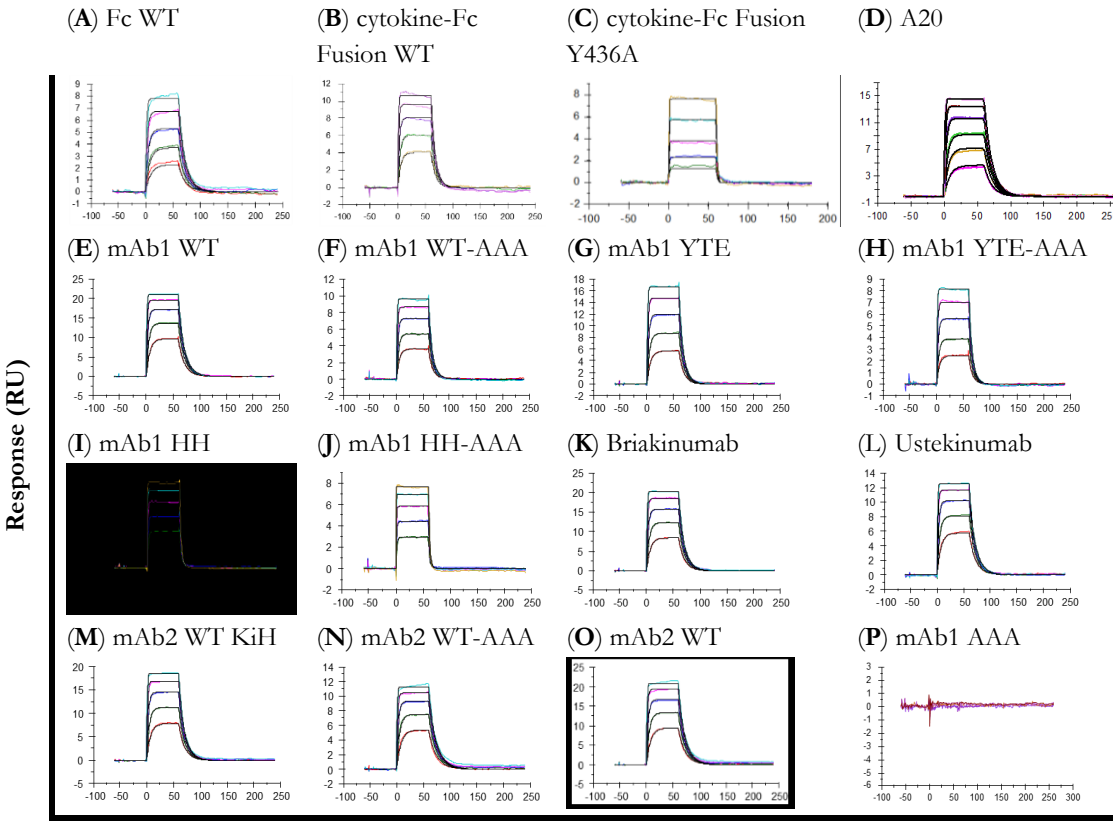

(Q)

Sample	k_{ON} ($M^{-1}s^{-1}$)	Error k_{ON} (M-1s-1)	k_{OFF} (s^{-1})	Error k_{OFF} (s-1)	K_D (M)	Error K_D (M)	$t_{1/2}$ (s)
(A) Fc WT	1.57E+06	1.84E-01	1.02E-01	1.40E-03	6.51E-08	8.89E-10	6.8
(B) cytokine-Fc Fusion WT	2.18E+06	2.20E+04	1.13E-01	1.10E-03	5.19E-08	7.27E-10	6.1
(C) cytokine-Fc Fusion Y436A	2.94E+05	2.10E+04	2.25E+00	1.60E-01	7.67E-06	7.72E-07	0.3
(D) A20	1.92E+06	8.20E+03	8.76E-02	2.60E-04	4.56E-08	2.37E-10	7.9
(E) mAb1 WT	2.33E+06	5.22E+03	9.94E-02	2.11E-04	4.27E-08	1.32E-10	7.0
(F) mAb1 WT-AAA	2.66E+06	1.41E+04	1.05E-01	8.48E-04	3.95E-08	4.58E-10	6.6
(G)mAb1 YTE	2.14E+06	1.05E+04	1.60E-01	7.67E-04	7.48E-08	5.13E-10	4.3
(H) mAb1 YTE-AAA	2.04E+06	1.55E+04	1.89E-01	1.40E-03	9.26E-08	9.83E-10	3.7
(I) mAb1 HH	4.74E+06	4.18E+04	4.77E-01	4.17E-03	1.01E-07	1.25E-09	1.5
(J) mAb1 HH-AAA	3.63E+06	4.67E+04	4.34E-01	5.49E-03	1.20E-07	2.16E-09	1.6
(K) Briakinumab	2.20E+06	7.49E+03	1.15E-01	3.74E-04	5.23E-08	2.46E-10	6.0
(L) Ustekinumab	2.46E+06	1.01E+04	1.04E-01	4.08E-04	4.23E-08	2.40E-10	6.7
(M) mAb2 WT KiH	2.38E+06	1.11E+04	1.18E-01	5.30E-04	4.96E-08	3.21E-10	5.9

(N) mAb2 WT-AAA	2.34E+06	2.21E+04	9.01E-02	8.12E-04	3.85E-08	5.03E-10	7.7
(O) mAb2 WT	2.09E+06	1.49E+04	9.30E-02	6.30E-04	4.45E-08	4.38E-10	7.5
(P) mAb1 AAA	NA	NA	NA	NA	NA	NA	NA

Figure S 2 SPR sensorgrams of (antibody) Fc constructs and variants captured onto the biosensor surface (immobilized ligand) and PRYSPRY domain in solution (analyte). PRYSPRY was injected in five different concentration as two-fold dilution series with a highest concentration of (**A-B, D-H, K-O**) 500 nM, (**C+P**) 2000 nM, (**I+J**) 1000 nM. Each plot shows the measured raw data (colored lines) and the global fit analysis as solid lines (black). (**Q**) Summary of the SPR derived kinetic rate parameters of affinity measurements The (antibody) Fc constructs are captured and TRIM21 PRYSPRY domain is in solution. The k_{ON}, k_{OFF} and K_D values are results from a global fit analysis ± fitting error.

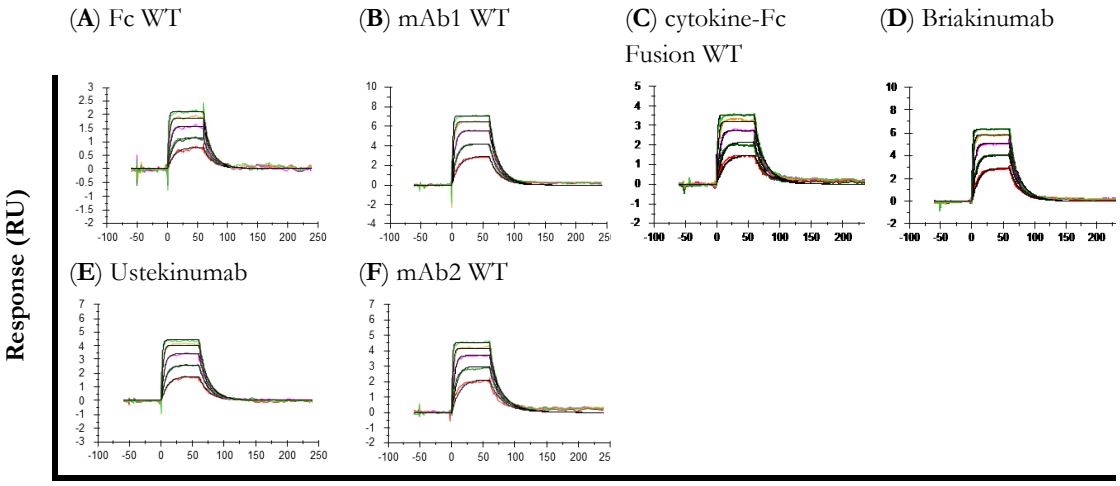

(G)							
Sample	**k_{ON} ($M^{-1}s^{-1}$)**	**Error k_{ON} (M-1s-1)**	**k_{OFF} (s^{-1})**	**Error k_{OFF} (s-1)**	**K_D (M)**	**Error K_D (M)**	**$t_{1/2}$ (s)**
(A) Fc WT	5.09E+06	1.33E+05	1.32E-01	3.40E-03	2.59E-08	9.52E-10	5.3
(B) mAb1 WT	4.36E+06	5.31E+04	9.15E-02	1.07E-03	2.10E-08	3.54E-10	7.6
(C) cytokine-Fc Fusion WT	5.88E+06	1.57E+05	1.19E-01	3.12E-03	2.02E-08	7.57E-10	5.8
(D) Briakinumab	6.14E+06	7.68E+04	1.02E-01	1.24E-03	1.66E-08	2.90E-10	6.8
(E) Ustekinumab	3.89E+06	3.76E+04	8.84E-02	8.18E-04	2.27E-08	3.04E-10	7.8
(F) mAb2 WT	7.36E+06	1.74E+05	1.20E-01	2.78E-03	1.63E-08	5.40E-10	5.8

Figure S 3 SPR sensorgrams of PRYSPRY domain immobilized onto the biosensor surface (ligand) and (antibody) Fc constructs and variants in solution (analyte). Fc variants were injected in five different concentrations as two-fold dilution series with a highest concentration of (A-F) 200 nM. Each plot shows the measured raw data (coloured lines) and the global fit analysis as solid lines (black). The interaction is described by a monophasic fit model reflecting the affinity binding mode. (G) Summary of the SPR derived kinetic rate parameters of affinity measurements. TRIM21 PRYSPRY domain is immobilized and (antibody) Fc constructs are in solution. The k_{ON}, k_{OFF} and K_D values are results from a global fit analysis ± fitting error.

(**A**)

				TRIM21 CC + mAb1 Fc variants: Molar Ratios								
				mAb1 WT			mAb1 WT-AAA			mAb1 AAA		
	Molar Ratio T21-CC:mAb1	Species	$Mass_{exp.}$ (kDa)	Mean (kDa)	SD (kDa)	Gaussian Fit (%)	Mean (kDa)	SD (kDa)	Gaussian Fit (%)	Mean (kDa)	SD (kDa)	Gaussian Fit (%)
T21-CC 2.5 nM & mAb1 7.5 nM	1:3	T21	86	75	12.6	3	76	14.9	6	77	17.9	4
		IgG	146	144	12.9	92	144	13.8	90	141	13.9	94
		T21-IgG	232	228	40	1.4	NA	NA	NA	NA	NA	NA
T21-CC 5 nM & mAb1 5 nM	1:1	T21	86	74	16.8	10	75	15	17	75	16	18
		IgG	146	148	13.2	78	145	12.3	80	144	12.5	80
		T21-IgG	232	236	13.8	7	228	45	1.8	NA	NA	NA
T21-CC 7.5 nM & mAb1 2.5 nM	3:1	T21	86	76	12.4	32	76	13.9	33			
		IgG	146	141	11.2	51	145	14.1	64			
		T21-IgG	232	231	12.7	15	240	45	2			
T21-CC 22.5 nM & mAb1 2.5 nM	10:1	T21	86	75	14.5	63	75	14.9	66	75	14.1	66
		IgG	146	138	18.5	9	144	26	34	141	23	33
		T21-IgG	232	233	16.7	24	234	45	1.6	NA	NA	NA

(**B**)

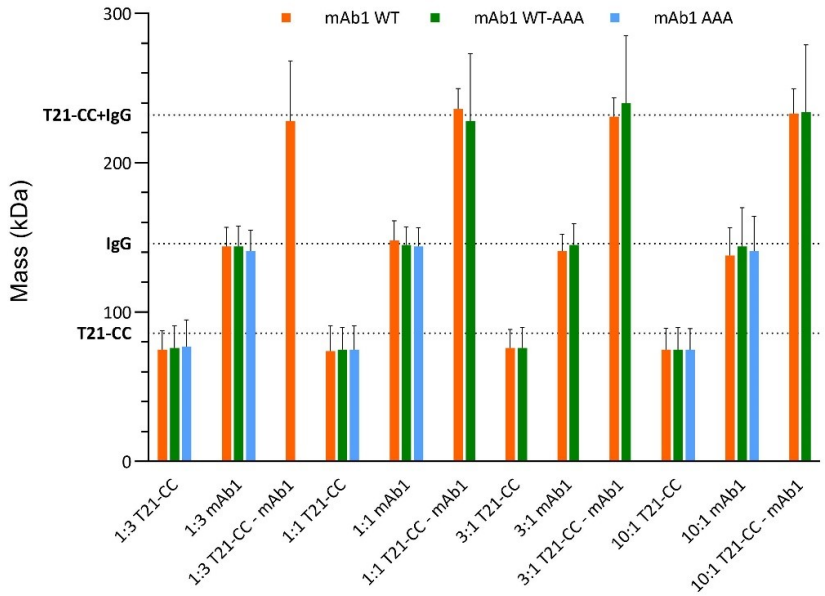

Figure S 4 Molecular weight determined via mass photometry of TRIM21-CC complexed with mAb1 Fc variants WT, WT-AAA and AAA applying Gaussian Distribution Fit Model (**A**). (**B**) Data from (A) is visualized applying Gaussian Distribution Fit Model over the applied stoichiometric ratios.

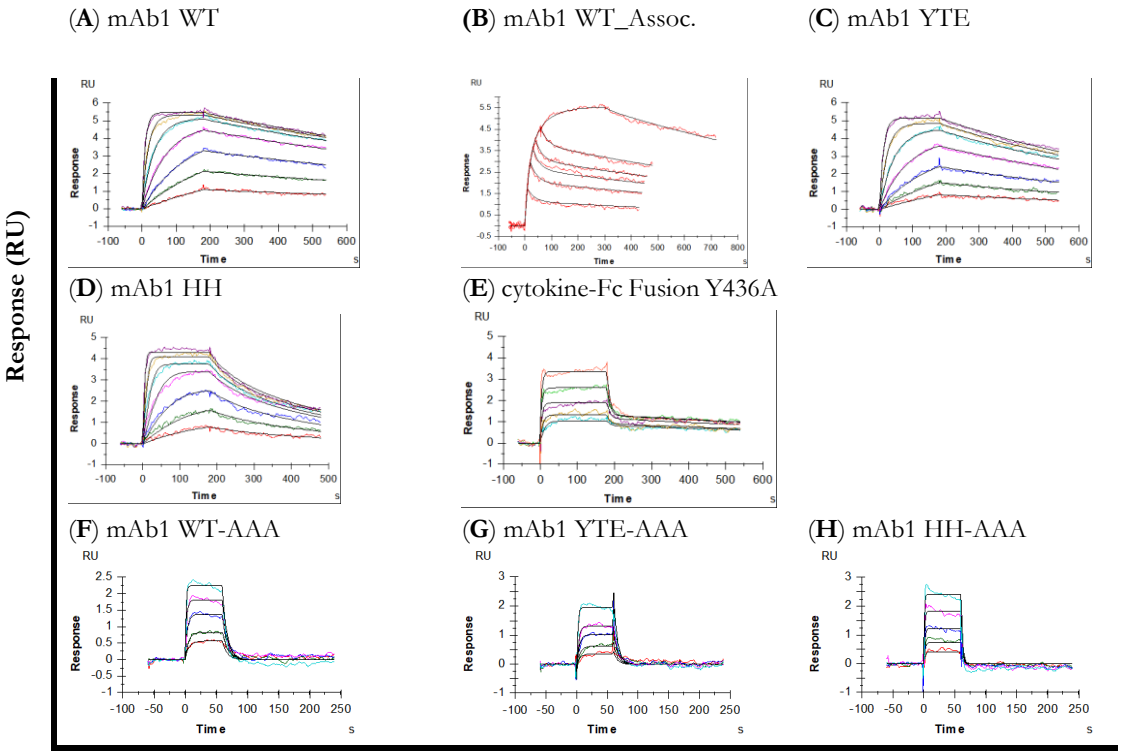

(**I**)

Sample	k_{ON} ($M^{-1}s^{-1}$)	Error k_{ON} (M-1s-1)	k_{OFF} (s^{-1})	Error k_{OFF} (s-1)	K_D (M)	Error K_D (M)	$t_{1/2}$ (s)
(**A**) TRIM21-CC - mAb1 WT	1.11E+06	1.30E+03	7.62E-04	9.30E-07	6.873E-10	1.16E-12	910.2
(**C**) TRIM21-CC - mab1 YTE	8.65E+05	1.40E+03	1.27E-03	1.50E-06	1.466E-09	2.94E-12	546.6
(**D**) TRIM21-CC - mAb1 HH	4.74E+06	3.90E+04	6.51E-03	4.00E-05	1.374E-09	1.41E-11	106.5
(**E**) TRIM21-CC - cytokine-Fc Fusion Y436A	2.46E+05	3.70E+03	0.132	0.0012	5.359E-07	9.41E-09	5.3
(**F**) TRIM21-CC - mAb1 WT-AAA	1.10E+06	2.00E+04	0.1285	0.0013	1.165E-07	2.42E-09	5.4
(**G**) TRIM21-CC - mab1 YTE-AAA	7.58E+05	1.40E+04	0.1669	0.0015	2.201E-07	4.52E-09	4.2
(**H**) TRIM21-CC - mAb1 HH-AAA	9.21E+05	2.10E+04	0.4367	0.0085	4.742E-07	1.42E-08	1.6

(**J**)

Sample	k_{ON1} ($M^{-1}s^{-1}$)	Error k_{ON1} (M-1s-1)	k_{OFF1} (s^{-1})	Error k_{OFF1} (s-1)	k_{ON2} (s^{-1})	Error k_{ON2} (s-1)	k_{OFF2} (s^{-1})	Error k_{OFF2} (s-1)	K_D (M)	Error K_D (M)
(**B**) mAb1 WT_Assoc	2.04E+06	1.40E+04	0.01885	1.90E-04	0.02228	1.10E-04	0.001669	6.80E-06	**6.44E-10**	1.13E-10

Figure S 5 SPR sensorgrams of (antibody) Fc variants (symmetric and asymmetric) immobilized onto the biosensor surface (ligand) and TRIM21-CC in solution (analyte). TRIM21-CC was injected in several different concentrations as two-fold dilution series with a highest concentration of (**A, C-D**) 100 nM, (**B**) 25 nM, (**E**) 400 nM, (**F-G**) 500 nM and (**H**) 1000 nM. Each plot shows the measured raw data (coloured lines) and the global fit analysis as solid lines (black). The interaction is described by a monophasic fit model, reflecting the

affinity (**F - H**) or avidity (**A –E**) binding mode, expected for (**B**) where the two state model was applied. (**I-J**) Summary of the SPR derived kinetic rate parameters of affinity and avidity measurements.(**I**) The k_{ON}, k_{OFF} and K_D values are results from a global fit analysis ± fitting error (1:1 Langmuir Fit). (**J**) 25nM of TRIM21-CC are injected with different association times (10 sec - 300 sec). The k_{ON}, k_{OFF} and K_D values are results from a global fit analysis ± fitting error (Two State Model).

(**A**) 5nM mAb2 WT

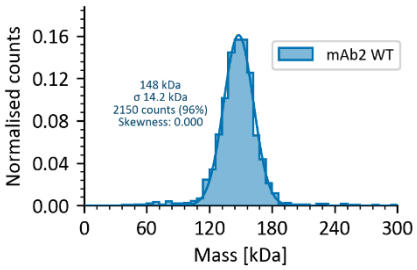

(**B**) Fc WT / cytokine-Fc Fusion WT / cytokine-Fc Fusion WT-AAA (equivalent mass to cytokine-Fc Fusion Y436A)

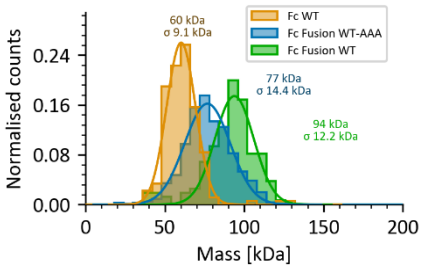

(**C**) mAb1 WT / YTE / HH

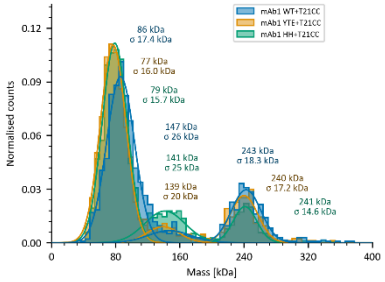

(**D**) mAb 2 WT / WT-AAA

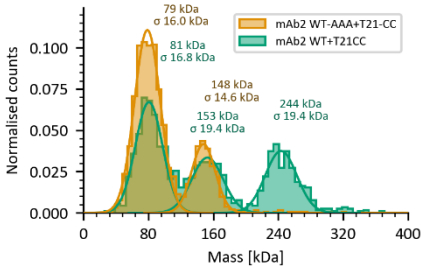

(**E**) Fc WT / WT-AAA

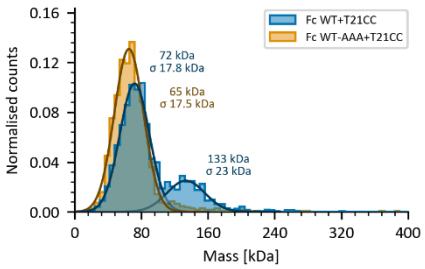

(**F**) cytokine-Fc Fusion WT / WT-AAA / Y436A

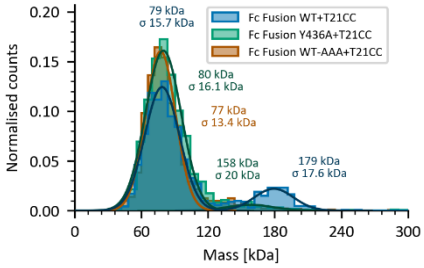

(**G**) mAb1 YTE-AAA / HH-AAA

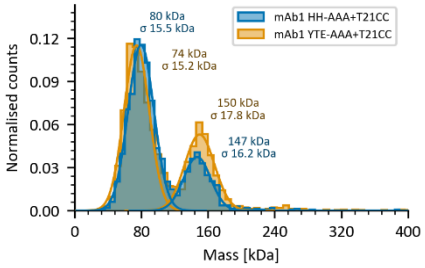

(**H**) Briakinumab / Ustekinumab

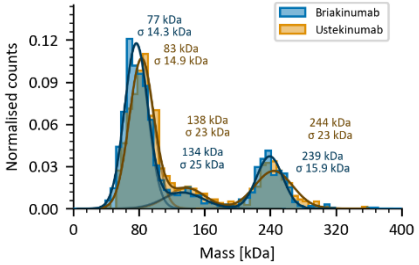

Figure S 6 Molecular weight determined via mass photometry of TRIM21-CC complexed with (antibody) Fc variants applying Gaussian Distribution Fit Model to the occurring

species. 2.5 nM Fc variants are measured in the presence of 22.5 nM TRIM21-CC using MP One device. Data is shown in **Table S 2**.

Controls / Individual Mass				
Sample	**$Mass_{theo.}$(kDa)**	**$Mass_{exp.}$ (kDa)**		**Gaussian Fit (%)**
(**A**) 5 nM mAb2 WT	146	148 ± 114		96
(**B**) Fc WT	52	60 ± 9		100
(**B**) cytokine-Fc Fusion WT-AAA (equals cytokine-Fc Fusion Y436A in mass)	71	77 ± 14		98
(**B**) Fc Fusion WT	91	94 ± 12		93
TRIM21 CC (22.5nM) + Fc variants (2.5 nM): Molar Ratio 10:1				
Sample: TRIM21-CC +		**Species**		
		TRIM21-CC	Fc variant	TRIM21-CC + Fc variant
(C) mAb1 WT				
$Mass_{theo.}$ (kDa)		86	146	232
$Mass_{exp.}$ (kDa) ± SD		86 ± 17	147 ± 26	243 ± 18
Gaussian Fit (%)		69	8	23
(C) mAb1 YTE				
$Mass_{theo.}$ (kDa)		86	146	232
$Mass_{exp.}$ (kDa) ± SD		77 ± 16	139 ± 20	240 ± 17
Gaussian Fit (%)		74	8	19
(C) mAb1 HH				
$Mass_{theo.}$ (kDa)		86	146	232
$Mass_{exp.}$ (kDa) ± SD		79 ± 16	141 ± 25	241 ± 15
Gaussian Fit (%)		73	19	12
(D) mAb2 WT				
$Mass_{theo.}$ (kDa)		86	146	232
$Mass_{exp.}$ (kDa) ± SD		81 ± 17	153 ± 20	244 ± 20
Gaussian Fit (%)		44	25	28
(D) mAb2 WT-AAA				
$Mass_{theo.}$ (kDa)		86	146	232
$Mass_{exp.}$ (kDa) ± SD		79 ± 16	148 ± 15	NA
Gaussian Fit (%)		74	25	NA
(E) Fc WT				
$Mass_{theo.}$ (kDa)		86	52	138
$Mass_{exp.}$ (kDa) ± SD		72 ± 18 (overlapping)		133 ± 23
Gaussian Fit (%)		77 (overlapping)		24
(E) Fc WT-AAA				
$Mass_{theo.}$ (kDa)		86	52	138
$Mass_{exp.}$ (kDa) ± SD		65 ± 18 (overlapping)		NA
Gaussian Fit (%)		96 (overlapping)		NA
(F) cytokine-Fc Fusion WT				
$Mass_{theo.}$ (kDa)		86	91	177
$Mass_{exp.}$ (kDa) ± SD		79 ± 16 (overlapping)		179 ± 18
Gaussian Fit (%)		82 (overlapping)		16
(F) cytokine-Fc Fusion Y436A				
$Mass_{theo.}$ (kDa)		86	71	157
$Mass_{exp.}$ (kDa) ± SD		80 ± 16 (overlapping)		158 ± 20
Gaussian Fit (%)		95 (overlapping)		4
(F) cytokine-Fc Fusion WT-AAA				
$Mass_{theo.}$ (kDa)		86	71	157
$Mass_{exp.}$ (kDa) ± SD		77 ± 14 (overlapping)		NA
Gaussian Fit (%)		90 (overlapping)		NA
(G) mAb1 YTE-AAA				

$Mass_{theo.}$ (kDa)		86	146	157
$Mass_{exp.}$ (kDa) ± SD				NA
Gaussian Fit (%)				NA
(G) mAb1 HH-AAA				
$Mass_{theo.}$ (kDa)		86	146	232
$Mass_{exp.}$ (kDa) ± SD		74 ± 15	150 ± 18	NA
Gaussian Fit (%)		63	34	NA
(H) BriakinumAb				
$Mass_{theo.}$ (kDa)		86	146	232
$Mass_{exp.}$ (kDa) ± SD		77 ± 14	134 ± 25	239 ± 16
Gaussian Fit (%)		64	11	23
(H) UstekinumAb				
$Mass_{theo.}$ (kDa)		86	146	232
$Mass_{exp.}$ (kDa) ± SD		83 ± 15	138 ± 23	244 ± 23
Gaussian Fit (%)		62	13	24

Table S 2 Molecular weight determined via mass photometry of TRIM21-CC complexed with (antibody) Fc variants applying Gaussian Distribution Fit Model. The mass photometry data was analyzed using the DiscoverMP 2.5.0 software.

(**A**) A20 WT

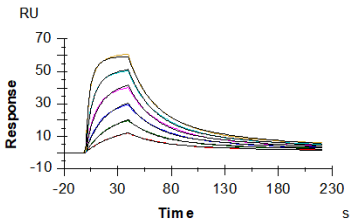

(**B**) A20 half WT

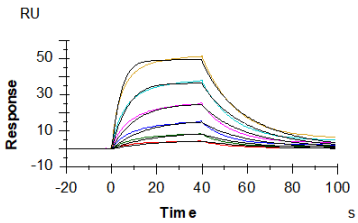

(**C**) A20 half WT-AAA

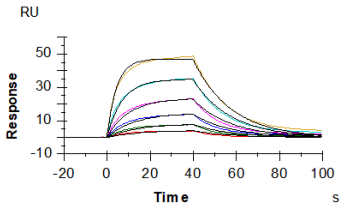

(**D**)

Sample	k_{ON1} ($M^{-1}s^{-1}$)	Error k_{ON1} ($M^{-1}s^{-1}$)	k_{OFF1} (s^{-1})	Error k_{OFF1} (s^{-1})	k_{ON2} (s^{-1})	Error k_{ON2} (s^{-1})	k_{OFF2} (s^{-1})	Error k_{OFF2} (s^{-1})	K_{D1} (M)	Error K_{D1} (M)	K_{D2} (M)	Error K_{D2} (M)
(**A**) A20 WT	5.91E+05	3.50E+03	0.04481	1.10E-04	1.46E+06	3.00E+03	0.007248	2.90E-05	7.59E-08	4.87E-10	4.96E-09	2.23E-11
(**B**) A20 half WT	7.33E+05	1.20E+04	0.06817	9.30E-04					9.31E-08	1.98E-09		
(**C**) A20 half WT-AAA	4.16E+05	2.50E+03	0.05738	1.00E-04					1.38E-07	8.63E-10		

Figure S 7 SPR sensorgrams of AAV2 immobilized (standard amine coupling) onto the biosensor surface and A20 antibody variants in solution. A20 variants were injected in six different concentrations as two-fold dilution series with a highest concentration of (**A**) 200 nM and (**B-C**) 400 nM. Each plot shows the measured raw data (colored lines) and the global fit analysis as solid lines (black). The interaction for (**B-C**) is described by a monophasic fit model, reflecting the affinity-binding mode. (**A**) is a bivalent analyte (A20 WT) and can be described by a heterogeneous model reflecting affinity and avidity. Kinetic rate parameters are displayed in (**D**). The k_{ON}, k_{OFF} and K_D values are results from a global fit analysis ± fitting error (Heterogeneous model (**A**) and 1:1 Langmuir Fit (**B-C**)).

(**A**) A20 WT / TRIM21-CC

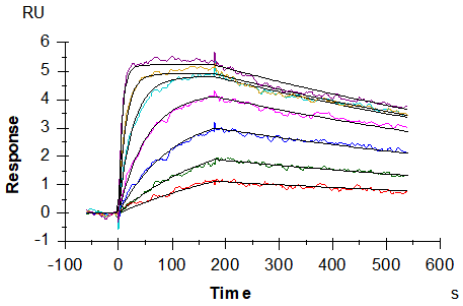

(**B**)

Sample	k_{ON} ($M^{-1}s^{-1}$)	Error k_{ON} ($M^{-1}s^{-1}$)	k_{OFF} (s^{-1})	Error k_{OFF} (s^{-1})	K_D (M)	Error K_D (M)	$t_{1/2}$ (s)
TRIM21-CC – A20 WT	1.44E+06	3.40E+03	9.83E-04	1.50E-06	6.847E-10	1.93E-12	705.4

Figure S 8 SPR sensorgrams of A20 WT immobilized onto the biosensor surface (ligand) and TRIM21-CC in solution (analyte). (**A**) TRIM21-CC was injected in several different concentrations as two-fold dilution series with a highest concentration of 100 nM. Each plot shows the measured raw data (coloured lines) and the global fit analysis as solid lines (black). (**B**) The interaction is described by a monophasic fit model, reflecting the avidity-binding mode. The k_{ON}, k_{OFF} and K_D values are results from a global fit analysis ± fitting error (1:1 Langmuir Fit).

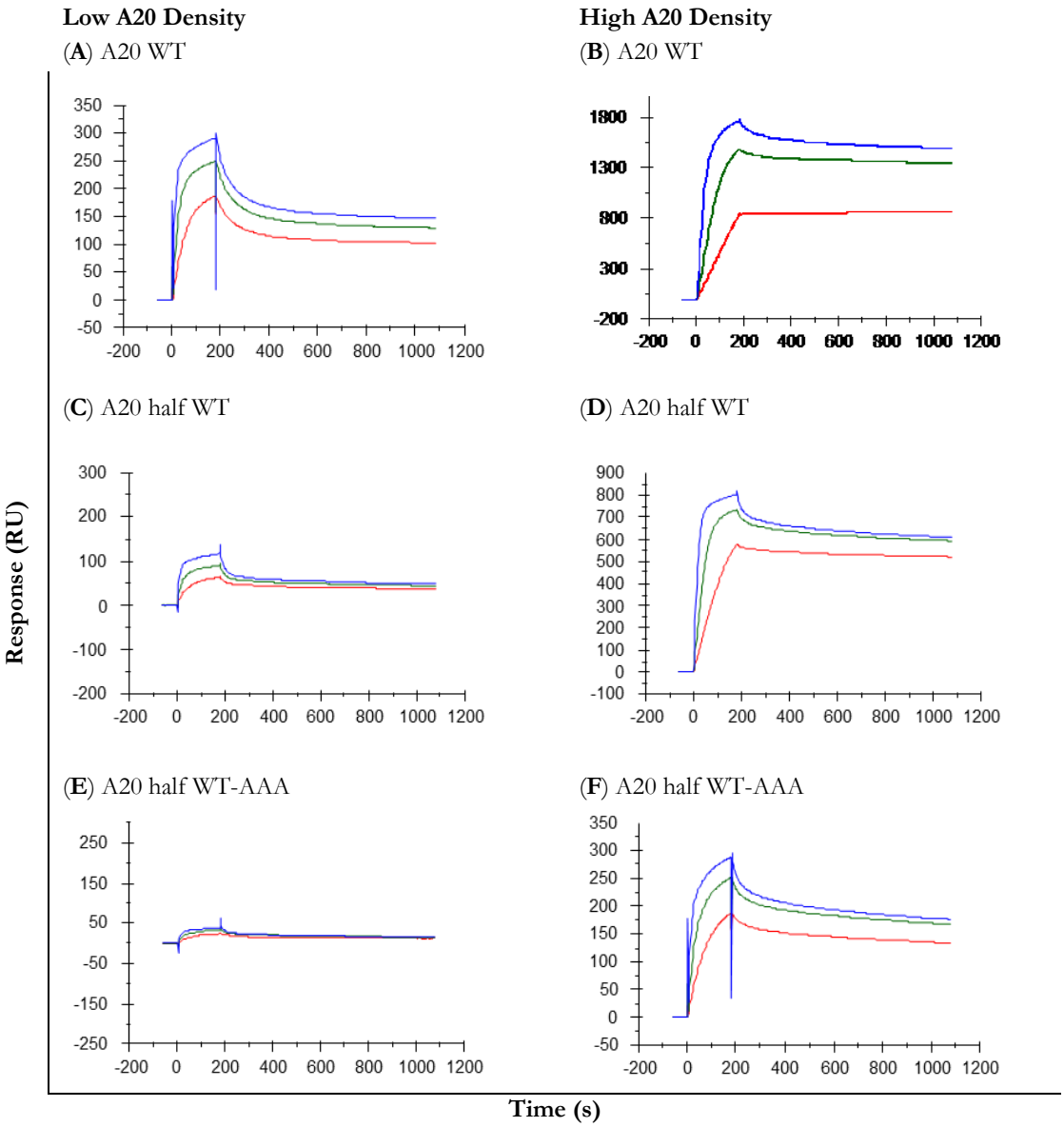

Figure S 9 SPR Sensorgrams showing AAV2 binding to captured anti-capsid antibody A20 variants on a low or high (8x) TRIM21-CC ligand density. Injections of 3 concentrations of rAAVv-2 3-fold dilution with a highest concentration of 3.32 nM.

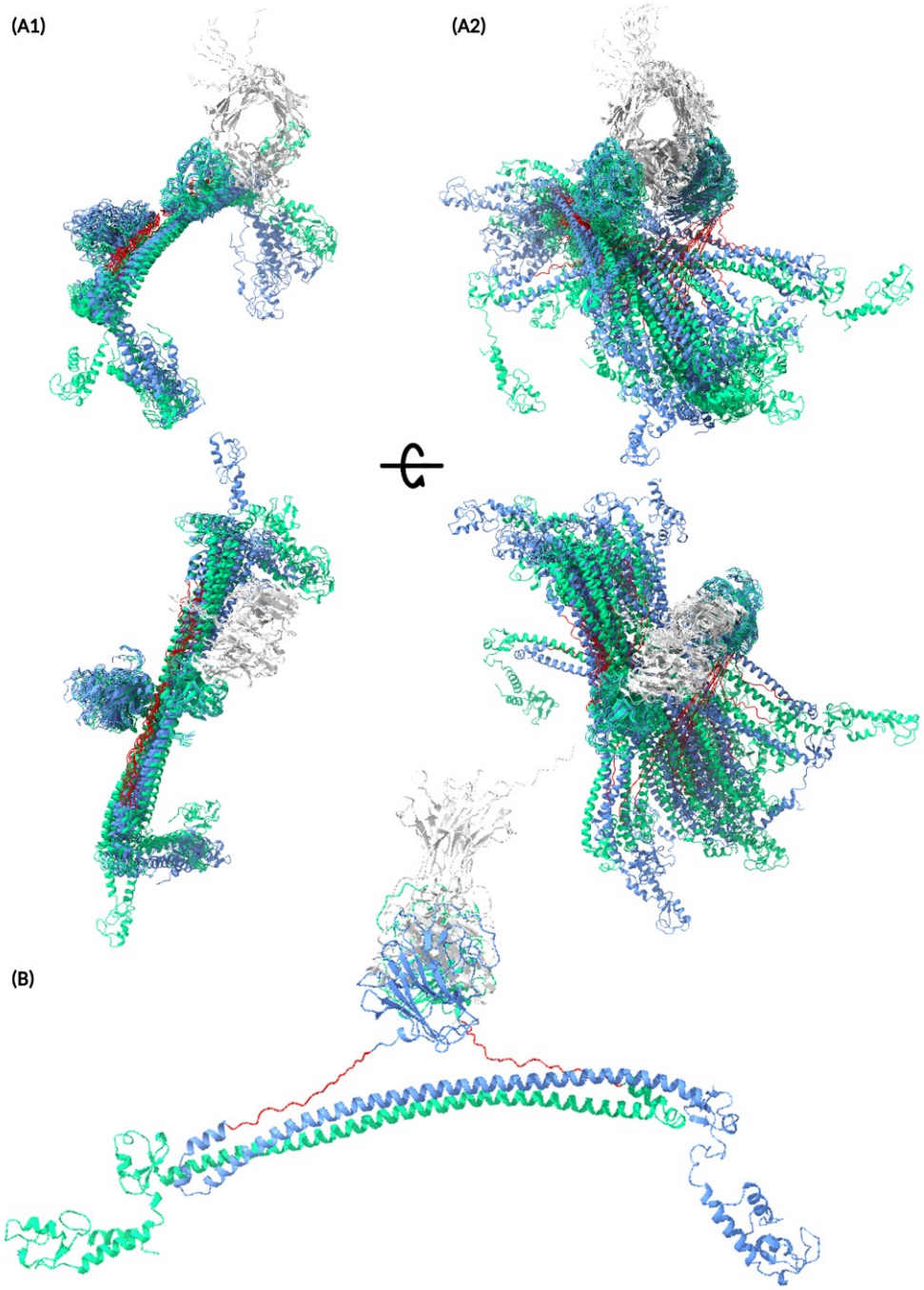

Figure S 10 Model predictions of TRIM21 and mode of action (PDB-ID: 2IWG, Uniprot ID P19474). (**A-B**) Structural predictions of alphafold of 2 copies of full length TRIM21 as well as an Fc domain. A minority of predictions maintain the association of the PRYSPRY domain with the coiled coil domain (**A1**) whereas the majority of structures release this association (**A2**). Variations in structural predictions for the coiled-coil domain are much higher when the PRYSPRY domain is not associating with it and the RBCC predictions vary highly after binding the Fc domain in both model variants. (**B**) Highlighted prediction of Alphafold2 for the TRIM21 - Fc complex showing dislodged PRYSPRY as well as variation in RB domain.

8

Bibliography

1. Lobo ED, Hansen RJ, Balthasar JP. Antibody Pharmacokinetics and Pharmacodynamics. *J Pharm Sci* (2004) 93(11):2645-68. Epub 2004/09/25. doi: 10.1002/jps.20178.

2. Cruse JM, Lewis RE. *Atlas of Immunology*. 3rd ed. Boca Raton, FL: CRC Press/Taylor & Francis (2010). 940 p. p.

3. Lefranc MPL, G. Immunoglobulins or Antibodies: Imgt((R)) Bridging Genes, Structures and Functions. *Biomedicines* (2020) 8(9). Epub 2020/09/04. doi: 10.3390/biomedicines8090319.

4. Schroeder HW, Jr., Cavacini L. Structure and Function of Immunoglobulins. *J Allergy Clin Immunol* (2010) 125(2 Suppl 2):S41-52. Epub 2010/03/05. doi: 10.1016/j.jaci.2009.09.046.

5. Janeway C, Travers P. *Immunobiology : The Immune System in Health and Disease*. 3rd ed. London; San Francisco; New York: Current Biology ; Garland Pub. (1997).

6. Kuijpers TW, Weening RS, Out TA. Igg Subclass Deficiencies and Recurrent Pyogenic Infections, Unresponsiveness against Bacterial Polysaccharide Antigens. *Allergol Immunopathol (Madr)* (1992) 20(1):28-34. Epub 1992/01/01.

7. Nahm MH, Scott MG, Shackelford PG. Expression of Human Igg Subclasses. *Ann Clin Lab Sci* (1987) 17(3):183-96. Epub 1987/05/01.

8. Sandin S, Ofverstedt LG, Wikstrom AC, Wrange O, Skoglund U. Structure and Flexibility of Individual Immunoglobulin G Molecules in Solution. *Structure* (2004) 12(3):409-15. Epub 2004/03/16. doi: 10.1016/j.str.2004.02.011.

9. Murphy K, Weaver C. *Janeway's Immunobiology*. 9th edition. ed. New York, NY: Garland Science/Taylor & Francis Group, LLC (2016). xx, 904 pages p.

10. Jefferis R. Recombinant Antibody Therapeutics: The Impact of Glycosylation on Mechanisms of Action. *Trends Pharmacol Sci* (2009) 30(7):356-62. Epub 2009/06/26. doi: 10.1016/j.tips.2009.04.007.

11. Mould DR, Green B. Pharmacokinetics and Pharmacodynamics of Monoclonal Antibodies: Concepts and Lessons for Drug Development. *BioDrugs* (2010) 24(1):23-39. Epub 2010/01/09. doi: 10.2165/11530560-000000000-00000.

12. Reff ME, Heard C. A Review of Modifications to Recombinant Antibodies: Attempt to Increase Efficacy in Oncology Applications. *Crit Rev Oncol Hematol* (2001) 40(1):25-35. Epub 2001/10/02. doi: 10.1016/s1040-8428(01)00132-9.

13. Kaveri SV, Lecerf M, Saha C, Kazatchkine MD, Lacroix-Desmazes S, Bayry J. Intravenous Immunoglobulin and Immune Response. *Clin Exp Immunol* (2014) 178 Suppl 1(Suppl 1):94-6. Epub 2014/12/30. doi: 10.1111/cei.12526.

14. Sedlacek HH, Gronski P, Hofstaetter T, Kanzy EJ, Schorlemmer HU, Seiler FR. The Biological Properties of Immunoglobulin G and Its Split Products [F(Ab')2 and Fab]. *Klin Wochenschr* (1983) 61(15):723-36. Epub 1983/08/01. doi: 10.1007/BF01497399.

15. Sanders LA, Feldman RG, Voorhorst-Ogink MM, de Haas M, Rijkers GT, Capel PJ, et al. Human Immunoglobulin G (Igg) Fc Receptor Iia (Cd32) Polymorphism and Igg2-Mediated Bacterial Phagocytosis by Neutrophils. *Infect Immun* (1995) 63(1):73-81. Epub 1995/01/01. doi: 10.1128/iai.63.1.73-81.1995.

16. Raghavan M, Bjorkman PJ. Fc Receptors and Their Interactions with Immunoglobulins. *Annu Rev Cell Dev Biol* (1996) 12:181-220. Epub 1996/01/01. doi: 10.1146/annurev.cellbio.12.1.181.

17. Tay MZ, Wiehe K, Pollara J. Antibody-Dependent Cellular Phagocytosis in Antiviral Immune Responses. *Front Immunol* (2019) 10:332. Epub 2019/03/16. doi: 10.3389/fimmu.2019.00332.

18. Montano RF, Morrison SL. Influence of the Isotype of the Light Chain on the Properties of Igg. *J Immunol* (2002) 168(1):224-31. Epub 2001/12/26. doi: 10.4049/jimmunol.168.1.224.

19. Pyzik M, Kozicky LK, Gandhi AK, Blumberg RS. The Therapeutic Age of the Neonatal Fc Receptor. *Nat Rev Immunol* (2023) 23(7):415-32. Epub 2023/02/03. doi: 10.1038/s41577-022-00821-1.

20. Mallery DL, McEwan WA, Bidgood SR, Towers GJ, Johnson CM, James LC. Antibodies Mediate Intracellular Immunity through Tripartite Motif-Containing 21 (Trim21). *Proc National Acad Sci* (2010) 107(46):19985-90. doi: 10.1073/pnas.1014074107.

21. Crescioli S, Kaplon H, Chenoweth A, Wang L, Visweswaraiah J, Reichert JM. Antibodies to Watch in 2024. *MAbs* (2024) 16(1):2297450. Epub 2024/01/05. doi: 10.1080/19420862.2023.2297450.

22. Nelson AL, Dhimolea E, Reichert JM. Development Trends for Human Monoclonal Antibody Therapeutics. *Nat Rev Drug Discov* (2010) 9(10):767-74. Epub 2010/09/03. doi: 10.1038/nrd3229.

23. Kohler G, Milstein C. Continuous Cultures of Fused Cells Secreting Antibody of Predefined Specificity. *Nature* (1975) 256(5517):495-7. Epub 1975/08/07. doi: 10.1038/256495a0.

24. Beck A, Wurch T, Bailly C, Corvaia N. Strategies and Challenges for the Next Generation of Therapeutic Antibodies. *Nat Rev Immunol* (2010) 10(5):345-52. Epub 2010/04/24. doi: 10.1038/nri2747.

25. Kaplon H, Crescioli S, Chenoweth A, Visweswaraiah J, Reichert JM. Antibodies to Watch in 2023. *MAbs* (2023) 15(1):2153410. Epub 2022/12/07. doi: 10.1080/19420862.2022.2153410.

26. Almagro JC, Daniels-Wells TR, Perez-Tapia SM, Penichet ML. Progress and Challenges in the Design and Clinical Development of Antibodies for Cancer Therapy. *Front Immunol* (2017) 8:1751. Epub 2018/01/31. doi: 10.3389/fimmu.2017.01751.

27. Hust M, Frenzel A, Meyer T, Schirrmann T, Dubel S. Construction of Human Naive Antibody Gene Libraries. *Methods Mol Biol* (2012) 907:85-107. Epub 2012/08/22. doi: 10.1007/978-1-61779-974-7_5.

28. Booth BJ, Ramakrishnan B, Narayan K, Wollacott AM, Babcock GJ, Shriver Z, et al. Extending Human Igg Half-Life Using Structure-Guided Design. *MAbs* (2018) 10(7):1098-110. Epub 2018/06/28. doi: 10.1080/19420862.2018.1490119.

29. Foss S, Watkinson RE, Grevys A, McAdam MB, Bern M, Høydahl LS, et al. Trim21 Immune Signaling Is More Sensitive to Antibody Affinity Than Its Neutralization Activity. *J Immunol* (2016) 196(8):3452-9. doi: 10.4049/jimmunol.1502601.

30. Ng PML, Kaliaperumal N, Lee CY, Chin WJ, Tan HC, Au VB, et al. Enhancing Antigen Cross-Presentation in Human Monocyte-Derived Dendritic Cells by Recruiting the Intracellular Fc Receptor Trim21. *J Immunol* (2019) 202(8):2307-19. doi: 10.4049/jimmunol.1800462.

31. Brinkmann U, Kontermann RE. The Making of Bispecific Antibodies. *MAbs* (2017) 9(2):182-212. Epub 2017/01/11. doi: 10.1080/19420862.2016.1268307.

32. Kontermann RE, Brinkmann U. Bispecific Antibodies. *Drug Discov Today* (2015) 20(7):838-47. Epub 2015/03/03. doi: 10.1016/j.drudis.2015.02.008.

33. Brambell FW. The Transmission of Immunity from Mother to Young and the Catabolism of Immunoglobulins. *Lancet* (1966) 2(7473):1087-93. Epub 1966/11/19. doi: 10.1016/s0140-6736(66)92190-8.

34. Brambell FW, Hemmings WA, Morris IG. A Theoretical Model of Gamma-Globulin Catabolism. *Nature* (1964) 203(4952):1352-4. Epub 1964/09/26. doi: 10.1038/2031352a0.

35. Junghans RP. Finally! The Brambell Receptor (Fcrb). Mediator of Transmission of Immunity and Protection from Catabolism for Igg. *Immunol Res* (1997) 16(1):29-57. Epub 1997/02/01. doi: 10.1007/BF02786322.

36. Simister NE, Rees AR. Isolation and Characterization of an Fc Receptor from Neonatal Rat Small Intestine. *Eur J Immunol* (1985) 15(7):733-8. Epub 1985/07/01. doi: 10.1002/eji.1830150718.

37. Simister NE, Mostov KE. An Fc Receptor Structurally Related to Mhc Class I Antigens. *Nature* (1989) 337(6203):184-7. Epub 1989/01/12. doi: 10.1038/337184a0.

38. Bjorkman PJ, Parham P. Structure, Function, and Diversity of Class I Major Histocompatibility Complex Molecules. *Annu Rev Biochem* (1990) 59:253-88. Epub 1990/01/01. doi: 10.1146/annurev.bi.59.070190.001345.

39. Bjorkman PJ, Saper MA, Samraoui B, Bennett WS, Strominger JL, Wiley DC. The Foreign Antigen Binding Site and T Cell Recognition Regions of Class I Histocompatibility Antigens. *Nature* (1987) 329(6139):512-8. Epub 1987/10/08. doi: 10.1038/329512a0.

40. Bjorkman PJ, Saper MA, Samraoui B, Bennett WS, Strominger JL, Wiley DC. Structure of the Human Class I Histocompatibility Antigen, Hla-A2. *Nature* (1987) 329(6139):506-12. Epub 1987/10/08. doi: 10.1038/329506a0.

41. Garrett TP, Saper MA, Bjorkman PJ, Strominger JL, Wiley DC. Specificity Pockets for the Side Chains of Peptide Antigens in Hla-Aw68. *Nature* (1989) 342(6250):692-6. Epub 1989/12/07. doi: 10.1038/342692a0.

42. Huber AH, Kelley RF, Gastinel LN, Bjorkman PJ. Crystallization and Stoichiometry of Binding of a Complex between a Rat Intestinal Fc Receptor and Fc. *J Mol Biol* (1993) 230(3):1077-83. Epub 1993/04/05. doi: 10.1006/jmbi.1993.1220.

43. Burmeister WP, Gastinel LN, Simister NE, Blum ML, Bjorkman PJ. Crystal Structure at 2.2 a Resolution of the Mhc-Related Neonatal Fc Receptor. *Nature* (1994) 372(6504):336-43. Epub 1994/11/24. doi: 10.1038/372336a0.

44. Burmeister WP, Huber AH, Bjorkman PJ. Crystal Structure of the Complex of Rat Neonatal Fc Receptor with Fc. *Nature* (1994) 372(6504):379-83. Epub 1994/11/24. doi: 10.1038/372379a0.

45. Pyzik M, Sand KMK, Hubbard JJ, Andersen JT, Sandlie I, Blumberg RS. The Neonatal Fc Receptor (Fcrn): A Misnomer? *Front Immunol* (2019) 10:1540. Epub 2019/07/30. doi: 10.3389/fimmu.2019.01540.

46. Firan M, Bawdon R, Radu C, Ober RJ, Eaken D, Antohe F, et al. The Mhc Class I-Related Receptor, Fcrn, Plays an Essential Role in the Maternofetal Transfer of Gamma-Globulin in Humans. *Int Immunol* (2001) 13(8):993-1002. Epub 2001/07/27. doi: 10.1093/intimm/13.8.993.

47. Jauniaux E, Jurkovic D, Gulbis B, Liesnard C, Lees C, Campbell S. Materno-Fetal Immunoglobulin Transfer and Passive Immunity During the First Trimester of Human Pregnancy. *Hum Reprod* (1995) 10(12):3297-300. Epub 1995/12/01. doi: 10.1093/oxfordjournals.humrep.a135906.

48. Malek A, Sager R, Kuhn P, Nicolaides KH, Schneider H. Evolution of Maternofetal Transport of Immunoglobulins During Human Pregnancy. *Am J Reprod Immunol* (1996) 36(5):248-55. Epub 1996/11/01. doi: 10.1111/j.1600-0897.1996.tb00172.x.

49. Latvala S, Jacobsen B, Otteneder MB, Herrmann A, Kronenberg S. Distribution of Fcrn across Species and Tissues. *J Histochem Cytochem* (2017) 65(6):321-33. Epub 2017/04/14. doi: 10.1369/0022155417705095.

50. Roopenian DC, Akilesh S. Fcrn: The Neonatal Fc Receptor Comes of Age. *Nat Rev Immunol* (2007) 7(9):715-25. Epub 2007/08/19. doi: 10.1038/nri2155.

51. Zhu X, Meng G, Dickinson BL, Li X, Mizoguchi E, Miao L, et al. Mhc Class I-Related Neonatal Fc Receptor for Igg Is Functionally Expressed in Monocytes, Intestinal Macrophages, and Dendritic Cells. *J Immunol* (2001) 166(5):3266-76. Epub 2001/02/24. doi: 10.4049/jimmunol.166.5.3266.

52. Fan YY, Farrokhi V, Caiazzo T, Wang M, O'Hara DM, Neubert H. Human Fcrn Tissue Expression Profile and Half-Life in Pbmcs. *Biomolecules* (2019) 9(8). Epub 2019/08/25. doi: 10.3390/biom9080373.

53. Ward ES, Ober RJ. Chapter 4: Multitasking by Exploitation of Intracellular Transport Functions the Many Faces of Fcrn. *Adv Immunol* (2009) 103:77-115. Epub 2009/09/17. doi: 10.1016/S0065-2776(09)03004-1.

54. D'Hooghe L, Chalmers AD, Heywood S, Whitley P. Cell Surface Dynamics and Cellular Distribution of Endogenous Fcrn. *PLoS ONE* (2017) 12(8):e0182695. Epub 2017/08/18. doi: 10.1371/journal.pone.0182695.

55. Bern M, Sand KM, Nilsen J, Sandlie I, Andersen JT. The Role of Albumin Receptors in Regulation of Albumin Homeostasis: Implications for Drug Delivery. *J Control Release* (2015) 211:144-62. Epub 2015/06/10. doi: 10.1016/j.jconrel.2015.06.006.

56. Blumberg LJ, Humphries JE, Jones SD, Pearce LB, Holgate R, Hearn A, et al. Blocking Fcrn in Humans Reduces Circulating Igg Levels and Inhibits Igg Immune Complex-Mediated Immune Responses. *Sci Adv* (2019) 5(12):eaax9586. Epub 2020/01/04. doi: 10.1126/sciadv.aax9586.

57. Chaudhury C, Mehnaz S, Robinson JM, Hayton WL, Pearl DK, Roopenian DC, et al. The Major Histocompatibility Complex-Related Fc Receptor for Igg (Fcrn) Binds Albumin and Prolongs Its Lifespan. *J Exp Med* (2003) 197(3):315-22. Epub 2003/02/05. doi: 10.1084/jem.20021829.

58. Ghetie V, Ward ES. Multiple Roles for the Major Histocompatibility Complex Class I- Related Receptor Fcrn. *Annu Rev Immunol* (2000) 18:739-66. Epub 2000/06/03. doi: 10.1146/annurev.immunol.18.1.739.

59. Roopenian DC, Christianson GJ, Sproule TJ, Brown AC, Akilesh S, Jung N, et al. The Mhc Class I-Like Igg Receptor Controls Perinatal Igg Transport, Igg Homeostasis, and Fate of Igg-Fc-Coupled Drugs. *J Immunol* (2003) 170(7):3528-33. Epub 2003/03/21. doi: 10.4049/jimmunol.170.7.3528.

60. Schmidt MM, Townson SA, Andreucci AJ, King BM, Schirmer EB, Murillo AJ, et al. Crystal Structure of an Hsa/Fcrn Complex Reveals Recycling by Competitive Mimicry of Hsa Ligands at a Ph-Dependent Hydrophobic Interface. *Structure* (2013) 21(11):1966-78. Epub 2013/10/15. doi: 10.1016/j.str.2013.08.022.

61. Ward ES, Gelinas D, Dreesen E, Van Santbergen J, Andersen JT, Silvestri NJ, et al. Clinical Significance of Serum Albumin and Implications of Fcrn Inhibitor Treatment in Igg-Mediated Autoimmune Disorders. *Front Immunol* (2022) 13:892534. Epub 2022/06/28. doi: 10.3389/fimmu.2022.892534.

62. Dickinson BL, Badizadegan K, Wu Z, Ahouse JC, Zhu X, Simister NE, et al. Bidirectional Fcrn-Dependent Igg Transport in a Polarized Human Intestinal Epithelial Cell Line. *J Clin Invest* (1999) 104(7):903-11. Epub 1999/10/08. doi: 10.1172/JCI6968.

63. Jones EA, Waldmann TA. The Mechanism of Intestinal Uptake and Transcellular Transport of Igg in the Neonatal Rat. *J Clin Invest* (1972) 51(11):2916-27. Epub 1972/11/01. doi: 10.1172/JCI107116.

64. Kobayashi N, Suzuki Y, Tsuge T, Okumura K, Ra C, Tomino Y. Fcrn-Mediated Transcytosis of Immunoglobulin G in Human Renal Proximal Tubular Epithelial Cells. *Am J Physiol Renal Physiol* (2002) 282(2):F358-65. Epub 2002/01/15. doi: 10.1152/ajprenal.0164.2001.

65. Rodewald R. Selective Antibody Transport in the Proximal Small Intestine of the Neonatal Rat. *J Cell Biol* (1970) 45(3):635-40. Epub 1970/06/01. doi: 10.1083/jcb.45.3.635.

66. Spiekermann GM, Finn PW, Ward ES, Dumont J, Dickinson BL, Blumberg RS, et al. Receptor-Mediated Immunoglobulin G Transport across Mucosal Barriers in Adult Life: Functional Expression of Fcrn in the Mammalian Lung. *J Exp Med* (2002) 196(3):303-10. Epub 2002/08/07. doi: 10.1084/jem.20020400.

67. Yoshida M, Masuda A, Kuo TT, Kobayashi K, Claypool SM, Takagawa T, et al. Igg Transport across Mucosal Barriers by Neonatal Fc Receptor for Igg and Mucosal Immunity. *Springer Semin Immunopathol* (2006) 28(4):397-403. Epub 2006/10/20. doi: 10.1007/s00281-006-0054-z.

68. Baker K, Qiao SW, Kuo TT, Aveson VG, Platzer B, Andersen JT, et al. Neonatal Fc Receptor for Igg (Fcrn) Regulates Cross-Presentation of Igg Immune Complexes by Cd8-Cd11b+ Dendritic Cells. *Proc Natl Acad Sci U S A* (2011) 108(24):9927-32. Epub 2011/06/02. doi: 10.1073/pnas.1019037108.

69. Baker K, Rath T, Flak MB, Arthur JC, Chen Z, Glickman JN, et al. Neonatal Fc Receptor Expression in Dendritic Cells Mediates Protective Immunity against Colorectal Cancer. *Immunity* (2013) 39(6):1095-107. Epub 2013/12/03. doi: 10.1016/j.immuni.2013.11.003.

70. Qiao SW, Kobayashi K, Johansen FE, Sollid LM, Andersen JT, Milford E, et al. Dependence of Antibody-Mediated Presentation of Antigen on Fcrn. *Proc Natl Acad Sci U S A* (2008) 105(27):9337-42. Epub 2008/07/05. doi: 10.1073/pnas.0801717105.

71. Wang W, Lu P, Fang Y, Hamuro L, Pittman T, Carr B, et al. Monoclonal Antibodies with Identical Fc Sequences Can Bind to Fcrn Differentially with Pharmacokinetic Consequences. *Drug Metab Dispos* (2011) 39(9):1469-77. Epub 2011/05/26. doi: 10.1124/dmd.111.039453.

72. Ward ES, Devanaboyina SC, Ober RJ. Targeting Fcrn for the Modulation of Antibody Dynamics. *Mol Immunol* (2015) 67(2 Pt A):131-41. Epub 2015/03/15. doi: 10.1016/j.molimm.2015.02.007.

73. Ward ES, Velmurugan R, Ober RJ. Targeting Fcrn for Therapy: From Live Cell Imaging to in Vivo Studies in Mice. *Immunol Lett* (2014) 160(2):158-62. Epub 2014/02/28. doi: 10.1016/j.imlet.2014.02.008.

74. Baldwin WM, 3rd, Valujskikh A, Fairchild RL. The Neonatal Fc Receptor: Key to Homeostasic Control of Igg and Igg-Related Biopharmaceuticals. *Am J Transplant* (2019) 19(7):1881-7. Epub 2019/03/25. doi: 10.1111/ajt.15366.

75. Oganesyan V, Damschroder MM, Cook KE, Li Q, Gao C, Wu H, et al. Structural Insights into Neonatal Fc Receptor-Based Recycling Mechanisms. *J Biol Chem* (2014) 289(11):7812-24. Epub 2014/01/29. doi: 10.1074/jbc.M113.537563.

76. Ben-Chetrit E, Chan EK, Sullivan KF, Tan EM. A 52-Kd Protein Is a Novel Component of the Ss-a/Ro Antigenic Particle. *J Exp Med* (1988) 167(5):1560-71. doi: 10.1084/jem.167.5.1560.

77. Moutsopoulos HM, Skopouli FN, Sarras AK, Tsampoulas C, Mavridis AK, Constantopoulos SH, et al. Anti-Ro(Ssa) Positive Rheumatoid Arthritis (Ra): A Clinicoserological Group of Patients with High Incidence of D-Penicillamine Side Effects. *Ann Rheum Dis* (1985) 44(4):215. doi: 10.1136/ard.44.4.215.

78. Chan EK, Hamel JC, Buyon JP, Tan EM. Molecular Definition and Sequence Motifs of the 52-Kd Component of Human Ss-a/Ro Autoantigen. *J Clin Investig* (1991) 87(1):68-76. doi: 10.1172/jci115003.

79. Hudson M, Pope J, Mahler M, Tatibouet S, Steele R, Baron M, et al. Clinical Significance of Antibodies to Ro52/Trim21 in Systemic Sclerosis. *Arthritis Res Ther* (2012) 14(2):R50. Epub 2012/03/08. doi: 10.1186/ar3763.

80. Itoh Y, Rader MD, Reichlin M. Heterogeneity of the Ro/Ssa Antigen and Autoanti-Ro/Ssa Response: Evidence of the Four Antigenically Distinct Forms. *Clin Exp Immunol* (1990) 81(1):45-51. doi: 10.1111/j.1365-2249.1990.tb05289.x.

81. Slobbe RL, Pruijn GJM, Damen WGM, Kemp JWCM, Venrooij WJ. Detection and Occurrence of the 60- and 52-Kd Ro (Ss-a) Antigens and of Autoantibodies against These Proteins. *Clin Exp Immunol* (1991) 86(1):99-105. doi: 10.1111/j.1365-2249.1991.tb05780.x.

82. Rhodes DA, Ihrke G, Reinicke AT, Malcherek G, Towey M, Isenberg DA, et al. The 52 000 Mw Ro/Ss-a Autoantigen in Sjogren's Syndrome/Systemic Lupus Erythematosus (Ro52) Is an Interferon-Gamma Inducible Tripartite Motif Protein Associated with Membrane Proximal Structures. *Immunology* (2002) 106(2):246-56. doi: 10.1046/j.1365-2567.2002.01417.x.

83. Salomonsson S, Sonesson S-E, Ottosson L, Muhallab S, Olsson T, Sunnerhagen M, et al. Ro/Ssa Autoantibodies Directly Bind Cardiomyocytes, Disturb Calcium Homeostasis, and Mediate Congenital Heart Block. *J Exp Med* (2005) 201(1):11-7. doi: 10.1084/jem.20041859.

84. Oke V, Wahren-Herlenius M. The Immunobiology of Ro52 (Trim21) in Autoimmunity: A Critical Review. *J Autoimmun* (2012) 39(1-2):77-82. Epub 2012/03/10. doi: 10.1016/j.jaut.2012.01.014.

85. McNab FW, Rajsbaum R, Stoye JP, O'Garra A. Tripartite-Motif Proteins and Innate Immune Regulation. *Curr Opin Immunol* (2011) 23(1):46-56. Epub 2010/12/07. doi: 10.1016/j.coi.2010.10.021.

86. James LC, Keeble AH, Khan Z, Rhodes DA, Trowsdale J. Structural Basis for Pryspry-Mediated Tripartite Motif (Trim) Protein Function. *Proc National Acad Sci* (2007) 104(15):6200-5. doi: 10.1073/pnas.0609174104.

87. Rhodes DA, Trowsdale J. Trim21 Is a Trimeric Protein That Binds Igg Fc Via the B30.2 Domain. *Mol Immunol* (2007) 44(9):2406-14. Epub 2006/11/23. doi: 10.1016/j.molimm.2006.10.013.

88. Marin I. Origin and Diversification of Trim Ubiquitin Ligases. *PLoS ONE* (2012) 7(11):e50030. Epub 2012/11/28. doi: 10.1371/journal.pone.0050030.

89. Ozato K, Shin DM, Chang TH, Morse HC, 3rd. Trim Family Proteins and Their Emerging Roles in Innate Immunity. *Nat Rev Immunol* (2008) 8(11):849-60. Epub 2008/10/07. doi: 10.1038/nri2413.

90. Reymond A, Meroni G, Fantozzi A, Merla G, Cairo S, Luzi L, et al. The Tripartite Motif Family Identifies Cell Compartments. *Embo J* (2001) 20(9):2140-51. doi: 10.1093/emboj/20.9.2140.

91. Jaworska AM, Wlodarczyk NA, Mackiewicz A, Czerwinska P. The Role of Trim Family Proteins in the Regulation of Cancer Stem Cell Self-Renewal. *Stem Cells* (2020) 38(2):165-73. Epub 2019/10/31. doi: 10.1002/stem.3109.

92. Keeble AH, Khan Z, Forster A, James LC. Trim21 Is an Igg Receptor That Is Structurally, Thermodynamically, and Kinetically Conserved. *Proc National Acad Sci* (2008) 105(16):6045-50. doi: 10.1073/pnas.0800159105.

93. Deshaies RJ, Joazeiro CA. Ring Domain E3 Ubiquitin Ligases. *Annu Rev Biochem* (2009) 78:399-434. Epub 2009/06/06. doi: 10.1146/annurev.biochem.78.101807.093809.

94. Fletcher AJ, Mallery DL, Watkinson RE, Dickson CF, James LC. Sequential Ubiquitination and Deubiquitination Enzymes Synchronize the Dual Sensor and Effector Functions of Trim21. *Proc National Acad Sci* (2015) 112(32):10014-9. doi: 10.1073/pnas.1507534112.

95. Kiss L, Zeng J, Dickson CF, Mallery DL, Yang J-C, McLaughlin SH, et al. A Tri-Ionic Anchor Mechanism Drives Ube2n-Specific Recruitment and K63-Chain Ubiquitination in Trim Ligases. *Nat Commun* (2019) 10(1):4502. doi: 10.1038/s41467-019-12388-y.

96. McEwan WA, Tam JCH, Watkinson RE, Bidgood SR, Mallery DL, James LC. Intracellular Antibody-Bound Pathogens Stimulate Immune Signaling Via the Fc Receptor Trim21. *Nat Immunol* (2013) 14(4):327. doi: 10.1038/ni.2548.

97. Kiss L, Clift D, Renner N, Neuhaus D, James LC. Ring Domains Act as Both Substrate and Enzyme in a Catalytic Arrangement to Drive Self-Anchored Ubiquitination. *Nat Commun* (2021) 12(1):1220. doi: 10.1038/s41467-021-21443-6.

98. Dickson C, Fletcher AJ, Vaysburd M, Yang J-C, Mallery DL, Zeng J, et al. Intracellular Antibody Signalling Is Regulated by Phosphorylation of the Fc Receptor Trim21. *Elife* (2018) 7:e32660. doi: 10.7554/elife.32660.

99. Zeng J, Santos AF, Mukadam AS, Osswald M, Jacques DA, Dickson CF, et al. Target-Induced Clustering Activates Trim-Away of Pathogens and Proteins. *Nat Struct Mol Biol* (2021):1-12. doi: 10.1038/s41594-021-00560-2.

100. Fiorentini F, Esposito D, Rittinger K. Does It Take Two to Tango? Ring Domain Self-Association and Activity in Trim E3 Ubiquitin Ligases. *Biochem Soc Trans* (2020) 48(6):2615-24. doi: 10.1042/bst20200383.

101. Sanchez JG, Okreglicka K, Chandrasekaran V, Welker JM, Sundquist WI, Pornillos O. The Tripartite Motif Coiled-Coil Is an Elongated Antiparallel Hairpin Dimer. *Proceedings of the National Academy of Sciences* (2014) 111(7):2494-9. doi: 10.1073/pnas.1318962111.

102. Wang H-T, Hur S. Substrate Recognition by Trim and Trim-Like Proteins in Innate Immunity. *Semin Cell Dev Biol* (2021) 111:76-85. doi: 10.1016/j.semcdb.2020.09.013.

103. Sanchez JG, Chiang JJ, Sparrer KMJ, Alam SL, Chi M, Roganowicz MD, et al. Mechanism of Trim25 Catalytic Activation in the Antiviral Rig-I Pathway. *Cell Rep* (2016) 16(5):1315-25. Epub 2016/07/19. doi: 10.1016/j.celrep.2016.06.070.

104. Dou H, Buetow L, Sibbet GJ, Cameron K, Huang DT. Birc7-E2 Ubiquitin Conjugate Structure Reveals the Mechanism of Ubiquitin Transfer by a Ring Dimer. *Nat Struct Mol Biol* (2012) 19(9):876-83. Epub 2012/08/21. doi: 10.1038/nsmb.2379.

105. Koliopoulos MG, Esposito D, Christodoulou E, Taylor IA, Rittinger K. Functional Role of Trim E3 Ligase Oligomerization and Regulation of Catalytic Activity. *Embo J* (2016) 35(11):1204-18. Epub 2016/05/08. doi: 10.15252/embj.201593741.

106. Plechanovova A, Jaffray EG, McMahon SA, Johnson KA, Navratilova I, Naismith JH, et al. Mechanism of Ubiquitylation by Dimeric Ring Ligase Rnf4. *Nat Struct Mol Biol* (2011) 18(9):1052-9. Epub 2011/08/23. doi: 10.1038/nsmb.2108.

107. Bidgood SR, Tam JCH, McEwan WA, Mallery DL, James LC. Translocalized Iga Mediates Neutralization and Stimulates Innate Immunity inside Infected Cells. *Proc National Acad Sci* (2014) 111(37):13463-8. doi: 10.1073/pnas.1410980111.

108. Zeng J, Slodkowicz G, James LC. Rare Missense Variants in the Human Cytosolic Antibody Receptor Preserve Antiviral Function. *Elife* (2019) 8. Epub 2019/10/16. doi: 10.7554/eLife.48339.

109. Foss S, Bottermann M, Jonsson A, Sandlie I, James LC, Andersen JT. Trim21—from Intracellular Immunity to Therapy. *Front Immunol* (2019) 10:2049. doi: 10.3389/fimmu.2019.02049.

110. Caddy SL, Vaysburd M, Wing M, Foss S, Andersen JT, O'Connell K, et al. Intracellular Neutralisation of Rotavirus by Vp6-Specific Igg. *Plos Pathog* (2020) 16(8):e1008732. doi: 10.1371/journal.ppat.1008732.

111. Vaysburd M, Watkinson RE, Cooper H, Reed M, O'Connell K, Smith J, et al. Intracellular Antibody Receptor Trim21 Prevents Fatal Viral Infection. *Proc National Acad Sci* (2013) 110(30):12397-401. doi: 10.1073/pnas.1301918110.

112. Watkinson RE, McEwan WA, James LC. Intracellular Antibody Immunity. *J Clin Immunol* (2014) 34(Suppl 1):30-4. doi: 10.1007/s10875-014-0017-4.

113. Watkinson RE, Tam JCH, Vaysburd MJ, James LC. Simultaneous Neutralization and Innate Immune Detection of a Replicating Virus by Trim21. *J Virol* (2013) 87(13):7309-13. doi: 10.1128/jvi.00647-13.

114. Watkinson RE, McEwan WA, Tam JC, Vaysburd M, James LC. Trim21 Promotes Cgas and Rig-I Sensing of Viral Genomes During Infection by Antibody-Opsonized Virus. *Plos Pathog* (2015) 11(10):e1005253. Epub 2015/10/28. doi: 10.1371/journal.ppat.1005253.

115. McEwan WA, James LC. Trim21-Dependent Intracellular Antibody Neutralization of Virus Infection. *Prog Mol Biol Transl* (2015) 129:167-87. doi: 10.1016/bs.pmbts.2014.10.006.

116. Foss S, Watkinson R, Sandlie I, James LC, Andersen JT. Trim21: A Cytosolic Fc Receptor with Broad Antibody Isotype Specificity. *Immunol Rev* (2015) 268(1):328-39. doi: 10.1111/imr.12363.

117. Fletcher AJ, James LC. Coordinated Neutralization and Immune Activation by the Cytosolic Antibody Receptor Trim21. *J Virol* (2016) 90(10):4856-9. doi: 10.1128/jvi.00050-16.

118. Hauler F, Mallery DL, McEwan WA, Bidgood SR, James LC. Aaa Atpase P97/Vcp Is Essential for Trim21-Mediated Virus Neutralization. *Proc National Acad Sci* (2012) 109(48):19733-8. doi: 10.1073/pnas.1210659109.

119. Lee AYS. A Review of the Role and Clinical Utility of Anti-Ro52/Trim21 in Systemic Autoimmunity. *Rheumatol Int* (2017) 37(8):1323-33. doi: 10.1007/s00296-017-3718-1.

120. Caddy SL, Vaysburd M, Papa G, Wing M, O'Connell K, Stoycheva D, et al. Viral Nucleoprotein Antibodies Activate Trim21 and Induce T Cell Immunity. *Embo J* (2020):e106228. doi: 10.15252/embj.2020106228.

121. McEwan WA, Falcon B, Vaysburd M, Clift D, Oblak AL, Ghetti B, et al. Cytosolic Fc Receptor Trim21 Inhibits Seeded Tau Aggregation. *Proc National Acad Sci* (2017) 114(3):574-9. doi: 10.1073/pnas.1607215114.

122. Sarri N, Papadopoulos N, Lennartsson J, Heldin C-H. The E3 Ubiquitin Ligase Trim21 Regulates Basal Levels of Pdgfrβ. *Int J Mol Sci* (2023) 24(9):7782. doi: 10.3390/ijms24097782.

123. Zhang L, Afolabi LO, Wan X, Li Y, Chen L. Emerging Roles of Tripartite Motif-Containing Family Proteins (Trims) in Eliminating Misfolded Proteins. *Front Cell Dev Biol* (2020) 8:802. doi: 10.3389/fcell.2020.00802.

124. Alomari M. Trim21 - a Potential Novel Therapeutic Target in Cancer. *Pharmacol Res* (2021):105443. doi: 10.1016/j.phrs.2021.105443.

125. Zhao Z, Wang Y, Yun D, Huang Q, Meng D, Li Q, et al. Trim21 Overexpression Promotes Tumor Progression by Regulating Cell Proliferation, Cell Migration and Cell Senescence in Human Glioma. *Am J cancer Res* (2019) 10(1):114-30.

126. Rakebrandt N, Lentes S, Neumann H, James LC, Neumann-Staubitz P. Antibody- and Trim21-Dependent Intracellular Restriction of Salmonella Enterica. *Pathog Dis* (2014) 72(2):131-7. doi: 10.1111/2049-632x.12192.

127. Kimura T, Jain A, Choi SW, Mandell MA, Schroder K, Johansen T, et al. Trim-Mediated Precision Autophagy Targets Cytoplasmic Regulators of Innate Immunity. *J Cell Biol* (2015) 210(6):973-89. Epub 2015/09/09. doi: 10.1083/jcb.201503023.

128. Vaughn DE, Bjorkman PJ. Structural Basis of Ph-Dependent Antibody Binding by the Neonatal Fc Receptor. *Structure* (1998) 6(1):63-73. Epub 1998/03/11. doi: 10.1016/s0969-2126(98)00008-2.

129. Martin WL, West AP, Jr., Gan L, Bjorkman PJ. Crystal Structure at 2.8 a of an Fcrn/Heterodimeric Fc Complex: Mechanism of Ph-Dependent Binding. *Mol Cell* (2001) 7(4):867-77. Epub 2001/05/05. doi: 10.1016/s1097-2765(01)00230-1.

130. West AP, Jr., Bjorkman PJ. Crystal Structure and Immunoglobulin G Binding Properties of the Human Major Histocompatibility Complex-Related Fc Receptor(,). *Biochemistry* (2000) 39(32):9698-708. Epub 2000/08/10. doi: 10.1021/bi000749m.

131. Raghavan M, Bonagura VR, Morrison SL, Bjorkman PJ. Analysis of the Ph Dependence of the Neonatal Fc Receptor/Immunoglobulin G Interaction Using Antibody and Receptor Variants. *Biochemistry* (1995) 34(45):14649-57. Epub 1995/11/14. doi: 10.1021/bi00045a005.

132. Goebl NA, Babbey CM, Datta-Mannan A, Witcher DR, Wroblewski VJ, Dunn KW. Neonatal Fc Receptor Mediates Internalization of Fc in Transfected Human Endothelial Cells. *Mol Biol Cell* (2008) 19(12):5490-505. Epub 2008/10/10. doi: 10.1091/mbc.e07-02-0101.

133. Kim JK, Tsen MF, Ghetie V, Ward ES. Localization of the Site of the Murine Igg1 Molecule That Is Involved in Binding to the Murine Intestinal Fc Receptor. *Eur J Immunol* (1994) 24(10):2429-34. Epub 1994/10/01. doi: 10.1002/eji.1830241025.

134. Ober RJ, Martinez C, Lai X, Zhou J, Ward ES. Exocytosis of Igg as Mediated by the Receptor, Fcrn: An Analysis at the Single-Molecule Level. *Proc Natl Acad Sci U S A* (2004) 101(30):11076-81. Epub 2004/07/20. doi: 10.1073/pnas.0402970101.

135. Ober RJ, Martinez C, Vaccaro C, Zhou J, Ward ES. Visualizing the Site and Dynamics of Igg Salvage by the Mhc Class I-Related Receptor, Fcrn. *J Immunol* (2004) 172(4):2021-9. Epub 2004/02/07. doi: 10.4049/jimmunol.172.4.2021.

136. Sun Y, Estevez A, Schlothauer T, Wecksler AT. Antigen Physiochemical Properties Allosterically Effect the Igg Fc-Region and Fc Neonatal Receptor Affinity. *MAbs* (2020) 12(1):1802135. Epub 2020/08/17. doi: 10.1080/19420862.2020.1802135.

137. Hubbard JJ, Pyzik M, Rath T, Kozicky LK, Sand KMK, Gandhi AK, et al. Fcrn Is a Cd32a Coreceptor That Determines Susceptibility to Igg Immune Complex-Driven Autoimmunity. *J Exp Med* (2020) 217(10). Epub 2020/07/14. doi: 10.1084/jem.20200359.

138. Wines BD, Powell MS, Parren PW, Barnes N, Hogarth PM. The Igg Fc Contains Distinct Fc Receptor (Fcr) Binding Sites: The Leukocyte Receptors Fc Gamma Ri and Fc Gamma Riia Bind to a Region in the Fc Distinct from That Recognized by Neonatal Fcr and Protein A. *J Immunol* (2000) 164(10):5313-8. Epub 2000/05/09. doi: 10.4049/jimmunol.164.10.5313.

139. Datta-Mannan A, Witcher DR, Lu J, Wroblewski VJ. Influence of Improved Fcrn Binding on the Subcutaneous Bioavailability of Monoclonal Antibodies in Cynomolgus Monkeys. *MAbs* (2012) 4(2):267-73. Epub 2012/03/02. doi: 10.4161/mabs.4.2.19364.

140. Giragossian C, Clark T, Piche-Nicholas N, Bowman CJ. Neonatal Fc Receptor and Its Role in the Absorption, Distribution, Metabolism and Excretion of Immunoglobulin G-Based Biotherapeutics. *Curr Drug Metab* (2013) 14(7):764-90. Epub 2013/08/21. doi: 10.2174/13892002113149990099.

141. Karulin A, Dzantiev BB. Polyvalent Interaction of Antibodies with Bacterial Cells. *Mol Immunol* (1990) 27(10):965-71. Epub 1990/10/01. doi: 10.1016/0161-5890(90)90119-k.

142. Ko S, Jo M, Jung ST. Recent Achievements and Challenges in Prolonging the Serum Half-Lives of Therapeutic Igg Antibodies through Fc Engineering. *BioDrugs* (2021) 35(2):147-57. Epub 2021/02/21. doi: 10.1007/s40259-021-00471-0.

143. Vaccaro C, Bawdon R, Wanjie S, Ober RJ, Ward ES. Divergent Activities of an Engineered Antibody in Murine and Human Systems Have Implications for Therapeutic Antibodies. *Proc Natl Acad Sci U S A* (2006) 103(49):18709-14. Epub 2006/11/23. doi: 10.1073/pnas.0606304103.

144. Vaccaro C, Zhou J, Ober RJ, Ward ES. Engineering the Fc Region of Immunoglobulin G to Modulate in Vivo Antibody Levels. *Nat Biotechnol* (2005) 23(10):1283-8. Epub 2005/09/28. doi: 10.1038/nbt1143.

145. Dall'Acqua WF, Kiener PA, Wu H. Properties of Human Igg1s Engineered for Enhanced Binding to the Neonatal Fc Receptor (Fcrn). *J Biol Chem* (2006) 281(33):23514-24. Epub 2006/06/24. doi: 10.1074/jbc.M604292200.

146. Martin WL, Bjorkman PJ. Characterization of the 2:1 Complex between the Class I Mhc-Related Fc Receptor and Its Fc Ligand in Solution. *Biochemistry* (1999) 38(39):12639-47. Epub 1999/10/03. doi: 10.1021/bi9913505.

147. Popov S, Hubbard JG, Kim J, Ober B, Ghetie V, Ward ES. The Stoichiometry and Affinity of the Interaction of Murine Fc Fragments with the Mhc Class I-Related Receptor, Fcrn. *Mol Immunol* (1996) 33(6):521-30. Epub 1996/04/01. doi: 10.1016/0161-5890(96)00004-1.

148. Abdiche YN, Yeung YA, Chaparro-Riggers J, Barman I, Strop P, Chin SM, et al. The Neonatal Fc Receptor (Fcrn) Binds Independently to Both Sites of the Igg Homodimer with Identical Affinity. *MAbs* (2015) 7(2):331-43. Epub 2015/02/07. doi: 10.1080/19420862.2015.1008353.

149. Tesar DB, Tiangco NE, Bjorkman PJ. Ligand Valency Affects Transcytosis, Recycling and Intracellular Trafficking Mediated by the Neonatal Fc Receptor. *Traffic* (2006) 7(9):1127-42. Epub 2006/09/28. doi: 10.1111/j.1600-0854.2006.00457.x.

150. Jensen PF, Larraillet V, Schlothauer T, Kettenberger H, Hilger M, Rand KD. Investigating the Interaction between the Neonatal Fc Receptor and Monoclonal Antibody Variants by Hydrogen/Deuterium Exchange Mass Spectrometry. *Mol Cell Proteomics* (2015) 14(1):148-61. Epub 2014/11/08. doi: 10.1074/mcp.M114.042044.

151. Piche-Nicholas NM, Avery LB, King AC, Kavosi M, Wang M, O'Hara DM, et al. Changes in Complementarity-Determining Regions Significantly Alter Igg Binding to the Neonatal Fc Receptor (Fcrn) and Pharmacokinetics. *MAbs* (2018) 10(1):81-94. Epub 2017/10/11. doi: 10.1080/19420862.2017.1389355.

152. Rossini S, Noe R, Daventure V, Lecerf M, Justesen S, Dimitrov JD. V Region of Igg Controls the Molecular Properties of the Binding Site for Neonatal Fc Receptor. *J Immunol* (2020) 205(10):2850-60. Epub 2020/10/21. doi: 10.4049/jimmunol.2000732.

153. Schlothauer T, Rueger P, Stracke JO, Hertenberger H, Fingas F, Kling L, et al. Analytical Fcrn Affinity Chromatography for Functional Characterization of Monoclonal Antibodies. *MAbs* (2013) 5(4):576-86. Epub 2013/06/15. doi: 10.4161/mabs.24981.

154. Schoch A, Kettenberger H, Mundigl O, Winter G, Engert J, Heinrich J, et al. Charge-Mediated Influence of the Antibody Variable Domain on Fcrn-Dependent Pharmacokinetics. *Proc Natl Acad Sci U S A* (2015) 112(19):5997-6002. Epub 2015/04/29. doi: 10.1073/pnas.1408766112.

155. Vidarsson G, Dekkers G, Rispens T. Igg Subclasses and Allotypes: From Structure to Effector Functions. *Front Immunol* (2014) 5:520. Epub 2014/11/05. doi: 10.3389/fimmu.2014.00520.

156. Bottermann M, Foss S, Tienen LMv, Vaysburd M, Cruickshank J, O'Connell K, et al. Trim21 Mediates Antibody Inhibition of Adenovirus-Based Gene Delivery and Vaccination. *Proc National Acad Sci* (2018) 115(41):201806314. doi: 10.1073/pnas.1806314115.

157. Bottermann M, James LC. Intracellular Antiviral Immunity. *Adv Virus Res* (2018) 100(Antioxid. Redox Signal. 22 2015):309-54. doi: 10.1016/bs.aivir.2018.01.002.

158. de Taeye SW, Rispens T, Vidarsson G. The Ligands for Human Igg and Their Effector Functions. *Antibodies* (2019) 8(2). Epub 2019/09/24. doi: 10.3390/antib8020030.

159. Raju TS. Terminal Sugars of Fc Glycans Influence Antibody Effector Functions of Iggs. *Curr Opin Immunol* (2008) 20(4):471-8. Epub 2008/07/09. doi: 10.1016/j.coi.2008.06.007.

160. Hoggan MD, Blacklow NR, Rowe WP. Studies of Small DNA Viruses Found in Various Adenovirus Preparations: Physical, Biological, and Immunological Characteristics. *Proc Natl Acad Sci U S A* (1966) 55(6):1467-74. Epub 1966/06/01. doi: 10.1073/pnas.55.6.1467.

161. Atchison RW, Casto BC, Hammon WM. Adenovirus-Associated Defective Virus Particles. *Science* (1965) 149(3685):754-6. Epub 1965/08/13. doi: 10.1126/science.149.3685.754.

162. Adams MJ, Lefkowitz EJ, King AM, Carstens EB. Ratification Vote on Taxonomic Proposals to the International Committee on Taxonomy of Viruses (2014). *Arch Virol* (2014) 159(10):2831-41. Epub 2014/06/08. doi: 10.1007/s00705-014-2114-3.

163. Weindler FW, Heilbronn R. A Subset of Herpes Simplex Virus Replication Genes Provides Helper Functions for Productive Adeno-Associated Virus Replication. *J Virol* (1991) 65(5):2476-83. Epub 1991/05/01. doi: 10.1128/JVI.65.5.2476-2483.1991.

164. Berns KI, Giraud C. Biology of Adeno-Associated Virus. *Curr Top Microbiol Immunol* (1996) 218:1-23. Epub 1996/01/01. doi: 10.1007/978-3-642-80207-2_1.

165. Rose JA, Berns KI, Hoggan MD, Koczot FJ. Evidence for a Single-Stranded Adenovirus-Associated Virus Genome: Formation of a DNA Density Hybrid on Release of Viral DNA. *Proc Natl Acad Sci U S A* (1969) 64(3):863-9. Epub 1969/11/01. doi: 10.1073/pnas.64.3.863.

166. Srivastava A, Lusby EW, Berns KI. Nucleotide Sequence and Organization of the Adeno-Associated Virus 2 Genome. *J Virol* (1983) 45(2):555-64. Epub 1983/02/01. doi: 10.1128/JVI.45.2.555-564.1983.

167. Madigan VJ, Asokan A. Engineering Aav Receptor Footprints for Gene Therapy. *Curr Opin Virol* (2016) 18:89-96. Epub 2016/06/05. doi: 10.1016/j.coviro.2016.05.001.

168. Nonnenmacher M, Weber T. Intracellular Transport of Recombinant Adeno-Associated Virus Vectors. *Gene Ther* (2012) 19(6):649-58. Epub 2012/02/24. doi: 10.1038/gt.2012.6.

169. Xie Q, Bu W, Bhatia S, Hare J, Somasundaram T, Azzi A, et al. The Atomic Structure of Adeno-Associated Virus (Aav-2), a Vector for Human Gene Therapy. *Proc Natl Acad Sci U S A* (2002) 99(16):10405-10. Epub 2002/07/24. doi: 10.1073/pnas.162250899.

170. Balakrishnan B, Jayandharan GR. Basic Biology of Adeno-Associated Virus (Aav) Vectors Used in Gene Therapy. *Curr Gene Ther* (2014) 14(2):86-100. Epub 2014/03/05. doi: 10.2174/1566523214666140302193709.

171. McCarty DM, Fu H, Monahan PE, Toulson CE, Naik P, Samulski RJ. Adeno-Associated Virus Terminal Repeat (Tr) Mutant Generates Self-Complementary Vectors to Overcome the Rate-Limiting Step to Transduction in Vivo. *Gene Ther* (2003) 10(26):2112-8. Epub 2003/11/20. doi: 10.1038/sj.gt.3302134.

172. Lusby E, Fife KH, Berns KI. Nucleotide Sequence of the Inverted Terminal Repetition in Adeno-Associated Virus DNA. *J Virol* (1980) 34(2):402-9. Epub 1980/05/01. doi: 10.1128/JVI.34.2.402-409.1980.

173. Xiaoyang Zhou, Guangping Gao, Roland A. Owens, You Lu, Roberto Calcedo, Jim Miller, et al. Roles of Inverted Terminal Repeats (Itrs) and Capsid Proteins from Novel Nhp Aavs in Raav Mediated Gene Transfer. *Molecular Therapy* (2005) 11. doi: 10.1016/j.ymthe.2005.06.407.

174. Chiorini JA, Wiener SM, Yang L, Smith RH, Safer B, Kilcoin NP, et al. The Roles of Aav Rep Proteins in Gene Expression and Targeted Integration. *Curr Top Microbiol Immunol* (1996) 218:25-33. Epub 1996/01/01. doi: 10.1007/978-3-642-80207-2_2.

175. Becerra SP, Koczot F, Fabisch P, Rose JA. Synthesis of Adeno-Associated Virus Structural Proteins Requires Both Alternative Mrna Splicing and Alternative Initiations from a Single Transcript. *J Virol* (1988) 62(8):2745-54. Epub 1988/08/01. doi: 10.1128/JVI.62.8.2745-2754.1988.

176. Flotte TR, Berns KI. Adeno-Associated Virus: A Ubiquitous Commensal of Mammals. *Hum Gene Ther* (2005) 16(4):401-7. Epub 2005/05/06. doi: 10.1089/hum.2005.16.401.

177. Sonntag F, Kother K, Schmidt K, Weghofer M, Raupp C, Nieto K, et al. The Assembly-Activating Protein Promotes Capsid Assembly of Different Adeno-Associated Virus Serotypes. *J Virol* (2011) 85(23):12686-97. Epub 2011/09/16. doi: 10.1128/JVI.05359-11.

178. Sonntag F, Schmidt K, Kleinschmidt JA. A Viral Assembly Factor Promotes Aav2 Capsid Formation in the Nucleolus. *Proc Natl Acad Sci U S A* (2010) 107(22):10220-5. Epub 2010/05/19. doi: 10.1073/pnas.1001673107.

179. Berns KI, Muzyczka N. Aav: An Overview of Unanswered Questions. *Hum Gene Ther* (2017) 28(4):308-13. Epub 2017/03/25. doi: 10.1089/hum.2017.048.

180. Summerford C, Samulski RJ. Membrane-Associated Heparan Sulfate Proteoglycan Is a Receptor for Adeno-Associated Virus Type 2 Virions. *J Virol* (1998) 72(2):1438-45. Epub 1998/01/28. doi: 10.1128/JVI.72.2.1438-1445.1998.

181. Pillay S, Meyer NL, Puschnik AS, Davulcu O, Diep J, Ishikawa Y, et al. An Essential Receptor for Adeno-Associated Virus Infection. *Nature* (2016) 530(7588):108-12. Epub 2016/01/28. doi: 10.1038/nature16465.

182. Pillay S, Zou W, Cheng F, Puschnik AS, Meyer NL, Ganaie SS, et al. Adeno-Associated Virus (Aav) Serotypes Have Distinctive Interactions with Domains of the Cellular Aav Receptor. *J Virol* (2017) 91(18). Epub 2017/07/07. doi: 10.1128/JVI.00391-17.

183. Berry GE, Asokan A. Cellular Transduction Mechanisms of Adeno-Associated Viral Vectors. *Curr Opin Virol* (2016) 21:54-60. Epub 2016/08/22. doi: 10.1016/j.coviro.2016.08.001.

184. Robinson TM, Ho ML, Wahlig B, Gough V, Banta A, Reyes Gamas K, et al. An Essential N-Terminal Serine-Rich Motif in the Aav Vp1 and Vp2 Subunits That May Play a Role in Viral Transcription. *Virology* (2020) 546:127-32. Epub 2020/05/27. doi: 10.1016/j.virol.2020.04.008.

185. Nonnenmacher ME, Cintrat JC, Gillet D, Weber T. Syntaxin 5-Dependent Retrograde Transport to the Trans-Golgi Network Is Required for Adeno-Associated Virus Transduction. *J Virol* (2015) 89(3):1673-87. Epub 2014/11/21. doi: 10.1128/JVI.02520-14.

186. Girod A, Wobus CE, Zadori Z, Ried M, Leike K, Tijssen P, et al. The Vp1 Capsid Protein of Adeno-Associated Virus Type 2 Is Carrying a Phospholipase A2 Domain Required for Virus Infectivity. *J Gen Virol* (2002) 83(Pt 5):973-8. Epub 2002/04/19. doi: 10.1099/0022-1317-83-5-973.

187. Stahnke S, Lux K, Uhrig S, Kreppel F, Hosel M, Coutelle O, et al. Intrinsic Phospholipase A2 Activity of Adeno-Associated Virus Is Involved in Endosomal Escape of Incoming Particles. *Virology* (2011) 409(1):77-83. Epub 2010/10/27. doi: 10.1016/j.virol.2010.09.025.

188. Sonntag F, Bleker S, Leuchs B, Fischer R, Kleinschmidt JA. Adeno-Associated Virus Type 2 Capsids with Externalized Vp1/Vp2 Trafficking Domains Are Generated Prior to Passage through the Cytoplasm and Are Maintained until Uncoating Occurs in the Nucleus. *J Virol* (2006) 80(22):11040-54. Epub 2006/09/08. doi: 10.1128/JVI.01056-06.

189. Bartlett JS, Wilcher R, Samulski RJ. Infectious Entry Pathway of Adeno-Associated Virus and Adeno-Associated Virus Vectors. *J Virol* (2000) 74(6):2777-85. Epub 2000/02/23. doi: 10.1128/jvi.74.6.2777-2785.2000.

190. Xiao PJ, Samulski RJ. Cytoplasmic Trafficking, Endosomal Escape, and Perinuclear Accumulation of Adeno-Associated Virus Type 2 Particles Are Facilitated by Microtubule Network. *J Virol* (2012) 86(19):10462-73. Epub 2012/07/20. doi: 10.1128/JVI.00935-12.

191. Johnson JS, Samulski RJ. Enhancement of Adeno-Associated Virus Infection by Mobilizing Capsids into and out of the Nucleolus. *J Virol* (2009) 83(6):2632-44. Epub 2008/12/26. doi: 10.1128/JVI.02309-08.

192. Nicolson SC, Samulski RJ. Recombinant Adeno-Associated Virus Utilizes Host Cell Nuclear Import Machinery to Enter the Nucleus. *J Virol* (2014) 88(8):4132-44. Epub 2014/01/31. doi: 10.1128/JVI.02660-13.

193. Ferrari FK, Samulski T, Shenk T, Samulski RJ. Second-Strand Synthesis Is a Rate-Limiting Step for Efficient Transduction by Recombinant Adeno-Associated Virus Vectors. *J Virol* (1996) 70(5):3227-34. Epub 1996/05/01. doi: 10.1128/JVI.70.5.3227-3234.1996.

194. Fisher KJ, Gao GP, Weitzman MD, DeMatteo R, Burda JF, Wilson JM. Transduction with Recombinant Adeno-Associated Virus for Gene Therapy Is Limited by Leading-Strand Synthesis. *J Virol* (1996) 70(1):520-32. Epub 1996/01/01. doi: 10.1128/JVI.70.1.520-532.1996.

195. Kotin RM, Siniscalco M, Samulski RJ, Zhu XD, Hunter L, Laughlin CA, et al. Site-Specific Integration by Adeno-Associated Virus. *Proc Natl Acad Sci U S A* (1990) 87(6):2211-5. Epub 1990/03/01. doi: 10.1073/pnas.87.6.2211.

196. Linden RM, Ward P, Giraud C, Winocour E, Berns KI. Site-Specific Integration by Adeno-Associated Virus. *Proc Natl Acad Sci U S A* (1996) 93(21):11288-94. Epub 1996/10/15. doi: 10.1073/pnas.93.21.11288.

197. Samulski RJ, Zhu X, Xiao X, Brook JD, Housman DE, Epstein N, et al. Targeted Integration of Adeno-Associated Virus (Aav) into Human Chromosome 19. *Embo J* (1991) 10(12):3941-50. Epub 1991/12/01. doi: 10.1002/j.1460-2075.1991.tb04964.x.

198. Surosky RT, Urabe M, Godwin SG, McQuiston SA, Kurtzman GJ, Ozawa K, et al. Adeno-Associated Virus Rep Proteins Target DNA Sequences to a Unique Locus in the Human Genome. *J Virol* (1997) 71(10):7951-9. Epub 1997/10/06. doi: 10.1128/JVI.71.10.7951-7959.1997.

199. Agbandje-McKenna M, Kleinschmidt J. Aav Capsid Structure and Cell Interactions. *Methods Mol Biol* (2011) 807:47-92. Epub 2011/10/29. doi: 10.1007/978-1-61779-370-7_3.

200. Laredj LN, Beard P. Adeno-Associated Virus Activates an Innate Immune Response in Normal Human Cells but Not in Osteosarcoma Cells. *J Virol* (2011) 85(24):13133-43. Epub 2011/10/01. doi: 10.1128/JVI.05407-11.

201. Popp L, Gomez E, Orji W, Ho M, Suh J, Segatori L. Tfeb-Mediated Activation of the Lysosome-Autophagy System Affects the Transduction Efficiency of Adeno-Associated Virus 2. *Virology* (2017) 510:1-8. Epub 2017/07/09. doi: 10.1016/j.virol.2017.06.030.

202. Zhang C, Zhou X, Yao T, Tian Z, Zhou D. Precision Fluorescent Labeling of an Adeno-Associated Virus Vector to Monitor the Viral Infection Pathway. *Biotechnol J* (2018) 13(4):e1700374. Epub 2018/01/23. doi: 10.1002/biot.201700374.

203. Dong JY, Fan PD, Frizzell RA. Quantitative Analysis of the Packaging Capacity of Recombinant Adeno-Associated Virus. *Hum Gene Ther* (1996) 7(17):2101-12. Epub 1996/11/10. doi: 10.1089/hum.1996.7.17-2101.

204. Grimm D, Kern A, Rittner K, Kleinschmidt JA. Novel Tools for Production and Purification of Recombinant Adenoassociated Virus Vectors. *Hum Gene Ther* (1998) 9(18):2745-60. Epub 1999/01/05. doi: 10.1089/hum.1998.9.18-2745.

205. Matsushita T, Elliger S, Elliger C, Podsakoff G, Villarreal L, Kurtzman GJ, et al. Adeno-Associated Virus Vectors Can Be Efficiently Produced without Helper Virus. *Gene Ther* (1998) 5(7):938-45. Epub 1998/11/14. doi: 10.1038/sj.gt.3300680.

206. McLaughlin SK, Collis P, Hermonat PL, Muzyczka N. Adeno-Associated Virus General Transduction Vectors: Analysis of Proviral Structures. *J Virol* (1988) 62(6):1963-73. Epub 1988/06/01. doi: 10.1128/JVI.62.6.1963-1973.1988.

207. Samulski RJ, Chang LS, Shenk T. Helper-Free Stocks of Recombinant Adeno-Associated Viruses: Normal Integration Does Not Require Viral Gene Expression. *J Virol* (1989) 63(9):3822-8. Epub 1989/09/01. doi: 10.1128/JVI.63.9.3822-3828.1989.

208. Xiao X, Li J, Samulski RJ. Production of High-Titer Recombinant Adeno-Associated Virus Vectors in the Absence of Helper Adenovirus. *J Virol* (1998) 72(3):2224-32. Epub 1998/03/14. doi: 10.1128/JVI.72.3.2224-2232.1998.

209. Kearns WG, Afione SA, Fulmer SB, Pang MC, Erikson D, Egan M, et al. Recombinant Adeno-Associated Virus (Aav-Cftr) Vectors Do Not Integrate in a Site-Specific Fashion in an Immortalized Epithelial Cell Line. *Gene Ther* (1996) 3(9):748-55. Epub 1996/09/01.

210. Nakai H, Yant SR, Storm TA, Fuess S, Meuse L, Kay MA. Extrachromosomal Recombinant Adeno-Associated Virus Vector Genomes Are Primarily Responsible for Stable Liver Transduction in Vivo. *J Virol* (2001) 75(15):6969-76. Epub 2001/07/04. doi: 10.1128/JVI.75.15.6969-6976.2001.

211. Buning H, Schmidt M. Adeno-Associated Vector Toxicity-to Be or Not to Be? *Mol Ther* (2015) 23(11):1673-5. Epub 2015/11/26. doi: 10.1038/mt.2015.182.

212. Donsante A, Miller DG, Li Y, Vogler C, Brunt EM, Russell DW, et al. Aav Vector Integration Sites in Mouse Hepatocellular Carcinoma. *Science* (2007) 317(5837):477. Epub 2007/07/28. doi: 10.1126/science.1142658.

213. Kumar SR, Markusic DM, Biswas M, High KA, Herzog RW. Clinical Development of Gene Therapy: Results and Lessons from Recent Successes. *Mol Ther Methods Clin Dev* (2016) 3:16034. Epub 2016/06/04. doi: 10.1038/mtm.2016.34.

214. Hitti FL, Yang AI, Gonzalez-Alegre P, Baltuch GH. Human Gene Therapy Approaches for the Treatment of Parkinson's Disease: An Overview of Current and Completed Clinical Trials. *Parkinsonism Relat Disord* (2019) 66:16-24. Epub 2019/07/22. doi: 10.1016/j.parkreldis.2019.07.018.

215. Luo J, Luo Y, Sun J, Zhou Y, Zhang Y, Yang X. Adeno-Associated Virus-Mediated Cancer Gene Therapy: Current Status. *Cancer Lett* (2015) 356(2 Pt B):347-56. Epub 2014/12/03. doi: 10.1016/j.canlet.2014.10.045.

216. Wang D, Tai PWL, Gao G. Adeno-Associated Virus Vector as a Platform for Gene Therapy Delivery. *Nat Rev Drug Discov* (2019) 18(5):358-78. Epub 2019/02/03. doi: 10.1038/s41573-019-0012-9.

217. Issa SS, Shaimardanova AA, Solovyeva VV, Rizvanov AA. Various Aav Serotypes and Their Applications in Gene Therapy: An Overview. *Cells* (2023) 12(5). Epub 2023/03/12. doi: 10.3390/cells12050785.

218. Manfredsson FP, Rising AC, Mandel RJ. Aav9: A Potential Blood-Brain Barrier Buster. *Mol Ther* (2009) 17(3):403-5. Epub 2009/02/28. doi: 10.1038/mt.2009.15.

219. Nathwani AC, Tuddenham EG, Rangarajan S, Rosales C, McIntosh J, Linch DC, et al. Adenovirus-Associated Virus Vector-Mediated Gene Transfer in Hemophilia B. *N Engl J Med* (2011) 365(25):2357-65. Epub 2011/12/14. doi: 10.1056/NEJMoa1108046.

220. Mendell JR, Al-Zaidy S, Shell R, Arnold WD, Rodino-Klapac LR, Prior TW, et al. Single-Dose Gene-Replacement Therapy for Spinal Muscular Atrophy. *N Engl J Med* (2017) 377(18):1713-22. Epub 2017/11/02. doi: 10.1056/NEJMoa1706198.

221. Oldenburg J. Phase 1-2 Trial of Aavs3 Gene Therapy in Patients with Hemophilia B. *N Engl J Med* (2022) 387(14):1336. Epub 2022/10/06. doi: 10.1056/NEJMc2210918.

222. Ozelo MC, Mahlangu J, Pasi KJ, Giermasz A, Leavitt AD, Laffan M, et al. Valoctocogene Roxaparvovec Gene Therapy for Hemophilia A. *N Engl J Med* (2022) 386(11):1013-25. Epub 2022/03/17. doi: 10.1056/NEJMoa2113708.

223. Pasi KJ, Rangarajan S, Mitchell N, Lester W, Symington E, Madan B, et al. Multiyear Follow-up of Aav5-Hfviii-Sq Gene Therapy for Hemophilia A. *N Engl J Med* (2020) 382(1):29-40. Epub 2020/01/02. doi: 10.1056/NEJMoa1908490.

224. Colella P, Ronzitti G, Mingozzi F. Emerging Issues in Aav-Mediated in Vivo Gene Therapy. *Mol Ther Methods Clin Dev* (2018) 8:87-104. Epub 2018/01/13. doi: 10.1016/j.omtm.2017.11.007.

225. Mingozzi F, High KA. Immune Responses to Aav Vectors: Overcoming Barriers to Successful Gene Therapy. *Blood* (2013) 122(1):23-36. Epub 2013/04/19. doi: 10.1182/blood-2013-01-306647.

226. Louis Jeune V, Joergensen JA, Hajjar RJ, Weber T. Pre-Existing Anti-Adeno-Associated Virus Antibodies as a Challenge in Aav Gene Therapy. *Hum Gene Ther Methods* (2013) 24(2):59-67. Epub 2013/02/28. doi: 10.1089/hgtb.2012.243.

227. Mingozzi F, High KA. Overcoming the Host Immune Response to Adeno-Associated Virus Gene Delivery Vectors: The Race between Clearance, Tolerance, Neutralization, and Escape. *Annu Rev Virol* (2017) 4(1):511-34. Epub 2017/09/30. doi: 10.1146/annurev-virology-101416-041936.

228. Vandamme C, Adjali O, Mingozzi F. Unraveling the Complex Story of Immune Responses to Aav Vectors Trial after Trial. *Hum Gene Ther* (2017) 28(11):1061-74. Epub 2017/08/25. doi: 10.1089/hum.2017.150.

229. Flotte TR. Liver Targeting with Raav7: Balancing Tropism with Immune Profiles. *Gene Ther* (2021) 28(3-4):115-6. Epub 2021/02/07. doi: 10.1038/s41434-021-00230-4.

230. Hajitou A. Targeted Systemic Gene Therapy and Molecular Imaging of Cancer Contribution of the Vascular-Targeted Aavp Vector. *Adv Genet* (2010) 69:65-82. Epub 2010/09/03. doi: 10.1016/S0065-2660(10)69008-6.

231. Calcedo R, Morizono H, Wang L, McCarter R, He J, Jones D, et al. Adeno-Associated Virus Antibody Profiles in Newborns, Children, and Adolescents. *Clin Vaccine Immunol* (2011) 18(9):1586-8. Epub 2011/07/22. doi: 10.1128/CVI.05107-11.

232. Shen W, Liu S, Ou L. Corrigendum: Raav Immunogenicity, Toxicity, and Durability in 255 Clinical Trials: A Meta-Analysis. *Front Immunol* (2022) 13:1104646. Epub 2023/02/07. doi: 10.3389/fimmu.2022.1104646.

233. Iorio RM, Syddall RJ, Sheehan JP, Bratt MA, Glickman RL, Riel AM. Neutralization Map of the Hemagglutinin-Neuraminidase Glycoprotein of Newcastle Disease Virus: Domains Recognized by Monoclonal Antibodies That Prevent Receptor Recognition. *J Virol* (1991) 65(9):4999-5006. Epub 1991/09/01. doi: 10.1128/JVI.65.9.4999-5006.1991.

234. Nicola AV, Ponce de Leon M, Xu R, Hou W, Whitbeck JC, Krummenacher C, et al. Monoclonal Antibodies to Distinct Sites on Herpes Simplex Virus (Hsv) Glycoprotein D Block Hsv Binding to Hvem. *J Virol* (1998) 72(5):3595-601. Epub 1998/04/29. doi: 10.1128/JVI.72.5.3595-3601.1998.

235. Wien MW, Filman DJ, Stura EA, Guillot S, Delpeyroux F, Crainic R, et al. Structure of the Complex between the Fab Fragment of a Neutralizing Antibody for Type 1 Poliovirus and Its Viral Epitope. *Nat Struct Biol* (1995) 2(3):232-43. Epub 1995/03/01. doi: 10.1038/nsb0395-232.

236. Wobus CE, Hugle-Dorr B, Girod A, Petersen G, Hallek M, Kleinschmidt JA. Monoclonal Antibodies against the Adeno-Associated Virus Type 2 (Aav-2) Capsid: Epitope Mapping and Identification of Capsid Domains Involved in Aav-2-Cell Interaction and Neutralization of Aav-2 Infection. *J Virol* (2000) 74(19):9281-93. Epub 2000/09/12. doi: 10.1128/jvi.74.19.9281-9293.2000.

237. Gurda BL, DiMattia MA, Miller EB, Bennett A, McKenna R, Weichert WS, et al. Capsid Antibodies to Different Adeno-Associated Virus Serotypes Bind Common Regions. *J Virol* (2013) 87(16):9111-24. Epub 2013/06/14. doi: 10.1128/JVI.00622-13.

238. Lochrie MA, Tatsuno GP, Christie B, McDonnell JW, Zhou S, Surosky R, et al. Mutations on the External Surfaces of Adeno-Associated Virus Type 2 Capsids That Affect Transduction and Neutralization. *J Virol* (2006) 80(2):821-34. Epub 2005/12/28. doi: 10.1128/JVI.80.2.821-834.2006.

239. McCraw DM, O'Donnell JK, Taylor KA, Stagg SM, Chapman MS. Structure of Adeno-Associated Virus-2 in Complex with Neutralizing Monoclonal Antibody A20. *Virology* (2012) 431(1-2):40-9. Epub 2012/06/12. doi: 10.1016/j.virol.2012.05.004.

240. Tseng YS, Agbandje-McKenna M. Mapping the Aav Capsid Host Antibody Response toward the Development of Second Generation Gene Delivery Vectors. *Front Immunol* (2014) 5:9. Epub 2014/02/14. doi: 10.3389/fimmu.2014.00009.

241. Fitzpatrick Z, Leborgne C, Barbon E, Masat E, Ronzitti G, van Wittenberghe L, et al. Influence of Pre-Existing Anti-Capsid Neutralizing and Binding Antibodies on Aav

Vector Transduction. *Mol Ther Methods Clin Dev* (2018) 9:119-29. Epub 2018/05/17. doi: 10.1016/j.omtm.2018.02.003.

242. Moskalenko M, Chen L, van Roey M, Donahue BA, Snyder RO, McArthur JG, et al. Epitope Mapping of Human Anti-Adeno-Associated Virus Type 2 Neutralizing Antibodies: Implications for Gene Therapy and Virus Structure. *J Virol* (2000) 74(4):1761-6. Epub 2000/01/22. doi: 10.1128/jvi.74.4.1761-1766.2000.

243. Schmidt M, Voutetakis A, Afione S, Zheng C, Mandikian D, Chiorini JA. Adeno-Associated Virus Type 12 (Aav12): A Novel Aav Serotype with Sialic Acid- and Heparan Sulfate Proteoglycan-Independent Transduction Activity. *J Virol* (2008) 82(3):1399-406. Epub 2007/11/30. doi: 10.1128/JVI.02012-07.

244. Chu WS, Ng J. Immunomodulation in Administration of Raav: Preclinical and Clinical Adjuvant Pharmacotherapies. *Front Immunol* (2021) 12:658038. Epub 2021/04/20. doi: 10.3389/fimmu.2021.658038.

245. Tse LV, Klinc KA, Madigan VJ, Castellanos Rivera RM, Wells LF, Havlik LP, et al. Structure-Guided Evolution of Antigenically Distinct Adeno-Associated Virus Variants for Immune Evasion. *Proc Natl Acad Sci U S A* (2017) 114(24):E4812-E21. Epub 2017/06/01. doi: 10.1073/pnas.1704766114.

246. Girod A, Ried M, Wobus C, Lahm H, Leike K, Kleinschmidt J, et al. Genetic Capsid Modifications Allow Efficient Re-Targeting of Adeno-Associated Virus Type 2. *Nat Med* (1999) 5(9):1052-6. Epub 1999/09/02. doi: 10.1038/12491.

247. Eichhoff AM, Borner K, Albrecht B, Schafer W, Baum N, Haag F, et al. Nanobody-Enhanced Targeting of Aav Gene Therapy Vectors. *Mol Ther Methods Clin Dev* (2019) 15:211-20. Epub 2019/11/07. doi: 10.1016/j.omtm.2019.09.003.

248. Hamann MV, Beschorner N, Vu XK, Hauber I, Lange UC, Traenkle B, et al. Improved Targeting of Human Cd4+ T Cells by Nanobody-Modified Aav2 Gene Therapy Vectors. *PLoS ONE* (2021) 16(12):e0261269. Epub 2021/12/21. doi: 10.1371/journal.pone.0261269.

249. Rue L, Jaspers T, Degors IMS, Noppen S, Schols D, De Strooper B, et al. Novel Human/Non-Human Primate Cross-Reactive Anti-Transferrin Receptor Nanobodies for Brain Delivery of Biologics. *Pharmaceutics* (2023) 15(6). Epub 2023/06/28. doi: 10.3390/pharmaceutics15061748.

250. Munch RC, Janicki H, Volker I, Rasbach A, Hallek M, Buning H, et al. Displaying High-Affinity Ligands on Adeno-Associated Viral Vectors Enables Tumor Cell-Specific and Safe Gene Transfer. *Mol Ther* (2013) 21(1):109-18. Epub 2012/09/13. doi: 10.1038/mt.2012.186.

251. Theuerkauf SA, Herrera-Carrillo E, John F, Zinser LJ, Molina MA, Riechert V, et al. Aav Vectors Displaying Bispecific Darpins Enable Dual-Control Targeted Gene Delivery. *Biomaterials* (2023) 303:122399. Epub 2023/11/23. doi: 10.1016/j.biomaterials.2023.122399.

252. Reul J, Frisch J, Engeland CE, Thalheimer FB, Hartmann J, Ungerechts G, et al. Tumor-Specific Delivery of Immune Checkpoint Inhibitors by Engineered Aav Vectors. *Front Oncol* (2019) 9:52. Epub 2019/03/07. doi: 10.3389/fonc.2019.00052.

253. Li C, Samulski RJ. Engineering Adeno-Associated Virus Vectors for Gene Therapy. *Nat Rev Genet* (2020) 21(4):255-72. Epub 2020/02/12. doi: 10.1038/s41576-019-0205-4.

254. Grimm D, Zolotukhin S. E Pluribus Unum: 50 Years of Research, Millions of Viruses, and One Goal--Tailored Acceleration of Aav Evolution. *Mol Ther* (2015) 23(12):1819-31. Epub 2015/09/22. doi: 10.1038/mt.2015.173.

255. Nonnenmacher M, van Bakel H, Hajjar RJ, Weber T. High Capsid-Genome Correlation Facilitates Creation of Aav Libraries for Directed Evolution. *Mol Ther* (2015) 23(4):675-82. Epub 2015/01/15. doi: 10.1038/mt.2015.3.

256. Nguyen HH, Park J, Kang S, Kim M. Surface Plasmon Resonance: A Versatile Technique for Biosensor Applications. *Sensors (Basel)* (2015) 15(5):10481-510. Epub 2015/05/08. doi: 10.3390/s150510481.

257. Drescher DG, Selvakumar D, Drescher MJ. Analysis of Protein Interactions by Surface Plasmon Resonance. *Adv Protein Chem Struct Biol* (2018) 110:1-30. Epub 2018/02/08. doi: 10.1016/bs.apcsb.2017.07.003.

258. Langer A, Hampel PA, Kaiser W, Knezevic J, Welte T, Villa V, et al. Protein Analysis by Time-Resolved Measurements with an Electro-Switchable DNA Chip. *Nat Commun* (2013) 4:2099. Epub 2013/07/11. doi: 10.1038/ncomms3099.

259. Rant U, Arinaga K, Scherer S, Pringsheim E, Fujita S, Yokoyama N, et al. Switchable DNA Interfaces for the Highly Sensitive Detection of Label-Free DNA Targets. *Proc Natl Acad Sci U S A* (2007) 104(44):17364-9. Epub 2007/10/24. doi: 10.1073/pnas.0703974104.

260. Muller-Landau H, Varela PF. Standard Operation Procedure for Switchsense Drx Systems. *Eur Biophys J* (2021) 50(3-4):389-400. Epub 2021/03/28. doi: 10.1007/s00249-021-01519-3.

261. Arinaga K, Rant U, Knezevic J, Pringsheim E, Tornow M, Fujita S, et al. Controlling the Surface Density of DNA on Gold by Electrically Induced Desorption. *Biosens Bioelectron* (2007) 23(3):326-31. Epub 2007/06/15. doi: 10.1016/j.bios.2007.04.012.

262. Ulrich Rant KA, Shozo Fujita, Naoki Yokoyama,Gerhard Abstreiter,and Marc Tornow. Dynamic Electrical Switching of Dnalayers on a Metal Surface. *Nano Lett 2004, 4, 12, 2441–2445* (2004). doi: 10.1021/nl0484494.

263. Kaiser W, Rant U. Conformations of End-Tethered DNA Molecules on Gold Surfaces: Influences of Applied Electric Potential, Electrolyte Screening, and Temperature. *J Am Chem Soc* (2010) 132(23):7935-45. Epub 2010/06/10. doi: 10.1021/ja908727d.

264. Rant U, Pringsheim E, Kaiser W, Arinaga K, Knezevic J, Tornow M, et al. Detection and Size Analysis of Proteins with Switchable DNA Layers. *Nano Lett* (2009) 9(4):1290-5. Epub 2009/02/28. doi: 10.1021/nl8026789.

265. Langer A, Kaiser W, Svejda M, Schwertler P, Rant U. Molecular Dynamics of DNA-Protein Conjugates on Electrified Surfaces: Solutions to the Drift-Diffusion Equation. *J Phys Chem B* (2014) 118(2):597-607. Epub 2014/01/01. doi: 10.1021/jp410640z.

266. Sendner C, Kim YW, Rant U, Arinaga K, Tornow M, Netz RR. Dynamics of End Grafted DNA Molecules and Possible Biosensor Applications. *physica status solidi (a)* (2006) 203(14):3476-91. doi: 10.1002/pssa.200622444.

267. Daub H, Traxler L, Ismajli F, Groitl B, Itzen A, Rant U. The Trimer to Monomer Transition of Tumor Necrosis Factor-Alpha Is a Dynamic Process That Is Significantly Altered by Therapeutic Antibodies. *Sci Rep* (2020) 10(1):9265. Epub 2020/06/11. doi: 10.1038/s41598-020-66123-5.

268. Daub HA. At the Far Ends of Kinetic Analysis - Very Fast and Slow Binding Transitions Resolved with a Novel Fluorescence-Based Biosensor. *Technische Universität München, Fakultät für Chemie* (2020).

269. Hampel PA, Strasser R, Fischer F, Rant U. Assembly and Characterization of a Slingshot DNA Nanostructure for the Analysis of Bivalent and Bispecific Analytes with Biosensors. *Langmuir* (2018) 34(49):14796-801. Epub 2018/10/03. doi: 10.1021/acs.langmuir.8b02124.

270. Knezevic J, Langer A, Hampel PA, Kaiser W, Strasser R, Rant U. Quantitation of Affinity, Avidity, and Binding Kinetics of Protein Analytes with a Dynamically Switchable Biosurface. *J Am Chem Soc* (2012) 134(37):15225-8. Epub 2012/09/06. doi: 10.1021/ja3061276.

271. Langer A, Schraml M, Strasser R, Daub H, Myers T, Heindl D, et al. Polymerase/DNA Interactions and Enzymatic Activity: Multi-Parameter Analysis with Electro-Switchable Biosurfaces. *Sci Rep* (2015) 5:12066. Epub 2015/07/16. doi: 10.1038/srep12066.

272. Staffler RP, R. Hils, M. Kaiser, W. Moller, F. M. Nucleotide Binding Kinetics and Conformational Change Analysis of Tissue Transglutaminase with Switchsense. *Anal Biochem* (2020) 605:113719. Epub 2020/07/23. doi: 10.1016/j.ab.2020.113719.

273. Mak S, Marszal A, Matscheko N, Rant U. Kinetic Analysis of Ternary and Binary Binding Modes of the Bispecific Antibody Emicizumab. *MAbs* (2023) 15(1):2149053. Epub 2022/12/02. doi: 10.1080/19420862.2022.2149053.

274. Young G, Kukura P. Interferometric Scattering Microscopy. *Annu Rev Phys Chem* (2019) 70:301-22. Epub 2019/04/13. doi: 10.1146/annurev-physchem-050317-021247.

275. Young G, Hundt N, Cole D, Fineberg A, Andrecka J, Tyler A, et al. Quantitative Mass Imaging of Single Biological Macromolecules. *Science* (2018) 360(6387):423-7. Epub 2018/04/28. doi: 10.1126/science.aar5839.

276. Hundt N. Label-Free, Mass-Sensitive Single-Molecule Imaging Using Interferometric Scattering Microscopy. *Essays Biochem* (2021) 65(1):81-91. Epub 2020/12/10. doi: 10.1042/EBC20200023.

277. Verschueren H. Interference Reflection Microscopy in Cell Biology: Methodology and Applications. *J Cell Sci* (1985) 75:279-301. Epub 1985/04/01. doi: 10.1242/jcs.75.1.279.

278. Ortega-Arroyo J, Kukura P. Interferometric Scattering Microscopy (Iscat): New Frontiers in Ultrafast and Ultrasensitive Optical Microscopy. *Phys Chem Chem Phys* (2012) 14(45):15625-36. Epub 2012/09/22. doi: 10.1039/c2cp41013c.

279. Barr VA, Bunnell SC. Interference Reflection Microscopy. *Curr Protoc Cell Biol* (2009) Chapter 4:Unit 4 23. Epub 2009/12/17. doi: 10.1002/0471143030.cb0423s45.

280. Cole D, Young G, Weigel A, Sebesta A, Kukura P. Label-Free Single-Molecule Imaging with Numerical-Aperture-Shaped Interferometric Scattering Microscopy. *ACS Photonics* (2017) 4(2):211-6. Epub 2017/03/04. doi: 10.1021/acsphotonics.6b00912.

281. Higuchi Y, Suzuki T, Arimori T, Ikemura N, Mihara E, Kirita Y, et al. Engineered Ace2 Receptor Therapy Overcomes Mutational Escape of Sars-Cov-2. *Nat Commun* (2021) 12(1):3802. Epub 2021/06/23. doi: 10.1038/s41467-021-24013-y.

282. Yin V, Lai S-H, Caniels TG, Brouwer PJM, Brinkkemper M, Aldon Y, et al. Probing Affinity, Avidity, Anti-Cooperativity, and Competition in Antibody and Receptor Binding to the Sars-Cov-2 Spike by Single Particle Mass Analyses. (2021). doi: 10.1101/2021.06.18.448939.

283. Soltermann F, Foley EDB, Pagnoni V, Galpin M, Benesch JLP, Kukura P, et al. Quantifying Protein-Protein Interactions by Molecular Counting with Mass Photometry. *Angew Chem Int Ed Engl* (2020) 59(27):10774-9. Epub 2020/03/14. doi: 10.1002/anie.202001578.

284. Naftaly A, Izgilov R, Omari E, Benayahu D. Revealing Advanced Glycation End Products Associated Structural Changes in Serum Albumin. *ACS Biomater Sci Eng* (2021) 7(7):3179-89. Epub 2021/06/19. doi: 10.1021/acsbiomaterials.1c00387.

285. Olerinyova A, Sonn-Segev A, Gault J, Eichmann C, Schimpf J, Kopf AH, et al. Mass Photometry of Membrane Proteins. *Chem* (2021) 7(1):224-36. Epub 2021/01/30. doi: 10.1016/j.chempr.2020.11.011.

286. Sonn-Segev A, Belacic K, Bodrug T, Young G, VanderLinden RT, Schulman BA, et al. Quantifying the Heterogeneity of Macromolecular Machines by Mass Photometry. *Nat Commun* (2020) 11(1):1772. Epub 2020/04/15. doi: 10.1038/s41467-020-15642-w.

287. Oostindie SC, Lazar GA, Schuurman J, Parren P. Avidity in Antibody Effector Functions and Biotherapeutic Drug Design. *Nat Rev Drug Discov* (2022) 21(10):715-35. Epub 2022/07/06. doi: 10.1038/s41573-022-00501-8.

288. Diebolder CA, Beurskens FJ, de Jong RN, Koning RI, Strumane K, Lindorfer MA, et al. Complement Is Activated by Igg Hexamers Assembled at the Cell Surface. *Science* (2014) 343(6176):1260-3. Epub 2014/03/15. doi: 10.1126/science.1248943.

289. Rouge L, Chiang N, Steffek M, Kugel C, Croll TI, Tam C, et al. Structure of Cd20 in Complex with the Therapeutic Monoclonal Antibody Rituximab. *Science* (2020) 367(6483):1224-30. Epub 2020/02/23. doi: 10.1126/science.aaz9356.

290. Hiramoto E, Tsutsumi A, Suzuki R, Matsuoka S, Arai S, Kikkawa M, et al. The Igm Pentamer Is an Asymmetric Pentagon with an Open Groove That Binds the Aim Protein. *Sci Adv* (2018) 4(10):eaau1199. Epub 2018/10/17. doi: 10.1126/sciadv.aau1199.

291. Patel KR, Roberts JT, Barb AW. Multiple Variables at the Leukocyte Cell Surface Impact Fc Gamma Receptor-Dependent Mechanisms. *Front Immunol* (2019) 10:223. Epub 2019/03/07. doi: 10.3389/fimmu.2019.00223.

292. Sondermann P, Szymkowski DE. Harnessing Fc Receptor Biology in the Design of Therapeutic Antibodies. *Curr Opin Immunol* (2016) 40:78-87. Epub 2016/04/03. doi: 10.1016/j.coi.2016.03.005.

293. Chiu ML, Goulet DR, Teplyakov A, Gilliland GL. Antibody Structure and Function: The Basis for Engineering Therapeutics. *Antibodies* (2019) 8(4). Epub 2019/12/11. doi: 10.3390/antib8040055.

294. Goulet DR, Zwolak A, Williams JA, Chiu ML, Atkins WM. Design and Characterization of Novel Dual Fc Antibody with Enhanced Avidity for Fc Receptors. *Proteins* (2020) 88(5):689-97. Epub 2019/11/09. doi: 10.1002/prot.25853.

295. Labrijn AF, Janmaat ML, Reichert JM, Parren P. Bispecific Antibodies: A Mechanistic Review of the Pipeline. *Nat Rev Drug Discov* (2019) 18(8):585-608. Epub 2019/06/09. doi: 10.1038/s41573-019-0028-1.

296. Wang Y, Yang S. Multispecific Drugs: The Fourth Wave of Biopharmaceutical Innovation. *Signal Transduct Target Ther* (2020) 5(1):86. Epub 2020/06/06. doi: 10.1038/s41392-020-0201-3.

297. Karush F. Multivalent Binding and Functional Affinity. *Contemp Top Mol Immunol* (1976) 5:217-28. Epub 1976/01/01. doi: 10.1007/978-1-4684-8142-6_8.

298. Yeung YA, Leabman MK, Marvin JS, Qiu J, Adams CW, Lien S, et al. Engineering Human Igg1 Affinity to Human Neonatal Fc Receptor: Impact of Affinity Improvement on Pharmacokinetics in Primates. *J Immunol* (2009) 182(12):7663-71. Epub 2009/06/06. doi: 10.4049/jimmunol.0804182.

299. Klein C, Schaefer W, Regula JT. The Use of Crossmab Technology for the Generation of Bi- and Multispecific Antibodies. *MAbs* (2016) 8(6):1010-20. Epub 2016/06/11. doi: 10.1080/19420862.2016.1197457.

300. Mazor Y, Sachsenmeier KF, Yang C, Hansen A, Filderman J, Mulgrew K, et al. Enhanced Tumor-Targeting Selectivity by Modulating Bispecific Antibody Binding Affinity and Format Valence. *Sci Rep* (2017) 7(1):40098. Epub 2017/01/10. doi: 10.1038/srep40098.

301. Mazor Y, Yang C, Borrok MJ, Ayriss J, Aherne K, Wu H, et al. Enhancement of Immune Effector Functions by Modulating Igg's Intrinsic Affinity for Target Antigen. *PLoS ONE* (2016) 11(6):e0157788. Epub 2016/06/21. doi: 10.1371/journal.pone.0157788.

302. Rudnick SI, Adams GP. Affinity and Avidity in Antibody-Based Tumor Targeting. *Cancer Biother Radio* (2009) 24(2):155-61. Epub 2009/05/05. doi: 10.1089/cbr.2009.0627.

303. Sellmann C, Doerner A, Knuehl C, Rasche N, Sood V, Krah S, et al. Balancing Selectivity and Efficacy of Bispecific Epidermal Growth Factor Receptor (Egfr) X C-Met Antibodies and Antibody-Drug Conjugates. *J Biol Chem* (2016) 291(48):25106-19. Epub 2016/10/04. doi: 10.1074/jbc.M116.753491.

304. Yang T, Baryshnikova OK, Mao H, Holden MA, Cremer PS. Investigations of Bivalent Antibody Binding on Fluid-Supported Phospholipid Membranes: The Effect of Hapten Density. *J Am Chem Soc* (2003) 125(16):4779-84. Epub 2003/04/17. doi: 10.1021/ja029469f.

305. Carman CV, Springer TA. Integrin Avidity Regulation: Are Changes in Affinity and Conformation Underemphasized? *Curr Opin Cell Biol* (2003) 15(5):547-56. Epub 2003/10/02. doi: 10.1016/j.ceb.2003.08.003.

306. Mitroulis I, Alexaki VI, Kourtzelis I, Ziogas A, Hajishengallis G, Chavakis T. Leukocyte Integrins: Role in Leukocyte Recruitment and as Therapeutic Targets in Inflammatory Disease. *Pharmacol Therapeut* (2015) 147:123-35. Epub 2014/12/03. doi: 10.1016/j.pharmthera.2014.11.008.

307. Vauquelin G, Charlton SJ. Exploring Avidity: Understanding the Potential Gains in Functional Affinity and Target Residence Time of Bivalent and Heterobivalent Ligands. *Brit J Pharmacol* (2013) 168(8):1771-85. Epub 2013/01/22. doi: 10.1111/bph.12106.

308. Mack ET, Snyder PW, Perez-Castillejos R, Whitesides GM. Using Covalent Dimers of Human Carbonic Anhydrase Ii to Model Bivalency in Immunoglobulins. *J Am Chem Soc* (2011) 133(30):11701-15. Epub 2011/06/16. doi: 10.1021/ja2038084.

309. MacKenzie CR, Hirama T, Deng SJ, Bundle DR, Narang SA, Young NM. Analysis by Surface Plasmon Resonance of the Influence of Valence on the Ligand Binding Affinity and Kinetics of an Anti-Carbohydrate Antibody. *J Biol Chem* (1996) 271(3):1527-33. Epub 1996/01/19. doi: 10.1074/jbc.271.3.1527.

310. Cooper MA, Williams DH. Kinetic Analysis of Antibody-Antigen Interactions at a Supported Lipid Monolayer. *Anal Biochem* (1999) 276(1):36-47. Epub 1999/12/10. doi: 10.1006/abio.1999.4333.

311. Zhang J, Tanha J, Hirama T, Khieu NH, To R, Tong-Sevinc H, et al. Pentamerization of Single-Domain Antibodies from Phage Libraries: A Novel Strategy for the Rapid Generation of High-Avidity Antibody Reagents. *J Mol Biol* (2004) 335(1):49-56. Epub 2003/12/09. doi: 10.1016/j.jmb.2003.09.034.

312. Steinfeld T, Hughes AD, Klein U, Smith JA, Mammen M. Thrx-198321 Is a Bifunctional Muscarinic Receptor Antagonist and Beta2-Adrenoceptor Agonist (Maba) That Binds in a Bimodal and Multivalent Manner. *Mol Pharmacol* (2011) 79(3):389-99. Epub 2010/12/09. doi: 10.1124/mol.110.069120.

313. Pisarchick ML, Thompson NL. Binding of a Monoclonal Antibody and Its Fab Fragment to Supported Phospholipid Monolayers Measured by Total Internal Reflection Fluorescence Microscopy. *Biophys J* (1990) 58(5):1235-49. Epub 1990/11/01. doi: 10.1016/S0006-3495(90)82464-4.

314. Tang Y, Lou J, Alpaugh RK, Robinson MK, Marks JD, Weiner LM. Regulation of Antibody-Dependent Cellular Cytotoxicity by Igg Intrinsic and Apparent Affinity for Target Antigen. *J Immunol* (2007) 179(5):2815-23. Epub 2007/08/22. doi: 10.4049/jimmunol.179.5.2815.

315. Schmidt MM, Thurber GM, Wittrup KD. Kinetics of Anti-Carcinoembryonic Antigen Antibody Internalization: Effects of Affinity, Bivalency, and Stability. *Cancer Immunol Immunother* (2008) 57(12):1879-90. Epub 2008/04/15. doi: 10.1007/s00262-008-0518-1.

316. Adams GP, Schier R, McCall AM, Crawford RS, Wolf EJ, Weiner LM, et al. Prolonged in Vivo Tumour Retention of a Human Diabody Targeting the Extracellular

Domain of Human Her2/Neu. *Brit J Cancer* (1998) 77(9):1405-12. Epub 1998/07/04. doi: 10.1038/bjc.1998.233.

317. Adams GP, Tai MS, McCartney JE, Marks JD, Stafford WF, 3rd, Houston LL, et al. Avidity-Mediated Enhancement of in Vivo Tumor Targeting by Single-Chain Fv Dimers. *Clin Cancer Res* (2006) 12(5):1599-605. Epub 2006/03/15. doi: 10.1158/1078-0432.CCR-05-2217.

318. Muller KM, Arndt KM, Pluckthun A. Model and Simulation of Multivalent Binding to Fixed Ligands. *Anal Biochem* (1998) 261(2):149-58. Epub 1998/08/26. doi: 10.1006/abio.1998.2725.

319. Vauquelin G. Simplified Models for Heterobivalent Ligand Binding: When Are They Applicable and Which Are the Factors That Affect Their Target Residence Time. *Naunyn-schmiedeberg's Archives Pharmacol* (2013) 386(11):949-62. Epub 2013/07/03. doi: 10.1007/s00210-013-0881-0.

320. Vauquelin G, Bricca G, Van Liefde I. Avidity and Positive Allosteric Modulation/Cooperativity Act Hand in Hand to Increase the Residence Time of Bivalent Receptor Ligands. *Fundam Clin Pharm* (2014) 28(5):530-43. Epub 2013/10/15. doi: 10.1111/fcp.12052.

321. Crothers DM, Metzger H. The Influence of Polyvalency on the Binding Properties of Antibodies. *Immunochemistry* (1972) 9(3):341-57. Epub 1972/03/01. doi: 10.1016/0019-2791(72)90097-3.

322. Gurbaxani B. Mathematical Modeling as Accounting: Predicting the Fate of Serum Proteins and Therapeutic Monoclonal Antibodies. *Clin Immunol* (2007) 122(2):121-4. Epub 2006/11/28. doi: 10.1016/j.clim.2006.10.001.

323. Gurbaxani BM, Morrison SL. Development of New Models for the Analysis of Fc-Fcrn Interactions. *Mol Immunol* (2006) 43(9):1379-89. Epub 2005/09/27. doi: 10.1016/j.molimm.2005.08.002.

324. Kaufman EN, Jain RK. Effect of Bivalent Interaction Upon Apparent Antibody-Affinity - Experimental Confirmation of Theory Using Fluorescence Photobleaching and Implications for Antibody-Binding Assays. *Cancer Res* (1992) 52(15):4157-67.

9
Acknowledgements

I am deeply grateful for the opportunity to have worked alongside so many remarkable individuals during my thesis journey.

I would like to express my profound gratitude to **PD Dr. Christian Klein** and **PD Dr. Gregor Witte**, my thesis advisors, for granting me the opportunity to pursue my PhD, and for their support and encouragement throughout my studies. Their insightful feedback has been invaluable to my research.

Immense thanks are due to **Dr. Laurent Larivière** and **Dr. Tilman Schlothauer**, whose guidance and expertise, along with their constructive critiques and valuable suggestions, have significantly shaped my work and facilitated my personal growth as an academic.

My sincere appreciation extends to my fellow researchers and friends - **Joachim**, **Thomas**, **and Ellis** - for their endless support, stimulating scientific discussions, assistance in designing new experiments when challenges arose, and, of course, for all the fun we have shared over the years.

I must also acknowledge the entire **FC department** for their consistent support whenever I reached out for assistance.

On a personal note, I would like to thank my parents, **Martina and Frank**, whose love and guidance are with me in whatever I pursue.
I reserve special thanks for my beloved wife, **Monja**, and my son, **Levi**, for enduring this long process with me, providing unwavering encouragement, and for all of the sacrifices that paved the way to this achievement. You are always there providing a loving environment that allowed me to momentarily set aside my work. This accomplishment would not have been possible without you.